Cosmic String Radiation with Adaptive Mesh Refinement

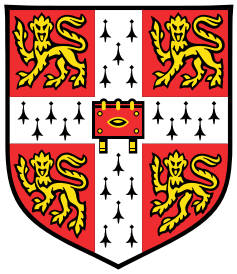

Amelia Louise Drew

Department of Applied Mathematics and Theoretical Physics
University of Cambridge

This thesis is submitted for the degree of
Doctor of Philosophy

Gonville and Caius College December 2020

Declaration

This thesis is the result of my own work and includes nothing which is the outcome of work done in collaboration except as specified in the text.

It is not substantially the same as any that I have submitted, or, is being concurrently submitted for a degree or diploma or other qualification at the University of Cambridge or any other University or similar institution.

I further state that no substantial part of my thesis has already been submitted, or, is being concurrently submitted for any such degree, diploma or other qualification at the University of Cambridge or any other University or similar institution.

This thesis does not exceed the prescribed word limit for the relevant Degree Committee.

Amelia Louise Drew
December 2020

Cosmic String Radiation with Adaptive Mesh Refinement

Amelia Louise Drew

Cosmic strings are a fundamental feature of many physically-motivated field theories which inevitably form in the early Universe, as a result of a symmetry breaking phase transition. An important example is the Peccei-Quinn mechanism, from which strings emerge as a potential source of dark matter axions. They are also a strong source of gravitational wave (GW) emission, with the potential for detection by the Laser Interferometer Gravitational-Wave Observatory (LIGO) and other GW experiments.

The nonlinear evolution of cosmic strings has been extensively studied using large-scale numerical simulations. However, the vast difference in scale between a typical string width and the string curvature poses a significant computational challenge. This is usually addressed by approximating the string to have either zero or fixed comoving width, resulting in inconsistencies in predictions between different methods. One technique that can address this issue is adaptive mesh refinement (AMR), which allows the resolution of the numerical grid to adapt to the scale of the features of interest in the simulation. This thesis uses `GRChombo`, a sophisticated code originally designed for numerical relativity, to perform the first AMR simulations of global cosmic strings. We also present our numerical contributions to `GRChombo` as a core developer, including novel diagnostic tools and performance enhancement.

We perform a detailed quantitative investigation of single sinusoidally displaced string configurations, comparing oscillating string trajectories with a backreaction model accounting for radiation energy losses. We conclude that analytic radiation modelling in the thin-string (Nambu-Goto) limit provides the appropriate picture for cosmological evolution. We also investigate the resulting massless (Goldstone boson or axion) and massive (Higgs) radiation signals, using quantitative diagnostic tools to determine their eigenmode decomposition. We find that the massless quadrupole is dominant and massive radiation is strongly suppressed with increasing mass, with a complex wavepacket structure that is sensitive to numerical resolution. String network configurations are also simulated, with advanced visualisation of radiation used to reveal new qualitative phenomena as strings reconnect and small loops decay. The thesis concludes with the cosmological implications of this work, considering dark matter axions radiated by cosmic strings and the outlook for gravitational wave signatures.

Acknowledgements

This thesis would not have been possible without the support and guidance of my friends, family and colleagues. I would first like to thank my supervisor, Paul Shellard, for his invaluable help and advice throughout the PhD, particularly for his encyclopedic knowledge of cosmic strings. I would also like to thank my advisor, Ulrich Sperhake, for his guidance and many useful conversations about numerical relativity.

I have thoroughly enjoyed being part of the `GRChombo` collaboration, and look forward to continuing work on code optimisation and development in the future. I would especially like to thank Kacper Kornet for his invaluable technical support, as well as Katy Clough, Pau Figueras and Eugene Lim for organising several enjoyable and productive collaboration meetings and providing advice and support. I would also like to thank Thomas Helfer, Josu Aurrekoetxea and Miren Radia for many insightful conversations about cosmic strings and code development, and all of the members of the `GRChombo` collaboration for creating such a supportive research environment.

I would further like to thank the `Chombo` developers at Lawrence Berkeley National Laboratory for their insight and collaboration on the optimisation of `GRChombo`, including for hosting me at Berkeley. I would particularly like to thank Dan Martin, Hans Johansen and Peter McCorquodale for their direct and continued input.

I would also like to thank the Intel Visualisation team, led by Jim Jeffers, notably the collaboration on in-situ visualisation with Carson Brownlee which has led to the production of some remarkable images of cosmic string radiation. I look forward to continuing this work in the future.

I would like to thank all of my friends in and outside Cambridge for their support during the last four years, especially to Chandrima, Izzy, Lander, Marissa and Martin. I would also particularly like to thank my housemates Ben, Navo, Joep and Liz for making writing up my thesis during COVID-19 an unexpectedly enjoyable experience, and to my friends and colleagues at DAMTP for four years of fascinating conversations over coffee.

I would finally like to thank my family for their ongoing love and support, especially to my parents for their encouragement and understanding throughout my PhD and prior education, and to my Nana, Dorothy, whose kindness and hard work continue to inspire me.

This PhD was funded by an EPSRC iCASE Studentship in partnership with Intel (EP/N509620/1, Voucher 16000206). Travel grants were also provided by Gonville and Caius College, used primarily towards attending academic conferences. I would like to thank the organisers of the Cosmic Topological Defects Workshop at the Lorentz Center, Leiden in 2018 for facilitating many particularly interesting discussions. I would also like to acknowledge networking support provided by the GWverse COST Action CA16104, 'Black holes, gravitational waves and fundamental physics.'

The majority of the simulations in this thesis were undertaken on the COSMOS supercomputer at the Department of Applied Mathematics and Theroretical Physics, University of Cambridge, funded by BEIS National E-infrastructure capital grants ST/J005673/1 and STFC grants ST/H008586/1, ST/K00333X/1. The Cambridge CSD3 part of the STFC DiRAC HPC Facility was also used, funded by BEIS capital funding via STFC capital grants ST/P002307/1 and ST/R002452/1 and STFC operations grant ST/R00689X/1.

Table of Contents

Declaration **iii**

Abstract **v**

Acknowledgements **vii**

1 Introduction **1**

2 Origin and Evolution of Cosmic Strings **7**

2.1 Cosmological Context 8

2.2 Field Theory of Cosmic Strings 8

2.2.1 Global $U(1)$ Field Theory 9

2.2.2 Local Strings in the Abelian-Higgs Model 15

2.3 Thin String Evolution and Radiation 16

2.3.1 Nambu-Goto Action and Equations of Motion for Local Strings . . 17

2.3.2 Kalb-Ramond Action for Global Strings 21

2.3.3 Radiation from Cosmic Strings 23

2.4 Separation of Scales and Current Discrepancies 25

3 Numerical Implementation with `GRChombo` **29**

3.1 Motivation for AMR 29

3.2 GRChombo . . . 34
3.2.1 Implementation of Adaptive Mesh Refinement . . . 34
3.2.2 Parallelism and Load Balancing . . . 37
3.2.3 Simulation Parameters . . . 39
3.2.4 Visualisation . . . 48
3.3 Initial Conditions . . . 48
3.3.1 Individual Oscillating Strings . . . 48
3.3.2 Travelling Waves . . . 53
3.3.3 Networks . . . 54
3.4 Diagnostic Tools . . . 54
3.4.1 Radiation Cylinder . . . 54
3.4.2 String Core Position . . . 59
3.5 Profiling and Code Development . . . 60
3.5.1 Separating Evolution from Diagnostic Variables . . . 62
3.5.2 Optimisation of FourthOrderFillPatch::fillInterp . . . 63

4 Massless (Axion) Radiation 65

4.1 Analytic Radiation Expectations . . . 66
4.1.1 Massive and Massless Radiation Modes . . . 66
4.1.2 Separation from Self-Field . . . 68
4.1.3 Separable Radiation Eigenmodes . . . 70
4.1.4 Dual Radiation Calculations and String Backreaction . . . 74
4.2 Massless Radiation Analysis . . . 79
4.2.1 Small Amplitude Oscillations . . . 80
4.2.2 Large Amplitude Oscillations . . . 85
4.3 String Radiation Backreaction . . . 90
4.3.1 Inverse Square Amplitude Model . . . 93

4.3.2 Exponential Damping 97

5 Massive Radiation **99**

5.1 Analytic Radiation Expectations 100

5.1.1 Massive Thresholds 100

5.1.2 Calculating α 102

5.1.3 Radiation Properties 104

5.1.4 Separation from Self-Field 106

5.2 Massive Radiation Analysis 106

5.2.1 Mode Decomposition 107

5.2.2 Relative Energy Loss to Massive and Massless Modes 113

5.2.3 Radiation Harmonics and λ-Dependence 117

5.2.4 Exponential Dependence of Massive Radiation 124

6 Towards Cusps and Networks **129**

6.1 Cusps 131

6.2 Networks 132

7 Conclusion and Future Directions **143**

7.1 Dark Matter Axions 145

7.2 Gravitational Wave Signatures 146

References **149**

Chapter 1

Introduction

Throughout history, theoretical physicists have striven to create accurate models of the Universe around us. These models are often built on the core assumption that there exists some underlying mathematical structure which underpins the laws that govern nature. The hallmark of a truly powerful theory therefore often lies in its ability to unite previously disparate physical concepts. One such example is symmetries and symmetry breaking in field theories, a fundamental pillar of particle physics that forms the basis of particle creation, whilst also providing a framework to describe phenomena that occur in condensed matter, such as the creation of domains in ferromagnetism. The universality of symmetry breaking suggests that it may have important applications to other areas of physics, including to the Universe as a whole.

A generic consequence of symmetry breaking is the formation of topological defects. These are localised, high-energy field configurations that can arise in systems which possess an underlying symmetry that is broken due to some external physical process. For a system taken initially to be in a high energy state, as the total energy of the system is lowered, a transition may occur such that a different configuration of the field becomes energetically favoured. This is conceptually similar, for example, to the conditions under which water freezes to ice. In certain scenarios, it is also possible that more than one degenerate lowest energy state may arise. If different areas of physical space fall into different energy minima, this can result in the formation of topologically non-trivial field configurations. This has been observed directly in condensed matter systems, such as the formation of vortices in liquid crystals [1].

Topological defects were first predicted in the context of nonlinear field theory in the 1960s [2], initially postulated to exist as particle-like solutions with a form similar to those observed in superconductivity [3, 4]. They were loosely suggested to be relevant in cosmology within the next few years [5], but were not seriously investigated prior to the discovery of explicit defect solutions in particle physics models, notably the one-dimensional Nielsen-Oleson vortex [6] and zero-dimensional 't Hooft-Polyakov monopole [7, 8]. The case for a cosmological application was further strengthened a few years prior [9, 10], where it was suggested that high temperatures can restore spontaneously broken symmetries in field theories, similarly to in condensed matter systems. In a groundbreaking paper that is widely considered to be the birth of the field [11], cosmological topological defects were postulated to have emerged as a result of a phase transition and spontaneous symmetry breaking in the early Universe as it cooled below some critical temperature. It was further proposed that the class of defect to form (domain walls, strings, monopoles or textures) is dependent on the underlying topology of the vacuum manifold. In this thesis, we investigate the properties and evolution of cosmic strings, one-dimensional, line-like defects predicted to constitute a complex network that spans our Universe [12].

Since their initial theoretical prediction, cosmic strings and their cosmological implications have become the focus of a particularly rich area of study. It has been shown that strings are physically well-motivated, being produced generically in Grand Unified Theories (GUTs) [13], in the context of string theory as superstrings [14–17] and as a source of dark matter axions in the Peccei-Quinn model [18, 19]. Their detection or constraint would therefore provide deep insight into fundamental physics, such as the nature of matter and the evolution of the early stages of the Universe. However, the complex non-linear dynamics of cosmic strings means that characterisation of their evolution and predicted observational signatures is highly non-trivial, and continues to be the subject of significant debate.

Over the last few decades, several efforts have been made to detect cosmic strings directly and indirectly by experiment. They have a wide variety of cosmological consequences, including gravitational lensing of galaxies [20–22], production of cosmic rays by decay into particle radiation [23–31], creation of anisotropies in the cosmic microwave background (CMB) [32, 33] and direct emission of gravitational waves [34, 35]. Experimental constraints on cosmic strings are typically presented as bounds on the string tension for so-called 'local' strings, formed from the breaking of a local $U(1)$ gauge symmetry. These are characterised by the dimensionless parameter $G\mu$, where G is Einstein's constant and μ is the string energy density. Until recently, the most stringent bounds were obtained from CMB experiments such

as Planck [36], which currently constrains $G\mu \lesssim \mathscr{O}(10^{-7})$ [37]. This has been superseded in the last five years by pulsar timing measurements of the stochastic gravitational wave background (SGWB) [38, 39], from which the bound $G\mu \lesssim \mathscr{O}(10^{-11})$ has been obtained [40]. However, perhaps the most promising channel for future detection or more stringent constraints is currently provided by experiments for the direct detection of gravitational radiation.

The recent Nobel-Prize-winning detection of gravitational waves by the Laser Interferometer Gravitational-Wave Observatory (LIGO) has opened up a brand new window into observational cosmology. Signals detected from stellar mass binary black hole [41–47] and neutron star mergers [48] have acted as a catalyst for research into other potential gravitational wave sources which have the potential to be detected by future experiments, such as the Laser Interferometer Space Antenna (LISA) [49]. These range from further astrophysical systems, such as supermassive black hole mergers and extreme mass ratio inspirals (EMRIs) [50], to sources from the early Universe, including cosmological phase transitions [51–53] and cosmic strings [54]. In order to identify different sources reliably, it is necessary to obtain theoretical waveforms against which experimental measurements can be compared. It is therefore vital to develop accurate models of potential sources to facilitate future detections.

As outlined briefly above, cosmic strings are particularly challenging to model due to their complex non-linear evolution. The primary method used for analytical predictions is the Nambu-Goto approximation, which assumes that the strings effectively have zero width. This means that degrees of freedom internal to the string core can be integrated out, significantly simplifying the equations of motion [55]. Within this model, local cosmic strings are predicted to decay primarily into gravitational radiation through emission from relativistic configurations that arise on string loops [56–63]. These take the form of cusps, configurations for which the string reaches the speed of light, and kinks [64–66], where the string has a discontinuous tangent vector. Both emit localised 'burst' signals which, when superposed incoherently, can also make up an approximately scale-invariant SGWB [67]. The precise form and strength of these signals depends significantly on certain network properties, such as the distribution of loop sizes, the effects of radiation backreaction and the string tension. These are not analytically predetermined, meaning that key parameters must be input by hand or obtained from numerical simulations.

Large-scale simulations of Nambu-Goto string networks have been performed by several authors [68–79] to determine their evolution and observational signatures in an expanding cosmological background. Comparison of these simulations with experimental results forms

the basis of the majority of empirical string bounds presented in the literature, such as constraints from the CMB [80–82]. It is widely agreed that networks evolve towards a 'scaling' solution, where the typical length scale associated with the network is proportional to the cosmological horizon scale [55, 83]. This can be modelled analytically using the velocity-dependent one-scale model [84–87]. However, uncertainty over the appropriate parameters to include, for example, to determine gravitational backreaction and loop production, significantly affects predicted radiative signatures and constraints. This means that it is often necessary to consider multiple string models to encompass an appropriate range of parameter space (see the review [88]). This is reflected clearly in a recent paper published by the LIGO Scientific Collaboration and Virgo Collaboration [89], which uses data from the first Advanced LIGO observing run to calculate constraints on local strings, employing three different numerical models to determine the distribution of loop sizes [55, 58, 66, 75, 90–93]. It is shown that strings are constrained by $G\mu \lesssim 10^{-8}$ for a uniform large loop distribution, but that this bound is significantly weaker for models with a lower density of loops. More recent results obtained using Advanced LIGO's second observing run [94] constrain $G\mu \lesssim 10^{-6}$ and $G\mu \lesssim 10^{-14}$ for different non-uniform loop distribution models, where the stronger bound applies for a higher proportion of small loops. These contradictory results strongly demonstrate the need to clarify the appropriate network model.

In contrast to the Nambu-Goto approximation, it has been proposed by some authors [95–97] that a more appropriate method to model cosmic strings is to instead evolve the underlying fundamental fields. Unlike Nambu-Goto simulations, field theory simulations automatically incorporate the full physical effects of radiation backreaction [98–101], leading some to argue that this approach is more accurate. However, the vast difference in scale between the typical string width δ and the string curvature scale R (usually set by the Hubble radius $R \lesssim H^{-1}$), characterised by $\ln R/\delta \sim 100$ for GUT strings, means that evolution on a standard fixed numerical grid is not able to accurately resolve the string cores in a realistic cosmological context, typically only achieving $\ln R/\delta \sim 6$. In order to attain sufficient dynamic range in an expanding universe, the string is therefore typically fixed at finite (or finite comoving) width [102–107]. This alternative model yields further quantitative discrepancies in the literature regarding the typical string network density and the primary decay mechanism of radiating strings (for example, see [108]). In particular, it is predicted in some cases that string loops decay primarily through particle emission rather than by gravitational waves, and hence that no SGWB is produced. Recent work has shown particle emission to be an important decay channel for small loops, while gravitational emission dominates for large loops [109, 110].

This significantly affects the predicted gravitational spectrum and weakens bounds obtained by gravitational wave experiments.

The ambiguity between the Nambu-Goto and field theory methods of evolution is reflected further in the lack of understanding of 'global' or axion string networks, generated from the breaking of a $U(1)$ global symmetry. Global cosmic strings are not constrained gravitationally as strongly as local strings, as they decay primarily into Goldstone bosons rather than gravitational radiation. However, they can be constrained in the context of the Peccei-Quinn model, where an additional $U(1)$ global symmetry is introduced to the Standard Model to dynamically suppress CP violation. When broken, this symmetry produces the 'axion' particle, which can be considered as a cold dark matter candidate [111]. To identify the axion mass m_a that corresponds with the observed dark matter abundance, two potential scenarios must be considered; symmetry breaking before or after cosmic inflation. If we consider a symmetry breaking before inflation, the observed cold axion dark matter density is determined by the random initial value of the axion field, and can therefore be provided by any coupling constant $f_a \gtrsim 10^{10}$GeV. However, if symmetry breaking occurs after inflation, this prediction becomes more dependent on the axion string model, where strings have an approximate ratio of scales $\ln R/\delta \sim 70$. This is where the primary uncertainty enters, and is the basis for significant current research [112–117]. The current range predicted for the axion mass in this post-inflation scenario is $26\mu\text{eV} \lesssim m_a \lesssim 1\text{meV}$ [118, 119] (see also the review [120]).

In this thesis, we propose a resolution for the above disagreements using the computational technique, adaptive mesh refinement (AMR). AMR facilitates accurate simulations of cosmic string evolution by adapting the refinement of the numerical grid to the local scale of the problem, employing finer resolution at the string core. This allows for a much greater dynamic range, removing the need to approximate strings as having either zero or fixed comoving width, thereby providing a potential bridge between Nambu-Goto and field theory models. We perform extensive simulations of cosmic strings using the AMR code `GRChombo` [121], which is based on the `Chombo` adaptive mesh framework [122].

In Chapter 2, we begin by providing an outline of the formation of cosmic strings in both local and global symmetry breaking models, including a more detailed discission of the structure and properties of global strings. We also derive the Nambu-Goto and field theory methods often used to model string evolution in the literature, including their predicted power spectra for axion and gravitational radiation. We finally describe the current research landscape of string simulations, outlining current discrepancies between the two methods.

Chapter 3 introduces the GRChombo code and outlines the motivation behind using AMR for cosmic string simulations. We describe how GRChombo is used to simulate and quantitatively analyse global strings, including its implementation of AMR, parallelism and load balancing, the choosing of appropriate AMR parameters and the use of three-dimensional visualisation. We outline the methods used to obtain appropriate initial conditions, as well as the introduction of new diagnostic tools and optimisation of code performance. Some of the optimisation work in this chapter was performed together with other GRChombo core developers, as well as developers of the base code, Chombo, from Lawrence Berkeley National Laboratory.

In Chapters 4 and 5, we present a detailed analysis of the radiation emitted from global string configurations using GRChombo. We derive new quantitative diagnostics to separate the massless and massive modes, as well as the self-field from the propagating radiation. Quantitative diagnostic tools are used to determine the eigenmode decomposition, finding that the quadrupole signal of massless radiation is strongly dominant across all available channels, as predicted by theory. We present results from analytic radiation modelling in the thin-string (Nambu-Goto) limit, concluding this to be the appropriate approach to describe global strings in a cosmological context. For massive radiation, eigenmode decomposition and three-dimensional visualisation reveals a complex wavepacket structure that is sensitive to numerical resolution and requires careful application of regridding parameters and numerical dissipation. We find that massive radiation is exponentially suppressed with increasing mass, but can become competitive with massless channels for low mass, relativistic configurations. Finally, we investigate the mass (λ) dependence of the lowest propagating harmonic, identifying distinct thresholds over a range of low λ.

In Chapter 6, we discuss preliminary results from simulations of relativistic cusp-like configurations using two different sets of initial conditions; a sinusoidal configuration with extreme initial amplitude, and a travelling wave solution with two colliding Gaussians. We find that for the travelling wave solution, a burst of massless radiation is emitted at the point of collision. We also present qualitative observations from simulations of a network of global strings, revealing novel features such as bursts of massive radiation from loop decay and sites of string intercommutation, where strings travel at relativistic speeds.

Finally, in Chapter 7, we present our conclusions and discuss the future directions of this work. We outline its application to an accurate estimation of the dark matter axion mass, as well as to the potential future detection of cosmic strings using gravitional waves.

Chapter 2

Origin and Evolution of Cosmic Strings

In this chapter, we outline the formation mechanism of cosmic strings in the early Univese, as well as the two primary methods used to model their evolution; the field theory and Nambu-Goto methods. For each method, we describe two specific examples; so-called 'local' or 'Abelian-Higgs' strings, and 'global' strings, formed from the breaking of local and global $U(1)$ symmetries respectively. Finally, we discuss the current discrepancies in predictions in the literature using these different models, the reasons behind them and the application of AMR as a potential method to address them.

Throughout this chapter, Greek letters such as μ and ν indicate spacetime indices $\{0,1,2,3\}$ and Latin letters a and b indicate spatial indices $\{1,2,3\}$. We employ Einstein notation, where repeated sub- and super-script letters indicate summation over the indices. Sub- and super-script symbols , and ; denote partial and covariant differentiation of tensors respectively, defined below for a general tensor y with coordinates x_μ:

$$y_{\mu\nu\ldots,\sigma} \equiv \frac{\partial y_{\mu\nu\ldots}}{\partial x^\sigma}\,, \qquad\qquad y^\mu_{;\nu} = y^\mu_{,\nu} + \Gamma^\mu_{\sigma\nu} y^\sigma\,, \tag{2.1}$$

where $\Gamma^\mu_{\nu\sigma}$ is the Christoffel symbol

$$\Gamma^\mu_{\nu\sigma} = \frac{1}{2} g^{\mu\tau}(g_{\tau\nu,\sigma} + g_{\tau\sigma,\nu} - g_{\nu\sigma,\tau}) \tag{2.2}$$

for the spacetime metric $g_{\mu\nu}$. The metric signature is taken to be $(+,-,-,-)$. Finally, the default units used are 'natural' units, where we set the reduced Planck constant $\hbar$, the speed of light c and the Boltzmann constant k_B as follows:

$$\hbar = c = k_B = 1\,. \tag{2.3}$$

2.1 Cosmological Context

Cosmic strings are a class of one-dimensional topological defect that can arise as the result of spontaneous symmetry breaking. In general, topological defects can be studied in elementary particle physics models in the context of scalar fields, such as the Higgs, and vector fields, such as gauge fields. Generically, defects can arise if a given field theory has more than one degenerate lowest energy state, either with discrete values or a continuous symmetry. If different areas of physical space fall into different minima, high energy boundaries or defects will form between the regions. In the case of cosmic strings, the lowest energy state is invariant under phase transformations, so traversing a closed path in physical space can surround a point with an undefined phase. To resolve this inconsistency, the magnitude of the field at this point must be set to zero, creating a point of high energy within the loop. If extended to three dimensions, this creates a string-like defect.

In a cosmological context, it is possible for a network of strings to have formed in the early Universe as a result of a symmetry breaking phase transition. The defect formation process in this context is described by the 'Kibble mechanism' [11], which states that the effective potential of the Universe $V_{\text{eff}}(\varphi, T)$ is dependent on temperature T. It is postulated that above a certain critical temperature T_c, the potential has only one global minimum, but that a symmetry-breaking potential will develop below T_c. Once spontaneous symmetry breaking has occurred, topological defects will 'freeze-out' as the Universe cools due to its rapid expansion after the Big Bang. This can lead to the formation of string networks on cosmological scales, with potentially observable signatures.

2.2 Field Theory of Cosmic Strings

In this section, we describe the field theory formulation of cosmic strings, following closely the outline presented in the relevant chapters of [55]. This model uses the scalar and gauge fields themselves to characterise the spontaneous symmetry breaking, the internal structure

of the string and the different available radiative modes. We begin by describing 'global' strings which arise from the breaking of a global $U(1)$ symmetry with a single complex scalar field, discussing in detail their energy density and internal structure. We subsequently describe the formation of so-called 'local' strings, those that are formed by the breaking of a local $U(1)$ gauge symmetry in the Abelian-Higgs model, with a gauge vector field and complex scalar field. This model is the most relevant in particle physics scenarios, such as scalar electrodynamics [123], and is the most widely studied.

Although it is necessary to outline the theory of local strings for completeness, we do not focus predominantly on these during the course of the thesis. Instead, we concentrate on global strings, primarily because they are simpler to simulate numerically as there are fewer fundamental fields to evolve. Further to this, for local strings it is necessary both to choose an appropriate gauge condition and to ensure that this condition does not numerically 'drift,' using techniques such as constraint damping. By simplifying the evolution equations to the global case, we aim to focus as much as possible on the string dynamics and to minimise numerical uncertainties. This will be discussed in detail in later chapters.

2.2.1 Global $U(1)$ Field Theory

Global cosmic strings are analytically the simplest case of string formation, arising from a $U(1)$ symmetry breaking with a single complex scalar field φ. We consider the Goldstone model, which has Lagrangian density given by

$$\mathscr{L} = (\partial_\mu \bar{\varphi})(\partial^\mu \varphi) - V(\varphi)\,. \tag{2.4}$$

The potential $V(\varphi)$ is given by

$$V(\varphi) = \frac{1}{4}\lambda(\bar{\varphi}\varphi - \eta^2)^2\,, \tag{2.5}$$

where λ and η are real constants, with a diagram shown in Figure 2.1. The constant λ sets the symmetry breaking scale, and η sets the vacuum expectation value, or lowest energy state.

The Goldstone Lagrangian (2.4) is invariant under the symmetry transformation

$$\varphi(x) \to e^{i\alpha}\varphi(x)\,, \tag{2.6}$$

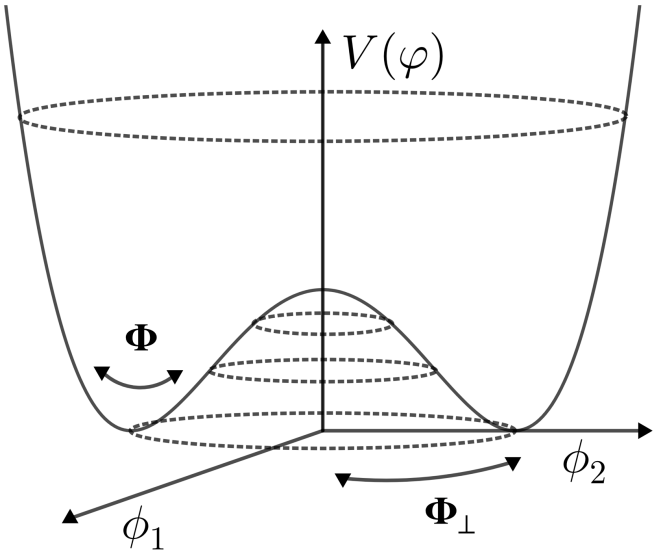

Fig. 2.1 Diagram of the $U(1)$ symmetry breaking potential $V(\varphi)$, plotted against the real and imaginary components ϕ_1 and ϕ_2 of the complex scalar field $\varphi = \phi_1 + i\phi_2$. The orthogonal oscillation directions, $\mathbf{\Phi}$ and $\mathbf{\Phi}_\perp$ for radial and phase oscillations respectively, are indicated (see also (4.9 - 4.10)).

where α is a global phase independent of spacetime location. However, if we apply this transformation to the lowest energy vacuum state

$$\langle 0|\varphi|0\rangle = \eta e^{i\theta} \tag{2.7}$$

where θ is the complex phase, a different expectation value

$$\langle 0|\varphi|0\rangle = \eta e^{i(\theta+\alpha)} \tag{2.8}$$

is obtained, spontaneously breaking the symmetry.

In order to develop a clearer intuition of how cosmic strings are formed, we consider the configuration of the complex scalar field φ in physical space. Figure 2.2 shows an illustration of a cosmic string surrounded by a closed path L, where the phase θ has changed by $\Delta\theta = 2\pi$, taking values around the degenerate circle of minima in Figure 2.1. This means the field has developed a non-trivial 'winding,' which is characterised in general by a constant integer n, defined by $\Delta\theta = n2\pi$. In the case where we have a non-trivial winding around a closed loop, there will be a point within the loop at which the phase is not well-defined. In order for the field to be continuous, it is necessary to set the magnitude of the field to be $|\varphi| = 0$,

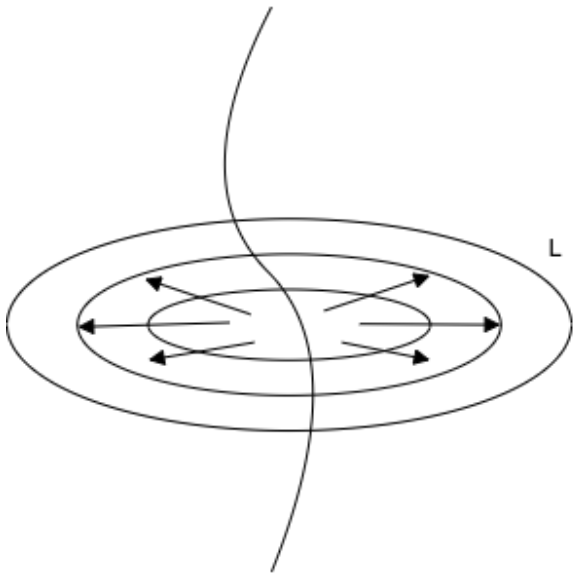

Fig. 2.2 Diagram of string surrounded by closed loop L, with arrows to indicate the phase θ of the complex scalar field φ surrounding it.

corresponding to a non-zero energy density, also known as a 'vortex' solution. Extending this configuration in three dimensions, these connected points of high energy density form a cosmic string defect.

To derive the equations of motion, we first decompose the complex scalar field φ into its real and imaginary parts $\phi_{1,2}$ as follows:

$$\varphi = \phi_1 + i\phi_2 \,. \tag{2.9}$$

The Euler-Lagrange equations are then given by

$$\frac{\partial^2 \phi_{1,2}}{\partial t^2} - \nabla^2 \phi_{1,2} + \frac{\lambda}{2}\phi_{1,2}(|\varphi|^2 - \eta^2) = 0\,, \tag{2.10}$$

as can be derived from (2.4). From these, we can deduce the global string cross-section along with the energy density (which is significantly more complex than for local strings). We discuss these in detail in the next subsection.

Finally, we note from Figure 2.1 that there are both massive and massless (Goldstone) radiative modes available from radial and phase oscillations respectively, indicated by $\mathbf{\Phi}$ and $\mathbf{\Phi}_\perp$. This will be investigated in detail in subsequent chapters.

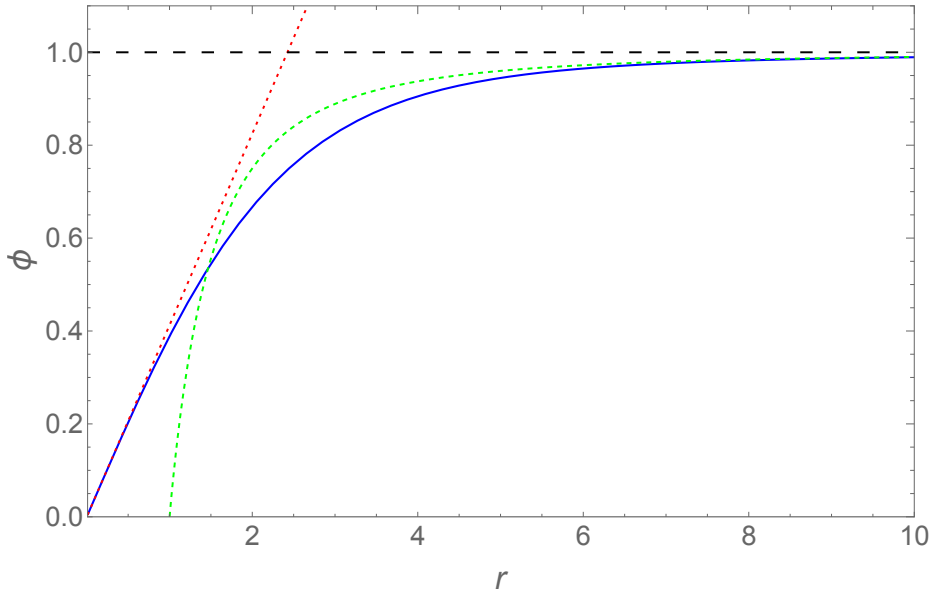

Fig. 2.3 Radial profile of a global cosmic string $\phi(r)$ for $\lambda = 1$ with approximate width $\delta \sim 1$. Also plotted are the asymptotic regimes $\phi = 0.412\,r$ for $r \to 0$ (red dotted) and $1 - r^{-2}$ as $r \to \infty$ (green dashed).

Structure of Global Strings

As discussed above, the possibility of non-trivial windings about a circular vacuum topology leads to the existence of vortex solutions in two dimensions or line-like strings in three dimensions. To find the initial field configuration for global strings, we postulate the static *ansatz* solution to (2.10)

$$\varphi(r,\theta) = \phi(r)e^{in\theta}\,, \tag{2.11}$$

where n is the topological winding number and $\phi = |\varphi|$. This radial ansatz can be substituted into the static part of the Euler-Lagrange equations (2.10) to yield an ordinary differential equation for $\phi(r)$

$$\frac{d^2\phi}{dr^2} + \frac{1}{r}\frac{d\phi}{dr} - \frac{n^2\phi}{r^2} - \frac{\lambda}{2}\phi(\phi^2 - \eta^2) = 0\,, \tag{2.12}$$

subject to the boundary conditions $\phi(0) = 0$ at the string core and $\phi(r) \to \eta$ as $r \to \infty$. The radial equation (2.12) can be solved numerically to obtain the string cross-section or profile $\phi(r)$, plotted in Figure 2.3 for a single winding $n = 1$ string. This simple solution allows us to infer the width of the string core, defined to be

$$\delta \approx m_H^{-1} \equiv (\sqrt{\lambda}\,\eta)^{-1}\,, \tag{2.13}$$

where m_H^{-1} is the Compton wavelength of the massive particle (see Section 4.1.1 for further discussion). As can be seen from Figure 2.3, the 'half width' of the string core is larger than this, given by $\delta_{1/2} = 1.35\,\delta$ where $\phi = 0.5$ (or $1.68\,\delta$ using the same criteria with the energy density). In subsequent calculations, we perform a rescaling to set $\eta = 1$ (using $\phi \to \phi/\eta$ and $r \to \eta r$), but retain λ as a free parameter to modify the string width.

The energy density $\rho(r)$ of the string in cylindrical coordinates can be calculated using the energy-momentum tensor $T_{\mu\nu}$, defined as

$$T_{\mu\nu} = \partial_\mu \varphi \partial_\nu \varphi - g_{\mu\nu}\mathscr{L}\,. \tag{2.14}$$

The energy density is given by $\rho = T^{00}$, which splits into the following contributions:

$$\rho(r) = \left(\frac{d\phi}{dr}\right)^2 + \frac{\lambda}{4}\left(\phi^2 - 1\right)^2 + \left(\frac{n\phi}{r}\right)^2 . \tag{2.15}$$

The first two terms are the gradient and potential energies associated with deviations of the massive field from the vacuum, i.e. for $\phi \lesssim 1$. These provide the dominant contribution to the 'local core' within a radial distance $r \lesssim 2\delta$, as illustrated in Figure 2.4. This massive contribution to the energy density converges rapidly to the vacuum as $1 - r^{-2}$, and integrating out to $r \to \infty$ yields a core energy density μ_0. The third contribution is due to the 'winding' of the long-range massless field about the string core, which generically dominates the overall energy density beyond $r \gtrsim 2\delta$ (also shown in Figures 2.4–2.5). In principle, this massless contribution is logarithmically divergent,

$$\mu_\theta(R) \approx \int_\delta^R \left(\frac{1}{r}\frac{\partial\phi}{\partial\theta}\right)^2 2\pi r dr = 2\pi\eta^2 \ln\left(R/\delta\right) . \tag{2.16}$$

However, in practice, it will be cutoff at some radius R associated with the curvature radius of the string, at which point the correlations implied by the ansatz (2.11) will be washed out or cancelled. For axion strings on cosmological scales, we expect $\mu_\theta \gg \mu_0$. In fact, (2.16) provides an accurate estimate even on much smaller scales, with the total energy density

$$\mu(R) = \mu_0 + \mu_\theta(R) \;\approx\; 2\pi\eta^2 \ln\left(R/\delta\right) \;\; (\text{for } R \gtrsim 2)\,, \tag{2.17}$$

achieving better than 2% accuracy for $R \gtrsim 10$ and 0.1% on cosmological scales (see Figure 2.5).

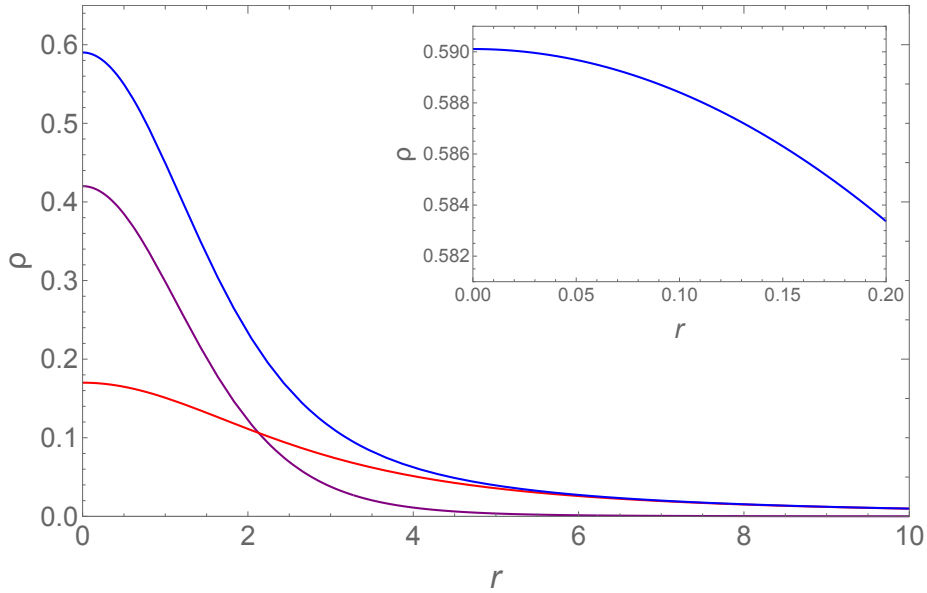

Fig. 2.4 String energy density ρ (blue) as a function of radius r for $\lambda = 1$, showing both the core contribution from massive modes (purple) and exterior massless modes (red) which dominate beyond $r \gtrsim 2$. Inset is the energy density close to $r = 0$ showing a flattened centre which allows small 'zero-mode' excitations within the string core $\Delta r \approx \mathcal{O}(\delta/10)$.

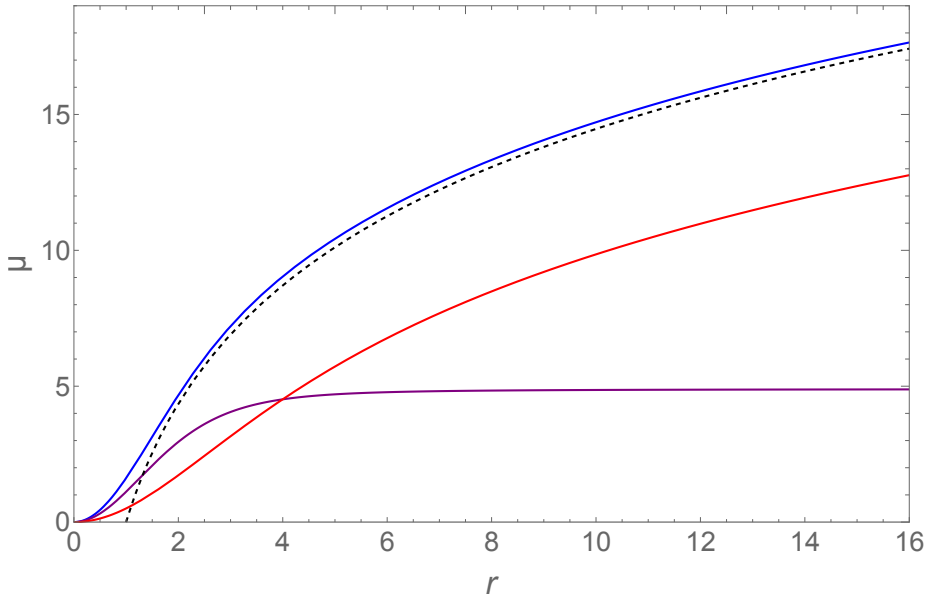

Fig. 2.5 Integrated string energy per unit length $\mu(R)$ as a function of cutoff radius $r = R$ for $\lambda = 1$, showing the total energy density (blue), the massive core (purple) and the long-range massless contribution (red) which renormalizes μ. Agreement with the simple logarithmic fit $\mu \approx 2\pi \ln(R/\delta)$ is shown for $R \gtrsim 2$ (dotted line).

The internal structure of global strings is an important factor for numerical simulations, which inherently have a limited dynamic range. We can identify the positions of string cores in space $\mathbf{x}$ by locating the zeroes of the field where $\phi(\mathbf{x}) = 0$. However, this might not represent the actual string centre of mass because of internal excitations within the string radius. Inset in Figure 2.4 is a zoomed view of the energy density around $r = 0$ close to the string core, showing that it becomes 'flat' and varies by only 1% ($\rho_0 - \rho(r) \lesssim 0.01$) within a radius $r \lesssim 0.2\delta$. This means there is an internal 'zero mode' allowing the string core to move short distances at little or no energy cost, without actually moving the bulk string. We can expect such finite width effects to be present when studying small amplitude oscillations comparable to the string width $A \sim \delta$.

2.2.2 Local Strings in the Abelian-Higgs Model

Local cosmic strings are formed by spontaneously broken symmetries in the context of gauge theories [55]. The simplest of these models is the Abelian-Higgs model for scalar electrodynamics, with a gauge vector field A_μ and a complex scalar field φ. This theory has the Lagrangian

$$\mathscr{L} = (\bar{\mathscr{D}}_\mu \bar{\varphi})(\mathscr{D}^\mu \varphi) - V(\varphi) - \frac{1}{4} F_{\mu\nu} F^{\mu\nu}, \tag{2.18}$$

where $\mathscr{D}_\mu = \partial_\mu - ieA_\mu$, $F_{\mu\nu} = \partial_\mu A_\nu - \partial_\nu A_\mu$ is an antisymmetric tensor, e is the gauge coupling and $V(\varphi)$ is the potential for a broken $U(1)$ symmetry given by (2.1).

The Lagrangian (2.18) is invariant under the group of $U(1)$ local gauge transformations:

$$\varphi(x) \to e^{i\alpha(x)} \varphi(x), \qquad A_\mu(x) \to A_\mu(x) + e^{-1} \partial_\mu \alpha(x), \tag{2.19}$$

where $\alpha(x)$ is a phase dependent on spacetime location x. However, if the scalar field φ falls into the potential minimum of $V(\varphi)$, the symmetry is spontaneously broken. This can be demonstrated by expanding about the minimum $|\varphi| = \eta$, choosing $\varphi = \eta + \phi_1/\sqrt{2}$, from which we obtain

$$\mathscr{L} = \frac{1}{2}(\partial_\mu \phi_1)^2 - \frac{1}{2}\mu^2 \phi_1^2 - \frac{1}{4} F_{\mu\nu} F^{\mu\nu} + \frac{1}{2} M^2 A_\mu A^\mu + \text{higher order terms}, \tag{2.20}$$

where, we have defined

$$\mu = \sqrt{\lambda}\eta, \qquad M = \sqrt{2} e \eta. \tag{2.21}$$

We deduce from (2.20) that, unlike for global strings, there is no massless Goldstone boson, and that this degree of freedom has instead been absorbed by the gauge field, which becomes massive.

The equations of motion for the fields are given by the Euler-Lagrange equations:

$$(\partial_\mu - ieA_\mu)(\partial^\mu - ieA^\mu)\varphi + \frac{\lambda}{2}\varphi(\varphi\bar{\varphi} - \eta^2) = 0 \tag{2.22}$$

and

$$\partial_\mu F^{\mu\nu} = j^\nu\,, \tag{2.23}$$

where we have defined the current j^ν

$$j^\nu \equiv 2e\mathscr{I}[\bar{\varphi}(\partial^\nu - ieA^\nu)\varphi]\,. \tag{2.24}$$

We will not go into much further detail of local strings here, as they are not studied in detail in the remainder of the thesis. However, it can be shown that cylindrically symmetric solutions to equations (2.22-2.24) can be obtained [124, 6], confirming the existence of local string configurations.

Finally, one particularly important property of local strings is their finite energy density, in contrast to the logarithmically divergent energy density of global strings. It can be shown that, in the Lorenz gauge $\partial_\mu A^\mu = 0$, the scalar and gauge fields asymptotically approach

$$\varphi \approx \eta e^{in\theta} \qquad \text{and} \qquad A_\mu \approx \frac{1}{ie}\partial_\mu \ln\varphi \tag{2.25}$$

respectively at distances far from the string core. This means that $D_\mu\varphi \approx 0$ and $F_{\mu\nu} \approx 0$ at large distances from the string, and the energy density falls off exponentially. It can be shown that the mass per unit length μ of a local string is therefore given approximately by

$$\mu \sim \eta^2\,. \tag{2.26}$$

2.3 Thin String Evolution and Radiation

Having presented the field theory equations of motion above, in this section, we outline how cosmic string evolution can be modelled using an effective string action, S. This approach is useful at low temperatures and away from highly curved regions, where massive excitations

within the string core can be integrated out to create a low energy effective theory. This can be performed both for local and global strings to obtain the Nambu-Goto [125, 126] and Kalb-Ramond [127] actions respectively. In this case, we begin by considering local strings, which are easier to model due to their finite energy density. Both subsequent outlines follow detailed derivations given in [55]. We then discuss the radiative spectra from both types of string, drawing parallels between massless global string radiation and gravitational radiation from local strings.

2.3.1 Nambu-Goto Action and Equations of Motion for Local Strings

We first consider the action for the Abelian-Higgs model (2.18) in a general spacetime with metric $g_{\mu\nu}$. This is given by

$$S = \int d^4y\sqrt{-g}\{|\mathscr{D}_\mu\varphi|^2 - \frac{1}{4}F_{\mu\nu}F^{\mu\nu} - V(\varphi)\}\,, \tag{2.27}$$

where $g = \det g_{\mu\nu}$ and y^μ are the spacetime coordinates of a general point. In order to obtain the effective action for a string, it is necessary to integrate out the massive transverse degrees of freedom from an approximate field theory string solution. We can reparametrise the action (2.27) as follows:

$$y^\mu(\xi) = x^\mu(\zeta) + \rho^A n^\mu_A(\zeta)\,, \tag{2.28}$$

where we define the spacetime coordinates of the string itself $x^\mu(\zeta)$ as the two-dimensional area swept out by the zeroes of the complex field φ, also called the string 'worldsheet.' These are given by

$$x^\mu = x^\mu(\zeta^a)\,, \qquad a = 0,\,1, \tag{2.29}$$

where $\zeta^{0,1}$ are timelike and spacelike coordinates. We further define $n^A_\mu(\xi)$ as vectors orthonormal to the tangent vectors to the string $x^\mu_{,a}$, such that $n^A_\mu x^\mu_{,a} = 0$ and $g^{\mu\nu}n^A_\mu n^B_\nu = -\delta^{AB}$, and ρ^A as radial coordinates, with $A = 1, 2$. The reparametrisation (2.28) hence defines $y^\mu = y^\mu(\xi)$ in terms of coordinates $\xi^\mu = (\zeta^a, \rho^A)$, separating the worldsheet coordinates from the radial degrees of freedom. This is illustrated in Figure 2.6.

To perform the integration in (2.27) with respect to ξ, we must derive an expression for the Jacobian as follows:

$$\sqrt{-g}\det\left(\frac{\partial y}{\partial \xi}\right) = (-\det M_{\alpha\beta})^{1/2}\,, \tag{2.30}$$

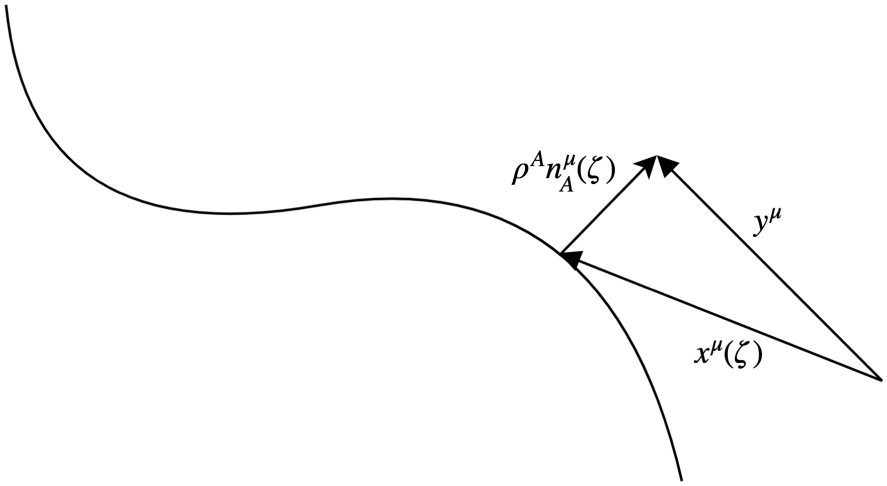

Fig. 2.6 Coordinate reparametrisation close to the string, adapted from [55].

where

$$M_{\alpha\beta} = \left(g_{\mu\nu} \frac{\partial y^\mu}{\partial \xi^\alpha} \frac{\partial y^\nu}{\partial \xi^\beta} \right) = \mathrm{diag}(\gamma_{ab}, -\delta_{AB}) + \mathscr{O}(r/R) \tag{2.31}$$

and α and β are spacetime indices. The two-dimensional worldsheet metric

$$\gamma_{ab} = g_{\mu\nu} x^\mu_{,a} x^\nu_{,b} \tag{2.32}$$

is defined by considering the spacetime interval between two nearby points on the worldsheet

$$ds^2 = g_{\mu\nu} x^\mu_{,a} x^\nu_{,b} d\zeta^a d\zeta^b \,. \tag{2.33}$$

We observe straightforwardly from (2.31) that

$$\mathrm{det} M_{\alpha\beta} \approx \gamma, \tag{2.34}$$

where $\gamma \equiv \det \gamma_{ab}$, and further recall that integrating over radial degrees of freedom yields the string energy per unit length, μ. Taking account of the exponential fall-off of the $\mathscr{O}(r/R)$ terms, it can hence be shown to the lowest order that the string can be modelled by

$$S = -\mu \int d^2\zeta \sqrt{-\gamma}, \tag{2.35}$$

which is the Nambu-Goto action [125, 126]. This is an important result that is used frequently in analysis of cosmic string dynamics.

Having obtained an effective action (2.35) for the string, we can vary with respect to the spacetime coordinates $x^\mu(\zeta^a)$ to obtain equations of motion. Note that in contrast to the Euler-Lagrange equations given by equations (2.22-2.24), the equations of motion obtained using the Nambu action are given in terms of spacetime coordinates of the string core, rather than the fields themselves. Varying (2.35) with respect to $x^\mu(\zeta^a)$, it can be shown that the equations of motion are given by

$$x^{\mu\ ;a}_{,a} + \Gamma^\mu_{\nu\sigma}\gamma^{ab}x^\nu_{,a}x^\sigma_{,b} = 0\,, \tag{2.36}$$

where $\Gamma^\mu_{\nu\sigma}$ is the Christoffel symbol defined by equation (2.2) and the covariant Laplacian $x^{\mu\ ;a}_{,a}$ is given by

$$x^{\mu\ ;a}_{,a} = \frac{1}{\sqrt{-\gamma}}\partial_a\left(\sqrt{-\gamma}\gamma^{ab}x^\mu_{,b}\right)\,. \tag{2.37}$$

In a flat spacetime $g_{\mu\nu} = \eta_{\mu\nu}$ with $\Gamma^\mu_{\nu\sigma} = 0$, we obtain the simplified equations of motion from (2.36)

$$\partial_a(\sqrt{-\gamma}\gamma^{ab}x^\mu_{,b}) = 0\,. \tag{2.38}$$

The Nambu action (2.35) is invariant under reparametrisations of the worldsheet,

$$\zeta^a \to \tilde{\zeta}^a(\zeta^b) \tag{2.39}$$

so we can choose any convenient gauge to simplify the equations of motion even further. For a flat spacetime, we choose the so-called 'conformal' gauge, which can be written as

$$\dot{x}\cdot x' = 0 \tag{2.40}$$

$$\dot{x}^2 + x'^2 = 0 \tag{2.41}$$

where dots indicates the derivative with respect to the timelike worldsheet coordinate ζ^0 and dashes for the spacelike ζ^1. Equation (2.38) can then be written as the two-dimensional wave equation

$$\ddot{x}^\mu - x^{\mu\prime\prime} = 0\,. \tag{2.42}$$

There is a residual gauge freedom that can be removed by setting

$$t \equiv x^0 = \zeta^0\,. \tag{2.43}$$

Applying the gauge (2.43), we can finally write the equations of motion for a cosmic string in flat space in terms of the three-vector $\mathbf{x}(\zeta,t)$, where $\zeta \equiv \zeta^1$, from equations (2.40-2.41) and (2.42),

$$\dot{\mathbf{x}} \cdot \mathbf{x}' = 0\,, \tag{2.44}$$

$$\dot{\mathbf{x}}^{\mathbf{2}} + \mathbf{x}'^{\mathbf{2}} = 1\,, \tag{2.45}$$

$$\ddot{\mathbf{x}} - \mathbf{x}'' = 0\,. \tag{2.46}$$

Having significantly simplified the string dynamics, we can now derive specific solutions to the equations of motion (2.44-2.46). A general solution to equation (2.46) is given by

$$\mathbf{x}(\zeta,t) = \frac{1}{2}[\mathbf{a}(\zeta - t) + \mathbf{b}(\zeta + t)]\,, \tag{2.47}$$

where the left- and right-moving modes are subject to constraints derived from (2.44) and (2.45)

$$\mathbf{a}'^{\mathbf{2}} = \mathbf{b}'^{\mathbf{2}} = 1\,. \tag{2.48}$$

It can be shown that a family of loop solutions can be found by decomposing the general solution (2.47) into Fourier modes. For example, a simple planar circular solution is given by [128, 129]

$$\mathbf{x}(\zeta,t) = \frac{L}{4\pi}\{\hat{\mathbf{e}}_{\mathbf{1}}[\sin\sigma_- + \sin\sigma_+] - \hat{\mathbf{e}}_{\mathbf{2}}[\cos\sigma_- + \cos\sigma_+]\}\,. \tag{2.49}$$

Here, L is the invariant length of the loop defined by $L = \varepsilon/\mu$, where ε is the energy given by

$$\varepsilon = \int T_0^0 d^3x = \mu \int d\zeta \tag{2.50}$$

and $\sigma_\pm = (2\pi/L)\zeta_\pm$, with $\zeta_\pm = \zeta \pm t$ and $\hat{\mathbf{e}}_\mathbf{i}$ defined as unit vectors in the directions of the Cartesian axes.

Finally, we can also derive local string solutions in the cosmological context of an expanding Universe.[1] This can be described by the Friedmann–Lemaître–Robertson–Walker (FLRW) metric

$$ds^2 = a^2(\tau)(d\tau^2 - d\mathbf{x}^2)\,, \tag{2.51}$$

where τ is conformal time defined by $d\tau = dt/a(t)$ and $a(t)$ is the cosmological scale factor. Varying the Nambu action (2.35) with respect to $\mathbf{x}(\zeta,\tau)$ [130], using a similar method to

[1] In this description we assume a general knowledge of cosmology. For further background information, please refer to [55].

above for a curved spacetime, it can be shown that the string equations of motion are given by

$$\ddot{\mathbf{x}} + 2\frac{\dot{a}}{a}(1-\dot{\mathbf{x}}^2)\dot{\mathbf{x}} = \varepsilon^{-1}(\varepsilon^{-1}\mathbf{x}')', \tag{2.52}$$

$$\dot{\varepsilon} = -2\frac{\dot{a}}{a}\varepsilon\dot{\mathbf{x}}^2, \tag{2.53}$$

where we have defined

$$\varepsilon = \left(\frac{\mathbf{x}'^2}{1-\dot{\mathbf{x}}^2}\right)^{1/2}. \tag{2.54}$$

These can be used to calculate the cosmic string energy and momentum in an expanding Universe, as well as the general string dynamics.

2.3.2 Kalb-Ramond Action for Global Strings

The effective action for a global cosmic string requires a more nuanced derivation than for local strings. This is primarily due to the fact that there is a long-range coupling between the string and the massless Goldstone boson field, as shown by equation (2.16). As we have seen, this means that the total string energy is not finite, so more energy is stored in the massless field at large distances than in the core itself. However, an effective action can be derived using the general relation between a real massless scalar field ϑ and two-index antisymmetric tensor $B^{\mu\nu}$, where the interaction with the string becomes analytically analagous to an electric field around a point charge in electromagnetism. This theory was first developed in the low energy limit in [131, 132]. Here, we present the alternative derivation outlined in [133].

We first note the general relation between a massive field ϕ, massless scalar field ϑ and antisymmetric tensor $B^{\mu\nu}$, given by

$$\phi^2\partial_\mu\vartheta = \frac{\eta}{2}\varepsilon_{\mu\nu\lambda\rho}\partial^\nu B^{\lambda\rho}, \tag{2.55}$$

along with the equation of motion for $B^{\mu\nu}$

$$\partial_\mu H^{\mu\nu\lambda} = 0. \tag{2.56}$$

Here we have defined the field strength tensor

$$H^{\mu\nu\lambda} = \partial^\mu B^{\nu\lambda} + \partial^\lambda B^{\mu\nu} + \partial^\nu B^{\lambda\mu}. \tag{2.57}$$

The action for the Goldstone model in a flat spacetime can be written down using the Lagrangian (2.4)

$$\begin{aligned} S &= \int d^4x\{\partial_\mu\bar{\varphi}\partial^\mu\varphi - V(\phi)\} \\ &= \int d^4x\{(\partial_\mu\phi)^2 + \phi^2(\partial_\mu\vartheta)^2 - V(\phi)\}\,. \end{aligned} \tag{2.58}$$

Substituting the relation (2.55), it can be shown that this action is equivalent to

$$S = \int d^4x\{(\partial_\mu\phi)^2 + \frac{\eta^2}{6\phi^2}H^2 - V(\phi)\}\,. \tag{2.59}$$

However, in the case that strings are present, it is necessary to add in a source term $j^{\mu\nu}$ to account for the vortex cores, defined by

$$j^{\mu\nu} = \frac{\eta}{2}\int \delta^{(4)}[x - x(\zeta^a)]d\sigma^{\mu\nu}\,, \tag{2.60}$$

where $x(\zeta^a)$ are the worldsheet parameters and

$$d\sigma^{\mu\nu} = \varepsilon^{ab}x^\mu_{,a}x^\nu_{,b}d^2\zeta \tag{2.61}$$

is the worldsheet area element. This can be accounted for in the action by adding the term

$$4\pi\int B_{\mu\nu}j^{\mu\nu}d^4x = 2\pi\eta\int B_{\mu\nu}d\sigma^{\mu\nu}\,. \tag{2.62}$$

Integrating radially over the massive degrees of freedom as in Section 2.3.1 and incorporating (2.62), this description yields the Kalb-Ramond action [127]

$$S = -\mu_0\int\sqrt{-\gamma}d^2\zeta + \frac{1}{6}\int H^2d^4x + 2\pi\eta\int B_{\mu\nu}d\sigma^{\mu\nu}\,. \tag{2.63}$$

Here, the first term is the Nambu action for a local string as derived in Section 2.3.1, where μ_0 is the core mass per unit length associated with the massive field and final term accounts for the vortex current $j^{\mu\nu}$ as outlined above.

2.3.3 Radiation from Cosmic Strings

Massless Radiation from Global Strings

We can use the formalism described in the previous section to derive the power spectrum of massless radiation from a global string. It can be shown [134] that for a global string loop, the power spectrum per unit solid angle Ω is given by

$$\frac{dP_n}{d\Omega} = 2w_n^2 \tilde{j}^*_{\mu\nu}(w_n, \hat{\mathbf{r}}) \tilde{j}^{\mu\nu}(w_n, \hat{\mathbf{r}}) \,, \tag{2.64}$$

where $w_n = 4\pi n/L$, L is the invariant length of the loop as defined in Section 2.3.1 and $j^{\mu\nu}(\mathbf{x},t)$ is given by

$$j^{\mu\nu}(\mathbf{x},t) = \frac{\eta}{2} \int_0^L d\sigma \delta^{(3)}(\mathbf{x} - \mathbf{x}(\sigma,t))(\dot{x}^\mu x'^\nu - \dot{x}^\nu x'^\mu) \,. \tag{2.65}$$

The power spectrum can be written in terms of right- and left-moving modes $\mathbf{a}$ and $\mathbf{b}$ as used in the general solution to the Nambu equations (2.47) as follows:

$$\frac{dP_n}{d\Omega} = \frac{\eta^2 n^2}{4\pi^2} |I_n(\hat{\mathbf{n}}_1) J_n(\hat{\mathbf{n}}_2) - I_n(\hat{\mathbf{n}}_2) J_n(\hat{\mathbf{n}}_1)|^2 \,. \tag{2.66}$$

The integrals $I_n(\hat{\mathbf{n}})$ and $J_n(\hat{\mathbf{n}})$ are defined by

$$\begin{aligned} I_n(\hat{\mathbf{n}}) &= \frac{1}{L} \int_0^L d\zeta \, \mathbf{a}'(\zeta) \cdot \hat{\mathbf{n}} \exp[-\frac{i}{2}(\omega_n \zeta + \mathbf{k} \cdot \mathbf{a})] \,, \\ J_n(\hat{\mathbf{n}}) &= \frac{1}{L} \int_0^L d\zeta \, \mathbf{b}'(\zeta) \cdot \hat{\mathbf{n}} \exp[\frac{i}{2}(\omega_n \zeta - \mathbf{k} \cdot \mathbf{b})] \,, \end{aligned} \tag{2.67}$$

where $\hat{\mathbf{n}}_1$ and $\hat{\mathbf{n}}_2$ are unit normal vectors orthogonal to the wavevector $\mathbf{k}$ and $\omega_n = 2\pi n/T$ is the frequency of the nth harmonic with period T.

It is further shown in [135] using these results and those from [136] that the linearised expression for the power spectrum from an infinitely long periodic string lying along the z-direction can also be decomposed in terms of left- and right-moving modes $\mathbf{U}^\perp$ and $\mathbf{V}^\perp$ as follows:

$$\frac{dP}{dz} = \frac{8\pi^3 \eta^2}{L} \sum_{n=1}^{\infty} n \sum_{\substack{|m|<n \\ m+n \text{ even}}} |\mathbf{U}^\perp|^2 |\mathbf{V}^\perp|^2 + |\mathbf{U}^{\perp *} \cdot \mathbf{V}^\perp|^2 - |\mathbf{U}^\perp \cdot \mathbf{V}^\perp|^2 \,, \tag{2.68}$$

where $\mathbf{U}^{\perp}$ and $\mathbf{V}^{\perp}$ are the linearised variables

$$\mathbf{U}^{\perp} = \int_0^L \frac{du}{L}\,\partial_u \mathbf{X}_R^{\perp} e^{i\pi(m+n)u/L},$$
$$\mathbf{V}^{\perp} = \int_0^L \frac{dv}{L}\,\partial_v \mathbf{X}_L^{\perp} e^{i\pi(m-n)v/L}, \tag{2.69}$$

and we note that, from the symmetry of the system, we obtain the 'selection rule' that $m+n$ must be *even*. Here, we have defined $u = \sigma - \tau$ and $v = \sigma + \tau$ as null coordinates on the string worldsheet, and $X^{\mu} = X_R^{\mu} + X_L^{\mu}$ are the worldsheet coordinates split into right- and left-moving modes (with the split first performed in [137]).

Gravitational Radiation from Local Strings

Similarly to the massless radiation characterised above, the Nambu-Goto action can be used to derive the power spectrum of gravitational waves from local strings. For a closed loop, it can be shown [137, 134] that the power spectrum is given by

$$\frac{dP_n}{d\Omega} = \frac{w_n^2}{\pi}\{\tilde{T}^*_{\mu\nu}(w_n,\hat{\mathbf{r}})\tilde{T}^{\mu\nu}(w_n,\hat{\mathbf{r}}) - \tfrac{1}{2}|\tilde{T}^{\lambda}_{\lambda}(w_n,\hat{\mathbf{r}})|^2\}, \tag{2.70}$$

where $T^{\mu\nu}(\mathbf{x},t)$ is given by

$$T^{\mu\nu}(\mathbf{x},t) = \mu\int_0^L d\sigma\,\delta^{(3)}(\mathbf{x}-\mathbf{x}(\sigma,t))(\dot{x}^{\mu}\dot{x}^{\nu} - x'^{\mu}x'^{\nu}). \tag{2.71}$$

Again, the solution can be split into left and right-moving modes, with the power radiated per unit solid angle Ω given by

$$\frac{dP_n}{d\Omega} = 8\pi G\mu^2 n^2\{|I_n(\hat{\mathbf{n}}_1)J_n(\hat{\mathbf{n}}_1) - I_n(\hat{\mathbf{n}}_2)J_n(\hat{\mathbf{n}}_2)|^2$$
$$+ |I_n(\hat{\mathbf{n}}_1)J_n(\hat{\mathbf{n}}_2) - I_n(\hat{\mathbf{n}}_2)J_n(\hat{\mathbf{n}}_1)|^2\}. \tag{2.72}$$

For a long string oriented along the z-axis, it can be shown [35, 135] that the linearised power spectrum equation for gravitational radiation is given by

$$\frac{dP}{dz} = \frac{64\pi G\mu_0^2}{L}\sum_{n=1}^{\infty} n \sum_{\substack{|m|<n \\ m+n\,\text{even}}} |\mathbf{U}^{\perp}|^2|\mathbf{V}^{\perp}|^2 - |\mathbf{U}^{\perp *}\cdot\mathbf{V}^{\perp}|^2 + |\mathbf{U}^{\perp}\cdot\mathbf{V}^{\perp}|^2. \tag{2.73}$$

Comparing the expressions (2.66) with (2.72) and (2.68) with (2.73), we observe that the power spectra of massless radiation from global strings and gravitational radiation from local strings take very similar functional forms. It is therefore reasonable to deduce that the power spectrum of gravitational waves from a local cosmic string can be inferred by analysing the massless radiation from a global string. This has been demonstrated, for example, for certain loop configurations [132, 134].

2.4 Separation of Scales and Current Discrepancies

In the previous two sections, we have outlined the primary methods that are generally used to study the evolution of cosmic strings; the field theory and Nambu-Goto approaches. The one-dimensional Nambu-Goto equations allow us to explore a huge dynamic range, but require us to integrate out internal degrees of freedom and do not directly include backreaction, unless added explicitly. In contrast, the three-dimensional solutions of the full field theory include radiation backreaction and internal degrees of freedom, but have a limited dynamic range. These different approximations appear to produce different outcomes for string evolution, which are interpreted by some researchers as contradictory. A particularly important consequence is quantitative uncertainty about the amplitude and spectrum of string network decay products, where topological strings radiate primarily into the lowest mass channels available (see Section 2.3.3). This has been an outstanding concern in the literature on string network simulations for many years, so renewed effort is needed to establish whether these approaches converge on cosmological scales. Here, we focus on the discrepancies in predictions for global or axion cosmic strings, although similar issues arise for local strings.

An example of the aforementioned discrepancies arises in the study of dark matter axions. As outlined in the Introduction, there has recently been renewed interest in the axion as a dark matter candidate in light of the increasingly stringent constraints on supersymmetric weakly interacting massive particles (WIMPs) (for example, see [138]). Axions arise as a solution to the strong CP problem of QCD, where topological strings are formed in an exactly analogous manner to the $U(1)$ symmetry breaking that occurs in the Goldstone model discussed in Section 2.2.1 (see [139] for further details). Despite the apparent simplicity of axion strings, the exact nature of axion radiation has proved controversial to characterise quantitively due to the limited dynamic range of numerical simulations. By analogy with (2.17), a global

axion string has a logarithmically divergent linear energy density

$$\mu = 2\pi f_a^2 \ln(R/\delta)\,, \tag{2.74}$$

where $f_{\rm a}$ is the Peccei-Quinn energy breaking scale, $\delta \sim f_{\rm a}^{-1}$ is the typical width of the core of the string and R is the large-scale cut-off set by the typical curvature of the string. For a typical axion model with $f_{\rm a} \sim 10^{11}\,\text{GeV}$, the width $\delta \sim 10^{-23}\,\text{m}$ whereas the cut-off $R \sim 1/200\,\text{MeV} \sim 1\,\text{m}$ at the QCD scale. The natural logarithm in a cosmological context is therefore about

$$\ln(R/\delta) \sim 70\,. \tag{2.75}$$

In contrast, numerical simulations have difficulty probing a dynamic range in excess of $\ln(R/\delta) \sim 6$. This means that numerical axion strings generally have more than an order of magnitude stronger relative coupling to massless radiative modes than their cosmological counterparts. For this reason, rather than extrapolating results from strongly coupled numerical simulations, most authors have argued that cosmological axion strings behave qualitatively more like (local) Nambu-Goto strings [19, 132, 135] and use semianalytic approaches to estimate network radiation into axions [100, 139].

For global cosmic strings near the GUT-scale, the difference between typical length scales is even greater, given approximately by

$$\ln(R/\delta) \sim 100\,, \tag{2.76}$$

with less than 1% of the energy per unit length in the string core μ_0/μ (see (2.17)). Under these circumstances, one would expect the Nambu-Goto approach to be a good approximation. However, despite the much larger dynamic range available to Nambu-Goto simulations, it remains challenging to establish that the large-scale properties of networks converge to truly scale-invariant behaviour, let alone the behaviour of fractal-like small-scale features which continue evolving, including the key loop production function (for example, see [90]). Moreover, there is no clear prescription for including radiative backreaction in Nambu-Goto simulations (although see [140]). (As an aside, we note that for axion strings the presence of much stronger radiative effects should influence and probably stabilise small-scale network properties.) In the context of gravitational wave predictions, disagreements in the literature have meant that the constraints on local cosmic strings recently published by LIGO consider three separate Nambu-Goto models [89].

In contrast, field theory simulations evolve the 'real' string equations of motion given by equation (2.10), allowing the full dynamics of the internal degrees of freedom to be captured. However, with current computational resources it is impossible to simulate string networks using fixed grid simulations with sufficient dynamic range to achieve convergent behaviour. It is usually necessary to adopt the so-called 'fat string' approach, growing the string width to match the comoving grid resolution [141, 95, 102, 104, 105, 107], essentially lowering the particle mass m_H and keeping light massive radiative channels competitive with massless modes. There have been sophisticated attempts to extrapolate from field theory simulations [105–107], but generally asymptotic scaling regimes differ on large scales by a factor of two from Nambu-Goto strings and the small-scale features are strongly affected by radiative effects around the comoving string width δ. Innovations adding more gauge fields [142] have enabled global axion string simulations with larger tensions comparable to (2.75) to be performed. However, this approach still uses the comoving width algorithm, so there remain artificially more massive radiation channels available.

These alternative approaches yield different predictions for radiation rates from global cosmic strings, in the case of axion strings yielding incompatible dark matter axion mass predictions and an uncertain guide for axion searches [120]. It is hence necessary to introduce new high resolution numerical techniques to accurately resolve these differences, concentrating computational power where it is needed near the radiating string core.

Chapter 3

Numerical Implementation with GRChombo

In this chapter, we describe the numerical methods used to perform cosmic string simulations with adaptive mesh refinement (AMR) using GRChombo. We discuss the motivation behind using AMR, as well as important elements of the specific structure of the code. We describe the adaptive mesh and other grid parameters that are important in simulations, the methods used to obtain appropriate initial conditions and the diagnostic tools that are used to extract physical information. Finally, we discuss profiling work that has been undertaken on GRChombo to significantly improve the code performance, including speedup and reduction of memory usage.

3.1 Motivation for AMR

In order to accurately numerically evolve cosmic strings, as well as non-linear systems in general, it is vital that simulations are able to resolve features that emerge on different length scales. To resolve small-scale features requires a simulation box with a sufficiently fine mesh. However, for a simulation to capture macroscopic effects, the grid must also be sufficiently large. Traditional 'fixed grid' numerical approaches will often be unable to satisfy this requirement if there are not enough computational resources available to evolve a sufficient number of grid points. One method that can be used to address this is to increase the resolution of the numerical grid in smaller regions where small-scale features of interest are present. This method is known as 'mesh refinement'.

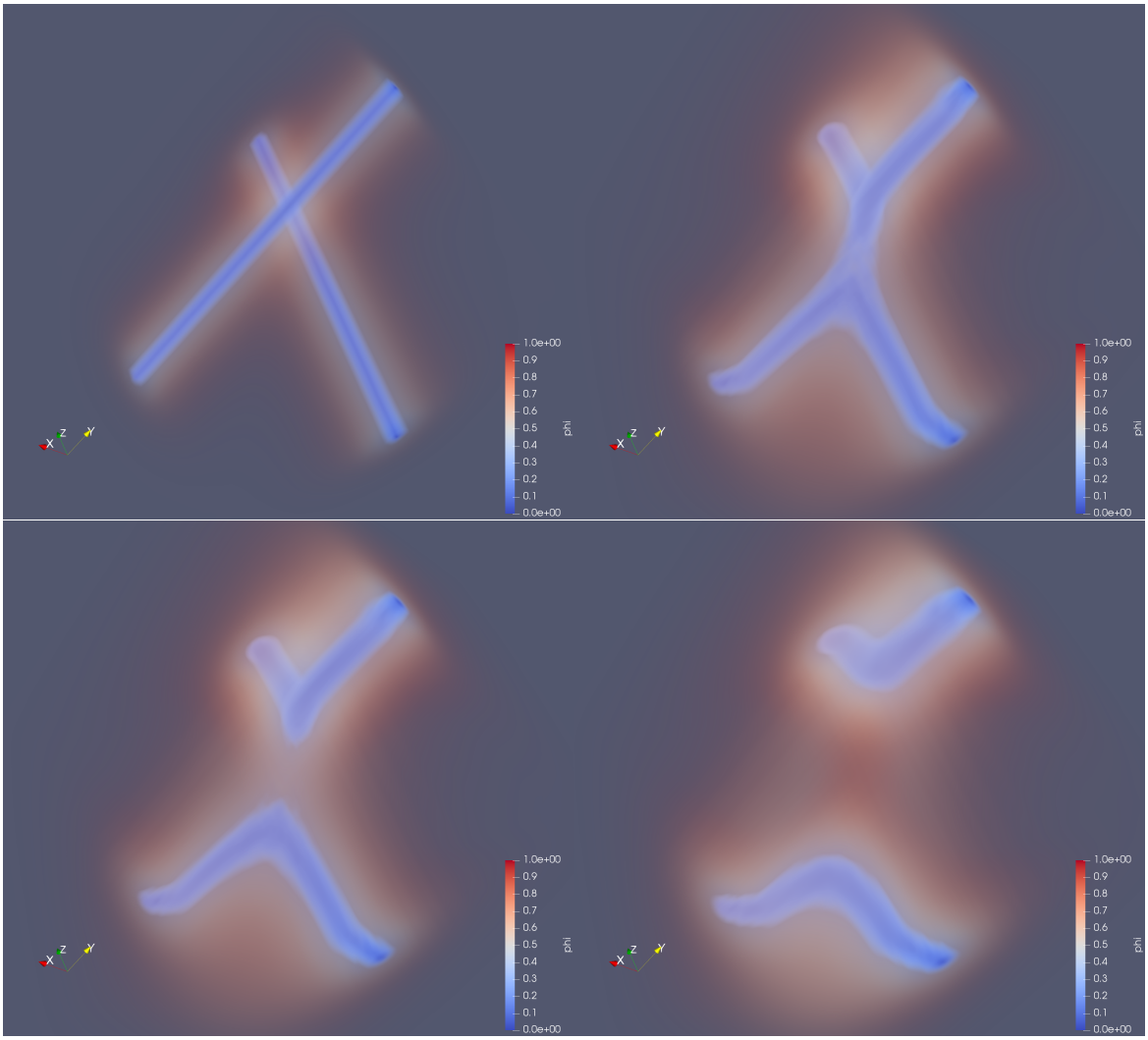

Fig. 3.1 Evolution of ϕ for two colliding global strings at right angles with velocity $v = 0.8$ towards each other. Strings are evolved using a fixed grid evolution algorithm on a 100^3 grid. Red to blue represents $\phi = 1$ to $\phi = 0$.

The importance of mesh refinement for cosmic string evolution can be clearly demonstrated by comparing simulations of high energy string configurations with and without grid refinement. In Figure 3.1, two straight global strings are set up at right angles and given a high velocity $v = 0.8$ towards each other, so that they collide at relativistic speeds.[1,2] The second order equations of motion (2.10) for the real and imaginary components of the complex scalar field $\varphi = \phi_1 + i\phi_2$ are then evolved on a 100^3 grid with fixed spacing Δx, without mesh refinement. The evolution scheme used is a standard second order 'leapfrog' algorithm, which uses values of $\phi_{1,2}$ from the previous two timesteps n and $n-1$ to determine $\phi_{1,2}$ at the next timestep $n+1$. The evolution equations themselves are obtained by discretising (2.10) using a centred finite difference scheme with

$$\frac{\partial^2 \phi_i}{\partial t^2} \equiv \frac{\phi_i^{n+1} - 2\phi_i^n + \phi_i^{n-1}}{\Delta t^2} \qquad \text{and} \qquad \partial_x^2 \phi_i \equiv \frac{\phi_{i+1}^n - 2\phi_i^n + \phi_{i-1}^n}{\Delta x^2}\,, \tag{3.1}$$

where Δt is the constant time interval between steps and i denotes the gridpoint coordinate.[3] Substituting into (2.10), the discretised equations of motion are given by

$$\phi_i^{n+1} = 2\phi_i^n - \phi_i^{n-1} + \frac{6\Delta t^2}{\Delta x^2}(\phi_{av} - \phi_i^n) + \Delta t^2 \left(-\frac{\lambda}{2}\phi\left(\phi\bar{\phi} - \eta^2\right)\right)\Bigg|_i^n\,, \tag{3.2}$$

where $\phi_{av} = (\phi_{i+1}^n + \phi_{i-1}^n + \phi_{j+1}^n + \phi_{j-1}^n + \phi_{k+1}^n + \phi_{k-1}^n)/6$ is the averaged value of ϕ for the current timestep n at $\{i, j, k\}$, and i, j and k index the x-, y- and z- coordinates of the gridpoints. We observe that the two strings move towards each other, connect, intercommute (exchange ends) and move off in opposite directions towards the boundaries.

Figure 3.2 shows the evolution of the same configuration of two highly relativistic global cosmic strings colliding at right angles. However, this simulation is performed using the adaptive mesh refinement (AMR) code `GRChombo`[4], which will be described in more detail in the rest of the section. `GRChombo` is constructed to evolve first order equations of motion,

[1] The code used for Figure 3.1 was adapted from a 'leapfrog' code provided by E. P. S. Shellard.

[2] This configuration of initial conditions is set up using a numerically obtained radial profile of the string, which is discussed in more detail in Section 3.3.

[3] Note that we have temporarily dropped the subscript $\{1,2\}$ for clarity.

[4] This simulation is performed using an early version of `GRChombo` which simulated the collision of cosmic strings in 2D, provided by M. Kunesch, 2017. I adapted this for 3D colliding strings.

so we decompose (2.10) as follows:

$$\dot{\phi} = \Pi \tag{3.3}$$

$$\dot{\Pi} = \partial_x^2\phi + \partial_y^2\phi + \partial_z^2\phi - \frac{\lambda}{2}\phi(\phi\bar{\phi} - \eta^2)\,, \tag{3.4}$$

where dot denotes differentiation with respect to time and ϕ and Π denote $\phi_{1,2}$ and $\Pi_{1,2}$. The four variables $\phi_{1,2}$ and $\Pi_{1,2}$ are evolved using (3.3) and (3.4) with the fourth order Runge-Kutta integration scheme built into GRChombo. In this example, five levels of mesh refinement are employed around the string core. Again, we observe that the two strings intercommute and move apart. However, in this case not only is the resolution dramatically improved, but a new string loop forms at the point of collision. Although these second- and fourth-order evolution schemes cannot be directly compared to high accuracy, the appearance of this coherent loop, as well as the substructure that emerges along the strings, contrasts significantly with the smooth evolution in Figure 3.1. This shows that mesh refinement offers a significant improvement, even revealing new features (e.g. [143]) that would otherwise be missed by fixed grid simulations.

In addition to demonstrating the effectiveness of mesh refinement in general, it is important to emphasise the specific value of *adaptive* mesh refinement for cosmic string evolution over other refinement methods. Many mesh refinement schemes require users to specify in advance the areas of the grid to refine and the size of refinement regions based on their knowledge and understanding of the physical system, either via setting a predetermined path or by tracking quantities of interest in the simulation. These so-called 'moving box' mesh refinement schemes, such as those built on the CACTUS framework [144–153], have been used successfully, for example, in astrophysical scenarios, where the user often has a good prior knowledge of the behaviour of the systems being studied. However, this method creates problems if we do not understand our system sufficiently well to predict where and how regions of refined mesh need to evolve. It is possible that refinement will be concentrated in the wrong place, or that it will not be applied to a sufficient level to give adequate resolution. In these cases, a more flexible approach is required, using regridding boxes of arbitrary shape and size where the level and position of regridding can be adapted as the simulation progresses. This method ensures that regridding is appropriately targeted and only performed in areas where it is required [154]. This fully adaptive method has been pivotal in facilitating the application of AMR to cosmic string simulations, particularly in the case of string networks, which would be almost impossible using a moving box scheme.

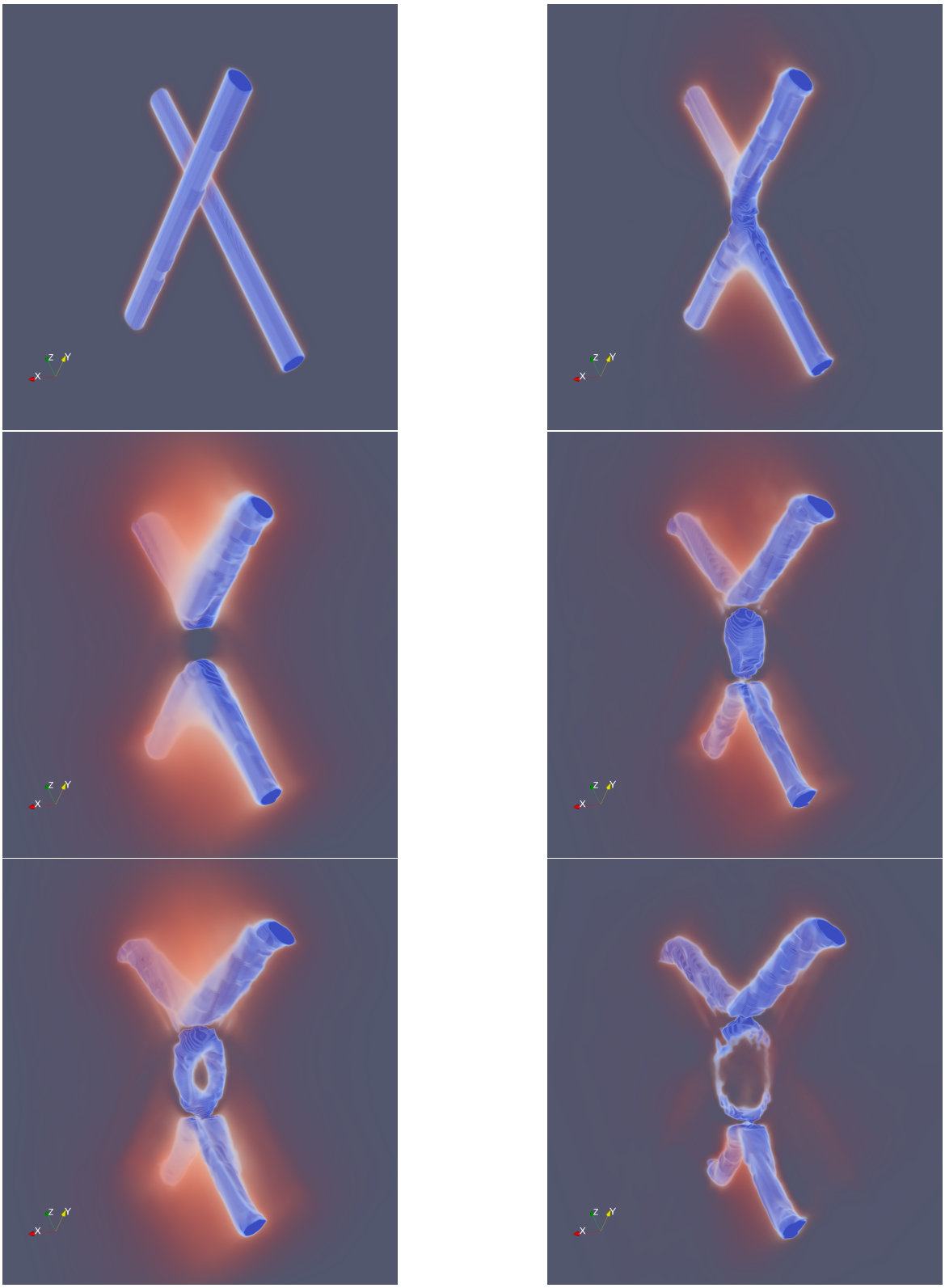

Fig. 3.2 Evolution of ϕ using `GRChombo` for two colliding global strings at right angles with velocity $v = 0.8$ towards each other. Adaptive mesh refinement is used with a 40^3 grid and five levels of refinement. Red to blue represents $\phi = 1$ to $\phi = 0$.

3.2 GRChombo

In this thesis, we use GRChombo [121] to perform hundreds of AMR simulations of cosmic strings. GRChombo is an open-source,[5] finite difference AMR code that allows for refinement of the simulation grid 'on-the-fly'. It has been used for a wide range of applications [155–167], from black hole-axion star collisions to inflation. Originally designed for numerical relativity, we use GRChombo to apply AMR to the cosmic string field equations without gravity, whilst leaving the door open for future analysis with full general relativity. As discussed in Section 2.4 and demonstrated in Section 3.1, it is vital for the accuracy of string simulations that the string core is appropriately resolved. This is especially difficult on a fixed grid given the large discrepancy in length scale between the string width and cosmological distances. Mesh refinement is therefore essential for accurate evolution.

In this section, we outline the features of GRChombo that make it useful for cosmic string evolution, primarily the adaptive mesh algorithm, as well as the parallelism and load balancing that enables large-scale simulations to be performed. We also describe the simulation parameters that are most important in determining code accuracy and performance, including high-frequency mode dissipation and the implementation of boundary conditions. Finally, we outline how GRChombo allows for three-dimensional visualisation of the simulation output.

3.2.1 Implementation of Adaptive Mesh Refinement

Mesh refinement is a computational tool that enables the 'fineness' of a numerical simulation grid to adapt as a simulation progresses, allowing features of interest to be resolved that may otherwise be missed using the base coarse mesh. At the most straightforward level, it allows for the spacing between gridpoints Δx to be tuned as required for accurate resolution. However, in practice, mesh refinement creates significant computational challenges. For example, it must be decided which criteria will be used for generating areas of higher refinement, what shape these areas will take, and whether they are predetermined or recalculated as the simulation progresses. Different refinement levels must also be kept synchronised to ensure that they do not artificially decouple.

In the work presented in this thesis, the underlying structure for the mesh refinement scheme used by GRChombo is provided by Chombo, the public AMR code on which it is built. Chombo is an open-source set of C++ classes which are designed to facilitate straightforward im-

[5] GRChombo is publicly available at https://github.com/GRChombo/.

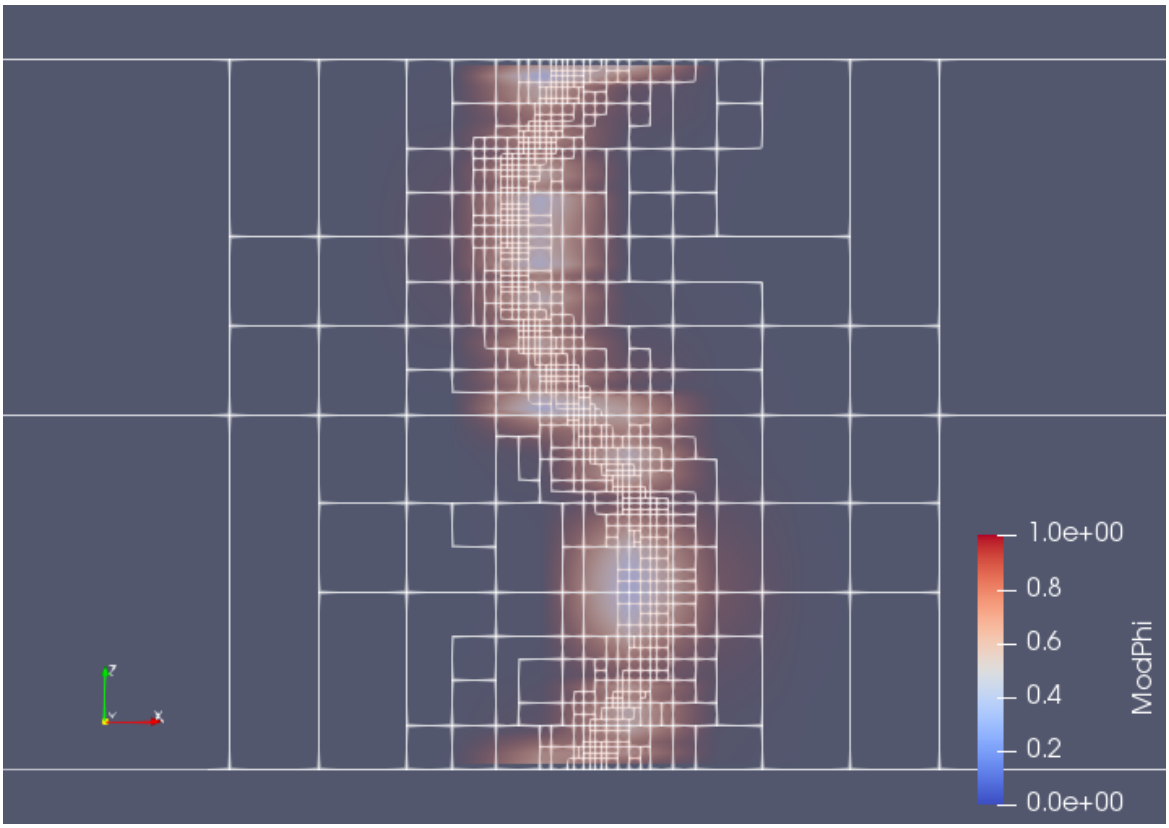

Fig. 3.3 Snapshot of an AMR simulation of a global string using GRChombo. This figure shows $|\varphi|$ for a sinusoidally displaced string with the outlines of AMR boxes for different refinement levels.

plementation of block-structured AMR, which can be complex to implement. Chombo uses Berger-Rigoutsos block-structured grid generation [168] to generate refinement levels using overlaid rectangular boxes. First, cells must be tagged to determine where to refine the mesh to higher precision. GRChombo assigns a value $f(x,y,z) = 1$ or 0, based on a user defined tagging criterion. In the case of a complex scalar field $\varphi = \phi_1 + i\phi_2$ for global cosmic strings, this is set to be

$$f(x,y,z) = \begin{cases} 1 & \text{if } \Delta x\sqrt{(\nabla\phi_1)^2 + (\nabla\phi_2)^2} > |\phi_{threshold}| \\ \\ 0 & \text{otherwise,} \end{cases} \tag{3.5}$$

where Δx is the grid spacing and $|\phi_{threshold}|$ is a custom threshold input by the user. (This choice of regridding threshold is further discussed in Section 3.2.3). The tagging information is passed to the relevant Chombo grid generation class, which efficiently partitions regions that require remeshing into rectangular blocks, which are subsequently refined. In GRChombo,

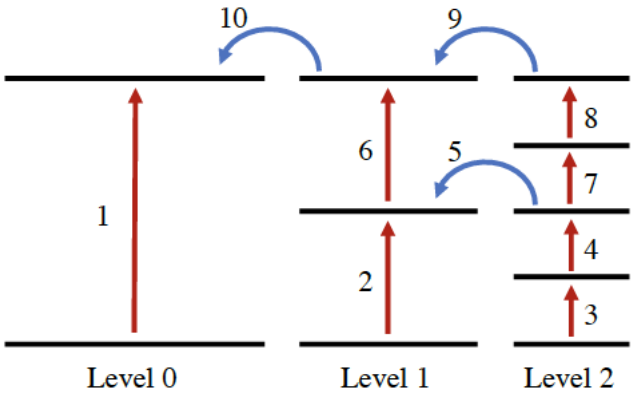

Fig. 3.4 Diagram of the order of subcycling in GRChombo, taken from [154], showing that the timestep Δt is scaled with the resolution. The Berger-Oliger timestepping algorithm evolves first the coarsest level by one timestep $\Delta t \equiv \Delta t_0$, then finer levels by $\Delta t_i = \Delta t_{i-1}/2$ etc. in the order shown, where Δt_i indicates the timestep for level i. Steps 5, 9 and 10 indicate where results from finer levels have been averaged and copied to the coarser level below. Data is also interpolated from coarser levels to fill ghost cells on finer levels (prolongation), as well as between subcycling steps within each level. For clarity, these steps are not included in the diagram.

the default 'refinement ratio' between one level and the next finest is 2, i.e. $\Delta x_{i+1} = \Delta x_i/2$ and $\Delta t_{i+1} = \Delta t_i/2$ where Δx_i and Δt_i indicate the grid spacing and timestep for refinement level i. This remeshing process repeats recursively until a preset number of refinement levels is reached, or there are no more tagged cells. We will not go into detail of the grid generation algorithm here, but further information can be found in [121] and [122]. An example of the application of this block-structured AMR scheme to a cosmic string is given by Figure 3.3, which shows a snapshot of a sinusoidally displaced string with the outlines of the AMR boxes in white. Smaller boxes concentrated towards the centre of the string indicate areas where a finer mesh has been used.

Having generated the structure of the refinement levels, GRChombo subsequently employs a Berger-Oliger time stepping algorithm to evolve the first order partial differential equations (3.3) and (3.4) using a fourth-order Runge-Kutta (RK4) method on the adaptive mesh [169, 170]. As demonstrated by Figure 3.4, the grid first evolves one full timestep from t to $t + \Delta t$ from the coarsest mesh, then proceeds to advance increasingly finer meshes until they all reach $t + \Delta t$. The levels are finally synchronised by averaging grid values from finer levels down to the coarser levels [121]. Figure 3.4 illustrates in detail the order of these evolution steps for multiple refinement levels.

GRChombo's implementation of adaptive mesh refinement ensures as far as possible that areas of finer resolution, and hence computational power, are concentrated in regions where they are most needed. This is vital in allowing us to increase the size and precision of simulations that can be performed using a given amount of computational resources [154]. As we will see, this has the potential to enable accurate simulations of cosmic strings to be performed on a significantly larger scale than has previously been possible.

3.2.2 Parallelism and Load Balancing

Parallelism is a key feature of GRChombo that significantly enhances the performance of the code. As discussed above, AMR is very useful for refining only areas of the grid where extra precision is necessary. However, running AMR simulations in serial, i.e. where operations are performed one after the other, may still result in the code performance being too slow to be practically useful. GRChombo uses hybrid parallelism, exploiting both Message Passing Interface (MPI) and OpenMP parallel processing to enhance code performance by enabling work to be split across a number of processors, allowing users to make full and efficient use of high performance computing (HPC) resources.

GRChombo uses MPI to divide the simulation grid into boxes which can be passed to different processors. The grid is partitioned according to the maximum and minimum box sizes provided by the user. An example of this is given by Figure 3.5, which shows a $256 \times 256 \times 32$ three-dimensional simulation grid of a cosmic string with a slice taken through the centre. We see from the white AMR box outlines that the coarsest level is divided into 64 32^3 boxes, each of which, given enough resources, is sent to a different processor. Finer levels are also similarly distributed, with the exact configuration determined by the load-balancing, as discussed later. When efficiently parallelised, use of MPI improves code performance roughly by a factor of the number of processors used (although the precise factor depends on the so-called 'strong scaling,' see [154]).

OpenMP is a parallelisation tool that assumes access to shared memory, enabling multiple 'threads' of work to run on one processor simultaneously, given enough available memory. Where MPI is designed to pass information between processors, the access of threads to shared memory means that parallelisation within a computational node using OpenMP can avoid the overhead associated with MPI. GRChombo uses OpenMP to allow separate threads to 'choose' a new box to run once they have finished with the previous one, again speeding up the overall evolution.

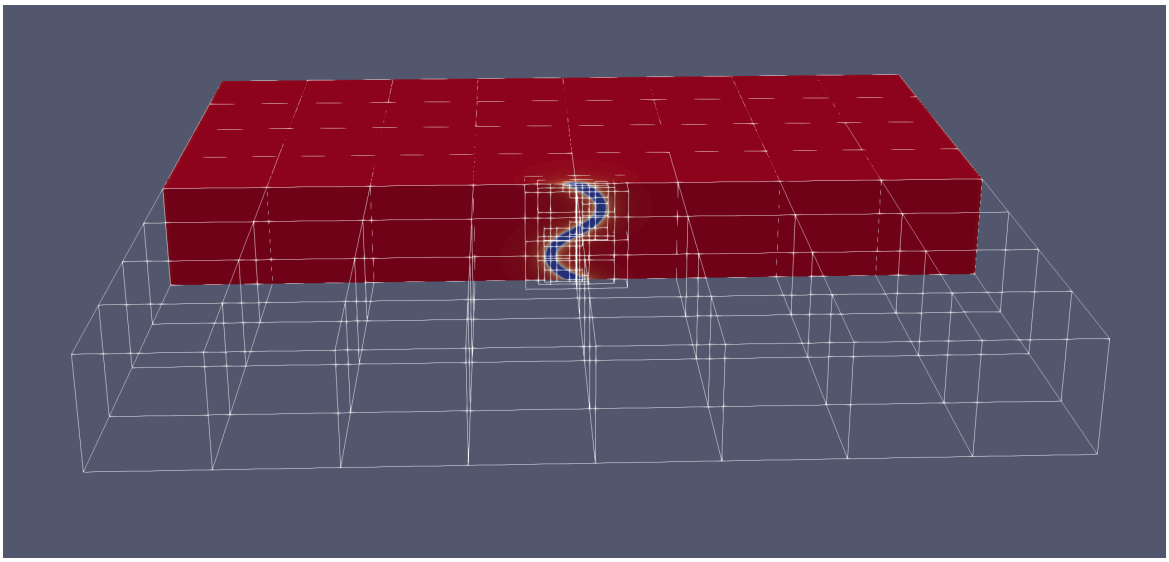

Fig. 3.5 $256 \times 256 \times 32$ 3D simulation grid of a cosmic string simulation with a slice taken through the centre. The coarsest level is divided into 64 32^3 AMR boxes, and smaller boxes indicating finer resolution are concentrated around the string core.

Load-balancing is a key aspect of parallelism that translates the partitioning performed using MPI and OpenMP into increased performance. It is used to distribute boxes between processors and multiple threads within each box. This allows work to be spread evenly between processors, so that once coarser areas of the simulation have finished running, areas with higher refinement can be allocated to the idle processor. Chombo uses the assumption that work is proportional to the number of grid points to balance the computational load between nodes. This means that less computational time is wasted and resources are used more efficiently. The most up-to-date profiling data for GRChombo is given here [154], along with further information about the code. Further details about the implementation of the parallelism are also given by [122].

In practice, when running simulations with GRChombo, a delicate balance must be reached when determining the amount of parallelism required. For example, if the maximum MPI box size is decreased to enable the number of processors to be increased, this may end up being counterproductive, as communication between the MPI ranks may take up more time than the time saved by using the extra processors. This also includes optimising load balancing, which can make a dramatic difference to the code performance. For $256 \times 256 \times 32$ simulations of cosmic strings, we also generally choose to use only one OpenMP thread, as we have found that increasing the number slows down performance, or is less effective than increasing the number of MPI ranks by the same ratio.

3.2.3 Simulation Parameters

GRChombo is a flexible code that allows many integral simulation parameters to be tailored by the user. Choosing appropriate parameters is necessary to apply the adaptive mesh correctly, for example to ensure a sufficient level of refinement is used and that refinement is applied in the appropriate areas. Certain parameters must be chosen to implement the desired boundary conditions or to tailor the amount of damping applied to address instabilities. Choosing appropriate refinement parameters is also vital for optimising code performance.

In this subsection, we outline the parameters that have been important in the work presented in this thesis, particularly for ensuring accuracy and tailoring performance. We outline the importance of choosing a suitable regridding threshold, regridding frequency, maximum refinement level and Kreiss-Oliger dissipation coefficient. We discuss the effect of each of these on performance, as well as on the spectra of certain modes of radiation which we find to be particularly sensitive, particularly in relation to the adaptive mesh regridding. We find that the regridding threshold and regridding frequency in particular are important, as they determine the balance between simulation accuracy and total simulation time. We also find more generally that these parameters are significantly less important in the dissipative evolution stage used to obtain appropriate initial conditions, described in Section 3.3, but do affect the radiation spectrum during the subsequent evolution. This can allow us to use less stringent regridding for the dissipation stage, significantly decreasing the total simulation time. Further information about these and other parameters, including example parameters files used in GRChombo runs, can be found at https://github.com/GRChombo/GRChombo/wiki/Guide-to-parameters.

Regridding Threshold

One important parameter to be chosen when performing string simulations is the regridding threshold $\phi_{threshold}$ for the adaptive mesh. This must be chosen so that higher levels of refinement are concentrated at the string core, in order for the string to evolve accurately and to properly resolve the outgoing radiation. This is particularly the case for higher λ, where the string radius becomes narrower and the wavelength of the lowest energy massive modes decreases. For global cosmic strings, we achieve this using the criterion

$$\Delta x \sqrt{(\nabla \phi_1)^2 + (\nabla \phi_2)^2} > |\phi_{threshold}|\,, \tag{3.6}$$

where Δx is the grid spacing. This determines the regions to refine based on the modulus of the spatial gradient of the complex scalar field φ. A lower threshold will make the simulation more sensitive to regridding, usually resulting in a higher total number of refinement levels and a higher precision at the string core.

For the string simulations in this thesis, we must consider the parameters used for two phases; initial dissipative evolution to obtain appropriate initial conditions (described further in Section 3.3) and subsequent evolution using the wave equations. We have observed that using low levels of mesh refinement in the initial damping phase doesn't affect final results. This means we can generate initial conditions very quickly, whatever levels of mesh refinement are required for the subsequent evolution.

However, in the evolution stage, we find that as λ is increased, a lower $\phi_{threshold}$ i.e. 'harsher' regridding, must be used to reach the level of refinement required to capture the evolution accurately. An example of insufficient regridding is given by Figure 3.6, which shows the trajectory of the string core[6] and also the massless Goldstone radiation emitted by a $\lambda = 10$ string with initial amplitude $A_0 = 4$ with no mesh refinement.[7,8] We see that the massless radiation is not accurately resolved, artificially dissipating as the simulation progresses, and that the string motion, tracked by the position of the string core, is also artificially damped. This should be compared to the corresponding case with appropriate refinement in Figures 4.15 and 4.12, where the amplitude of the string decays slowly and where there is a much more consistent propagating massless signal over time for all modes. Appropriate values for the regridding threshold have been determined for each value of λ by comparing string trajectories with different $\phi_{threshold}$ to determine the value above which no significant change in the oscillatory behaviour of the decaying string was observed. A regridding threshold $|\phi_{threshold}| = 0.25$ was judged sufficient for simulations with $\lambda < 10$ and $|\phi_{threshold}| = 0.1$ for those with $\lambda \geq 10$, where the base resolution $\Delta x_0 = 1$.

Through running several hundred simulations of global strings, we have also observed that massive radiation is very sensitive to the grid resolution and can be significantly affected by the adaptive remeshing.[9] We find that as λ is increased, a more refined grid is required to accurately capture the radiation and string motion. This manifests at higher λ by massive

[6] The algorithm used to track the string core is described in Section 3.4.2.

[7] We defer detailed discussion of the diagnostic used to characterise the massless radiation until Section 4.1. The algorithm used to extract the radiation is also described in Section 3.4.

[8] The amplitude is measured in units Δx.

[9] Again, we defer detailed discussion of the diagnostic used to characterise the massive radiation until Sections 4.1 and 5.1.

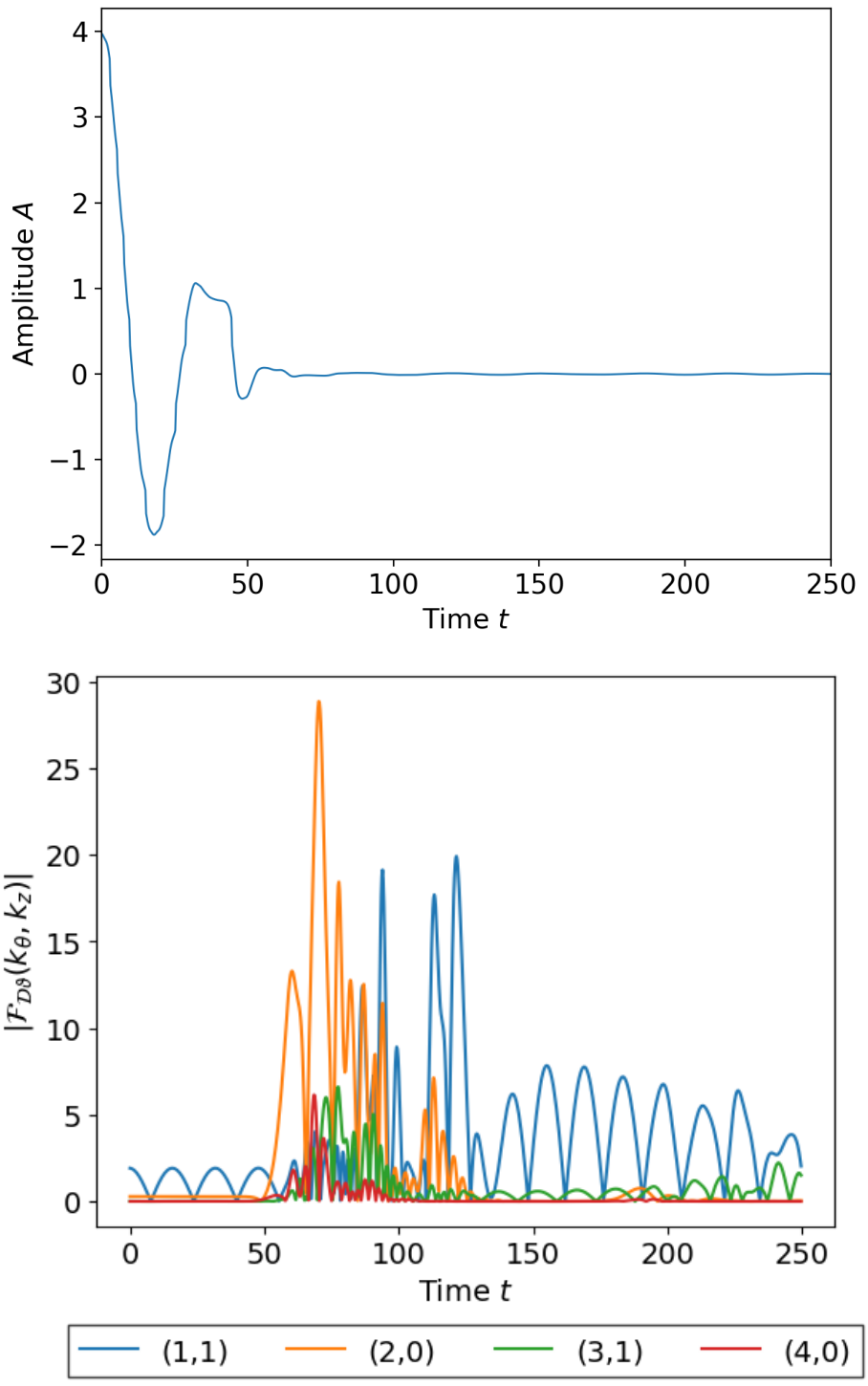

Fig. 3.6 Plot of the string amplitude over time (top) and the absolute value of the $\{mn\} = \{11\}, \{20\}, \{31\}$, and $\{40\}$ Fourier modes of the massless radiation (bottom) from a $\lambda = 10$ string with initial amplitude $A_0 = 4$, measured on a cylinder at $R = 64$ and evolved with no mesh refinement.

radiation becoming 'trapped' at the AMR boundaries where the grid refinement steps down. This is due to the creation of internal reflections, causing a resonant effect which accumulates over time, as shown in Figure 3.7. Further to this, we observe that the remeshing of the grid itself can introduce artificial massive radiation, due to the inevitably slightly inaccurate interpolation between finer and coarser refinement levels. These standing wave instabilities are a familiar shortcoming of AMR for which remedies include the introduction of artificial dissipation by using Kreiss-Oliger damping, discussed further later in this section.

Although it is necessary to use enough mesh refinement for accurate evolution, we must also ensure that we do not use too many refinement levels unnecessarily. This can result in the computational cost becoming too high, for example, with insufficient memory available to store gridpoints for a large number of levels, or insufficient processors available to complete the calculations in a reasonable timeframe. In practice, the necessity for an appropriate regridding threshold to obtain enough refinement for the required accuracy is what has so far limited simulations from being performed at $\lambda > 100$.

Finally, we choose to restrict regridding to within a radius of $R = 64$ from the centre of the grid, to prevent unnecessary refinement of the grid boundaries. This does not interfere with measurements on the radiation cylinder as, in practice,no refinement higher than the base level is ever required at this radius.

Maximum Level

The maximum level parameter can be set by the user to limit the maximum level of refinement, even if the regridding threshold criterion is still satisfied. This can be important for performance, as any unnecessary refinement can significantly increase the total runtime. In our cosmic string simulations, we do not set a maximum level during the string evolution under the wave equations, so the adaptive mesh will continue to regrid until the criterion (3.6) is no longer satisfied for any cells. However, we set a maximum level of one in the initial dissipative evolution stage, as we have found that increasing the maximum level in this case does not change the outcome of the subsequent evolution.

Regridding Interval

The regridding interval parameter sets the integer number of timesteps between each time that GRChombo performs cell tagging and regridding. It is set separately for each refinement level i as a multiple of the timestep Δt_i for that level. For example, setting regridding intervals $256, 256, 256\ldots$ will trigger a remeshing every 256 timesteps for each level, i.e. after $256\,\Delta t_0$

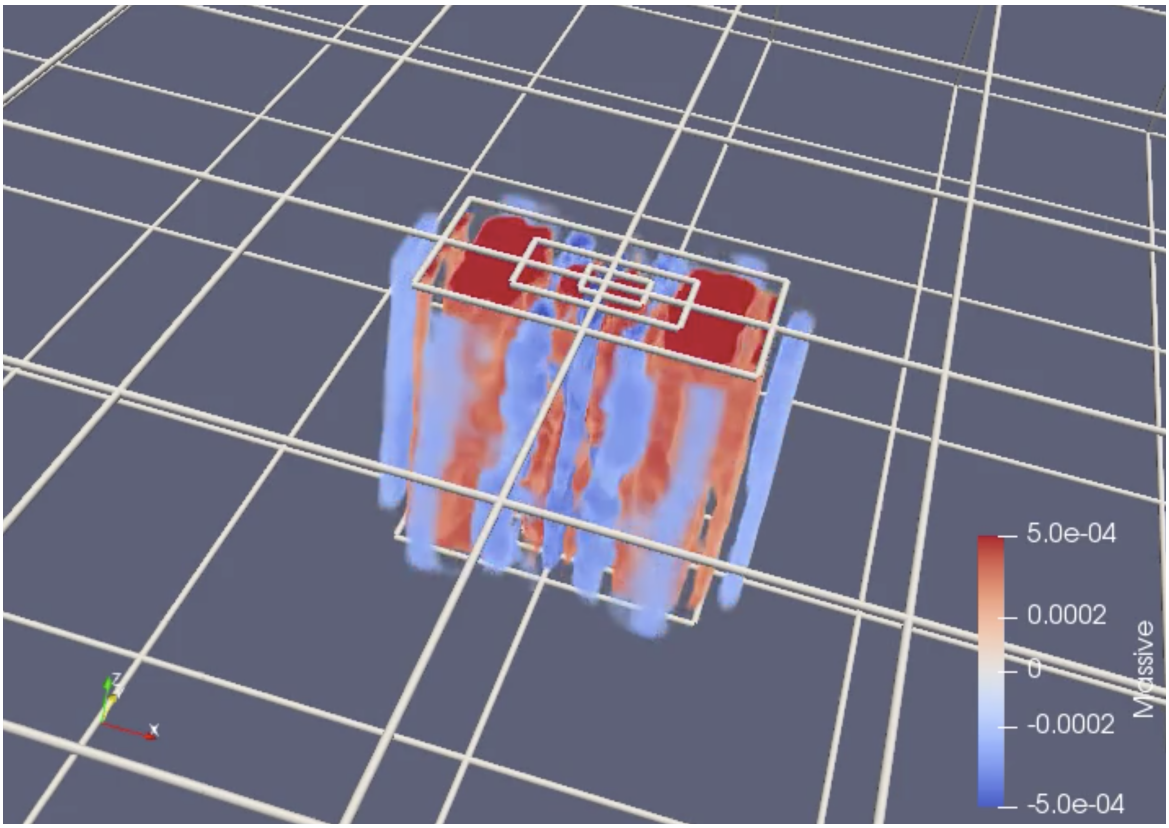

Fig. 3.7 Volume rendering in 3D space (x, y, z) of the massive radiation from a $\lambda = 3$ string, with AMR blocks outlined in white. Much of the radiation signal is trapped at the AMR boundary, and this short wavelength signal grows in amplitude over time.

on the coarsest level, $256\Delta t_1 = 128\Delta t_0$ on the next finest level, $256\Delta t_2 = 64\Delta t_0$ on the next finest etc. (where we recall that the refinement ratio between each level has been set to 2).

Setting appropriate regridding intervals is important as the process can be very computationally expensive. Remeshing too frequently will significantly increase the computation time, but regridding too infrequently means that the evolution may not be accurate, negating the point of implementing AMR at all. In practice, coarser levels may not need to regrid as frequently as finer levels, as they often cover a larger volume of the simulation grid. This means it will take more time for the simulation to evolve at scales of the order of the size of the refinement region.

We find for the dissipative evolution stage of cosmic string simulations that in fact, we do not need to regrid at all after the initial refinement level setup, as increasing the resolution does not affect the subsequent evolution stage. However, for the evolution stage, we find that simulations are sensitive to the regridding frequency, particularly for massive radiation, as discussed above. It is therefore usually necessary to tailor the regridding frequency depending on the specific physical scenario.

As discussed briefly in the previous subsection, we find not only that massive radiation can become trapped within the adaptive mesh boundaries, but that the regridding itself can generate artificial massive radiation. This is likely to be caused by the fact that the interpolation between levels is only first order, introducing numerical error to which massive radiation is particularly sensitive. However, it has also been found that overfitting with higher polynomials introduces errors of its own [121]. This can be addressed in theory by increasing the number of ghost cells, but this is not realistically feasible due to the additional storage required. We can also reduce the regridding frequency, but as previously discussed we still need to ensure that the refinement is appropriately targeted, and so cannot eliminate regridding entirely. We therefore find that the best way to address this issue is to use Kreiss-Oliger dissipation to reduce artifically introduced high frequency modes, as discussed in the next subsection.

Finally, we note that Chombo also has the functionality to incorporate a technique called 'refluxing,' where fluxes on a coarse mesh (currently computed individually for each gridpoint) are replaced with time-averaged fluxes from a finer mesh (see [171] for further details). This is required in flux-conservative systems to properly synchronise coarse and fine levels [121]. This is not currently implemented in GRChombo, as its primary use case of numerical general

relativity is not conservative. However, our system of global cosmic strings is conservative, so this would be an appropriate addition and may help to address the introduction of artificial modes. This will be addressed in future work.

Kreiss-Oliger Dissipation

Often in numerical simulations of non-linear systems, the stability of the evolution scheme can be disrupted by the inevitable introduction of numerical error. In order to maintain stability, it is important to incorporate artificial dissipation to damp artificial high frequency modes. For adaptive mesh refinement, the regridding itself can also generate errors which must be similarly addressed. The most commonly used scheme for this is Kreiss-Oliger dissipation [172] which adds an extra term to the right hand side of the evolution equations for all evolution variables. The term is given by

$$\partial_t \phi(t,x^i) \to \partial_t \phi(t,x^i) + \frac{(-1)^N \sigma}{2^{2N}\Delta x} \sum_i \nabla_i^{2N} \phi(t,x^i)\,, \tag{3.7}$$

where N is the order of the dissipation, σ is a positive parameter to control the amount of dissipation applied and ∇_i^{2N} denotes the centred difference operator of order $2N$. GRChombo uses $N = 3$ Kreiss-Oliger dissipation [172], hence the centred difference operator is given by

$$\nabla_i^6 \phi = \phi_{i+3} - 6\phi_{i+2} + 15\phi_{i+1} - 20\phi_i + 15\phi_{i-1} - 6\phi_{i-2} + \phi_{i-3}\,, \tag{3.8}$$

where ϕ is the evolution variable and $i+n$ labels the grid point i, where n is the total offset. The final correction is then given by

$$\partial_t \phi_i \to \partial_t \phi_i - \frac{\sigma}{64\Delta x}(\phi_{i+3} - 6\phi_{i+2} + 15\phi_{i+1} - 20\phi_i + 15\phi_{i-1} - 6\phi_{i-2} + \phi_{i-3})\,. \tag{3.9}$$

As with other numerical parameters, σ must be selected to achieve a balance between allowing enough damping but without artificially damping physically valid results or creating its own instability. It can be shown by a von Newmann stability analysis [171] for any N that the Kreiss-Oliger dissipation scheme is stable within the bounds:

$$0 \leq \sigma \Delta t/\Delta x \leq 2\,, \tag{3.10}$$

where the ratio $\Delta t/\Delta x$ is the 'Courant factor,' an empirically determined stable ratio between the timestep and grid spacing. We use a Courant factor of 0.25 in all of our simulations, so we set $\sigma < 8$ to ensure stability.

As with the previous parameters, we find that using Kreiss-Oliger dissipation during the initial damping phase has no effect on the final results of the evolution. We can therefore set σ to any value that obeys (3.10) for this stage. However, for the evolution stage, the damping coefficient does have an effect on the radiative spectrum. An example is given by Figure 3.8,[10] which shows the absolute value of the $\{mn\} = \{11\},\{20\},\{31\}$, and $\{40\}$ Fourier modes of the massive radiation from a $\lambda = 1$ string with two different Kreiss-Oliger coefficients, $\sigma = 0.1$ and $\sigma = 2$. Note that the $\{mn\}$ modes referred to here are characterised in Figure 4.2. We see that the higher damping coefficient significantly decreases the overall magnitude of this high frequency radiation, especially the initial burst from the highest $\{40\}$ mode.

Boundary Conditions

It is important in numerical simulations to choose boundary conditions for the grid that are consistent with the physical setup being evolved, and that, as far as possible, do not introduce numerical error. GRChombo supports periodic, fixed, reflective and Sommerfeld boundary conditions, as well as allowing for custom boundaries to be implemented. Each of these conditions can be applied independently to each boundary.

In the majority of our simulations, we implement periodic boundary conditions in the z-direction by filling ghost cells outside the numerical grid with cells from the same refinement level on the other side. This effectively creates an infinitely long string with an infinite radius of curvature. In the x- and y-directions, we use Sommerfeld boundary conditions which allow outgoing radiation to dissipated away. This is implemented for a field ϕ by modifying the equations of motion adjacent to the boundaries as follows [121]:

$$\frac{\partial \phi}{\partial t} = -\frac{v x_i}{r}\frac{\partial \phi}{\partial x_i} - v\,\frac{\phi - \phi_0}{r} \tag{3.11}$$

where $r = \sqrt{x^2 + y^2 + z^2}$ is the radial distance from the center of the grid, ϕ_0 is the desired field value at the boundary and v is the velocity of the radiation, which is typically chosen to be equal to 1.

[10] Again, we defer detailed discussion of the diagnostic used to characterise the massive radiation until Section 4.1.

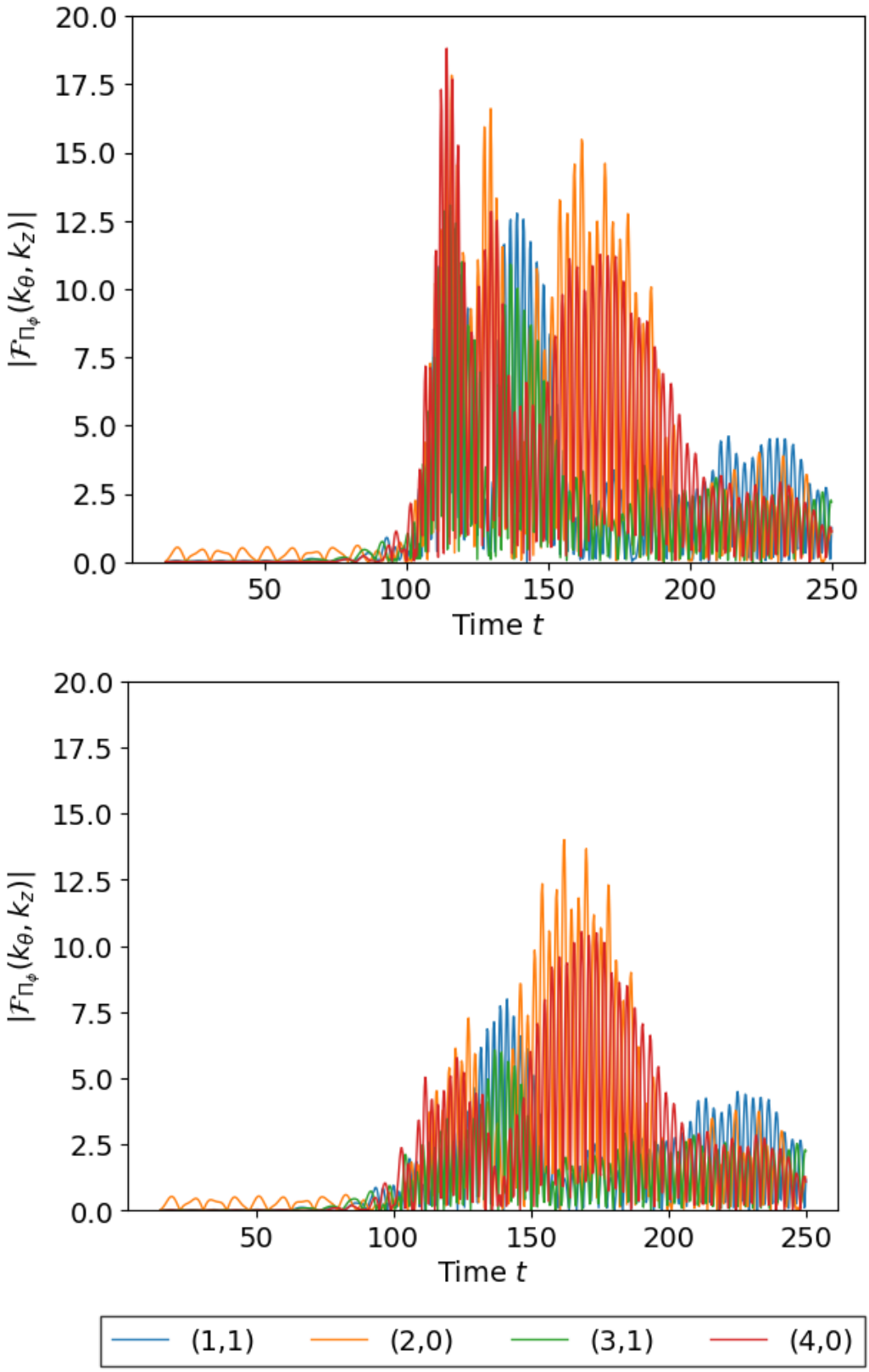

Fig. 3.8 Plot of the absolute value of the $\{mn\} = \{11\}, \{20\}, \{31\}$, and $\{40\}$ Fourier modes of the massive radiation from a $\lambda = 1$ string with initial amplitude $A_0 = 12$, measured on a cylinder at $R = 64$ with Kreiss-Oliger damping coefficients $\sigma = 0.1$ (top) and $\sigma = 2$ (bottom).

Despite implementing Sommerfeld boundary conditions, for some simulations we observe what appears to be small amounts of radiation reflected from the boundary being measured by the analysis cylinder for $t \geq 192$, i.e. the sum of the light crossing time from the centre of the grid to the boundary, and then back to the analysis cylinder. We take this into consideration when performing our analysis, as discussed in Chapters 4 and 5.

3.2.4 Visualisation

Visualisation of results is vital for numerical simulations, both for debugging code and for interpreting results. GRChombo facilitates visualisation by outputting HDF5 files as simulations run, at times specified by the user. These can either be plot files (for visualisation and analysis purposes only) or checkpoint files (from which the simulation can also be restarted). This allows the output to be easily visualised using software such as Paraview or VisIt, both of which support the Chombo HDF5 file format. All visualisations in this thesis, such as Figure 3.5, are created by reading output HDF5 output files in Paraview, allowing evolution variables to be plotted and AMR blocks to be seen.

Further to this, significant work has been performed with Intel using the simulations presented in this thesis on so-called 'in-situ visualisation.' This is a method of visualisation that enables large datasets to be displayed using software as the code is running, without requiring the data files to be stored in memory. This has potential application especially to exascale computing, which is a current area of focus for the development of supercomputers. This will be discussed in further detail in Chapter 6.

3.3 Initial Conditions

In this section, we describe how the initial conditions are generated for individual oscillating cosmic strings, travelling wave solutions and string networks. Oscillating strings and string networks both involve dissipative damping of a crude initial configuration, which can be subsequently evolved from a desired HDF5 checkpoint file. Travelling wave solutions can be evolved directly without an initial dissipation phase.

3.3.1 Individual Oscillating Strings

The majority of the work presented in this thesis studies the radiation from single oscillating strings. As a straightforward starting point, we would like to begin with a string that is

approximately sinusoidally displaced. However, there are several subtleties involved in obtaining appropriate initial conditions, the first of which is that we do not know their exact analytical form.

The initial conditions for a single 'sinusoidal' Nambu-Goto global string, i.e. for a periodic solution displaced only in one direction, are well established [135]. We can parametrise the solution in terms of left-moving ($u = \sigma + t$) and right-moving ($v = \sigma - t$) coordinates along the string, giving

$$\mathbf{X} = \left(\frac{\varepsilon}{2\Omega} \big[\cos \Omega u + \cos \Omega v \big], 0, \frac{1}{2\Omega} \big[\mathsf{E}(\Omega u, \varepsilon) + \mathsf{E}(\Omega v, \varepsilon) \big] \right). \tag{3.12}$$

where $\mathsf{E}(\phi, \varepsilon)$ is the incomplete elliptic integral of the second kind,

$$\mathsf{E}(\phi, \varepsilon) = \int_0^{\phi} d\theta \sqrt{1 - \varepsilon^2 \sin^2 \theta} \qquad (\varepsilon \leq 1). \tag{3.13}$$

We define ε to be the amplitude relative to the invariant string length or time period T, given by

$$\varepsilon = \frac{2\pi A}{T} \equiv \Omega A, \tag{3.14}$$

where A is the absolute amplitude and $\Omega = 2\pi/T$ is the fundamental frequency, approximated by $\Omega \approx 2\pi/L$ for $\varepsilon \ll 1$. We also define $0 \leq \sigma \leq T$ as a parameter along the string over one period, defined to be $T = \alpha L$ for a string directed along the z-direction, where $\alpha \geq 1$ is the fractional increased path length relative to a straight string of length L. However, it is not clear to what extent this Nambu-Goto solution applies to initial conditions for field theory simulations with a range of λ. We address this by setting up an initial sinusoidal configuration and applying a period of dissipative evolution, allowing relaxation towards a lower energy solution which is closer to (3.12).

The pre-dissipation initial configuration is obtained first by numerically solving the static field equation (2.12) to obtain the string cross-section or radial profile $\phi(r)$, as discussed in Section 2.2.1 and shown in Figure 2.3. We use $\phi(r)$ to set the initial values

$$\phi_1 = \phi \cos \theta, \qquad \phi_2 = \phi \sin \theta. \tag{3.15}$$

This two-dimensional initial data must be extended in the z-direction to create a three-dimensional string. We displace the radial profile in the x-direction from $x = 0$ as a function

of the z-coordinate, using

$$\mathbf{X}(z) = (A \sin \Omega_z z, 0, z) \,, \tag{3.16}$$

where $\Omega_z = 2\pi/L$ and the wavelength of the string L is set to be equivalent to the z-dimension of the box, as demonstrated in Figure 3.3. Note that this sinusoidal configuration diverges from (3.12) as A increases. Further to this, these 'crude' initial conditions set the normal of the string cross-section to be parallel to the z-direction. This introduces high frequency massive internal degrees of freedom, which interfere with the fundamental modes of radiation from the string oscillation that we would like to investigate. We therefore relax this initial configuration to obtain lower energy initial data with the normal of the cross-section approximately tangential to the string, thereby also relaxing the internal degrees of freedom. We achieve this by choosing an amplitude A approximately $1.5\times$ our desired initial A_0, then relaxing using dissipative evolution:

$$\frac{\partial \varphi}{\partial t} - \nabla^2 \varphi + \frac{\lambda}{2} \varphi (\varphi \bar{\varphi} - \eta^2) = 0 \,, \tag{3.17}$$

allowing the intial approximation to evolve to appropriate initial conditions with the required amplitude. For example, for a desired $A_0 = 1$, we choose to damp from $A = 1.5$.

To determine when the string has reached A_0, the exact position of the zero in the string core is calculated using an string core locating algorithm, discussed further in Section 3.4.2. This information is output into a text file and analysed using a python script to find the time at which the string reaches the desired amplitude. GRChombo allows for simulations to be restarted from HDF5 checkpoints [121], so the correct checkpoint for the given amplitude can be selected and the simulation evolved using the wave equations (3.3) and (3.4).

Figure 3.9 demonstrates the difference in oscillation trajectory between strings damped from $A = 12$ and with no damping, evolved from an amplitude of $A_0 = 8$. We see approximately a 4% difference in amplitude in the first oscillation. More significantly, Figure 3.10 shows a plot of the absolute value of the $\{mn\} = \{1\,1\}, \{2\,0\}, \{3\,1\}$, and $\{4\,0\}$ Fourier modes of the massless radiation for the same configurations, revealing approximately a 13% increase in the magnitude of the first maximum from the undamped $A_0 = 8$ compared to damped from $A = 12$. These results indicate, as expected, that the 'crude' sinusoidal initial conditions have artificially high energy, most likely due to the discontinuous initial input of the cross-section.

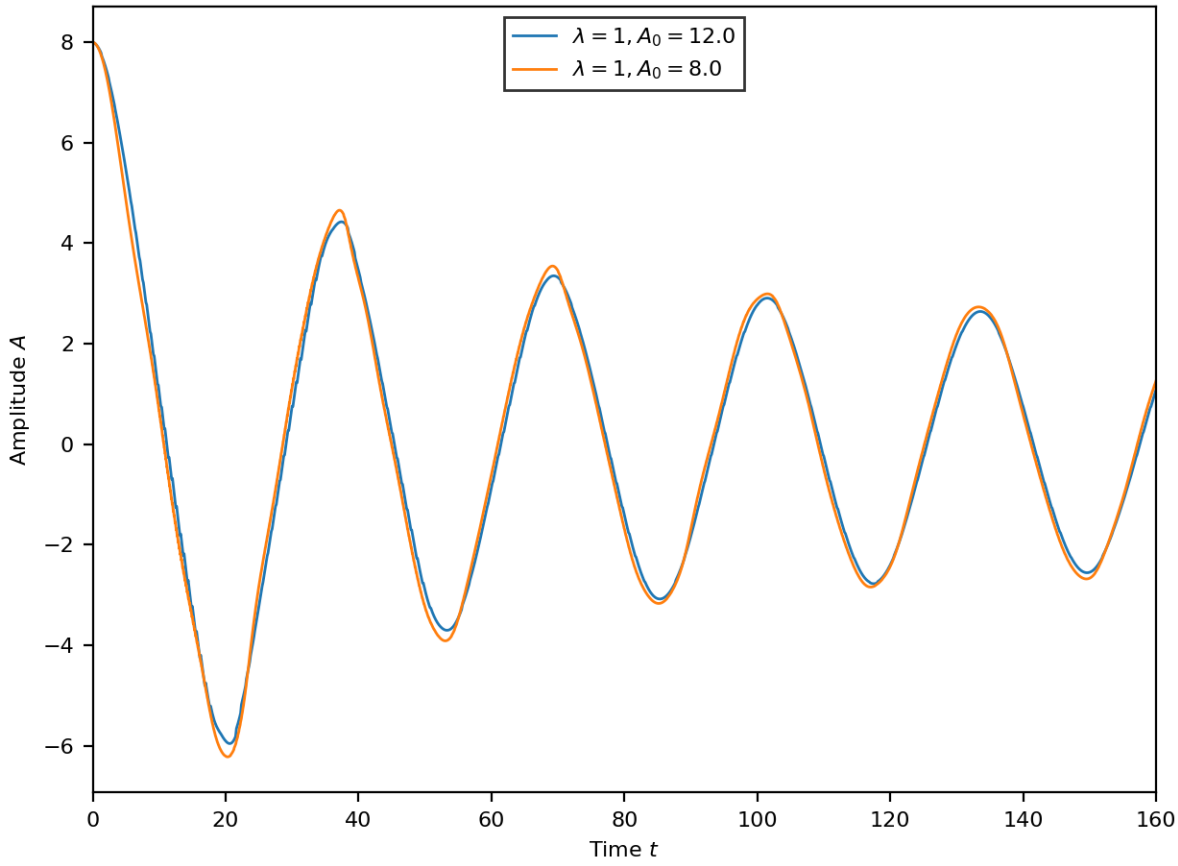

Fig. 3.9 Amplitude of $\lambda = 1$ string with an initial dissipative evolution from $A = 12$ to $A_0 = 8$ (blue), and with no initial dissipative evolution (yellow) i.e. evolution directly from $A_0 = 8$.

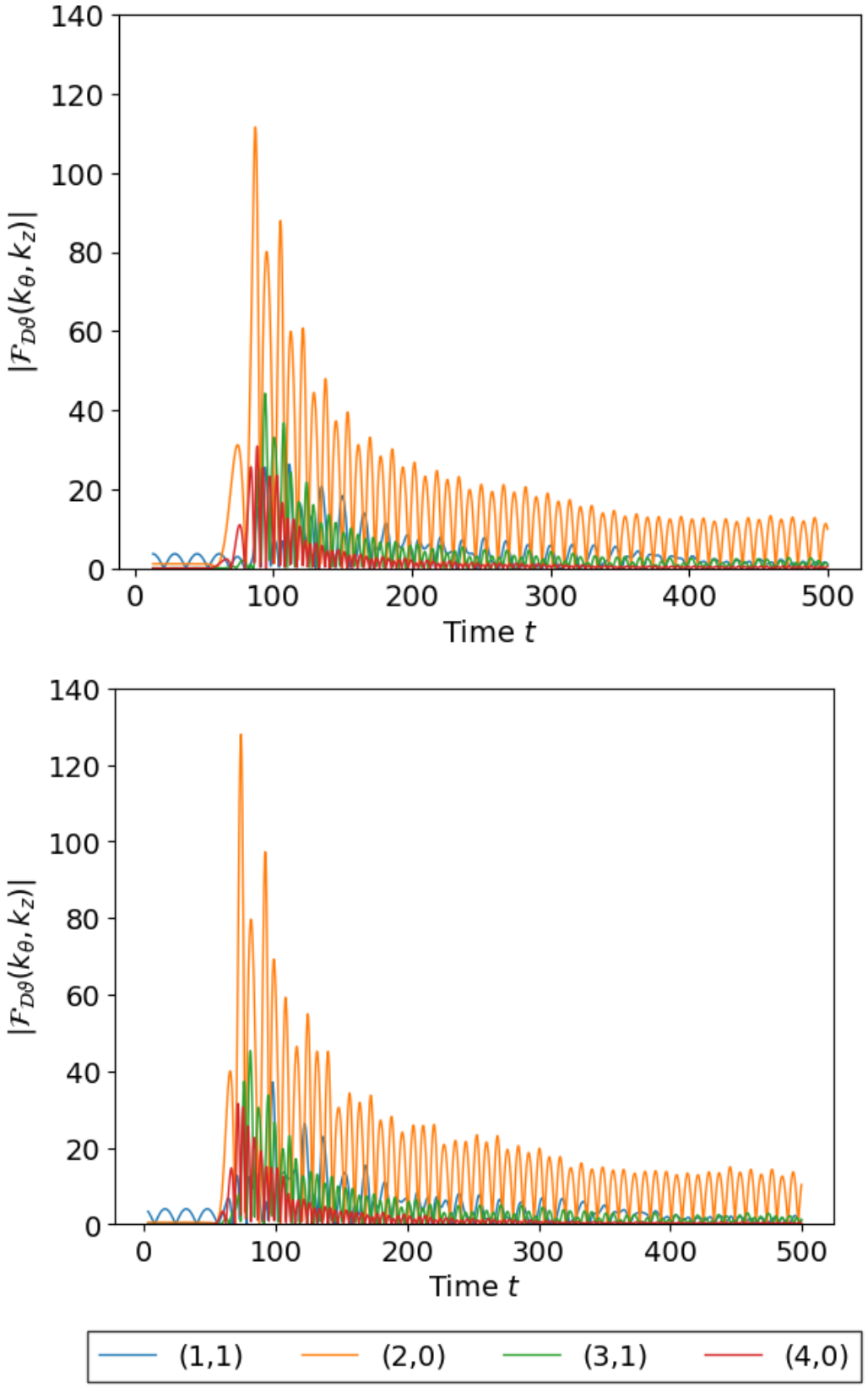

Fig. 3.10 Plot of the absolute value of the $\{mn\} = \{11\},\{20\},\{31\}$, and $\{40\}$ Fourier modes of the massless radiation $\mathscr{D}\vartheta \cdot \hat{\mathbf{r}}$ from a $\lambda = 1$ string with initial amplitude $A_0 = 8$, measured on a cylinder at $R = 64$. The top graph shows the spectrum from a simulation with initial dissipative evolution from $A = 12$, the bottom has no dissipative evolution.

3.3.2 Travelling Waves

Preliminary work has been undertaken in this thesis on generating cosmic string cusp configurations using travelling wave initial conditions. It has been shown by [173] that exact travelling wave solutions for Nambu-Goto global cosmic strings can be straightforwardly derived by redefining

$$X = x - \psi(t \pm z), \tag{3.18}$$

in the evolution equations, where $\psi(t \pm z)$ is some arbitrary function that indicates travel in the positive or negative z-direction. We can use this along with the radial profile $\phi(r)$ for a static string, defined by (2.11), to construct a solution with two Gaussian travelling waves of equal and opposite amplitude A propagating towards each other along the z-direction. We convert $\phi(r) = \phi(x,y)$ to $\Phi(R) = \Phi(X,Y)$, where for the desired configuration we set

$$X = x + A\left(\exp\left\{-\frac{(z-t+b)^2}{2\sigma_d^2}\right\} - \exp\left\{-\frac{(z+t-b)^2}{2\sigma_d^2}\right\}\right), \tag{3.19}$$

$Y = y$ and $R^2 = X^2 + Y^2 \equiv X^2 + y^2$, where b is the displacement of the Gaussian from $z = 0$ and σ_d is the standard deviation. The initial string profile is then given by

$$\varphi(r,\theta) \to \Phi(X,y)e^{i\Theta}, \tag{3.20}$$

so that the real and imaginary parts Φ_1 and Φ_2 are

$$\Phi_1 = \Phi(X,y)\cos\Theta, \qquad \Phi_2 = \Phi(X,y)\sin\Theta, \tag{3.21}$$

where $\tan\Theta = y/X$. The time derivatives $\Pi_{1,2}$ are then given by

$$\Pi_1 = \left.\frac{\partial X}{\partial t}\right|_{t=0}\left(\frac{X^2}{R^2}\frac{\partial\Phi}{\partial R} + \Phi\frac{y^2}{R^3}\right) \tag{3.22}$$

$$\Pi_2 = \left.\frac{\partial X}{\partial t}\right|_{t=0}\left(\frac{\partial\Phi}{\partial R}\frac{Xy}{R^2} - \Phi\frac{Xy}{R^3}\right), \tag{3.23}$$

where

$$\left.\frac{\partial X}{\partial t}\right|_{t=0} = \frac{A}{\sigma_d^2}\left((z+b)\exp\left\{-\frac{(z+b)^2}{2\sigma_d^2}\right\} + (z-b)\exp\left\{-\frac{(z-b)^2}{2\sigma_d^2}\right\}\right). \tag{3.24}$$

These initial conditions can then be evolved as before using the evolution equations (3.3) and (3.4).

3.3.3 Networks

Preliminary work has also been undertaken on networks of global strings, the configuration predicted to arise cosmologically as a result of a phase transition. The initial conditions for a string network can be obtained numerically by assigning a random phase $-\pi \leq \theta < \pi$ and magnitude $-0.01 \leq \phi \leq 0.01$ to each gridpoint on the coarsest level:

$$\phi_1 = \phi \cos\theta, \qquad \phi_2 = \phi \sin\theta\,, \tag{3.25}$$

simulating the field φ falling into the potential minimum of $V(\varphi)$ at different values of θ, as in Figure 2.1. As with the sinusoidal initial conditions, this initial configuration can then be evolved using the dissipative evolution equations (3.17) until a network of distinct strings has formed. We identify the formation of strings by visualising ϕ in three dimensions at various stages of damping, using `Paraview` to determine when regions between the strings have minimal energy and the string identity has stabilised, i.e. when high frequency internal degrees of freedom have been damped.[11] We subsequently evolve using the wave equations (3.3) and (3.4). This crude estimate has proved sufficient for the preliminary tests presented.

3.4 Diagnostic Tools

`GRChombo` allows for users to construct and implement diagnostic tools, for example to extract quantitative information from simulations. In this section, we present two tools built to extract information from simulations of single strings; a diagnostic cylinder from which we are able to extract radiation at a certain radius, as well as a tool used to calculate the position of the string core ($\phi = 0$) using the string winding. Information extracted using these tools forms the basis of the majority of the analysis performed in this thesis.

3.4.1 Radiation Cylinder

In order to extract the radiation emitted from oscillating strings, it is necessary to construct an analysis cylinder centred on the string core. This allows certain fields or radiation diagnostic quantities to be extracted and analysed, for example, by Fourier decomposition to determine the harmonic modes present. This is a similar technique to that used by the LIGO and Virgo

[11] Note that in a cosmological scenario, the mechanism for dissipation would come from the expansion of the Universe.

Collaborations in their analysis of gravitational waveforms from binary black holes, although here spherical extraction is used instead due to the different overall symmetry.

For our $256 \times 256 \times 32$ cosmic string simulations, we choose to implement an extraction cylinder with radius $R = 64$, a distance far enough from the string core to minimise the effect of the self-field (discussed further in Section 4.1), but far enough from the boundaries to allow extended analysis before any reflected radiation can affect the central region. We choose to use the diagnostics Π_ϕ and $\mathscr{D}\vartheta \cdot \hat{\mathbf{r}}$ as defined by (4.11) and (4.12) to analyse the massive and massless radiation respectively. An example of this setup is shown in Figure 3.11.

Throughout the course of this work, we use two different analysis cylinders, due to ongoing development of `GRChombo`. The first was implemented entirely by me, with field values interpolated bilinearly from the Cartesian grid onto the cylinder surface. Later, a spherical extraction tool was added to `GRChombo` with fourth order Lagrange polynomial interpolation, which was adapted for cylindrical extraction by me. Although the improvement in accuracy did not have a significant effect on our results, both cylinders are presented here for completeness and to highlight the code development performed. Further to this, a similar technique to that used for the original bilinear cylinder was also implemented for the string core finder in Section 3.4.2.

Bilinear Cylinder

The first extraction cylinder implemented uses second order accurate bilinear interpolation to interpolate field values from the simulation grid to the cylinder. As the cylinder is defined on a Cartesian grid, it is necessary to interpolate values from the 'nearest-neighbour' grid points to get an accurate value for the field on the surface itself. This is demonstrated by Figure 3.12, which shows a diagram of a section of diagnostic cylinder passing through a grid cell. Note that we only ever extract on the coarsest level where the radiation has propagated away from the string, so it is not necessary to consider the effects of grid refinement.

To set up the cylinder, we first choose the number of points around its circumference that we wish to sample. In our case, we choose 256, so the points are spaced by $2\pi/256$ radians. We also choose $\Delta z = 1$ for the spacing in the z-direction, as this is the refinement of the coarse mesh. The (x, y, z) coordinates of the points to sample are calculated using simple conversion from polar to Cartesian coordinates for each point.

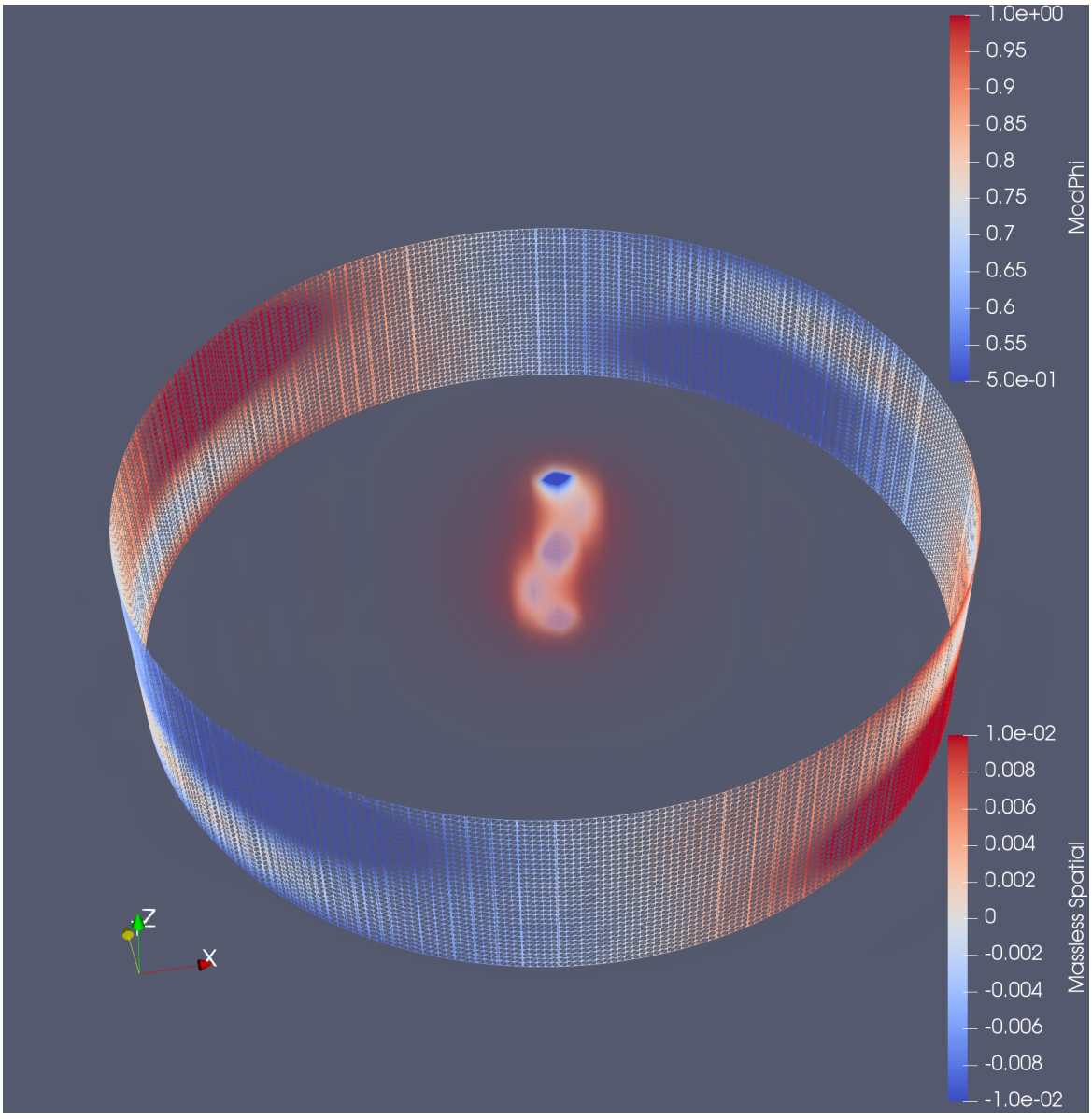

Fig. 3.11 Extraction of massless radiation diagnostic $\mathscr{D}\vartheta \cdot \hat{\mathbf{r}}$ on a cylinder at $R = 64$. The string in the centre is depicted by ϕ. We observe a dominant quadrupole signal on the cylinder surface.

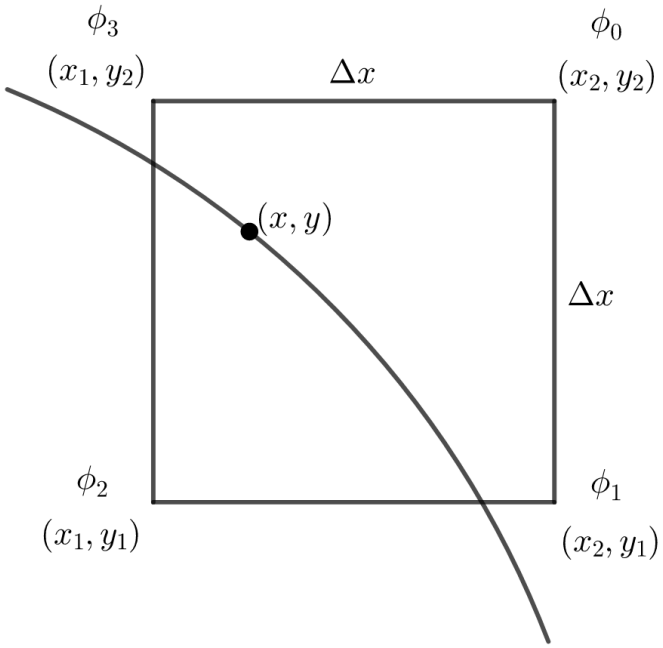

Fig. 3.12 Two-dimensional diagram of a grid cell to demonstrate two diagnostic tools: *1)* interpolation of radiation diagnostics onto a cylinder and *2)* calculation of the position of the string core. For *1)*, the arc represents a section of the cylinder on which radiation is analysed, where (x,y) is the point onto which we interpolate the field values ϕ_i and (x_i,y_j) are the coordinates of the corners of the cell. The value of the field ϕ at (x,y) is calculated using equation (3.26). For *2)*, the labels ϕ_i give the values of ϕ at the corners of a cell inside which has been detected a point of integer winding. We can substitute these values into (3.29) to calculate the position of the string core.

The extraction cylinder is subsequently implemented after each timestep of the simulation. Each grid cell on the coarsest level is iterated over to determine whether it contains an extraction point. If so, we perform bilinear interpolation of our chosen fields or diagnostic quantities onto this point to determine accurate values on the cylinder. The field value $\phi(x,y)$ is given by

$$\begin{aligned}\phi(x,y) \approx \frac{1}{(x_2-x_1)(y_2-y_1)}\,[&\phi(Q_{11})(x_2-x)(y_2-y)\\ &+\phi(Q_{21})(x-x_1)(y_2-y)+\phi(Q_{12})(x_2-x)(y-y_1)\\ &+\phi(Q_{22})(x-x_1)(y-y_1)]\end{aligned} \tag{3.26}$$

where $Q_{11}=(x_1,y_1)$, $Q_{12}=(x_1,y_2)$, $Q_{21}=(x_2,y_1)$, $Q_{22}=(x_2,y_2)$ and the coordinates $x_{1,2}$ and $y_{1,2}$ are defined as in Figure 3.12. From this, we output a 256×32 array of points to a text file for each of our chosen diagnostics, usually Π_ϕ and $\mathscr{D}\vartheta\cdot\hat{\mathbf{r}}$. A two-dimensional fast

Fourier transform (FFT) can be performed on this data to determine the modes present on the cylinder.

This bilinear extraction cylinder was very useful for radiation extraction in early production runs, and is used for the majority of the analysis presented in Chapter 4. However, it is clear that there are areas for which the performance could be improved; for example, it is inefficient to iterate over all grid cells to determine the extraction points. Elements of the operation were also unsuitable for parallelism. With this in mind, we later implement a slightly more accurate and higher level extraction tool, described below.

Fourth-Order Cylinder

The second extraction cylinder used in this work implements fourth order Lagrange polynomial interpolation to calculate values on the cylinder from the Cartesian gridpoints. This construction also allows for extraction on higher refinement levels than the base level (although this is not required in our work), as well as integration of variables over the surface. We currently implement integration by running Python scripts on the output data. However, we intend to implement this built in feature in the near future.

A `SurfaceExtraction` class is implemented to extract grid variables on one more two-dimensional surfaces, parameterised by u and v. The `SurfaceExtraction` class is templated over the `SurfaceGeometry` class, which contains the information about the geometry of the particular surface. In order to implement this setup, child classes `XExtraction` and `XGeometry` that inherit from the coinciding `Surface` classes must be defined by the user, where `X` is any desired extraction geometry that can be appropriately parametrised.[12]

For our simulations, as above we require a cylindrical geometry for extraction. To achieve this, `CylindricalExtraction` and `CylindricalGeometry` classes were implemented by me and have been made available in the public code. The `CylindricalExtraction` class defines the necessary constructors and `CylindricalGeometry` defines the parameters $u = \theta$ and $v = z$, along with the spacing of the points $dz = L/z_{\text{extract}}$ and $d\theta = 2\pi/\theta_{\text{extract}}$, where z_{extract} and θ_{extract} are integers defined by the user. Again, for our analysis we choose 256 points around the circumference and 32 points ($z_{\text{extract}} = 33$) in the z-direction. The area element is defined to be $rdrd\theta$, although again this is only needed for integration over the surface and is not currently used. From these, the Cartesian grid coordinates of the extraction points are calculated again using simple conversion from polar coordinates.

[12] Many thanks to the `GRChombo` collaboration for implementing this extraction framework, particularly to Miren Radia.

Similarly to the bilinear cylinder, the extraction is called after each timestep. In this case, the extraction cylinder is defined using a group of extraction parameters and the fields we would like to extract and is executed using the AMR interpolator. The extracted field values for each timestep are output into text files as previously, which can then be analysed.

3.4.2 String Core Position

Here we outline the implementation of the diagnostic to track the exact position of the string core. This is used for example, to determine the rate of energy loss, as well as to determine whether we have reached the desired amplitude A_0 from which to begin evolving the wave equation after obtaining initial conditions using dissipative evolution, as discussed in Section 3.3.1. We use a similar technique to the bilinear interpolation onto the diagnostic cylinder, but in reverse, scanning the whole domain ($R < 64$) to detect grid cells in which there is a non-zero winding. As we know that $\phi = 0$ at the string core, we can use the values of the complex scalar fields at the corners to fit a quadratic

$$ax^2 + bx + c = 0 \tag{3.27}$$

to the grid cell shown in Figure 3.12 and calculate the position of the zero. We simultaneously solve the system of equations

$$\begin{aligned}
a(x_0 + iy_0)^2 + b(x_0 + iy_0) + c &= \phi_2 \\
a(x_1 + iy_0)^2 + b(x_1 + iy_0) + c &= \phi_3 \\
a(x_0 + iy_1)^2 + b(x_0 + iy_1) + c &= \phi_1 \\
a(x_1 + iy_1)^2 + b(x_1 + iy_1) + c &= \phi_0
\end{aligned} \tag{3.28}$$

to obtain the constants a, b and c, where $\phi_{0,1,2,3}$ are defined by Figure 3.12 as the grid points at the corners of the relevant grid cell. We obtain the coefficients

$$\begin{aligned}
a &= \frac{-i}{8}(\phi_0 + \phi_2 - \phi_1 - \phi_3) \\
b &= \frac{i-1}{8}(\phi_0 - \phi_2 + i(\phi_3 - \phi_1)) \\
c &= \frac{1}{4}(\phi_0 + \phi_2 + \phi_1 + \phi_3)\,.
\end{aligned} \tag{3.29}$$

which can be substituted into equation (3.27), which can in turn be solved using the quadratic formula. The smallest root provides us with a fractional correction to the x-coordinate,

$x_{correct}$, such that

$$x_{core} \approx x_{centre} + x_{correct}\frac{\Delta x}{2},$$

where x_{core} is the true position of the string core and x_{centre} is the x-coordinate of the centre of the grid cell. We use this to calculate the x-coordinate of the string core within the cell to second-order accuracy. Note here that all refinement levels are scanned, so Δx is a parameter which changes depending on which level is being analysed.

3.5 Profiling and Code Development

In this section, we discuss methods that have been implemented throughout this work to optimise the performance of GRChombo. GRChombo is an ongoing project that is under continuous development and improvement by the GRChombo collaboration. Here, we focus on the specific measures that have been implemented or contributed to by me in collaboration with other GRChombo developers, or with the Chombo developers at Lawrence Berkeley National Laboratory.

The profiling in this section is performed predominantly using the timer function built into Chombo. The macro `CH_TIME("label")` can be inserted into any function in the code to produce an output file `time.table.x` for each MPI processor. An example of the output is given by Figure 3.13 for the evolution of a $\lambda = 3$ string with five levels of mesh refinement. This shows the total number of timers used, the time taken by each function, as well as the percentage of time taken by each 'child' function. These output files can be used to determine which operations take up the most simulation time, enabling us to target specific functions for optimisation.

To determine the total time taken by a function, it is usually necessary to sum the separate contributions by hand, as the majority of functions will be independently called by each refinement level. Table 3.1 summarises the timing information from the simulation profiled in Figure 3.13. We observe that the total simulation time is split primarily between four areas; advancing the right hand side, post timestep operations (such as computing averages to interpolate to coarser levels, filling ghost cells and computation of diagnostic quantities on the grid), regridding and writing plot files. The balance between these changes depending on the parameters used; for example if we stop plot files from being output entirely, this eradicates that contribution. This also means the time spent in each function can change between different λ. For example `GRAMRLevel::advance` takes proportionally more time

```
----------
Timer report 0 (1367 timers)
--------------
---------------------------------------------------------
[0]main 23224.91148 1
    100.0% 23220.30080        1 AMR::run [1] f=0
     0.0%    3.28766        1 AMR::setupForRestart [344] f=0
     0.0%    1.10045        1 AMR::conclude [442] f=0
     0.0%    0.00079        1 AMR::define [1183] f=0
     0.0%    0.00000        1 AMR::blockFactor [1362] f=0
     0.0%    0.00000        1 AMR::maxGridSize [1364] f=0
     0.0%    0.00000        1 AMR::fillRatio [1365] f=0
     0.0%    0.00000        1 AMR::gridBufferSize [1366] f=0
    100.0%                   Total
---------------------------------------------------------
[1]AMR::run 23220.30080 1
    89.4% 20765.29814     1938 AMR::timeStep [2] f=0
    10.5% 2437.59699     1938 AMR::writePlotFile [16] f=0
     0.1%   17.39339       19 AMR::writeCheckpointFile [212] f=0
     0.0%    0.00334     1938 AMR::assignDt [1083] f=0
    100.0%                   Total
---------------------------------------------------------
[2]AMR::timeStep 20765.29814 1938
    87.5% 18178.51230     1938 AMR::timeStep::finerLevels [3] f=0
    11.3% 2352.24509     1938 AMR::timeStep::postTimeStep [17] f=0
     1.1%  234.49362     1938 AMR::timeStep::advance [78] f=0
     0.0%    0.00195     1938 AMR::timeStep::newDt [1129] f=0
     0.0%    0.00125     1938 AMR::timeStep::regrid [1162] f=0
    100.0%                   Total
---------------------------------------------------------
[3]AMR::timeStep::finerLevels 18178.51230 1938
    100.0% 18178.50643     3876 AMR::timeStep [4] f=0
    100.0%                   Total
---------------------------------------------------------
[4]AMR::timeStep 18178.50643 3876
    89.9% 16333.92874     3872 AMR::timeStep::finerLevels [5] f=0
     5.7% 1034.38099     3876 AMR::timeStep::regrid [32] f=0
     3.3%  591.22375     3876 AMR::timeStep::advance [47] f=0
     1.2%  218.91104     3876 AMR::timeStep::postTimeStep [81] f=0
     0.0%    0.02319     1938 AMR::timeStep::subcycle [911] f=0
     0.0%    0.00308     3876 AMR::timeStep::newDt [1086] f=0
    100.0%                   Total
---------------------------------------------------------
[5]AMR::timeStep::finerLevels 16333.92874 3872
    100.0% 16333.91547     7744 AMR::timeStep [6] f=0
    100.0%                   Total
---------------------------------------------------------
[6]AMR::timeStep 16333.91547 7744
    84.4% 13792.21445     7740 AMR::timeStep::finerLevels [7] f=0
```

Fig. 3.13 Example `CH_TIME` output for a $\lambda = 3$ string with five levels of mesh refinement.

Table 3.1 Skeleton profile for $\lambda = 3$ string with five levels of mesh refinement from collating CH_TIME output.

Function	Percentage Time %
GRAMRLevel::advance	43.4
AMR::timeStep::postTimeStep	23.2
AMR::regrid	20.9
AMR::writePlotFile	10.5
Total:	98.0

for higher λ as more refinement levels are implemented and hence more grid points are evolved.

3.5.1 Separating Evolution from Diagnostic Variables

One of the most significant changes made to GRChombo during the course of this work has been the separation of evolution variables into two types; those that are evolved during the simulations and those that are used purely as diagnostics. As outlined in Section 3.2, GRChombo evolves its variables using a fourth-order Runge-Kutta (RK4) evolution scheme. This means that in order to evolve the system, three copies of each evolution variable must be stored in memory during each timestep.

Users of GRChombo will often need to calculate diagnostic variables on the grid for analysis or consistency checks. These variables do not need to be evolved, but must be stored on the grid in the same way as the evolution variables. In earlier versions of the code, this has meant that four copies of these diagnostic variables were generated as if they were going to be evolved by RK4, resulting in three extra copies being stored unnecessarily. This has meant that simulations calculating diagnostic variables use unnecessary extra random-access memory (RAM) storage and time generating these extra copies and interpolating them. This is particularly relevant to cosmic string simulations and other simulations of complex scalar fields in flat space. Here, the real and imaginary parts of the field and their conjugate momenta are the only four variables being evolved, so there is likely to be a high ratio of diagnostic to evolution variables. This inefficiency has motivated development of GRChombo to provide the ability to store evolution and diagnostic variables separately, allowing evolution variables to undergo RK4 with diagnostic variables being calculated and stored only as one copy.

Further to this, whilst undertaking production runs on several supercomputers including COSMOS and CSD3,[13] it was often observed that running with the maximum number of processors per node caused the simulation to crash due to lack of available memory. Having ruled out memory leaks using the debugging system Valgrind,[14] it was postulated that a contributing factor to this was likely to be the large amount of extraneous grid data that was being stored. Hence this issue is also addressed by splitting the variables.

Through discussion with `Chombo` and `GRChombo` developers, it was determined that the most straightforward and effective method to split the variables was to to create separate C++ namespaces for evolution and diagnostic variables. The diagnostic namespace can be used to define a separate set of AMR level data purely for diagnostic storage, that can be passed to functions separately from the evolution data. This was implemented into the public code on 2nd July 2020, where further details can be found regarding the specific changes to the code.[15] This change meant that it was necessary to break backward compatibility, but due to the significant performance gains it was exceptionally decided that this was a worthwhile trade-off.[16] Initial tests of the performance improvement have been undertaken for a complex scalar field evolved on a fixed Kerr metric background with five diagnostic variables, showing a significant $\sim 50\%$ speedup.[17]

3.5.2 Optimisation of `FourthOrderFillPatch::fillInterp`

As discussed in the introduction to this section, useful information about the time taken by different `GRChombo` and `Chombo` functions can be obtained using the inbuilt `CH_TIME` macro. The majority of time for global cosmic string simulations is normally taken by `GRAMRLevel::advance`, for example as shown in Table 3.1. Significant speedup of this function will therefore result in an improvement in performance.

Profiling of a $\lambda = 1$ string undertaken in September 2019 on COSMOS showed that approximately 83% of the total runtime of `GRAMRLevel::advance` (approximately 39% of the total runtime) was taken up by a `Chombo` function named `FourthOrderFillPatch::fillInterp` called within `GRAMRLevel::evalRHS`. This function interpolates ghost cells to the current

[13] See Acknowledgements for further information about these machines.

[14] https://valgrind.org/

[15] The link to the public commit is
https://github.com/GRChombo/GRChombo/commit/ffa4bbbda71f31453fcf532cb529e35ae15c4f7f.

[16] Many thanks to the `GRChombo` collaboration for joint input into implenting the diagnostic variables, particularly to Miren Radia and Katy Clough.

[17] Many thanks again to Katy Clough for providing these figures.

refinement level from the next coarsest in space and time (see Figure 3.4 for the order in which subcycling is performed). More specifically, approximately 80-90% of the total runtime of `FourthOrderFillPatch::fillInterp` itself was taken up by the function `FourthOrderFillPatch::fillInterpSpaceFromCoarsened`. Having identified that this function alone contributes such a significant proportion to the total simulation time, efforts have been concentrated on its optimisation. In order to simplify the workflow and enable contributions from other developers, we have found it useful to use the example of a binary black hole evolution provided in the public `GRChombo` repository to carry out and test the optimisation. We note that `FourthOrderFillPatch::fillInterp` is applied whenever AMR is used, so any improvement in its performance is also applicable to any other physical application that uses this capability.

In order to optimise `FourthOrderFillPatch::fillInterpSpaceFromCoarsened`, [18] it was determined that the data structure and function calls used to fill the ghost cell values on the finer level and to calculate the correct coarse stencil coefficients was too complex to be optimised by the compiler, causing the function to run slowly. To address this, a different version of the algorithm was implemented, covering the coarse/fine ghost cell regions with multiple `FArrayBox` (rectangular arrays of data) rather than looping through the `IntVectSet` of all ghost coarse cells (an arbitrary collection of points). The loop over `FArrayBox` was also optimised using a static data structure, and `OpenMP` pragmas were added to enable execution using parallel threads.

Profiling of the public binary black hole example to compare the optimised function `FourthOrderFillPatch::fillInterpSpaceFromCoarsened` with the original has been performed by me and `Chombo` developers.[19] A simulation was run on 8 Intel Haswell nodes with 4 OpenMP threads for 40 timesteps using the parameter file `params_expensive.txt` from the public example code, but using smaller 16^3 MPI boxes to force more coarse/fine interpolations. A speedup of $\sim 2\times$ was obtained for the function itself, with $\sim 1.4\times$ obtained overall. Running an equivalent simulation on COSMOS (Intel Sandy Bridge nodes) using the same parameters but restricting to 1 OpenMP thread, a $1.15\times$ speedup was obtained. This optimisation is still being tested, but is on track to being integrated into the public code in the near future.

[18] Many thanks to Hans Johansen at Lawrence Berkeley National Laboratory for performing this optimisation.

[19] Many thanks to Peter McCorquodale at Lawrence Berkeley National Laboratory for performing the Haswell node profiling.

Chapter 4

Massless (Axion) Radiation

In this chapter, we present a detailed analysis of the massless radiation from adaptive mesh refinement simulations of global cosmic strings, based on the co-authored publication [174]. Section 4.1 outlines a derivation of novel radiation diagnostics that can be used to characterise the massless and massive modes, obtained by considering time derivatives of fundamental fields in the complex plane. This is followed by a derviation of the solution to the massless wave equation in terms of the separable massless eigenmodes, as well as a model for radiation backreaction on the string. In Section 4.2, we present simulations of global strings with string widths spanning over an order of magnitude, determined by the parameter λ in the range $1 \leq \lambda \leq 100$. We survey several perturbation amplitudes from $1 \leq A_0 \leq 8$ (invariant amplitudes $0.2 \lesssim \varepsilon_0 \lesssim 1$) with initial conditions obtained using dissipative evolution, as outlined in Section 3.3.1. We analyse the propagating massless radiation modes generated by the strings using the derived diagnostics and analysis tools described in Section 3.4, as well as the detailed string trajectory as its oscillation energy decays, directly comparing with analytic predictions. Finally, in Section 4.3, we compare our results with the analytic backreaction model outlined in Section 4.1 and determine some key parameters.

All simulations in this chapter are carried out using `GRChombo`, with a coarse simulation box size of $256 \times 256 \times 32$ ($N_1 \times N_2 \times N_3$) with periodic boundary conditions in the z-direction and Sommerfeld (outgoing radiation) boundary conditions in the x- and y- directions. The spatial periodicity of the strings is fixed at $L \equiv N_3 = 32$. A base grid of resolution $\Delta x = 1$ is used with a base timestep $\Delta t = \Delta x/4$. We choose a regridding threshold $|\phi_{threshold}| = 0.25$ for simulations with $\lambda \leq 10$ and $|\phi_{threshold}| = 0.1$ for those with $\lambda > 10$. In total, over

one hundred high resolution simulations are performed, using up to six levels of mesh refinement.

4.1 Analytic Radiation Expectations

4.1.1 Massive and Massless Radiation Modes

An oscillating global string will emit both massless (Goldstone) modes and massive (Higgs) radiation. Analytic expectations are very different for these two channels, so it is important to develop robust diagnostic tools to be able to numerically extract and analyse them separately. This is a significant challenge because radiative modes must be separated from string self-fields, which are long-range and time-varying.

We first demonstrate the presence of massive and massless radiative modes around the broken symmetry vacuum state (2.5) using the general form of the Argand representation,

$$\varphi(x^\mu) = \phi(x^\mu)\, e^{i\,\vartheta(x^\mu)}\,, \tag{4.1}$$

where both the magnitude $\phi(x^\mu)=|\varphi(x^\mu)|$ and the phase $\vartheta(x^\mu)$ are real scalar fields associated with the orthogonal excitations illustrated in Figure 2.1 (and we have set $n=1$). The field equations (2.10) split into real and imaginary parts, respectively, as

$$\frac{\partial^2\phi}{\partial t^2} - \nabla^2\phi = \phi\left[\left(\frac{\partial\vartheta}{\partial t}\right)^2 - (\nabla\vartheta)^2 + \tfrac{\lambda}{2}(1-\phi^2)\right], \tag{4.2}$$

$$\frac{\partial^2\vartheta}{\partial t^2} - \nabla^2\vartheta = \frac{2}{\phi}\left(\frac{\partial\phi}{\partial t}\frac{\partial\vartheta}{\partial t} - \nabla\phi\nabla\vartheta\right). \tag{4.3}$$

Assuming that ϑ is nearly constant far from any strings, (4.2) becomes

$$\frac{\partial^2\phi}{\partial t^2} - \nabla^2\phi - \tfrac{\lambda}{2}\phi\left(1-\phi^2\right) = 0\,. \tag{4.4}$$

Expanding around the vacuum state $|\varphi| = \eta$ (where we have taken $\eta = 1$) by setting $\phi = 1+\chi$, we linearise to obtain the Klein-Gordon equation

$$\frac{\partial^2\chi}{\partial t^2} - \nabla^2\chi + m_H^2\chi = 0\,, \tag{4.5}$$

where $m_H = \sqrt{\lambda}\,\eta$. Hence, in this limit, we deduce that χ acts like a free massive scalar field. On the other hand, if ϕ is nearly constant, the second equation (4.3) reduces to the wave equation

$$\frac{\partial^2 \vartheta}{\partial t^2} - \nabla^2 \vartheta = 0\,, \tag{4.6}$$

where ϑ behaves as a massless scalar field. Asymptotically far from any strings, it should therefore be a good approximation to decompose radiation into these distinct massive and massless modes.

In order to determine individual contributions to the radiative spectrum from each mode, it will be useful to measure and separate the components of the energy-momentum tensor, given by

$$T_{\mu\nu} = 2\partial_{(\mu}\bar{\varphi}\partial_{\nu)}\varphi - g_{\mu\nu}\left(\partial_\sigma\bar{\varphi}\partial^\sigma\varphi - \tfrac{\lambda}{4}(\bar{\varphi}\varphi - 1)^2\right). \tag{4.7}$$

We can decompose the energy density $\rho = T^{00}$ into massive and massless modes using (4.1) as follows:

$$\begin{aligned} T^{00} &= \dot{\bar{\varphi}}\dot{\varphi} + \nabla_i\bar{\varphi}\nabla_i\varphi + \tfrac{\lambda}{4}(\bar{\varphi}\varphi - 1)^2 \\ &= \dot{\phi}^2 + (\nabla\phi)^2 + \phi^2\left(\dot{\vartheta}^2 + (\nabla\vartheta)^2\right) + \tfrac{\lambda}{4}(\phi^2 - 1)^2 \\ &= \dot{\phi}_1^2 + \dot{\phi}_2^2 + (\nabla\phi_1)^2 + (\nabla\phi_2)^2 + \tfrac{\lambda}{4}(\phi_1^2 + \phi_2^2 - 1)^2\,, \end{aligned} \tag{4.8}$$

where in the last line we have reintroduced the complex components (2.9). To determine the momentum components of the fields in the θ- and r- directions, we note the relations

$$\dot{\phi}^2 = \frac{1}{\phi^2}\left(\phi_1\dot{\phi}_1 + \phi_2\dot{\phi}_2\right)^2 \equiv (\dot{\mathbf{\Phi}}\cdot\hat{\mathbf{\Phi}})^2\,, \tag{4.9}$$

$$\phi^2\dot{\vartheta}^2 = \frac{1}{\phi^2}\left(\phi_2\dot{\phi}_1 - \phi_1\dot{\phi}_2\right)^2 \equiv (\dot{\mathbf{\Phi}}\cdot\hat{\mathbf{\Phi}}_\perp)^2\,, \tag{4.10}$$

where $\mathbf{\Phi} = (\phi_1, \phi_2)$ represents the radial direction in field space and $\mathbf{\Phi}_\perp = (\phi_2, -\phi_1)$ is orthogonal, as shown in Figure 2.1. Extrapolating from (4.9) and (4.10), we can therefore deduce a direct numerical diagnostic for the distinct massive and massless components of $T_{\mu\nu}$ by defining the momenta and spatial gradients

$$\Pi_\phi \equiv \frac{\phi_1\dot{\phi}_1 + \phi_2\dot{\phi}_2}{\phi}, \quad \mathscr{D}_i\phi \equiv \frac{\phi_1\nabla_i\phi_1 + \phi_2\nabla_i\phi_2}{\phi}, \tag{4.11}$$

$$\Pi_\vartheta \equiv \frac{\phi_1\dot{\phi}_2 - \phi_2\dot{\phi}_1}{\phi}, \quad \mathscr{D}_i\vartheta \equiv \frac{\phi_1\nabla_i\phi_2 - \phi_2\nabla_i\phi_1}{\phi}. \tag{4.12}$$

We can use these to express the energy density (4.8) in terms of massive and massless components in the following form:

$$T^{00} = \Pi_\phi^2 + (\mathscr{D}\phi)^2 + \Pi_\vartheta^2 + (\mathscr{D}\vartheta)^2 + \tfrac{\lambda}{4}(\phi^2-1)^2\,. \tag{4.13}$$

Furthermore, the relations (4.11) and (4.12) allow us explicitly to split the momentum component T^{0i} of the stress tensor into massive and massless components, given by

$$S_i \equiv T^{0i} = \Pi_\phi \mathscr{D}_i\phi + \Pi_\vartheta \mathscr{D}_i\vartheta\,. \tag{4.14}$$

For our massive and massless scalar radiation fields, the two quantities in (4.14) are equivalents of the electromagnetic Poynting vector describing the radiation energy fluxes. Choosing an outgoing radial direction, we can integrate the two components of $\mathbf{S}\cdot\hat{\mathbf{r}}$ on a distant surface to determine the energy flow out of the enclosed volume for each type of radiation.

4.1.2 Separation from Self-Field

Having split the radiation into massive and massless contributions, we now consider the separation of propagating radiation from the string self-field. The study of string radiation is plagued by long-range self-fields that prove difficult to numerically separate. Given our fixed cylinder at a finite distance R from the string, there is a prosaic explanation for this contamination due to the oscillating self-fields being offset from their central position. At small amplitude ($\varepsilon \ll 1$), the sinusoidal string solution (3.16) with the string field ansatz (2.11) yields an approximate massless self-field $\vartheta_{\rm sf}(t,\mathbf{x})$ of the following form:

$$\begin{aligned}\vartheta_{\rm sf}(t,\mathbf{x}) &\approx \tan^{-1}\left(y/X(t,\mathbf{x})\right)\,,\\ X(t,\mathbf{x}) &= x - A\cos\Omega_z t\,\sin\Omega_z z\,,\end{aligned} \tag{4.15}$$

where $\Omega_z = 2\pi/L$, which should be valid in the region $A \ll r \lesssim \mathscr{O}(\text{few}\times L)$. Taking the time derivative of the oscillating field $\vartheta_{\rm sf}$, we find on a cylinder at a distance $r = R$ that to leading order

$$\frac{\partial\vartheta_{\rm sf}}{\partial t}(t,r,\theta,z) \quad\approx\quad \frac{A\Omega_z}{R}\sin\theta\,\cos\Omega_z t\,\sin\Omega_z z\,, \tag{4.16}$$

so the non-propagating self-field at a fixed radius looks like a dipole field. (This corresponds to the mode $\{1\,1\,1\}$ derived in the next section, also see Figure 4.2). The radial derivative of $\partial\vartheta_{\rm sf}/\partial r$ yields the same dipole space and time dependence as (4.16), except that the

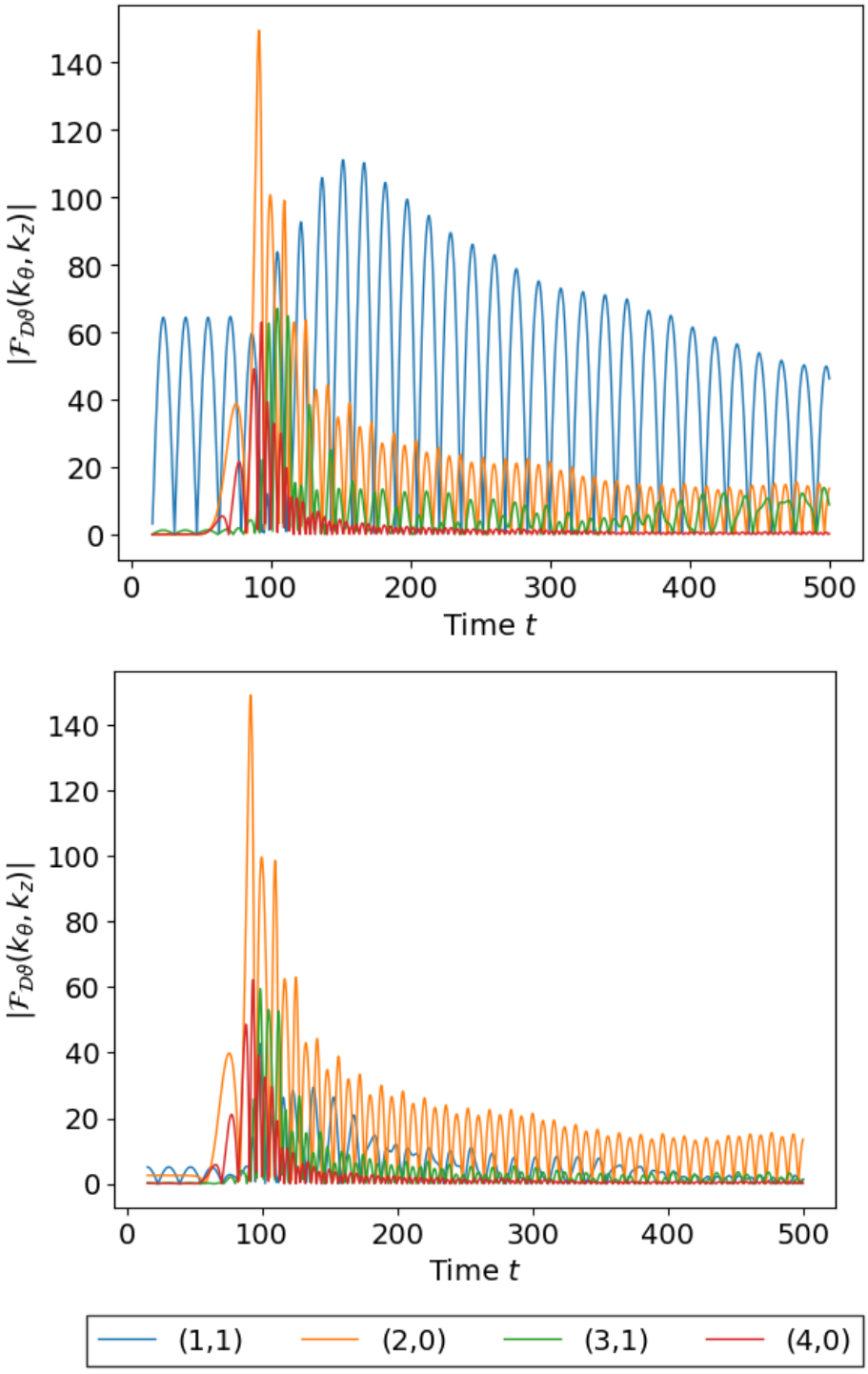

Fig. 4.1 Plot of the absolute value of the $\{mn\} = \{11\}, \{20\}, \{31\}$, and $\{40\}$ Fourier modes of the massless radiation Π_ϑ (top) and $\mathscr{D}\vartheta \cdot \hat{\mathbf{r}}$ (bottom) from a $\lambda = 1$ string with initial amplitude $A_0 = 12$, measured on a cylinder at $R = 64$.

pre-factor becomes A_0/R^2 so the amplitude falls off more steeply with distance than the time derivative $\dot{\vartheta}_{\rm sf}$. This means that the spatial radiation diagnostic $\mathscr{D}\vartheta$ in (4.12) is a more effective diagnostic for removing self-field contamination than the massless field momentum Π_ϑ. An example of this is shown in Figure 4.1, which shows a plot of the absolute value of the $\{mn\} = \{11\},\{20\},\{31\}$, and $\{40\}$ Fourier modes of the two massless radiation diagnostics from a $\lambda = 1$ string with initial amplitude $A_0 = 12$. We clearly observe that Π_ϑ is significantly more contaminated by the $\{11\}$ self-field signal, and that $\mathscr{D}\vartheta$ almost entirely removes this signal without affecting the other modes. This diagnostic is also therefore a very useful quantity for visualisation, producing much cleaner massless radiation signal. We finally note that massive radiation is more complex, with both Π_ϕ and $\mathscr{D}\phi\cdot\hat{\mathbf{r}}$ required to provide a full picture of the propagating modes. This will be discussed further in Chapter 5.

4.1.3 Separable Radiation Eigenmodes

To guide our analysis of the massless radiation emitted by an oscillating string, we shall assume as in Section 4.1.1 that we are far away from the source with the field very close to the vacuum state $\phi = 1$. The massless wave equation (4.6) in cylindrical coordinates $\vartheta(t,r,\theta,z)$ becomes

$$\frac{\partial^2\vartheta}{\partial t^2} - \frac{\partial^2\vartheta}{\partial r^2} - \frac{1}{r}\frac{\partial\vartheta}{\partial r} - \frac{1}{r^2}\frac{\partial^2\vartheta}{\partial\theta^2} - \frac{\partial^2\vartheta}{\partial z^2} = 0\,. \tag{4.17}$$

Taking a periodic oscillating string along the z-axis (with $0 \le z < L$), the massless radiative modes emitted will become outgoing solutions of (4.17) at large distances. We can solve the cylindrical wave equation via separation of variables with the ansatz

$$\vartheta(t,r,\varphi,z) = T(t)\,R(r)\,\Theta(\theta)\,Z(z)\,. \tag{4.18}$$

Substituting into equation (4.17), we obtain

$$\frac{T''(t)}{T(t)} - \frac{R''(r)+R'(r)/r}{R(r)} - \frac{1}{r^2}\frac{\Theta''(\theta)}{\Theta(\theta)} - \frac{Z''(z)}{Z(z)} = 0\,, \tag{4.19}$$

where each component can be solved in turn by introducing appropriate separation constants. We first obtain the time dependence $T(t)$ by setting $T''(t)/T(t) = -\omega_p^2$, where we take the convention of a negative sign for the outgoing mode and ω_p is the angular frequency given

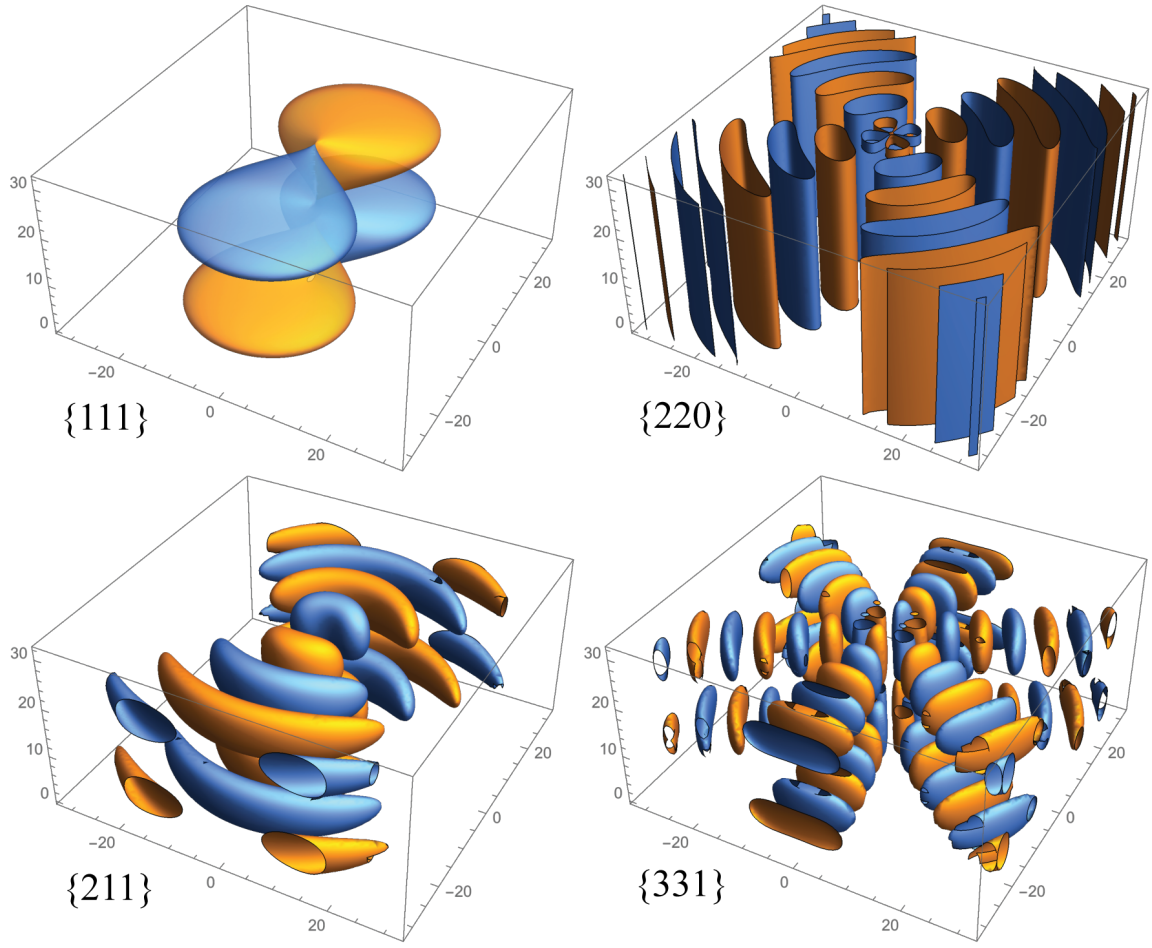

Fig. 4.2 Key radiation eigenmodes for a periodic oscillating string as labelled by their eigenvalues $\{t, \theta, z\} \to \{pmn\}$ with the key radial eigenvalue κ_{pn} given by the dispersion relation (4.27). The oscillating string self-field creates a non-propagating (evanescent) wave with $\{pmn\} = \{1\,1\,1\}$ (top left), while the dominant massless radiation mode is the quadrupole $\{2\,2\,0\}$ (shown top right). The next most important massless radiation mode is the third harmonic $\{3\,3\,1\}$ (bottom right) but there appears to be some contribution from a second harmonic dipole $\{2\,1\,1\}$ (bottom left). For massive scalar radiation, higher harmonic dipole modes $\{p\,1\,1\}$ can provide the leading contribution, but they compete with quadrupole $\{p\,2\,2\}$ and other higher modes.

by the period of the string oscillations or their pth harmonic

$$\omega_p = \frac{2\pi}{L}\frac{p}{\alpha} \equiv \Omega_z \frac{p}{\alpha}. \tag{4.20}$$

Here, p is a positive integer and the parameter $\alpha \geq 1$ is the fractional increase in the path length of the string. This relation is obtained by noting that the string oscillates with a period $T \equiv \alpha L \gtrsim L$ determined by its actual invariant length, where for small amplitude ($\varepsilon \to 0$) we have $\alpha \approx 1$. The time-dependence of the separable solution becomes

$$T_p(t) \propto e^{-i\Omega_z pt/\alpha}. \tag{4.21}$$

The fixed periodicity along the z-axis yields a further separation constant from $Z''(z)/Z(z) = -k_z^2 = -\Omega_z^2 n^2$, giving the z-dependence

$$Z_n(z) \propto e^{i\Omega_z nz}, \tag{4.22}$$

where n is an integer[1] and we have chosen a positive exponent.[2] Substituting these eigenmodes into equation (4.19), we obtain the radial dependence

$$\frac{R''(r)+R'(r)/r}{R(r)} + \frac{1}{r^2}\frac{\Theta''(\theta)}{\Theta(\theta)} = -\omega_p^2 + k_z^2 \tag{4.23}$$

and θ-dependence

$$\frac{\Theta''(\theta)}{\Theta(\theta)} = r^2\left(-\omega_p^2 + k_z^2 - \frac{R''(r)+R'(r)/r}{R(r)}\right), \tag{4.24}$$

where the right hand side is independent of θ and can be set to a constant. The azimuthal periodicity of θ (period 2π) gives $\Theta(\theta)''/\Theta(\theta) = -m^2$, with the θ-dependence becoming

$$\Theta_m(\theta) \propto e^{im\theta}, \tag{4.25}$$

where m is an integer. A final rearrangement gives

$$R''(r) + \frac{R'(r)}{r} + R(r)\left(\omega_p^2 - k_z^2 - \frac{m^2}{r^2}\right) = 0, \tag{4.26}$$

[1] Note that this n is not the winding number.

[2] This ensures we obtain oscillating solutions.

where from equation (4.23) and using the fact that $\Theta(\theta)''/\Theta(\theta)$ is constant, we identify the radial wavenumber $k_r^2 = \omega_p^2 - k_z^2$. We factor out the dependence on Ω_z from this dispersion relation, setting $k_r = \Omega_z \kappa_{pn}$ to obtain the important expression for the radial wavenumber for each harmonic

$$\kappa_{pn} = \sqrt{(p/\alpha)^2 - n^2}\,. \tag{4.27}$$

We note that the radial wavenumber depends on p and n only, and that the angular dependence m has decoupled. Substituting in this expression to (4.26), we obtain Bessel's equation

$$R''(r) + \frac{R'(r)}{r} + R(r)\left(\Omega_z^2 \kappa_{pn}^2 - \frac{m^2}{r^2}\right) = 0\,. \tag{4.28}$$

The radial equation (4.28) has solutions which are arbitrary linear combinations of Bessel functions of the first kind $J_m(k_r r)$ and second kind $Y_m(k_r r)$.[3] When we impose the Sommerfeld radiation condition

$$r^{1/2}\left(\frac{\partial}{\partial r} - ik_r\right)\vartheta \;\to 0 \;\text{ as }\; r \to \infty, \tag{4.29}$$

the solution is constrained to be a Hankel function of the first kind, with

$$R_{pmn}(r) \;\propto\; H_m^{(1)}(\Omega_z \kappa_{pn} r) = J_m(\Omega_z \kappa_{pn} r) + iY_m(\Omega_z \kappa_{pn} r)\,. \tag{4.30}$$

By comparing with the time-dependence (4.21), the outgoing mode from the asymptotic behaviour at large radial distances $\kappa_{n\ell} r \gg 1$ is given by

$$H_m^{(1)}(k_r r) \approx \sqrt{2/\pi k_r r}\,\exp\left[i\left(k_r r - \pi m/2 - \pi/4\right)\right]. \tag{4.31}$$

We note that there is an apparent divergence at $r = 0$ for $Y_m(k_r r)$, but that this can be modified and cut-off by the near-field dynamics and structure of the global string. Here, we are only seeking the matching asymptotic solution for the far-field with $k_r r \gg 1$. Finally, combining these results, we find the general outgoing radiation solution from a sum over the separable modes:

$$\vartheta(t,r,\theta,z) = \Re \sum_{pmn} A_{pnm}\; e^{im\theta} \;\times\; e^{-i\Omega_z[(p/\alpha)t - nz]}\; H_m^{(1)}\left(\Omega_z\, \kappa_{pn}\, r\right), \tag{4.32}$$

with amplitude A_{pmn} for the specific $\{t,\theta,z\}$ eigenmode labelled by the integers $\{pmn\}$ and with the key radial eigenvalue κ_{pn} given by (4.27).

[3] This can be straightforwardly shown using a substitution of variables $s = k_r r$ to rewrite equation (4.28) in the standard form.

We can make several observations about the radiation solution (4.32) using the associated dispersion relation (4.27). First, to aid with interpretation of the discussion, Figure 4.2 shows some of the most significant eigenmodes for string radiation $\{pnm\} = \{1\,1\,1\}$, $\{2\,0\,0\}$, $\{2\,1\,1\}$ and $\{3\,3\,1\}$. First, we know that the sinusoidal solution (3.16) has a long-range self-field which oscillates backwards and forwards with the string which can be associated with the eigenmode $\{pmn\}=\{1\,1\,1\}$. This is an apparent dipole, but it is not true radiation and it will not propagate in the outward direction because the radial wavenumber is imaginary, i.e. $\kappa_{11}^2 < 0$. This self-field contribution is therefore an evanescent wave with no net flux through our diagnostic radiation cylinder when averaged over a full oscillation period. The radiation mode predicted to be dominant is the quadrupole $\{2\,2\,0\}$, which propagates radially at the speed of light with $\omega_2 = k_r = \Omega_z \kappa_{20}$, where $\kappa_{20} = 2/\alpha \approx 2$ at small amplitude. In principle, the second harmonic $\{2\,1\,1\}$ can also propagate, but in practice we find in Section 4.2 that the third $\{3\,3\,1\}$ and fourth $\{4\,4\,0\}$ harmonics make the next most important contributions. The mode amplitudes are determined by the dynamics and symmetries of the near-field physics of the specific configuration of the oscillating string source. Finally, the dispersion relation (4.27) also reveals that not all modes propagate at the speed of light in the radial direction. If $n \neq 0$, then there is a wavevector component in the z-direction and the radial speed of propagation is $v_r = \partial\omega/\partial k_r = \kappa_{pn}/\omega_p < 1$. For example, for $\{2\,1\,1\}$ we have $v_r = 0.87$, while, for $\{3\,3\,1\}$ we have $v_r = 0.94$.

4.1.4 Dual Radiation Calculations and String Backreaction

In this subsection, we recall the model described in Section 3.3 for the string initial conditions, as well as the Goldstone boson radiation from global strings in Section 2.3.3. This will form the basis of our analysis for the radiation backreaction in our simulations.

As discussed in Section 3.3, for small amplitude $\varepsilon \ll 1$, our sinusoidal long string initial condition (3.16) in a box of length L approximates an analytic solution of the Nambu-Goto equations of motion with time period $T \approx L$. From (3.12), we recall

$$\mathbf{X} = \left(\frac{\varepsilon}{2\Omega} \big[\cos\Omega u + \cos\Omega v \big], 0, \frac{1}{2\Omega} \big[\mathsf{E}(\Omega u, \varepsilon) + \mathsf{E}(\Omega v, \varepsilon) \big] \right), \tag{4.33}$$

where $u = \sigma + t$ and $v = \sigma - t$ are coordinates along the string and $\varepsilon = 2\pi A/T = \Omega A$. Here, we expand the incomplete elliptic integral $\mathsf{E}(\phi, \varepsilon)$ in terms of linear and periodic contributions

as follows:

$$\begin{aligned} \mathsf{E}(\phi,\varepsilon) &= \int_0^{\phi} d\theta \sqrt{1-\varepsilon^2\sin^2\theta} \qquad (\varepsilon \leq 1) \\ &\approx \frac{2}{\pi}\left(\phi\,\mathsf{E}(\varepsilon) + \frac{\varepsilon^2}{8}\mathsf{K}(\varepsilon)\sin(2\phi) + ...\right) \end{aligned} \tag{4.34}$$

where $\mathsf{E}(\varepsilon) \equiv \mathsf{E}(\pi/2,\varepsilon) = \pi/2(1-\varepsilon^2/4-3\varepsilon^4/64+...)$ and $\mathsf{K}(\varepsilon) = \pi/2(1+\varepsilon^2/4+9\varepsilon^4/64+...)$ are the complete elliptic integrals of the second and first kind respectively. Due to the non-zero amplitude ε, the spatial coordinate σ measuring the invariant length along the string is no longer directly proportional to the z-coordinate of the numerical grid. From (4.33) and substituting the expression for $\mathsf{E}(\phi,\varepsilon)$, we obtain

$$z \approx 2\mathsf{E}(\varepsilon)\sigma/\pi + \text{periodic terms} \approx \sigma(1-\varepsilon^2/4-...)\,. \tag{4.35}$$

Imposing spatial periodicity L in the z-direction, the energy of the string in the same interval (setting $\sigma = T$) becomes

$$\begin{aligned} E(\varepsilon) &\equiv \mu T(\varepsilon) = \frac{\pi}{2\mathsf{E}(\varepsilon)}\mu L \\ &\approx \mu L\left(1+\tfrac{1}{4}\varepsilon^2+\tfrac{7}{64}\varepsilon^4+...\right), \end{aligned} \tag{4.36}$$

where μ is the energy per unit length. As ε increases, the true time periodicity T differs from the spatial periodicity L, with $T = \alpha L \geq L$. The increase in periodicity is illustrated by the oscillating string in Figure 4.15 with $A_0 = 4$ ($\varepsilon = 0.68$), which shows an initial periodicity about 11% longer than $L = 32$ (at large λ), though this is lower than the expected 15% due to long-range forces and radiative backreaction accelerating the string (and modifying ε). Relativistic effects become important as $\varepsilon \to 1$ ($A_0 = 8$) and, in this limit, two points along the string approach a cusp ($v \to 1$) twice each period. In this thesis, most quantitative tests will be undertaken at smaller ε where we can neglect these corrections.

As demonstrated in Section 2.3.3, calculations of the massless radiation power spectrum have been undertaken for periodic solutions like (3.12) using the antisymmetric tensor formalism (2.55), The radiation power P can be expressed as a sum over the n harmonics P_n, generally yielding combinations of Bessel functions [135]. A particularly interesting case is the periodic helix for which a full nonlinear analysis can be performed [136], showing that only harmonics with $m+n$ *even* radiate, with large n harmonics exponentially suppressed

$P_n \propto e^{-\alpha n}$, where α is larger at small amplitude ε [135].[4,5] As outlined in Section 2.3.3, this $m+n$ *even* selection rule also applies to the sinusoidal configurations (3.12) on which we focus here. Further to this, a linearised calculation of the leading-order radiation from the second harmonic using (2.68) yields a power per unit length of [135]

$$\frac{dP}{dz} = \frac{\pi^3 \eta^2}{16L} \varepsilon^4 . \tag{4.37}$$

The same calculation applied to more realistic configurations with a superposition of sinusoidal modes (even for a kink solution, i.e. a solution with a discontinuous tangent vector) also has the leading $P \propto \varepsilon^4$ dependence, summed over the contributing modes.

This generic quadrupole radiation rate can be developed into a simple analytic backreaction model describing the effect of radiation energy losses on string motion [135]. At small amplitude, we can see from (4.36) that the oscillation energy to leading order is given by the square of the amplitude ε, where $E = \mu L(1+\frac{1}{4}\varepsilon^2)$. Equating the rate of energy loss with the radiation power (4.37) yields the time-derivative of the energy per unit length,

$$\frac{1}{L}\frac{dE}{dt} = \frac{\mu}{4}\frac{d(\varepsilon^2)}{dt} = -\frac{\pi^3 \eta^2 (\varepsilon^2)^2}{16L} . \tag{4.38}$$

This can be easily integrated to obtain the solution for the invariant amplitude,

$$\frac{1}{\varepsilon^2} - \frac{1}{\varepsilon_0^2} = \frac{\beta t}{\bar{\mu} L} \quad \Rightarrow \quad \varepsilon = \varepsilon_0 \left(1 + \frac{\beta \varepsilon_0^2 t}{\bar{\mu} L}\right)^{-1/2} , \tag{4.39}$$

where $\beta = \pi^3/4$ and $\bar{\mu} = \mu/\eta^2 \approx 2\pi \ln(\sqrt{\lambda}\eta R)$, where the cutoff R is related to the curvature radius of the string (see discussion in Section 2.2.1). Note that (4.39) is a direct analytic prediction for the damping rate of a global string as a function of scale, which we will test numerically. In evaluating whether an oscillating string conforms with this model, it is easiest to use the first expression in (4.39), seeking a simple linear relation between time t and the inverse square of the invariant amplitude ε^{-2}.

The sinusoidal solution (3.12) assumes left- and right-moving modes of equal magnitude. It has been argued, when these are unequal, that exponential decay may be more typical of radiation damping processes ([135]). For our purposes, it is useful to have a second

[4] Here, α is an exponential decay constant, not to be confused with the fractional increase in path length.

[5] For this helix configuration, symmetry prevents radiation in the generic $n = 2$ quadrupole mode, so the lowest harmonic is $n = 3$.

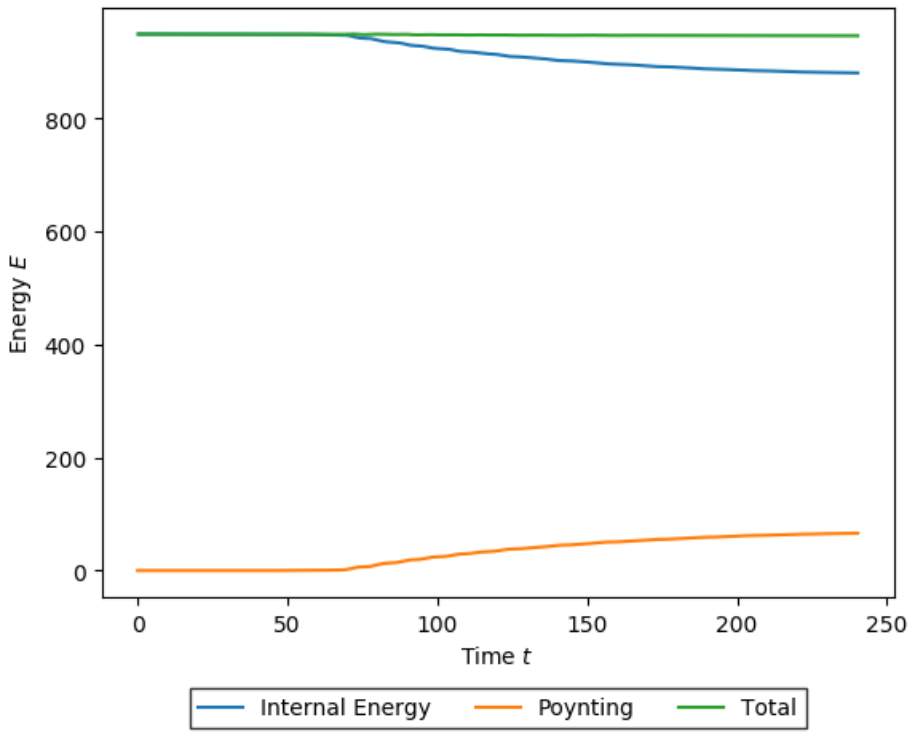

Fig. 4.3 Comparison of the total energy within the volume enclosed by the diagnostic cylinder (blue line) with the outgoing massless radiation energy determined by the time integral of $\mathscr{D}\vartheta \cdot \hat{\mathbf{r}}$ (orange line) for a $\lambda = 1$ string with initial amplitude $A_0 = 4$. The dominant energy loss mechanism is massless radiation as indicated by conservation of the sum (green line).

alternative model with which to compare the interpretation of results. In principle, cross-coupled modes can cause amplitude decay like that of a damped simple harmonic oscillator, so by analogy with the power law decay in (4.39) we consider the form:

$$\varepsilon = \varepsilon_0 \exp\left(-\frac{\beta t}{2\bar{\mu}L}\right). \tag{4.40}$$

Again we will test the model by seeking a linear relation, here between the time t and $\ln\varepsilon$. We can also introduce an amplitude dependence (for example, see [135]), so the damping rate becomes $\beta\varepsilon^2/2\bar{\mu}L$, where $\varepsilon^2 = |\varepsilon_L^2 - \varepsilon_R^2|$ represents the difference in amplitude between left- and right-moving modes.

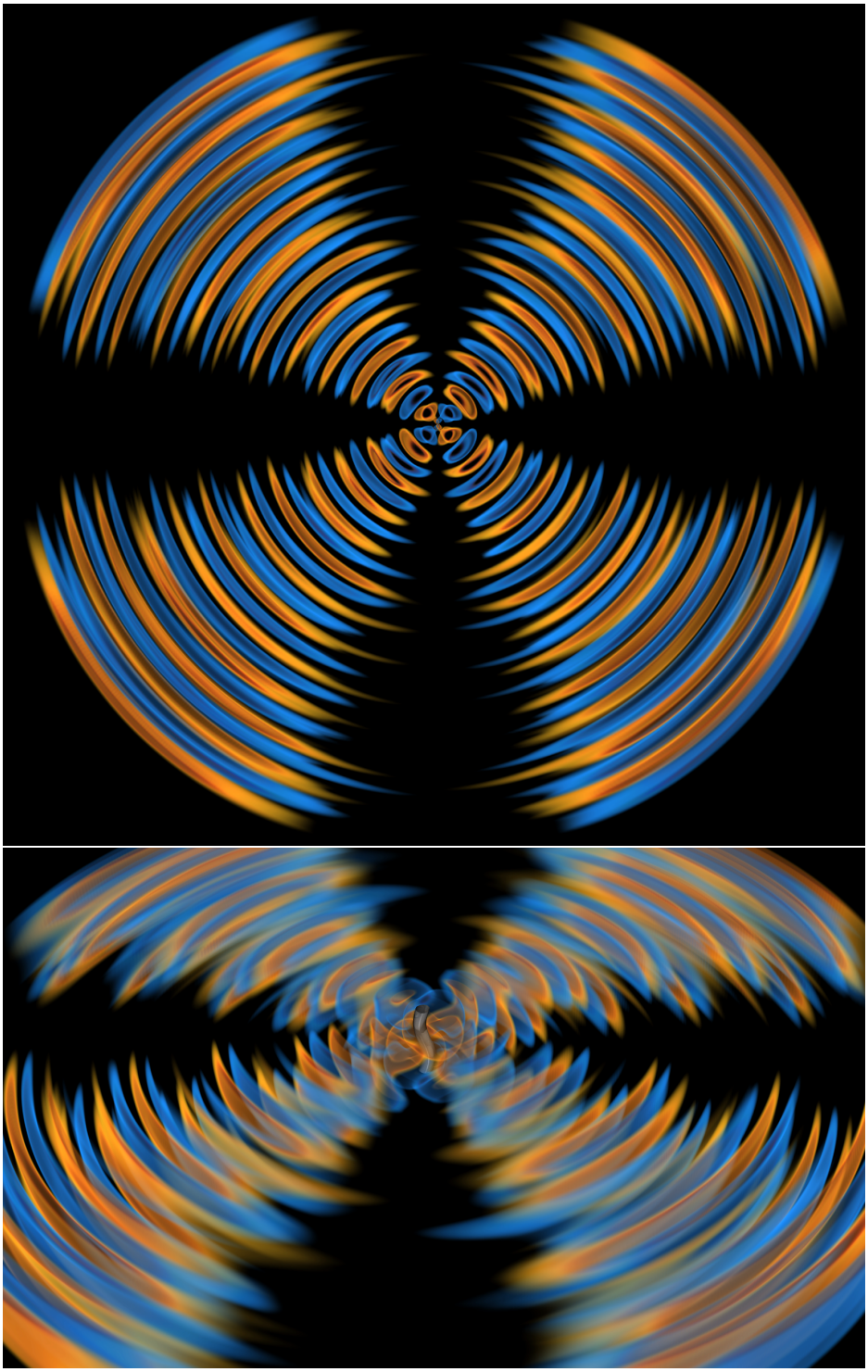

Fig. 4.4 Volume rendering in 3D space (x,y,z) of the massless radiation $\mathscr{D}\vartheta\cdot\hat{\mathbf{r}}$ from a $\lambda=1$ string with initial amplitude $A_0=4$. The radiation is emitted from a string at the centre of the grid, with the quadrupole mode $\{mn\}=\{20\}$ clearly dominant.

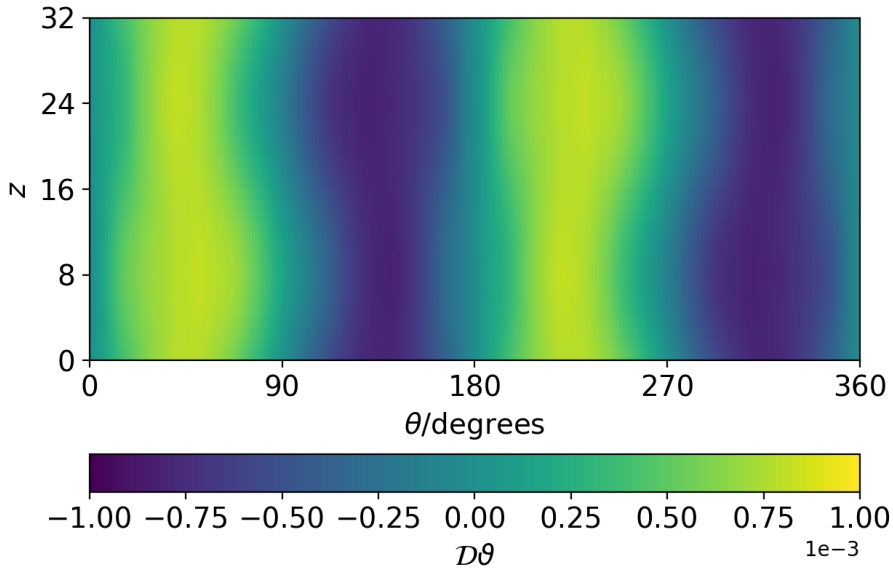

Fig. 4.5 Plot of the massless radiation $\mathscr{D}\vartheta \cdot \hat{\mathbf{r}}$ from a $\lambda = 1$ string with initial amplitude $A_0 = 1$ at late time $t = 167.5$, measured on a cylinder at $R = 64$, where θ is the azimuthal angle. The dominant quadrupole mode $\{mn\} = \{20\}$ can be clearly identified.

4.2 Massless Radiation Analysis

In this section, we present a quantitative analysis of the massless radiation from oscillating string configurations with small amplitude $A_0 = 1$ and larger amplitudes $A_0 = 4$ and $A_0 = 8$. Simulations are set up as described at the beginning of the chapter, and we investigate the cases $\lambda = 1$ and $\lambda = 10$. We analyse propagating massless radiation using the spatial diagnostic $\mathscr{D}\vartheta \cdot \hat{\mathbf{r}}$ defined by (4.12).

As an initial accuracy check, we establish energy conservation in our simulation setup. We integrate the energy within the cylindrical volume enclosed by $R = 64$ and the net massless radiation energy propagating across the cylinder, using the interior density ρ from (2.15) and the time integral of the massless component of the radial radiation Poynting vector $(\Pi_\vartheta \mathscr{D}\vartheta) \cdot \hat{\mathbf{r}}$ from (4.14). An example is shown in Figure 4.3 for a $\lambda = 1$ string with initial amplitude $A_0 = 4$. This confirms accurate energy conservation for the simulation, as well as the dominance of massless radiation losses at small amplitude.

To aid with physical understanding prior to the upcoming detailed discussion, we first present Figure 4.4, which shows a three-dimensional spatial visualisation of the massless radiation

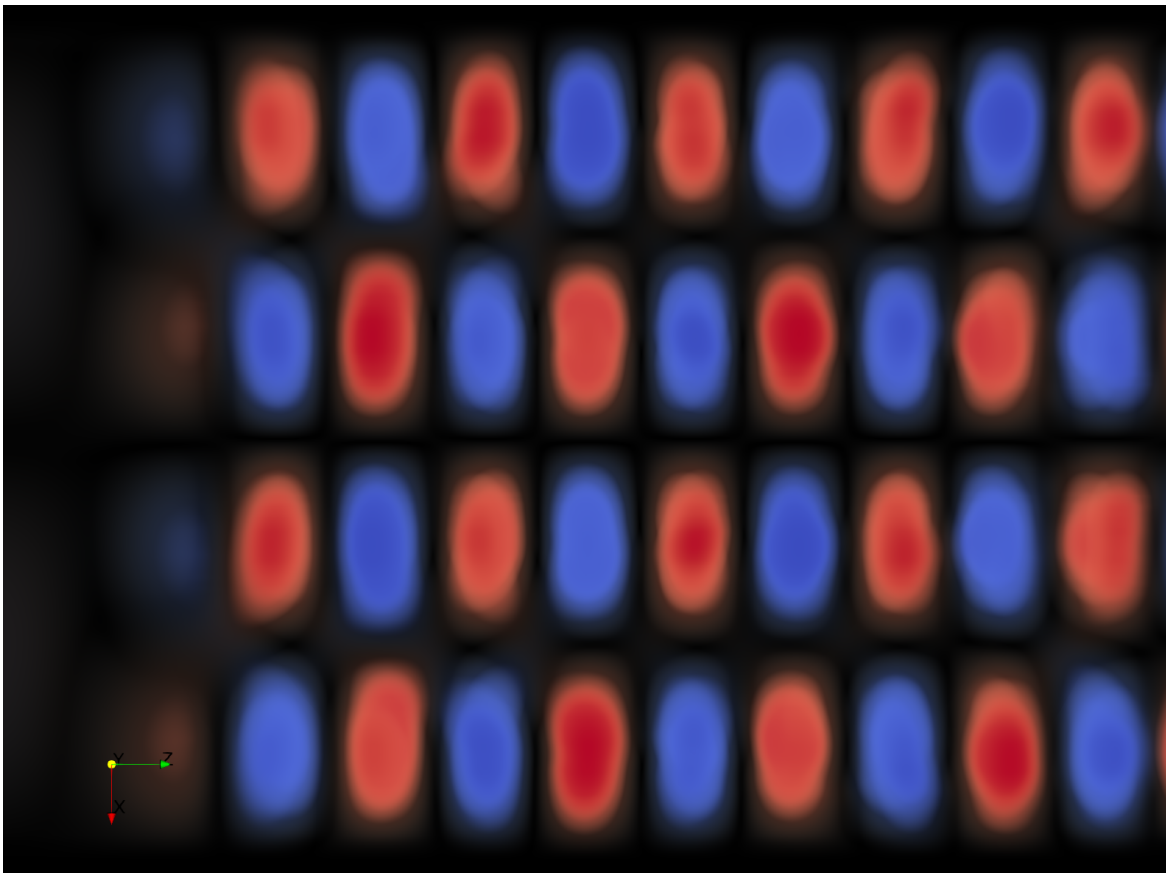

Fig. 4.6 Volume rendering in spacetime (t, θ, z) of the massless radiation $\mathscr{D}\vartheta \cdot \hat{\mathbf{r}}$ from a $\lambda = 10$ string with initial amplitude $A_0 = 1$ over time, measured on a cylinder at $R = 64$. The time axis runs left to right and azimuthal angle θ from bottom to top. The dominant quadrupole mode $\{pmn\} = \{220\}$ can be clearly identified.

for $\lambda = 1$ with an intermediate amplitude $A_0 = 4$. This late-time snapshot clearly shows the dominant quadrupole structure as predicted analytically by the solution to the massless wave equation (4.32). Detailed quantitative analysis of the different configurations is performed in subsequent sections by extracting and Fourier decomposing the massless radiation field over time on a cylinder at fixed radius $R = 64$.

4.2.1 Small Amplitude Oscillations

Here we present results of string simulations with small initial amplitude $A_0 = 1$ ($\varepsilon = 0.20$) for $\lambda = 1$ and $\lambda = 10$. We first present qualitative results from visualisation of the radiation extracted on the diagnostic cylinder. Figure 4.5 shows the massless radiation field extracted for one timestep at late time at $R = 64$, revealing an $m = 2$ angular dependence and, to a

first approximation, no z-dependence (i.e. $n = 0$). In Figure 4.6, the radiation field is plotted as a function of both space and time (2+1D), showing the consistent periodic behaviour of the propagating field. From this data, we can infer the time-dependence to be a second harmonic of the fundamental period ($p = 2$), so that the observed quadrupole corresponds to the $\{pmn\} = \{220\}$ eigenmode from the asymptotic general solution (4.32).

The extracted radiation field can be quantitatively analysed by decomposing into its constituent two-dimensional (2D) Fourier modes $\mathscr{F}_{\mathscr{D}\vartheta}(k_\theta, k_z)$ using a 2D FFT.[6] We can average these eigenmode signals over time to obtain a measure of their overall magnitude using

$$\mathscr{F}_{av,\mathscr{D}\vartheta}(k_\theta, k_z) = \sum_{t=-\Delta t}^{t=\Delta t} \mathscr{F}_{\mathscr{D}\vartheta}(k_\theta, k_z)/2\Delta t\,, \tag{4.41}$$

where Δt is approximately one period of oscillation of the string. Figure 4.7 plots the pattern of time-averaged $\{mn\}$ eigenmodes $\mathscr{F}_{av,\mathscr{D}\vartheta}$ for $\lambda = 1$ extracted at late time $t = 140.75$, at which point the propagating massless signals have reached the extraction cylinder. We obtain a 'checkerboard' pattern that confirms the analytic selection rule discussed in Section 4.1.4, i.e. that only $m+n$ *even* eigenmodes can be generated. From Figure 4.7, we determine the six highest magnitude propagating modes, for which the time-average is plotted over time in Figure 4.8 for both $\lambda = 1$ and $\lambda = 10$. A logarithmic scale is employed in both cases to highlight the wide separation in amplitudes between the different harmonics. We conclude that the quadrupole $\{220\}$ eigenmode offers the most significant radiation pathway, as predicted analytically by (4.37). We can see from Figure 4.8 that the next strongest propagating mode is the third harmonic dipole $\{311\}$ which has an approximate relative amplitude of 0.09, corresponding to a relative energy loss below 1% that of the quadrupole. We also note that the later arrival of the $\{311\}$ mode is consistent with $\sim$5% lower propagation velocity, as predicted by equation (4.27).

The absolute value (not time-averaged) of the four largest eigenmodes, $\{111\}$, $\{220\}$, $\{331\}$ and $\{440\}$, are shown in Figure 4.9 for both $\lambda = 1$ and $\lambda = 10$, where the time eigenvalue p is inferred from the time period. We note that the initial $\{111\}$ mode acquires a small $\{211\}$ contribution. The amplitudes and spectra of massless radiation for the two string widths with $\lambda = 1$ and $\lambda = 10$ are very similar. However, some subtle differences are discernible, including a smaller initial radiation amplitude for $\lambda = 1$ and a slightly faster amplitude decay rate. Regarding the former, the initial massless radiation amplitudes are

[6] In this work, we use the SciPy `fftpack`, https://docs.scipy.org/doc/scipy/reference/fftpack.html and perform our analysis using Python.

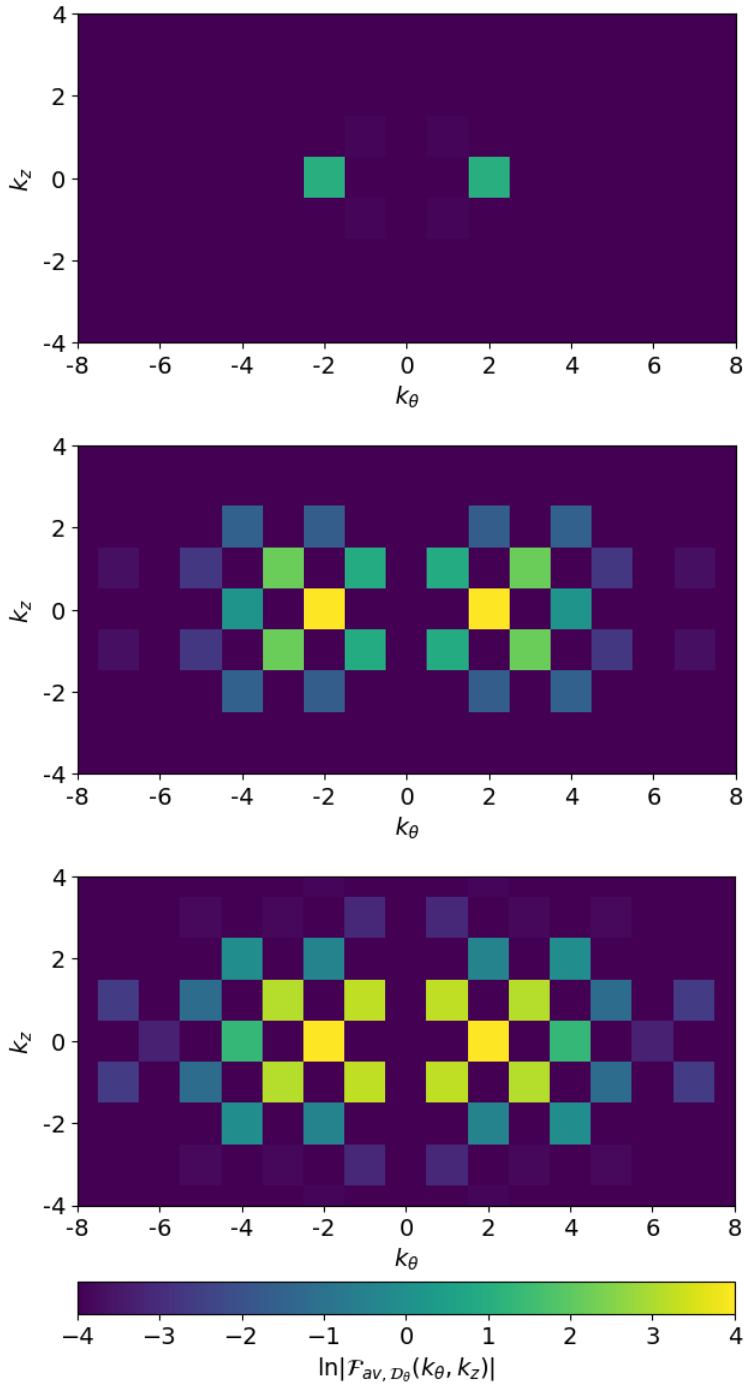

Fig. 4.7 Logarithmic plot of the 2D Fourier eigenmode amplitudes of the massless radiation $\mathscr{D}\vartheta \cdot \hat{\mathbf{r}}$ from a $\lambda = 1$ string at late time $t = 140.75$, measured on a cylinder at $R = 64$ and time averaged over approximate period $\Delta t = 33/4$. The horizontal axis is the angular eigenvalue m, while the vertical is the z-dependent wavenumber n. The top figure is for an initial amplitude $A_0 = 1$, the middle is for intermediate $A_0 = 4$ and the bottom is large $A_0 = 8$. In all cases, the quadrupole signal $\{pmn\} = \{220\}$ is dominant, but higher harmonics contribute at larger amplitudes, provided they satisfy the checkerboard selection rule: $m+n$ even.

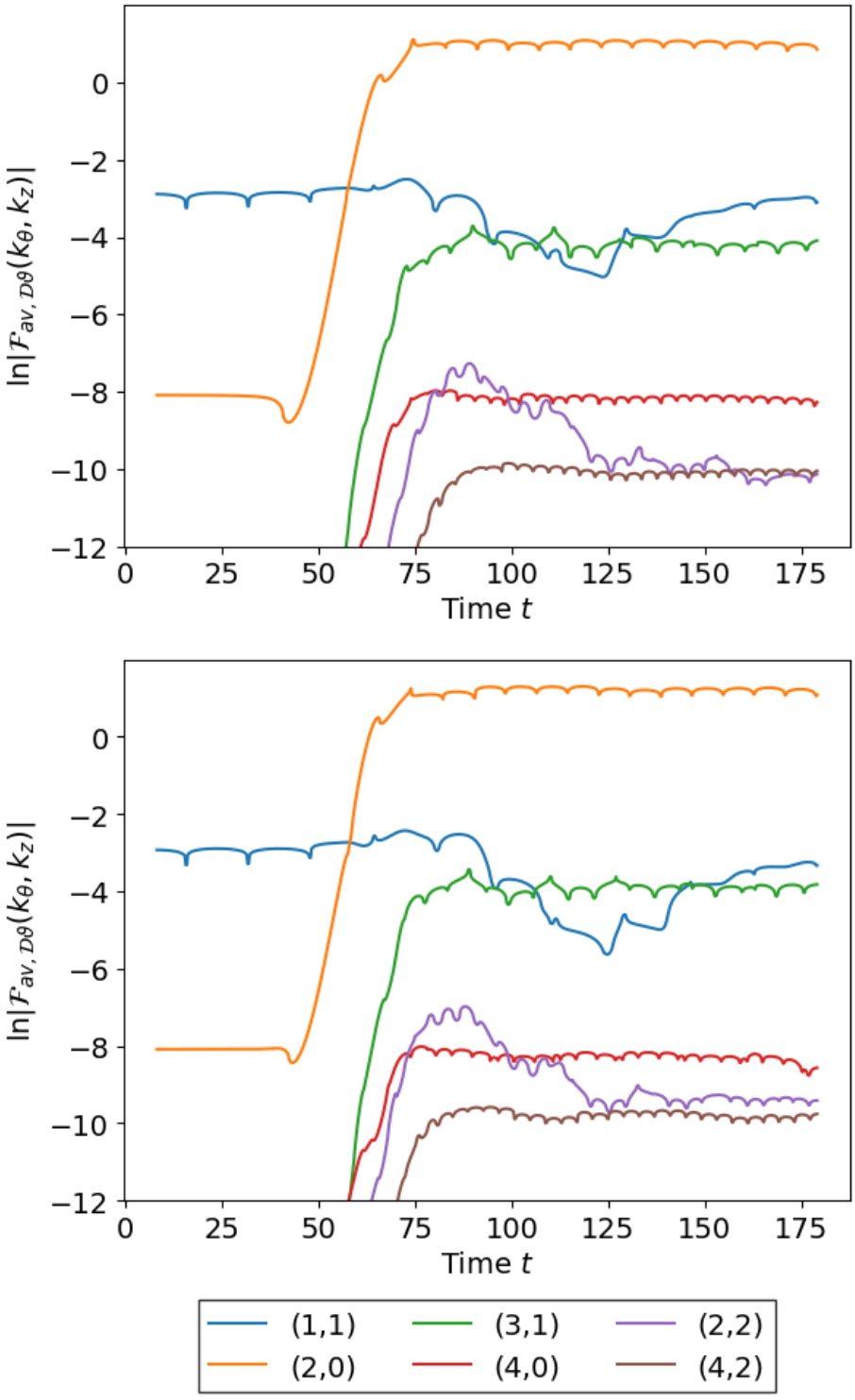

Fig. 4.8 Logarithmic plot of the dominant 2D Fourier modes of the massless radiation $\mathscr{D}\vartheta \cdot \hat{\mathbf{r}}$ from a $\lambda = 1$ (top) and $\lambda = 10$ (bottom) string with initial amplitude $A_0 = 1$, measured on a cylinder at $R = 64$ and time averaged over approximate period $\Delta t = 33/4$.

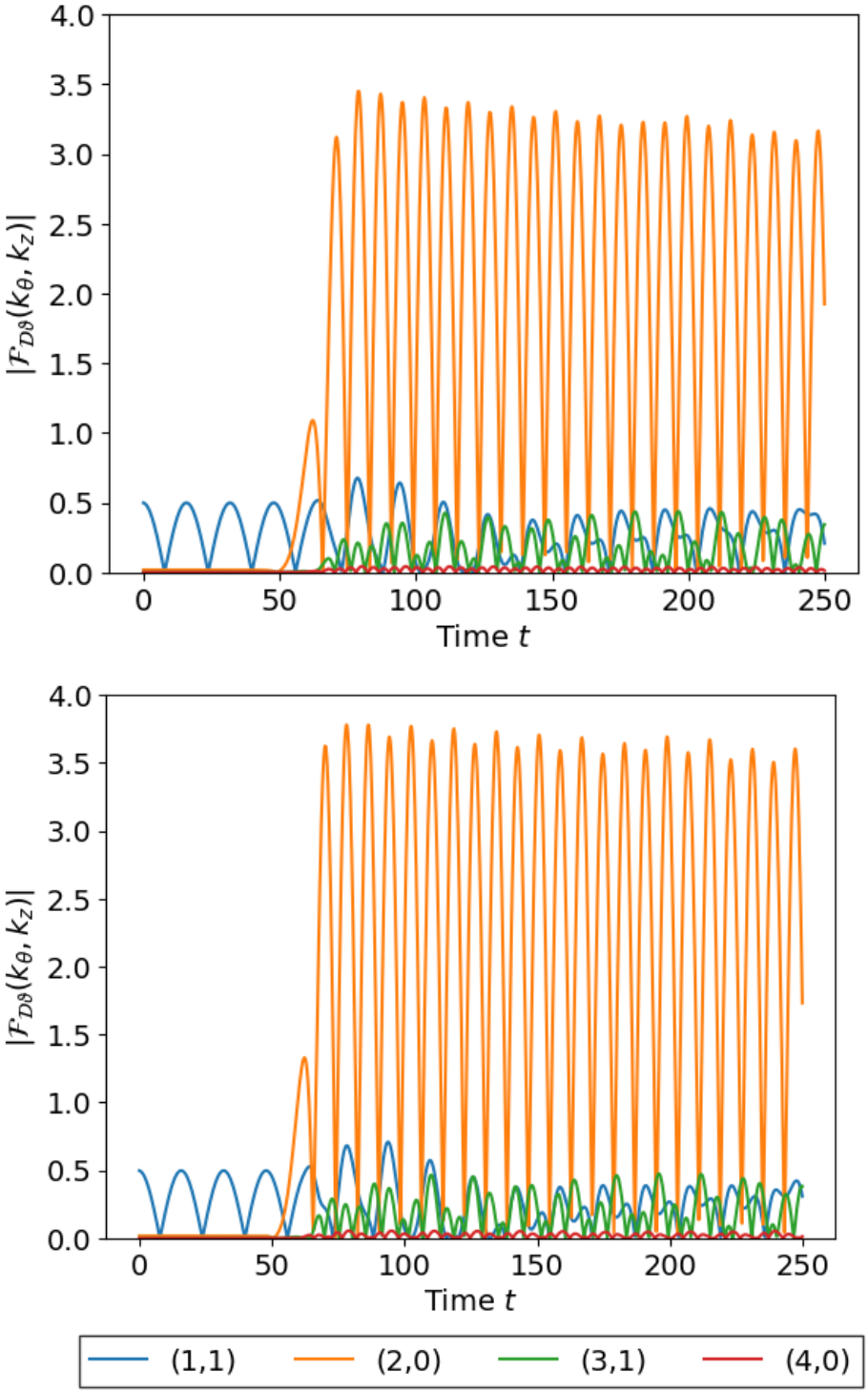

Fig. 4.9 Plot of the absolute value of the $\{mn\} = \{1\,1\}, \{2\,0\}, \{3\,1\}$, and $\{4\,0\}$ Fourier modes of the massless radiation $\mathscr{D}\vartheta \cdot \hat{\mathbf{r}}$ from a $\lambda = 1$ (top) and $\lambda = 10$ (bottom) string with initial amplitude $A_0 = 1$, measured on a cylinder at $R = 64$.

expected to be the same for all λ (with which we will see our results agree for $\lambda \gtrsim 3$ in the next section). However, for $\lambda = 1$ with $A_0 = 1$ and $L = 32$, finite size effects become important as the string core with $\phi < 1$ extends into the radiation zone (here, around $R \lesssim 4$), causing some suppression of the quadrupole amplitude (see Figure 2.3). The latter is a consequence of the $\lambda = 1$ string being lighter, so there is a larger relative effect from radiation backreaction, as we will discuss in the next section.

We finally note, from Figures 4.8 and 4.9, that the dipole mode $\{1\,1\,1\}$ is present from the beginning of the simulation before radiation has had time to propagate to the cylinder, indicating that it is a long-range self-field of the oscillating string. As discussed in Section 4.1.2, this can be understood from the offset motion of the oscillating string fields from the centre of the diagnostic cylinder. This apparent $\{1\,1\,1\}$ wave does not propagate, and so there should be no net flux over one period (if the amplitude remains constant). Using the spatial radiation diagnostic $\mathscr{D}\vartheta \cdot \hat{\mathbf{r}}$, the dipole self-field appears with an amplitude of 0.15 relative to the propagating quadrupole mode.

4.2.2 Large Amplitude Oscillations

Here we present massless radiation results for larger initial amplitudes $A_0 = 4$ ($\varepsilon = 0.68$) and $A_0 = 8$ ($\varepsilon \approx 1$), with string widths given by $\lambda = 1$ and $\lambda = 10$. Figure 4.10 shows a visualisation of the time-varying radiation measured on the diagnostic cylinder at $R = 64$ for the example $\lambda = 10$ and $A_0 = 4$. Although the $\{2\,2\,0\}$ quadrupole mode remains dominant, the signal is modulated by higher harmonics which have become significant. The presence of these eigenmodes is illustrated in the checkerboard lower panels in Figure 4.7, with many more modes excited for $A_0 \geq 4$ than for $A_0 = 1$ (upper panel).

Figures 4.11 and 4.12 show the time-averaged and absolute magnitude of the largest propagating eigenmodes, $\{2\,2\,0\}$, $\{3\,3\,1\}$ and $\{4\,4\,0\}$ for $A_0 = 4$, as well as the self-field $\{1\,1\,1\}$ which is now mixed with the propagating dipole $\{2\,1\,1\}$. We see again that the $\{2\,2\,0\}$ quadrupole mode is dominant for both $\lambda = 10$ and $\lambda = 1$, still contributing most of the outgoing radiation flux integrated across all modes. Even in the highly nonlinear regime with $A_0 = 8$ ($\varepsilon \approx 1$) and $\lambda = 1$ shown in Figure 4.13, the next harmonic $\{3\,3\,1\}$ has a maximum relative amplitude 0.42, i.e. initially contributing 18% of the quadrupole energy flux, with $\{4\,4\,0\}$ around 8% and $\{2\,1\,1\}$ 5%. We also note that the maximum quadrupole amplitude scales approximately with the invariant oscillation amplitude squared ε^2, in agreement with expectations from (4.37) that its energy flux scales as ε^4. Again, the amplitude of radiation from the lighter $\lambda = 1$ string always decays more rapidly than the $\lambda = 10$ string because they initially have

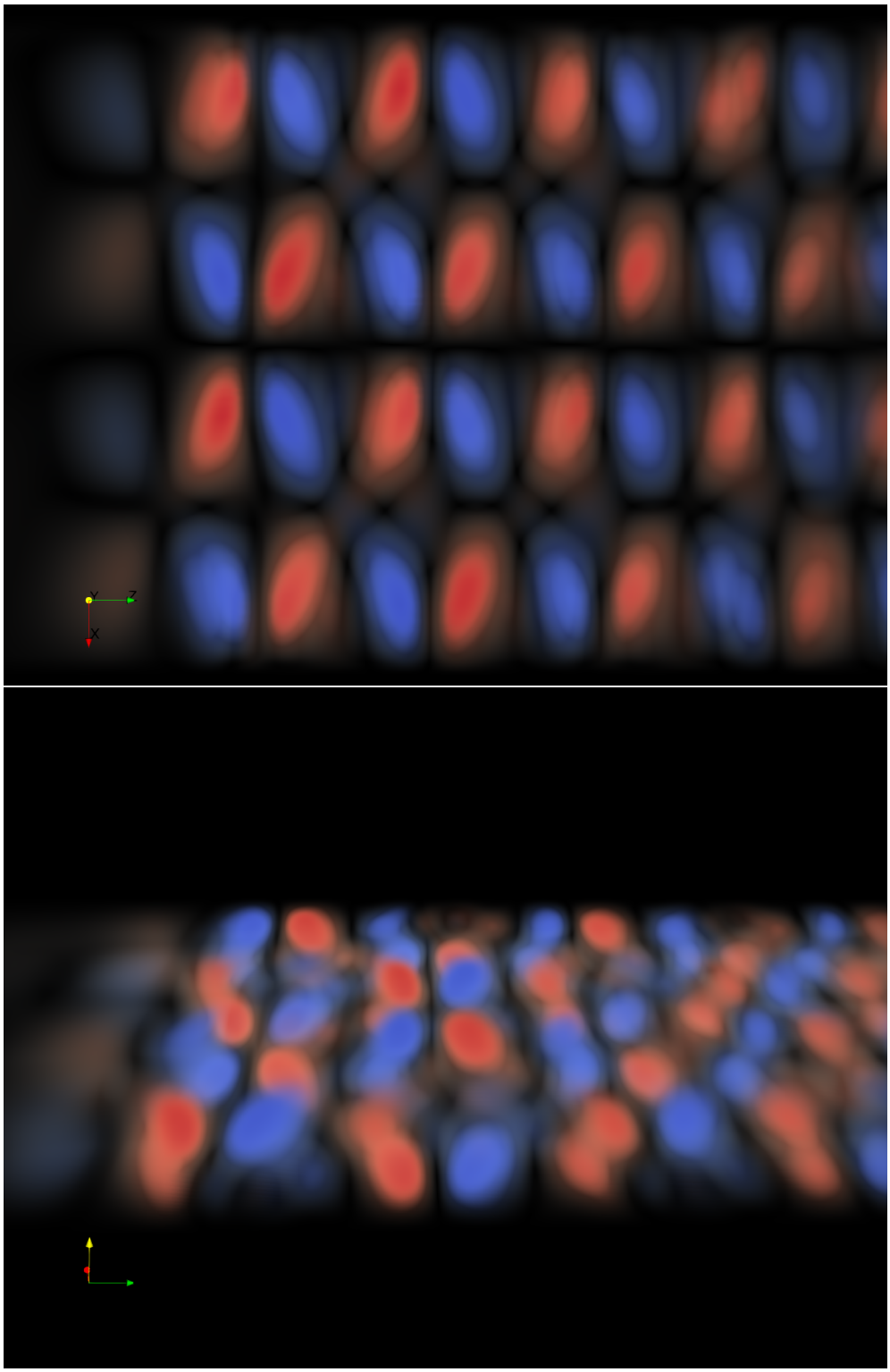

Fig. 4.10 Volume rendering in spacetime (t, θ, z) of the massless radiation $\mathscr{D}\vartheta \cdot \hat{\mathbf{r}}$ from a $\lambda = 10$ string with initial amplitude $A_0 = 4$ over time, measured on a cylinder at $R = 64$. The time axis runs left to right and azimuthal angle θ from bottom to top, with the view tilted away from the viewer in the bottom panel. The dominant quadrupole mode $\{pmn\} = \{220\}$ can be clearly identified, but is distorted by higher modes.

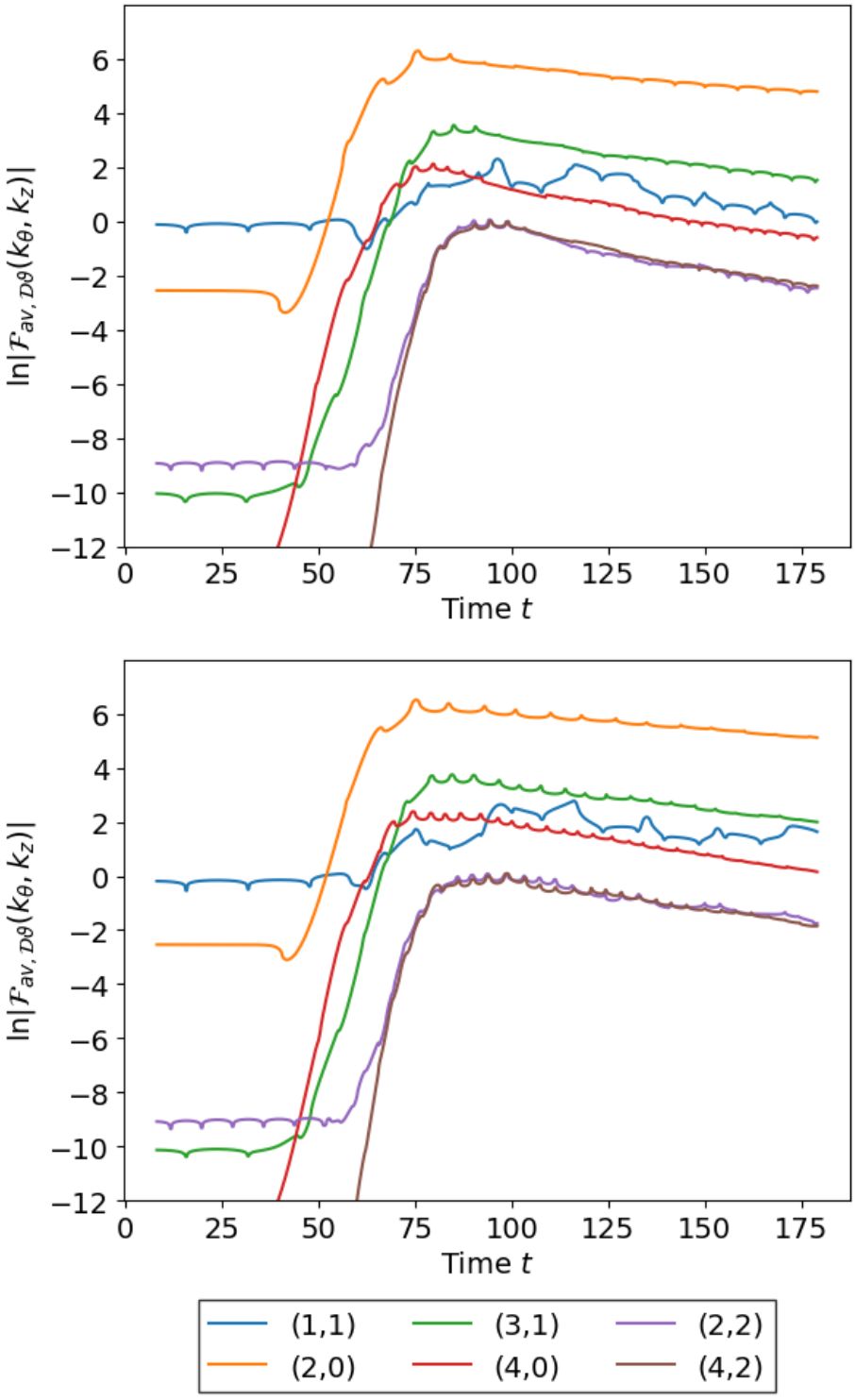

Fig. 4.11 Logarithmic plot of the dominant 2D Fourier modes of the massless radiation $\mathscr{D}\vartheta \cdot \hat{\mathbf{r}}$ from a $\lambda = 1$ (top) and $\lambda = 10$ (bottom) string with initial amplitude $A_0 = 4$, measured on a cylinder at $R = 64$ and time averaged over approximate period $\Delta t = 33/4$.

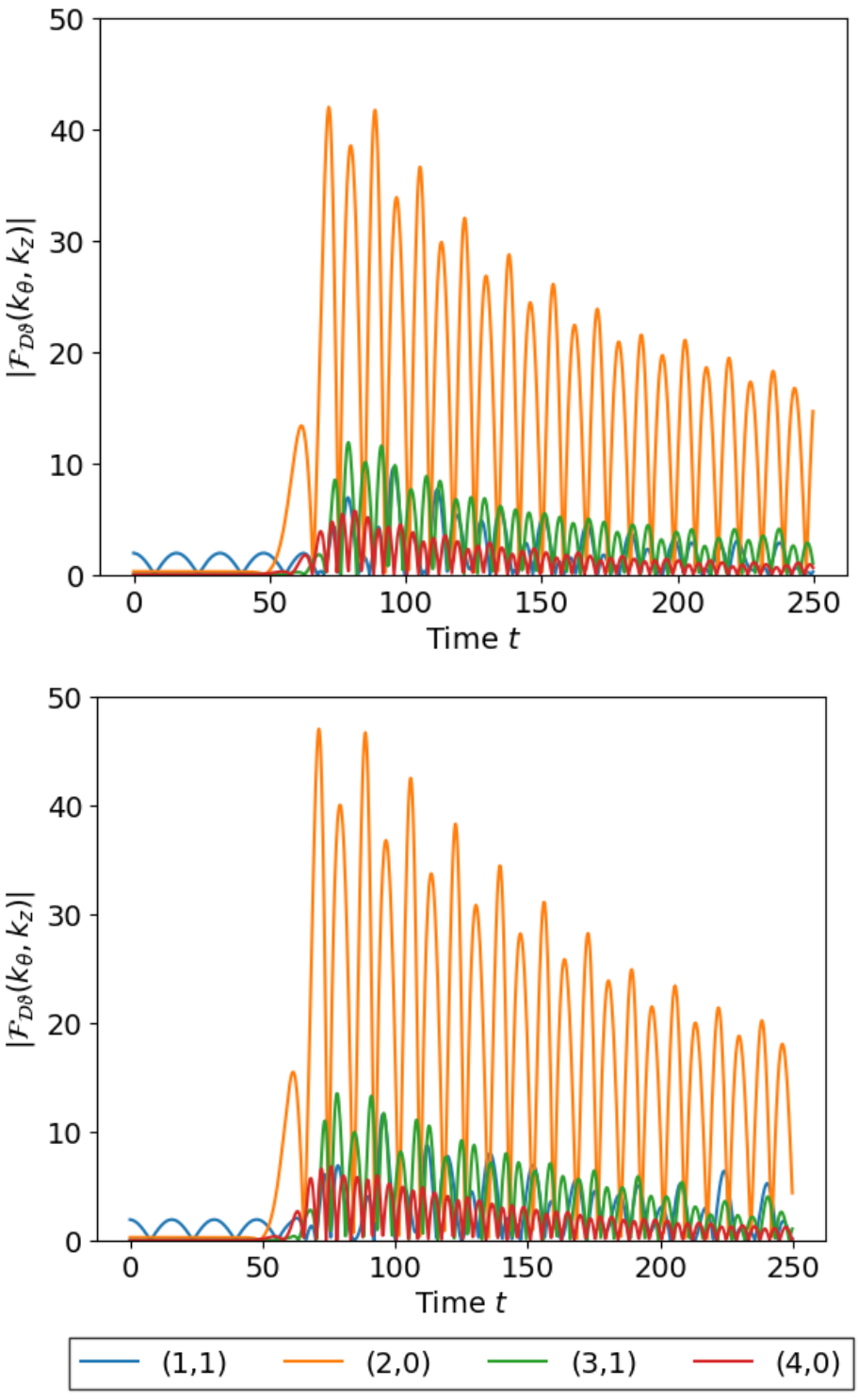

Fig. 4.12 Plot of the absolute value of the $\{mn\} = \{11\},\{20\},\{31\}$, and $\{40\}$ Fourier modes of the massless radiation $\mathscr{D}\vartheta \cdot \hat{\mathbf{r}}$ from a $\lambda = 1$ (top) and $\lambda = 10$ (bottom) string with initial amplitude $A_0 = 4$, measured on a cylinder at $R = 64$.

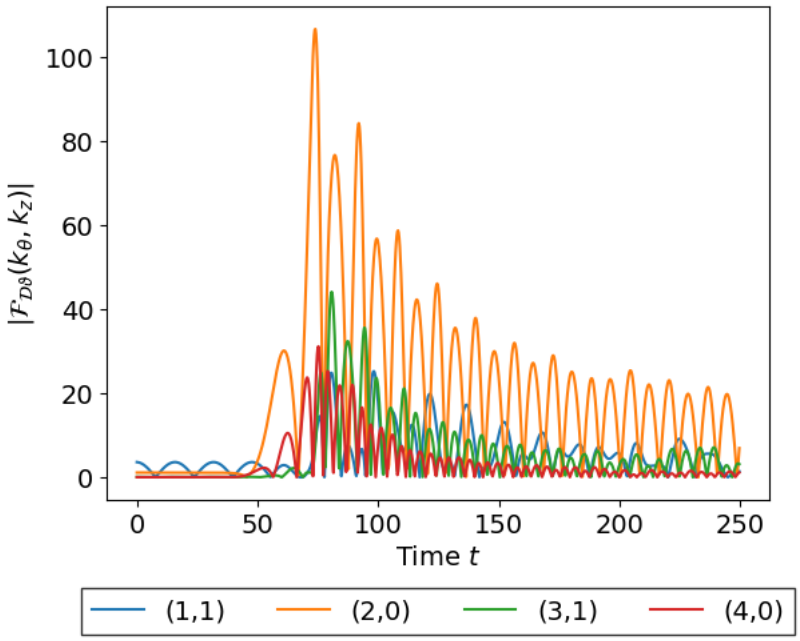

Fig. 4.13 Plot of the absolute value of the $\{mn\} = \{11\},\{20\},\{31\}$, and $\{40\}$ Fourier modes of the massless radiation $\mathscr{D}\vartheta \cdot \hat{\mathbf{r}}$ from a $\lambda = 1$ string with initial amplitude $A_0 = 8$, measured on a cylinder at $R = 64$.

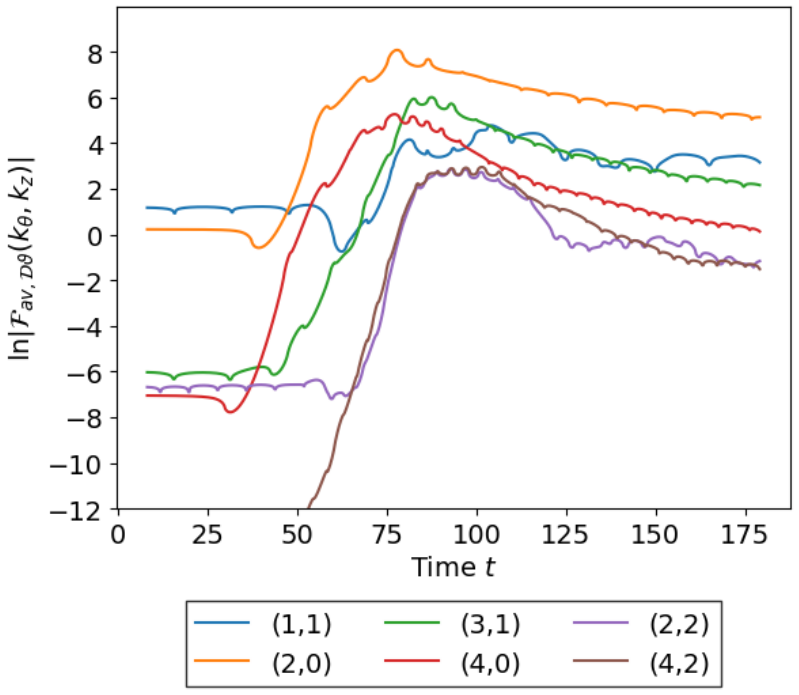

Fig. 4.14 Logarithmic plot of the dominant 2D Fourier modes of the massless radiation $\mathscr{D}\vartheta \cdot \hat{\mathbf{r}}$ from a $\lambda = 1$ string with initial amplitude $A_0 = 8$, measured on a cylinder at $R = 64$ and time averaged over approximate period $\Delta t = 33/4$.

the same massless radiation output, a backreaction effect we shall discuss in the next section. We note that the amplitude decay of high harmonics ($n > 2$) is considerably faster than the quadrupole, as illustrated in Figure 4.14.

4.3 String Radiation Backreaction

In this section, we analyse the detailed evolution of the oscillating string trajectories, observing the decay in amplitude due to radiation backreaction and comparing with analytic model predictions. Focussing on regimes where the AMR evolution is robust and accurate, we analyse two specific sets of string simulations with amplitudes $A_0 = 1$ and $A_0 = 3$ ($\varepsilon = 0.20, 0.54$), varying the string width parameter λ across the wide range $1 \leq \lambda \leq 100$. We note that in the present AMR implementation, large amplitude $A_0 \gtrsim 4$ ($\varepsilon \gtrsim 0.7$) oscillations at $\lambda \gtrsim 3$ (such as those illustrated in Figure 4.15) appear to be susceptible to small cumulative grid refinement effects at late times, which may have an effect on the evolution. This has been discussed in detail in Section 3.2.3.

We first plot string trajectories over time for a representative sample of λ in Figure 4.15, which shows the decay of the string amplitude. The amplitude is taken to be the position of the string core at the z-coordinate of maximum string displacement, $z = N_3/4 \equiv L/4$, calculated using the winding algorithm described in Section 3.4.2. We see that as λ increases, the rate of decay of the string generally decreases, indicating weaker radiation backreaction on strings with larger μ, as predicted.

We can model the rate of decay by extracting the maximum and minimum amplitude of the string for each period of oscillation. Figure 4.16 plots these values for the two data sets $A_0 = 1$ and $A_0 = 3$. The extrema of the oscillating string with small amplitude ($\varepsilon = 0.20$) shown in the top panel reveal nearly linear decay with a weak damping rate that decreases, as expected, with increasing λ (i.e. as the effective mass per unit length of the string increases). However, at small $\lambda \lesssim 3$, the radiative decay stalls and it becomes difficult to distinguish between different λ. In this regime, the oscillation amplitude $A_0 = 1$ is very close to the string width $\delta = 1/\sqrt{\lambda} \gtrsim 0.6$, where massive internal excitations within the string core can be expected to represent a non-negligible part of any string oscillation. These 'breather' modes mean that the motion of the zero ($\phi = 0$) at the string core is likely to be larger than the actual centre of mass oscillation, where the center of mass is determined by the motion of the dominant massless fields from which the radiation emanates. In our subsequent analysis, we shall endeavour to make a small correction for this finite width effect. We also note that

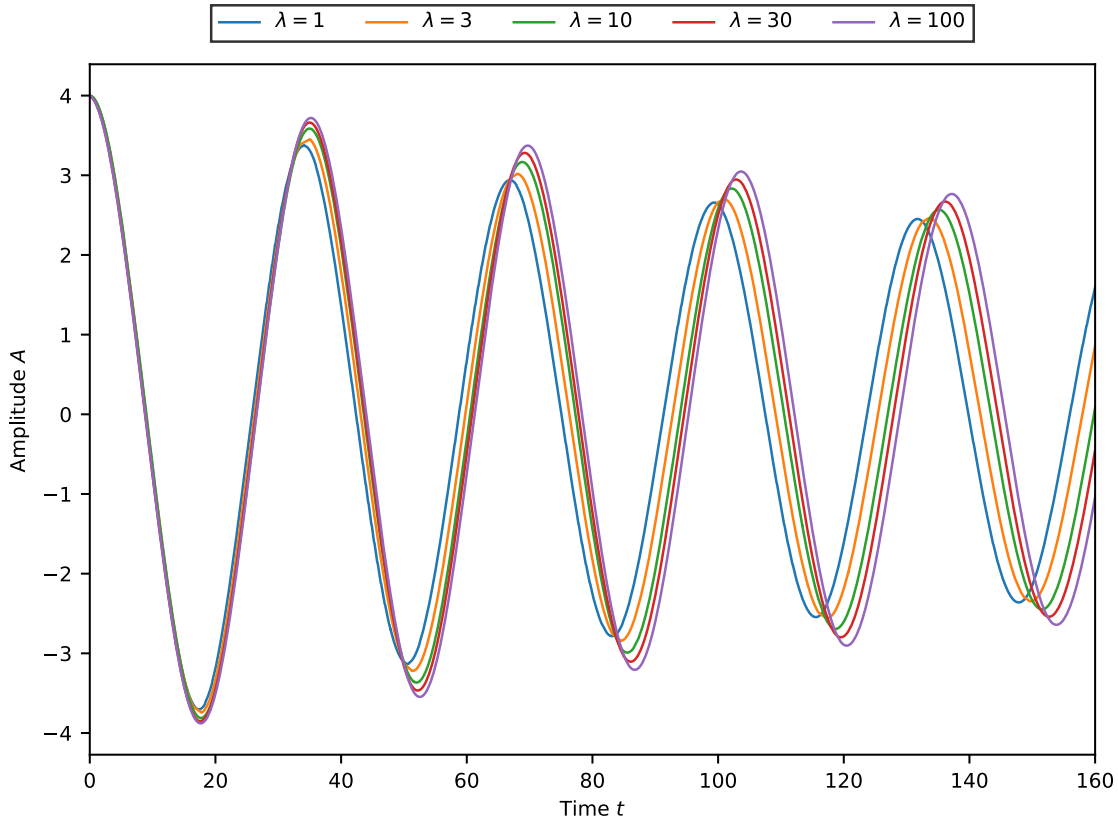

Fig. 4.15 Amplitude of strings over time for a selection of λ parameter values in the range $1 \leq \lambda \leq 100$ with an initial amplitude $A_0 = 4$.

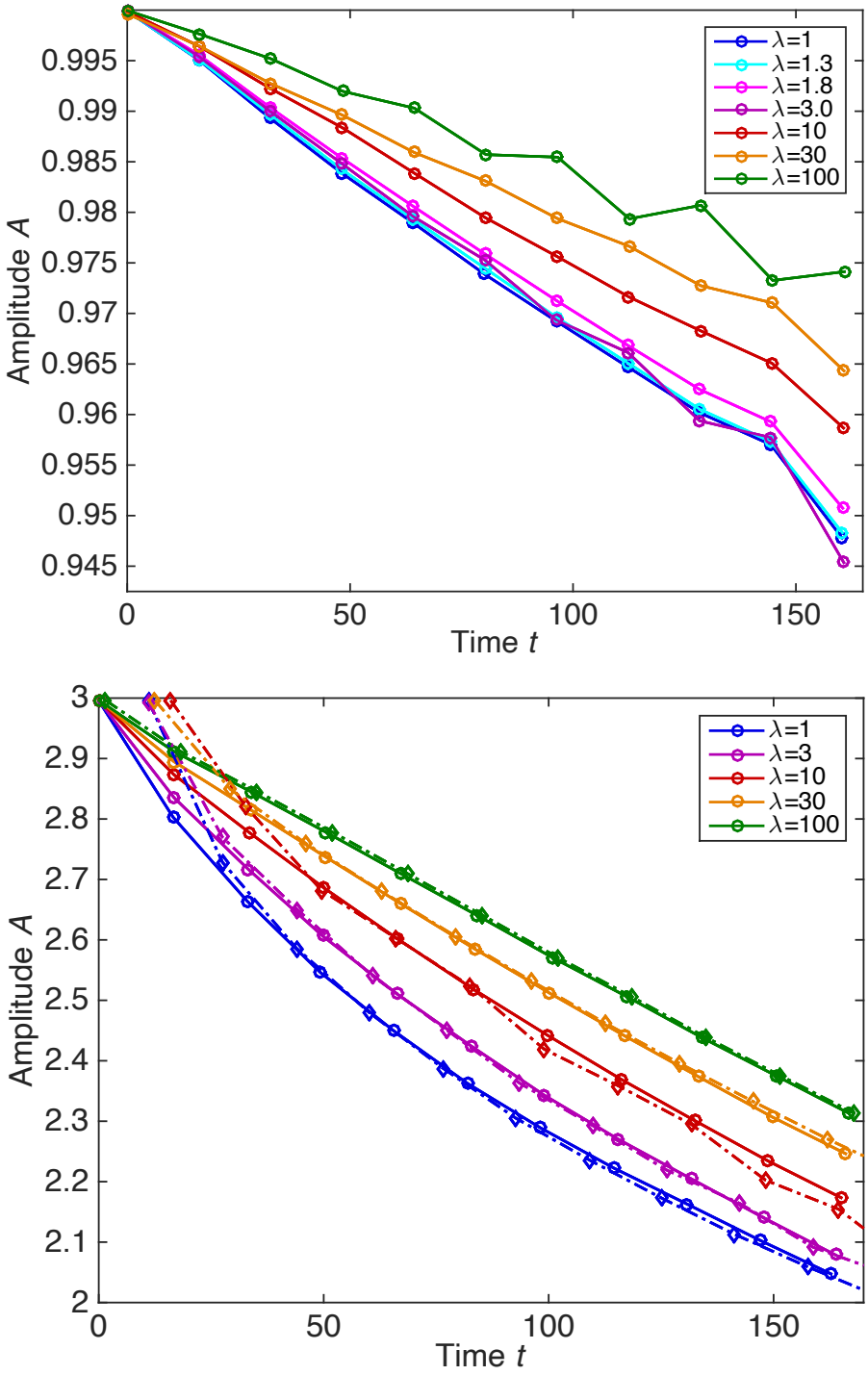

Fig. 4.16 Maximum amplitude of decaying string oscillations for small amplitude $A_0 = 1$ (top) and intermediate amplitude $A_0 = 3$ (bottom) for different λ at fixed length ($L = 32$). In both cases, thin global strings (large λ) have a slower decay rate as the energy density μ is higher. At small $\lambda < 3$, radiative decay reduces because of finite width effects. For $A_0 = 3$, additional data is plotted (diamond and dashed lines) for strings with initial conditions after enhanced relaxation. Here, the initial decay rate is faster but the asymptotic radiative decay is the same (as shown with appropriate time translations).

the $\lambda = 100$ string with $A_0 = 1$ appears to have drifted slightly from the centre from which the maximum amplitude is measured. This is due to the small difference in amplitude of the quadrupole radiation produced when the string is moving in the forward or backward direction relative to the propagation direction.

The bottom panel of Figure 4.16 shows the extrema from string oscillations of intermediate amplitude ($\varepsilon = 0.54$), showing trajectories with significant curvature, especially for the lighter strings (small λ) with more damping. This figure also illustrates the effect of different initial conditions due to changing the timescale of preceding relaxation before releasing the string to undergo relativistic hyperbolic evolution (see Section 3.3.1). The second set of data points (dotted lines) shows 'over-relaxed' initial conditions where the gradient flow phase was started much earlier, thus removing longer-range correlations of the massless self-field. This hastens the initial amplitude decay but, asymptotically, the radiating string settles into a steady state which closely matches that from the other initial conditions, as can be shown by a simple time translation. The 'under-relaxed' case (not shown here) exhibits opposite behaviour with a smaller initial decay, but again the same asymptotic limit. This observation may also be relevant for field theory simulations of string networks, and will be investigated further in future work. These simulations were performed using grid refinement levels at which there was no discernible improvement from increasing refinement further.

4.3.1 Inverse Square Amplitude Model

Analytic radiation calculations for a sinusoidal oscillatory string (3.16) yield a specific prediction for the backreaction effect on the string trajectory (4.39). The inverse square amplitude $1/A^2$ (or $1/\varepsilon^2$) is predicted to be linearly related to the time t. We find agreement with this for both data sets $A_0 = 1$ and $A_0 = 3$, as shown in Figure 4.17; not only are all the lines straight independent of A_0 and λ as predicted, the two data sets have approximately matching slopes for the same λ values, i.e. the string energy density $\bar{\mu}$ alone determines the damping rate (or, equivalently, $\bar{\mu} \sim \ln\lambda$) as predicted. We can understand this physically; given that the radiation power is independent of λ as shown by (4.37), it can be shown by straightforward manipulation that the greater oscillation energy (4.36) of the heavier strings with large λ causes the amplitude ε to decay more slowly.

Finite width effects for the fat lighter strings ($\lambda \lesssim 3$) at small amplitude ($\varepsilon = 0.20$) reduce the damping rate (slope) dependence on $\ln\lambda$, as discussed previously. Assuming that internal modes (within the string thickness δ) imply that the true string oscillation amplitude is slightly smaller than measured for all λ, we apply a finite width correction to all data by

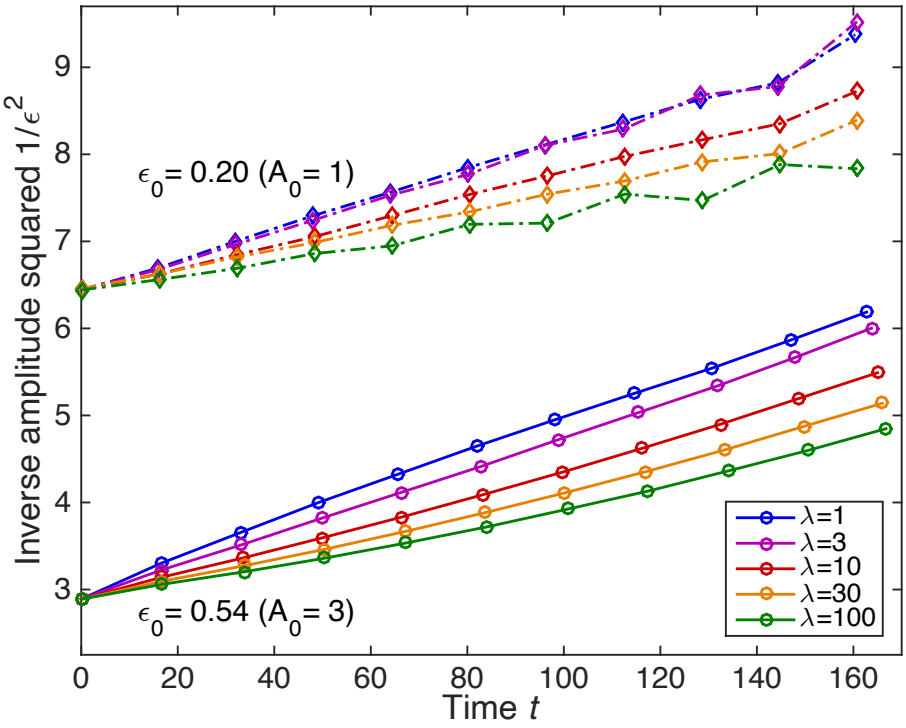

Fig. 4.17 Inverse of the squared amplitude A^2 for different oscillating strings as a function of time. The simple backreaction model (4.39) predicts that the linear slope depends on the string energy density (effectively $\ln\lambda$), but is independent of the amplitude A. (Note that $A_0 = 1$ data is offset by -20 with the slopes unchanged.)

modifying the raw amplitude A to a new value A' as follows:

$$A' = A - \xi/\sqrt{\lambda}\,. \tag{4.42}$$

A small correction $\xi = 0.08$ (i.e. only 8% of the string width) aligns the respective slopes of the $A_0 = 1$ and $A_0 = 3$ data sets remarkably well, as shown when they are superposed with zero intercept in Figure 4.18. We note that this small linear correction is not adequate to align the data with the backreaction model (also plotted in Figure 4.18) when $A_0 \sim \delta$, as for the $\lambda = 1$ case with $\delta \sim 1$ where much larger deviations are evident. For this reason, we exclude the $\lambda = 1$ string data from our asymptotic parameter estimates in the upcoming analysis. This is significant, as $\lambda = 1$ is the case on which most previous numerical studies have been based. There is also some evidence for deviation from linear behaviour at late times for the $\lambda = 100$ string at large amplitude $A_0 = 3$. We eliminate these last few time points from the analysis, as this behaviour is unphysical and due to a systematic effect linked to the numerical evolution (see Section 3.2.3). We perform a least-squares best fit for each

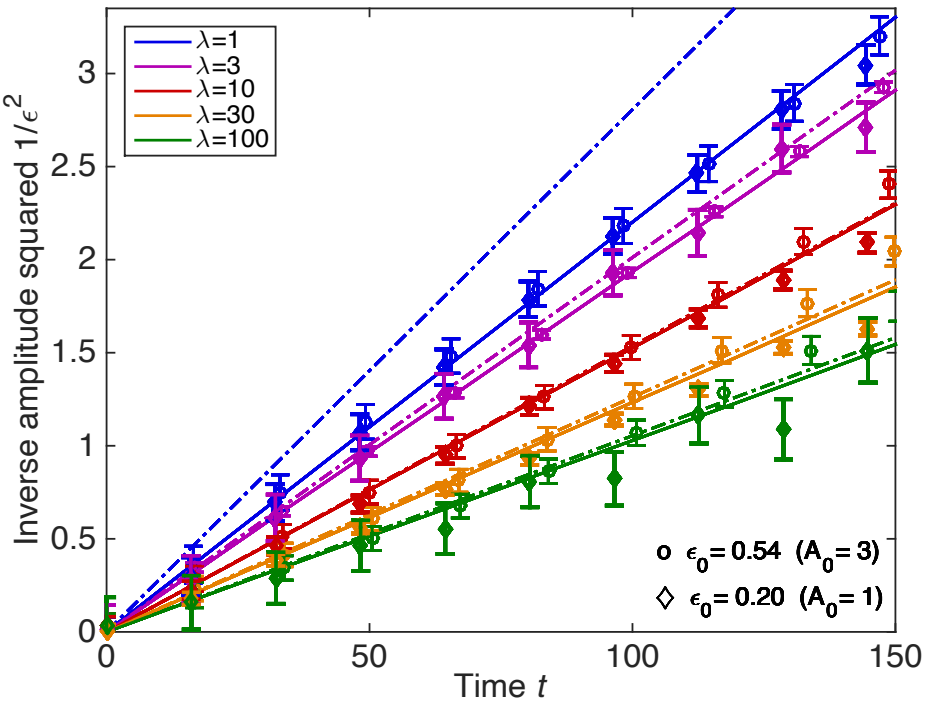

Fig. 4.18 Fit of oscillating string data to the simple backreaction model (4.39) for the inverse square of the invariant amplitude $\varepsilon = 2\pi A/T$ against time t. After a small 8% finite width correction, the $A_0 = 1$ ($\varepsilon = 0.20$) data (diamonds) align closely with the larger amplitude ($\varepsilon = 0.54$) data (circles), showing consistent linear behaviour for all λ. The analytic prediction from the inverse square model (4.39) is plotted (solid lines for $A_0 = 3$, dashed lines for $A_0 = 1$) for each λ, showing good agreement for all $\lambda > 3$.

data set shown in Figure 4.18, estimating the error for the resulting slope or damping rate. The best fit lines are plotted, further illustrating the consistency between the two data sets at different amplitudes.

From the analytic backreaction model prediction (4.39), the string amplitude ε is determined by $\beta/\bar{\mu}L = \beta/2\pi \ln(\sqrt{\lambda}\,R)L$, where $\beta = \pi^3/4$ and R is the long-range cut-off giving the effective width of the string. We must simultaneously estimate β and R from our data to determine the best fit. This is illustrated in Figure 4.19, where the string damping rate is plotted against the string energy density $\bar{\mu}$. When we take the cut-off scale $R \approx 3.75$, damping rates associated with $\lambda = 3, 10, 30$ and 100 align with the backreaction model, asymptotically projecting to zero damping as $\lambda \to \infty$. For this R, the analytic prediction (red line) shown in Figure 4.19 is in remarkable agreement, consistent with all damping rates, except those for $\lambda = 1$ where finite size effects become important (for $L = 32$). This agreement is also demonstrated in Figure 4.18 where the predicted analytic inverse square

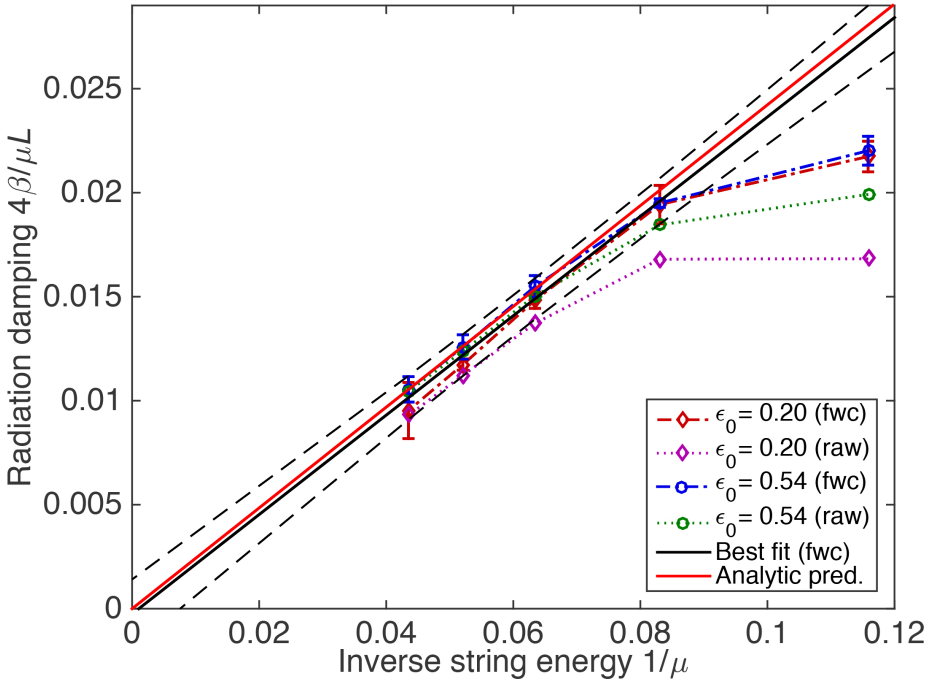

Fig. 4.19 Measured radiative damping rates plotted as a function of inverse string density μ^{-1} (essentially the inverse $\ln\lambda$), also showing errors in the extrapolated slope, Here we interpret the results with an effective string radius cutoff $R = 3.5$, for which the damping rate vanishes as $\mu \to \infty$ ($\lambda \to \infty$). We apply a finite size correction, but string width effects limit radiative damping at small λ.

amplitudes are shown (dashed lines) as a function of time. Despite this concordance with the inverse square model, there are fairly large uncertainties with a match possible within the parameter range:

$$\beta = 7.6 \pm 1.6\,, \quad \log R = 1.3 \pm 0.3 \ (R = 3.75)\,. \tag{4.43}$$

Without any finite width correction, the two data sets are less consistent, as reflected in larger uncertainties with $\beta = 9.5 \pm 3.5$ and $\log R = 1.6 \pm 0.6$ ($R = 5.2$). These values for the radial string cut-off $R \approx 4$ may seem lower than those anticipated for a periodicity scale given by $L = 32$. However, the maximum radius of curvature for a large amplitude perturbation is $R \lesssim L/4 = 8$, so half this scale for the effective radius is not unreasonable. Observing quadrupole radiation emanating from an oscillating global string heuristically indicates a delocalised process with radiation maxima appearing on a comparable scale (see Figure 4.4).

We conclude that the analytic inverse square model (4.39) offers an excellent description of an oscillating and radiating global string, predicting both the correct power law and

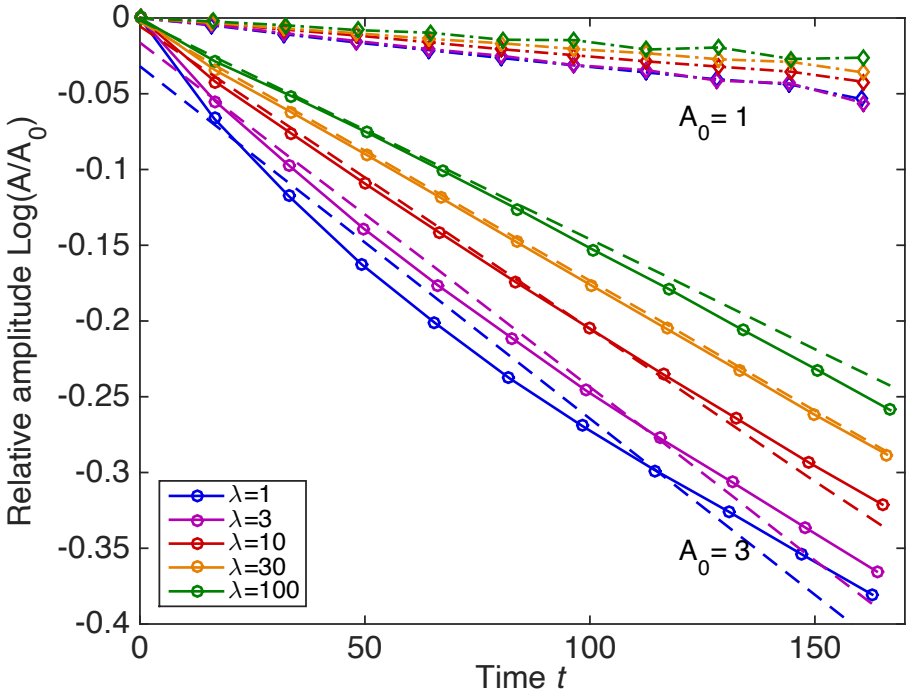

Fig. 4.20 The logarithm of the relative amplitude $\ln(A/A_0)$ for oscillating strings as a function of time t. The simple exponential decay model (4.40) does not match the observed behaviour with the decay rate strongly dependent on the initial amplitude A_0 (contrast the inverse square model Figure 4.18). The best fit lines (dashed) show clear deviations from exponential behaviour when there is larger damping at $A_0 = 3$.

magnitude of the radiation damping. Our results are consistent with the analytic damping rate $\beta = \pi^3/4 \approx 7.75$ and indicate an effective radial cutoff for the string $R \approx L/8$ ($\rho \equiv R/L \approx 0.12$), about half the string radius of curvature $L/4$. We also observe that finite width effects suppress radiative power in massless modes at small amplitudes comparable to the string width $A \sim \delta$. These AMR results have allowed us to probe the asymptotic small width regime for global strings, where dual radiation predictions from the Kalb-Ramond action (2.68) are shown to become increasingly accurate.

4.3.2 Exponential Damping

For comparison, we also endeavour to fit the oscillating string data for different λ to the simple exponential damping model (4.40). The analysis is plotted in Figure 4.20 using the logarithm of the relative amplitudes for different $\ln(A/A_0)$ as a function of time t. Although the leading-order behaviour is linear at small amplitude $A_0 = 1$, as it is also for the inverse square model (4.39), there are clearly significant deviations from exponential behaviour

at larger amplitude $A_0 = 3$ (with the best fit exponentials deviating from the measured amplitudes). More seriously, there is clearly a large decay rate dependence on the initial amplitude which is inconsistent with the simple model (4.40). Including an amplitude dependence ε_0^2 in the exponent improves the consistency of damping rates between the two amplitudes and so indicates that it may be applicable to situations with unequal left- and right-moving modes (see earlier discussion). For our sinusoidal solution here, with equal left- and right-moving modes, it is clear that the inverse square model (4.39) provides a better description of the observed damping behaviour.

Chapter 5

Massive Radiation

In this chapter, we present a detailed analysis of the massive radiation from adaptive mesh refinement simulations of global cosmic strings. Section 5.1 characterises the mode decomposition of the radiation, using the massive dispersion relation to determine its dependence on the mass threshold $m_H = \sqrt{\lambda}\eta$, as well as the string amplitude through the increased path length α. The radiation is further characterised by discussion of the different phase and group velocities, as well as the separation of the propagating modes from the string self-field. Section 5.2 presents detailed analysis of massive string radiation from the same simulations as described in Chapter 4, again with string widths spanning over an order of magnitude determined by $1 \leq \lambda \leq 100$ using the diagnostic tools presented in Section 3.4. This work is being prepared for a co-authored publication [175].

As previously, simulations in this section are carried out using `GRChombo` with a coarse simulation box size of $256 \times 256 \times 32$ ($N_1 \times N_2 \times N_3$) and the same boundary conditions, resolution and regridding parameters as outlined in Chapter 4; periodic boundary conditions in the z-direction and Sommerfeld boundary conditions in the x- and y- directions. In addition, approximately forty further simulations of global strings with finely spaced λ values from $0.3 \leq \lambda \leq 2.8$ are presented, with a typical spacing $\Delta\lambda \approx 0.1$, to allow comparison with the analytically determined mass thresholds. These primarily use a coarse simulation box size of $256 \times 256 \times 32$, but we also investigate configurations with $256 \times 256 \times 16$ in order to facilitate larger relative amplitudes with more highly relativistic string configurations.

5.1 Analytic Radiation Expectations

In this section, we determine the analytically predicted mode decomposition of massive radiation from global strings. We outline the properties of massive radiation, particularly the thresholds in λ that determine whether certain modes are able to propagate and their dependence on the string amplitude. We also describe its complex wavepacket structure, as well as outlining a method to analytically separate propagating radiation from self-field modes.

5.1.1 Massive Thresholds

We first recall from Section 4.1.1 that, by linear expansion of the field equations (2.10) around the vacuum state $|\varphi| = \eta = 1$ using $|\varphi| = 1 + \chi$, it can be demonstrated that radiation from global strings can be split into massless and massive components, where massive radiation obeys the Klein-Gordon equation

$$\frac{\partial^2 \chi}{\partial t^2} - \nabla^2 \chi + m_H^2 \chi = 0\,, \tag{5.1}$$

with $m_H = \sqrt{\lambda}\,\eta$. We further recall from Section 4.1.3 that the massless component can be decomposed into separable eigenmodes denoted by eigenvalues $\{pmn\}$, where p, m and n are positive integers used to denote the harmonics in t, θ and z respectively. Finally, we recall from equation (4.27) that the radial wavenumber κ_{pn} for each mode can be calculated as a function of the increased path length α, in order to determine whether or not a certain mode of radiation will propagate.

The radiation of massive modes from an oscillating global string is qualitatively different to massless radiation, due to the presence of the mass threshold $m_H = \sqrt{\lambda}\,\eta$. As demonstrated in Section 4.1, the periodic string solution (3.12) radiates into the lowest massless quadrupole mode $\{220\}$ for any initial amplitude. In contrast, massive modes must be sufficiently energetic to become propagating radiation with the lowest available mode depending on the mass threshold. This can be demonstrated similarly by deriving an expression for the massive radial wavenumber. Equation (5.1) can be rewritten in cylindrical coordinates as with the massless case, obtaining

$$\frac{\partial^2 \chi}{\partial t^2} - \frac{\partial^2 \chi}{\partial r^2} - \frac{1}{r}\frac{\partial \chi}{\partial r} - \frac{1}{r^2}\frac{\partial^2 \chi}{\partial \theta^2} - \frac{\partial^2 \chi}{\partial z^2} + m_H^2 \chi = 0\,. \tag{5.2}$$

This is again soluble using separable methods with an equivalent ansatz $\chi(t,r,\varphi,z) = T(t)R(r)\Theta(\theta)Z(z)$ to find asymptotic massive radiation modes in a similar form to the general massless solution (4.32). Substituting into (5.2), we obtain

$$\frac{T''(t)}{T(t)} - \frac{R''(r)+R'(r)/r}{R(r)} - \frac{1}{r^2}\frac{\Theta''(\theta)}{\Theta(\theta)} - \frac{Z''(z)}{Z(z)} + m_H^2 = 0\,. \tag{5.3}$$

Rearranging and substituting equivalent separation constants to the massless case, we obtain

$$\frac{R''(r)+R'(r)/r}{R(r)} - \frac{m^2}{r^2} = -\omega_p^2 + k_z^2 + m_H^2 = -k_r^2\,. \tag{5.4}$$

where we again have $\omega_p = 2\pi p/\alpha L = \Omega_z p/\alpha$ representing the p^{th} harmonic of the oscillating string, $k_z = \Omega_z n$ is the wavenumber in the z-direction and k_r is the radial wavenumber. From this, we deduce that the massive modes obey a modified version of the dispersion relation (4.27),

$$\omega_p^2 \;=\; k_r^2 + k_z^2 + m_H^2 \tag{5.5}$$

which, by analogy with equation (4.27), implies

$$k_r \equiv \Omega_z \kappa_{pn} = \Omega_z \sqrt{(p/\alpha)^2 - n^2 - m_H^2/\Omega_z^2}\,. \tag{5.6}$$

We can only have a radially propagating mode if k_r is real, so from (5.6), we obtain the expression for the lowest propagating harmonic

$$p_{\min} \;>\; \alpha\sqrt{m_H^2/\Omega_z^2 + n^2} \;\approx\; m_H/\Omega\,, \tag{5.7}$$

where in the last expression we have assumed that $L \gg m_H^{-1}$ and that α is close to unity. In principle, the quadrupole $\{pmn\} = \{p_{\min}20\}$ may be the lowest massive harmonic available at a given order p, but as we shall see in practice the dipole $\{p_{\min}11\}$ is favoured when also above threshold (see Figure 4.2).

We observe from equation (5.7) that, as λ increases and for a fixed L, a higher p_{min} is required to overcome the mass threshold and allow massive radiation to propagate. This effectively cuts off modes at lower frequencies, as they become evanescent. In order to determine the exact dependence of the massive spectrum on λ, equation (5.7) can be rearranged as follows:

$$\lambda < \lambda_{pn} = \left(\frac{2\pi}{L}\right)^2 \left(\frac{p^2}{\alpha^2} - n^2\right)\,, \tag{5.8}$$

where λ_{pn} is the threshold that λ must (perhaps counter-intuitively) be lower than for a given mode $\{pn\}$ to propagate.

5.1.2 Calculating α

In order to calculate the values of λ_{pn}, it is necessary to calculate the fractional increase in path length α of the displaced string relative to the periodicity in the z-direction, L. This is simply defined by $\alpha = T/L$, where T is the path length which also determines the period of oscillation of the string. To contextualise this calculation, we first recall from the static part of (3.12) that the solution for a displaced string in the Nambu-Goto model is given by the expression

$$\mathbf{X}(\sigma,\varepsilon) = \left(\varepsilon\cos\sigma, 0, \int_0^\sigma \sqrt{1-\varepsilon^2\sin^2\theta}\, d\theta\right), \tag{5.9}$$

where we have set $\Omega = 2\pi/T = 1$, the invariant amplitude ε with $0 \leq \varepsilon \leq 1$ and $0 \leq \sigma \leq 2\pi$ is a parameter along the string over a single period. As we are evolving the full field equations, it is not a given that this analytic solution is 'correct'. For this reason and for computational convenience, as previously discussed in Section 3.3.1, we use sinusoidal initial conditions which are then damped to an appropriate intermediate configuration, which may or may not correspond to either a sinusoidal or Nambu-Goto model. However, we note in any case that a sinusoidal model is approximately equivalent to the Nambu-Goto model at low amplitudes $\varepsilon \ll 1$. For these reasons, it is useful to calculate α directly for both models, which we expect to provide upper and lower bounds for the damped solution.

We begin by calculating α for the simpler case of a sinusoidal string. The string displacement in the x-direction from (3.16) is given by

$$\mathbf{X}(z) = (A\sin\Omega_z z, 0, z)\,. \tag{5.10}$$

We can determine the total path length T for one period of the sinusoidal string from the simple path integral

$$T_{\sin} = \int_0^L \sqrt{1+\left(\frac{\partial x}{\partial z}\right)^2}\, dz \tag{5.11}$$

$$= \int_0^L \sqrt{1+\Omega_z^2 A^2\cos^2\Omega_z z}\, dz\,, \tag{5.12}$$

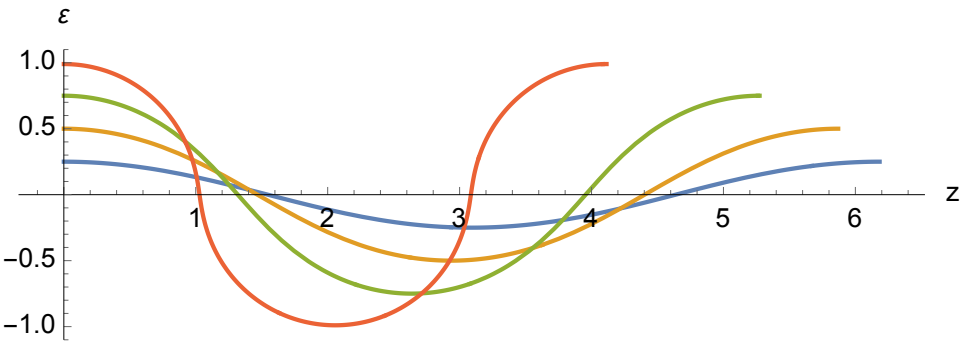

Fig. 5.1 Parametric plot of accurate Nambu-Goto string initial conditions for different amplitudes $\varepsilon = 0.25$ (blue), $\varepsilon = 0.5$ (yellow), $\varepsilon = 0.75$ (green) and $\varepsilon = 1$ (red).

where we integrate from $0 \leq z \leq L$. The increased path length α is then calculated simply as

$$\alpha_{\text{sin}} = \frac{1}{L}\int_0^L \sqrt{1+\Omega_z^2 A^2 \cos^2 \Omega_z z}\, dz\,. \tag{5.13}$$

In the sinusoidal case, the calculation of the increased path length is intuitive, as the path length $T_{\text{sin}} = T_{\text{sin}}(A)$ is a function of amplitude, with the z-periodicity being fixed at a constant L.

In the Nambu-Goto case (5.9), the calculation is less obvious due to the parametrisation by σ. The path length is calculated using the path integral

$$T_{\text{NG}} = \int_0^{2\pi} \sqrt{\left(\frac{\partial x}{\partial \sigma}\right)^2 + \left(\frac{\partial z}{\partial \sigma}\right)^2}\, d\sigma \tag{5.14}$$

$$= 2\pi\,, \tag{5.15}$$

where we integrate over $0 \leq \sigma \leq 2\pi$ for a single period. In this case, the string is fixed to be of parametric length 2π, so when the amplitude of the string is increased, the periodicity in z decreases accordingly. We therefore have the opposite situation to the sinusoidal case, which has a variable parametric path length that depends on the amplitude and fixed periodicity in z. Importantly, in the sinusoidal model, A can be chosen to have any value without changing the z-periodicity L, whereas for Nambu-Goto strings, $L = z(2\pi, \varepsilon)$ is analytically determined by the model via the fixed path length. This is demonstrated by Figure 5.1, which shows a parametric plot for four different invariant amplitudes $\varepsilon = 0.25, 0.5, 0.75$ and 1.0, demonstrating the decrease in $z(2\pi, \varepsilon)$ with increasing amplitude. From equation (5.9), the

periodicity L in z is given by

$$z(2\pi, \varepsilon) = \int_0^{2\pi} \sqrt{1 - \varepsilon^2 \sin^2\theta}\, d\theta\,, \qquad 0 \leq \varepsilon \leq 1\,. \tag{5.16}$$

The increase in path length α is then given by the ratio of the path length $T_{\rm NG}$ to the periodicity in the z-direction:

$$\alpha_{\rm NG} = \frac{T_{\rm NG}}{z(2\pi, \varepsilon)} \tag{5.17}$$

$$= \frac{2\pi}{\int_0^{2\pi} \sqrt{1 - \varepsilon^2 \sin^2\theta}\, d\theta}\,. \tag{5.18}$$

To compare with the sinusoidal model in the context of our fixed grid simulations, we need to compare α for different amplitudes A and a fixed z-periodicity L. Fixing L in the above Nambu-Goto model necessarily means that ε is determined by the model for a given A. We define $A_{\rm rel}$, the amplitude relative to the z-periodicity:

$$A_{\rm rel} = \frac{4A}{z(2\pi, \varepsilon)} = \frac{4A}{L}\,, \tag{5.19}$$

so that in the limit $A = L/4$, we have $A_{\rm rel} = \varepsilon = 1$. This equation is implicit in ε and must be solved numerically to find the desired ε such that $z(2\pi, \varepsilon) = L$.

Comparing values of α for different $A_{\rm rel}$ between the two models in Table 5.1, we observe that the additional path length contribution from the Nambu-Goto model compared to the sinusoidal approximation increases as $A_{\rm rel}$ increases, as predicted. We will see in Section 5.2 that this difference is significant when calculating λ_{pn} for the massive radiation.

5.1.3 Radiation Properties

Having derived an expression for the lowest propagating harmonic for a given amplitude and λ, we can now explore the properties of the propagating modes. Unlike massless radiation, it can be shown from the dispersion relation (5.5) that massive radiation has a separate phase velocity $v_{\rm ph}$ and group velocity $v_{\rm g}$,

$$v_{\rm ph} = \frac{\omega}{k}\,, \qquad\qquad v_{\rm g} = \frac{d\omega}{dk}\,, \tag{5.20}$$

Table 5.1 Fractional path length increase α for the Nambu-Goto ($\alpha_{\rm NG}$) and sinusoidal ($\alpha_{\rm sin}$) models for a range of relative amplitudes $A_{\rm rel}$.

$A_{\rm rel}$	α model	
	Sinusoidal $\alpha_{\rm sin}$	Nambu-Goto $\alpha_{\rm NG}$
0	1	1
0.1	1.00614	1.00616
0.25	1.0375	1.0382
0.5	1.13984	1.14909
0.75	1.28729	1.32541
0.875	1.37264	1.43739
0.95	1.42666	1.51362
1.0	1.4637	1.5708

with the latter representing the speed of energy transfer. The radial propagation velocity of the dominant massive modes will generally be considerably lower than the speed of light depending on how close the $p_{\rm min}$ harmonic is to the mass threshold. For example, for a string of unit mass ($\lambda = 1$) and oscillation periodicity $L = 32$ ($\Omega_z = 0.2$), the lowest propagating harmonic is $p_{\rm min} = 6$ with the quadrupole $\{6\,2\,0\}$ having $v_{\rm g} = 0.51$, and the dipole $\{6\,1\,1\}$ about 5% slower at $v_{\rm g} = 0.48$ (i.e. both at approximately half the speed of light). In principle, lower massive harmonics $p < p_{\rm min}$ will oscillate as evanescent waves, representing a 'self-field' (bound modes) moving with the string but not propagating away. However, the asymptotic evanescent modes predicted by (5.6) are exponentially suppressed on very short lengthscales, so any massive self-field modes present are better understood as a response to the long-range massless self-field (see next section).

Given that massive string radiation must typically be a high harmonic of the driving frequency Ω_z, we can expect its generation mechanism to be highly nonlinear and dependent on the self-interaction terms present in (4.3). With the fundamental frequency for our sinusoidal string solution generically well below the mass threshold $\Omega_z \lesssim m_H$, any radiation modes will be strongly suppressed given the high-order interactions required for their creation. For small oscillations $\varepsilon \ll 1$, we can expect the radiation amplitude to be suppressed as an exponential of the radiating harmonic p (or, alternatively, the string curvature scale R).[1] For this reason, we can anticipate that any massive radiation present will be strongly dominated by the lowest time harmonic available $p_{\rm min}$.

[1] Here, R is not to be confused with the extraction radius.

5.1.4 Separation from Self-Field

In addition to the propagating modes discussed above, we identify the presence of massive self-field modes in the massive mode equation (4.2) by substituting derivatives of the massless self-field (4.15) in the time-varying source term $\dot{\vartheta}^2 - (\nabla\vartheta)^2$ on the right hand side. We have argued already that the self-field dipole (4.16) from the time derivative term $\dot{\vartheta}^2$ is considerably larger than the radial derivative $(\partial\vartheta/\partial r)^2$, measured on a distant cylinder at fixed radius R (unlike propagating radial modes for which these terms cancel). However, we must also include contributions from the angular derivative $\partial\vartheta/\partial\theta$ and from the z-direction $\partial\vartheta/\partial z$. The leading source contribution is the static term r^{-2} arising from the angular derivative, already seen in (2.12), which means that ϕ approaches the vacuum state with an asymptotic power law $\phi \sim 1 - r^{-2}$, rather than exponentially as would be expected for a massive field. (We note that there are well-known radial oscillation modes in the string width and, in principle, these can create a small monopole mode.) The leading-order time-varying source contributions to the massive field equation (4.2) are then, using $\phi = 1 + \chi$ as in (4.5):

$$\begin{aligned} \frac{\partial^2\chi}{\partial t^2} - \nabla^2\chi \quad &= \quad -\tfrac{A_0^2\Omega_z^2}{4r^2}\,(1-\cos 2\theta)\sin 2\Omega_z t \\ &\quad + \tfrac{2A_0}{r^3}\cos\theta\,\sin\Omega_z z\,\sin\Omega_z t\,. \end{aligned} \tag{5.21}$$

The first source term arises directly from the square of the dipole term (4.16), so the time periodicity is that of the second harmonic, while $(\sin\theta)^2$ splits into monopole and quadrupole contributions, but with no z-dependence after adding $(\partial\vartheta/\partial z)^2$. The second line has a dipole cross term from $(\partial\vartheta/\partial\theta)^2$ which has the original time, angle and z-dependence of the string source (4.16). Given the simplicity of the linearised wave equation (5.21), the solutions (and first derivatives like Π_ϕ in (4.11)) will inherit the same t, θ and z-dependence as the right-hand side, whatever the resulting radial profile. This means that in any FFT analysis we can expect a non-propagating massive self-field to be present, contributing to the monopole $\{200\}$, quadrupole $\{220\}$ and dipole $\{111\}$ eigenmodes.

5.2 Massive Radiation Analysis

In this section, we present a quantitative analysis of the massive radiation from oscillating string configurations. We begin by presenting a detailed quantitative investigation of the massive radiation from $\lambda = 1$ and $\lambda = 10$ strings with small amplitude $A_0 = 1$ ($\varepsilon = 0.20$)

and larger amplitudes $A_0 = 4$ and $A_0 = 8$ ($\varepsilon = 0.68$ and 1). We again extract and Fourier decompose the radiation field Π_ϕ defined by equation (4.11) on a diagnostic cylinder at fixed radius $R = 64$. We subsequently perform a scan over $0.3 \leq \lambda \leq 2.8$ for λ spaced by $\Delta\lambda \approx 0.1$ to determine the λ-dependence of the massive spectrum, including the primary radiation modes and energy loss. For this finely spaced scan, we concentrate primarily on two relative amplitudes $A_{\rm rel} = 0.5$ from $A_0 = 4$ with $L = 32$ ($\varepsilon = 0.68$) and $A_{\rm rel} = 0.875$ from $A_0 = 3.5$ with $L = 16$ ($\varepsilon = 0.96$), where $A_{\rm rel}$ is defined by (5.19).

5.2.1 Mode Decomposition

As anticipated from the discussion in Section 5.1, the massive radiation from global strings is considerably more complex than the massless radiation presented in Chapter 4. A quantitative description of massive string radiation is therefore numerically challenging, and even AMR simulations are not a straightforward panacea. The massive radiation frequency, determined by $p_{\rm min}$, is a high harmonic of the fundamental frequency Ω, so this nonlinear process is highly sensitive to numerical resolution. This is particularly noticeable for string configurations where the massive signal is expected to be exponentially suppressed, at small amplitude $A_0 \to 0$ or at large mass $\lambda \gg 1$, where more regridding does not lead obviously to improved convergence. In practice, the energy loss from massive radiation is very suppressed for quasilinear string configurations. However, mesh regridding can lead to high frequency modes being generated and becoming trapped on finer grids near the string, a process which can lead to further radiation growth due to stimulated emission or resonance. This effect has been discussed further in detail in Section 3.2. We present massive radiation results for the two string widths $\lambda = 1$ and $\lambda = 10$, using the same simulation and damping parameters as in Chapter 4, for amplitudes $A_0 = 1$, 4 and 8 in regimes minimising these trapping effects.

The qualitatively different nature of massive radiation can be demonstrated clearly by visualising the massive diagnostic Π_ϕ in three dimensions. Taking $\lambda = 1$ and the intermediate amplitude $A_0 = 4$ as a representative example, the signal is illustrated in Figure 5.2, with the time evolution of the same signal extracted on the diagnostic cylinder shown in Figure 5.3. Although the radiation is predominantly dipole, the spectrum is significantly more complex than the massless quadrupole radiation from the same configuration shown in Figure 4.4, where this is also particularly evident in animations. It can be seen particularly in Figure 5.2 that the different phase and group velocities lead to short wavelength modes travelling rapidly forward within larger, slower-moving outgoing wavepackets.

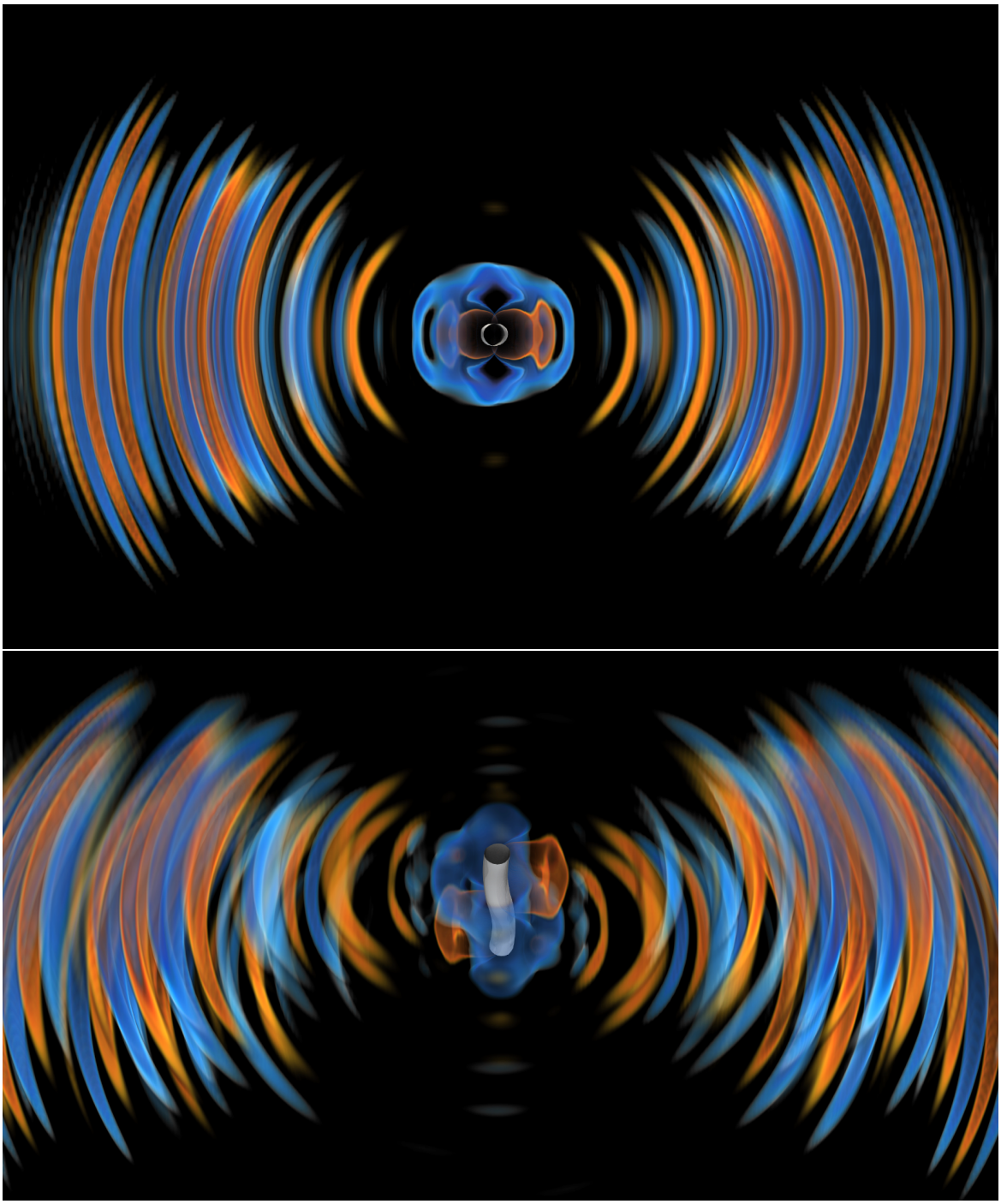

Fig. 5.2 Volume rendering in 3D space (x, y, z) of the massive radiation Π_ϕ from a $\lambda = 1$ string with initial amplitude $A_0 = 4$. The lowest propagating dipole eigenmode $\{pmn\} = \{6\,1\,1\}$ is dominant, but the different phase and group velocities give rise to a more complex structure of outgoing wavepackets.

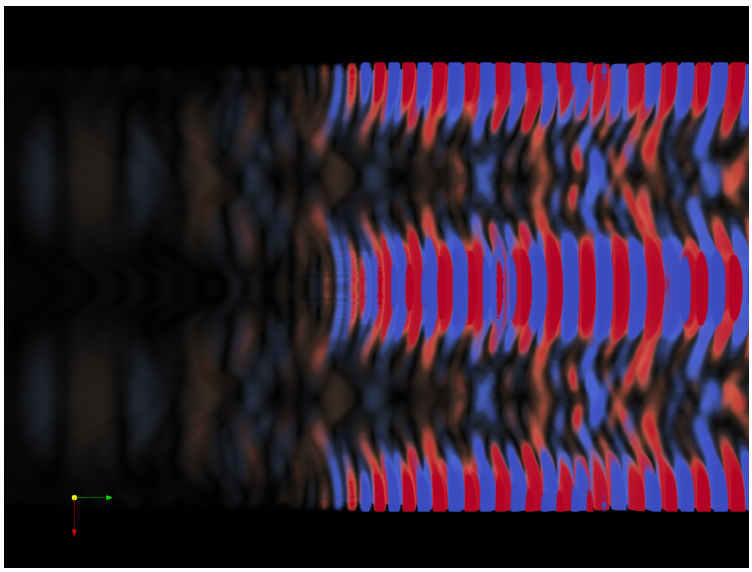

Fig. 5.3 Volume rendering in spacetime (t,θ,z) of the massive radiation Π_ϕ from a $\lambda = 1$ string with initial amplitude $A_0 = 4$ over time, measured on a cylinder at $R = 64$. The time axis runs left to right and azimuthal angle θ from bottom to top. The dipole $\{pmn\} = \{611\}$ is the dominant mode.

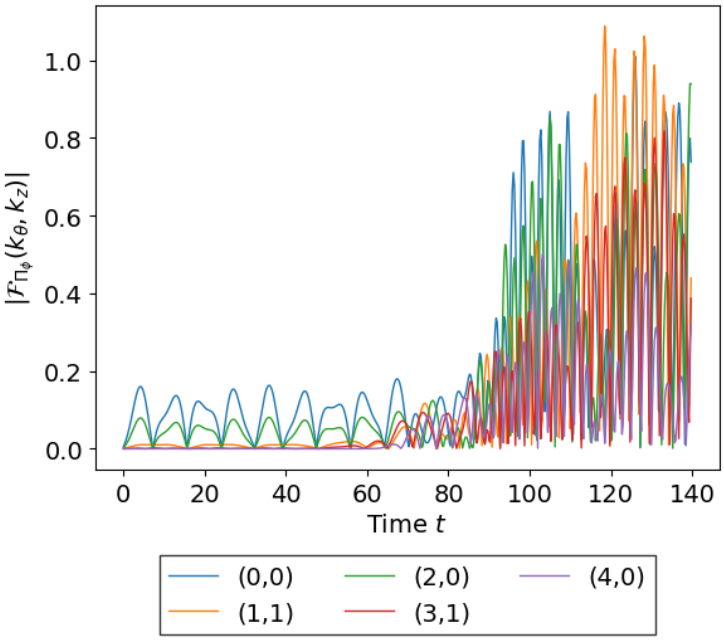

Fig. 5.4 Plot of the absolute value of the $\{mn\} = \{00\},\{11\},\{20\},\{31\}$, and $\{40\}$ Fourier modes of the massive radiation Π_ϕ from a $\lambda = 1$ string with initial amplitude $A_0 = 4$, measured on a cylinder at $R = 64$. The propagating radiation modes are $\{pmn\} = \{600\}$, $\{611\}$, $\{620\}$, $\{631\}$, and $\{640\}$, but we note also the initial presence of oscillating self-fields, $\{111\}$, $\{200\}$ and $\{220\}$.

We undertake a Fourier analysis of the massive radiation signal Π_ϕ on the diagnostic cylinder at $R = 64$ to quantify the effects described above. The time evolution of the largest amplitude eigenmodes is plotted in Figure 5.4 for $\lambda = 1$ and $A_0 = 4$, obtained using the same method as for the massless modes in Chapter 4. Measuring the time-dependence of the signals to obtain the value of the p harmonic, the dominant dipole eigenmode is $\{611\}$, with the $p = 6$ time-dependence consistent with the requirement that the frequency be above the (5.7) mass threshold, given approximately by $p > p_{\min} \approx 2\pi/L\sqrt{\lambda} \approx 5.1$ for $L = 32$. Altogether, we identify the massive propagating modes $\{600\}$, $\{611\}$, $\{620\}$, $\{631\}$ and $\{640\}$, as well as the long-range self-field excitations $\{111\}$, $\{200\}$ and $\{220\}$ sourced by the massless self-field, as discussed in the previous section. This means that despite having the appearance of a simple dipole in Figure 5.2, the radiation signal is in fact more complex, with monopole and quadrupole modes also present at comparable magnitude. One explanation for this apparent difference is that the radiation pattern is observed to be somewhat 'beamed,' requiring a combination of modes to achieve angular localisation in comparison with the pure $\{111\}$ dipole in Figure 4.2. Finally, we observe that the radiation propagation velocity $v_g \approx 0.5$ measured from first arrival agrees with the predicted $v_g = 0.48$.

Having investigated the radiation from $A_0 = 4$, we further analyse $A_0 = 1$ and $A_0 = 8$ for $\lambda = 1$ to determine the dependence on amplitude of high-order harmonics. Figure 5.5 shows the magnitude of all measured eigenmodes for $A_0 = 1, 4$ and 8. We observe that at small amplitude, only dipole radiation and self-field modes are present, but as the configurations probe higher (nonlinear) amplitudes as $\varepsilon \to 1$, higher frequency modes become activated and a checkerboard pattern emerges. The $m+n$ *even* selection rule applies as for the massless radiation modes in Figure 4.7, although the distribution of modes is quite different, being more constrained in the z-direction. There is also a much more nonlinear dependence of the total magnitude on the amplitude A, as can be observed from the different logarithmic scales required for each case compared to Figure 4.7, where the magnitude of the modes is approximately independent of amplitude. However, despite opening up more massive decay modes as $\varepsilon \to 1$, the total energy loss through massive radiation relative to the massless channel remains highly suppressed.

The additional complexity and challenge of higher order massive radiation is further illustrated by considering the spectrum for larger λ. The radiation pattern shown in Figure 5.6 is emitted by low amplitude $A_0 = 1$ for $\lambda = 10$. Overall, the signal has a significantly smaller magnitude and a higher $p_{\min}$ as, unlike massless radiation which is independent of λ to leading order, massive radiation becomes more strongly suppressed as λ increases

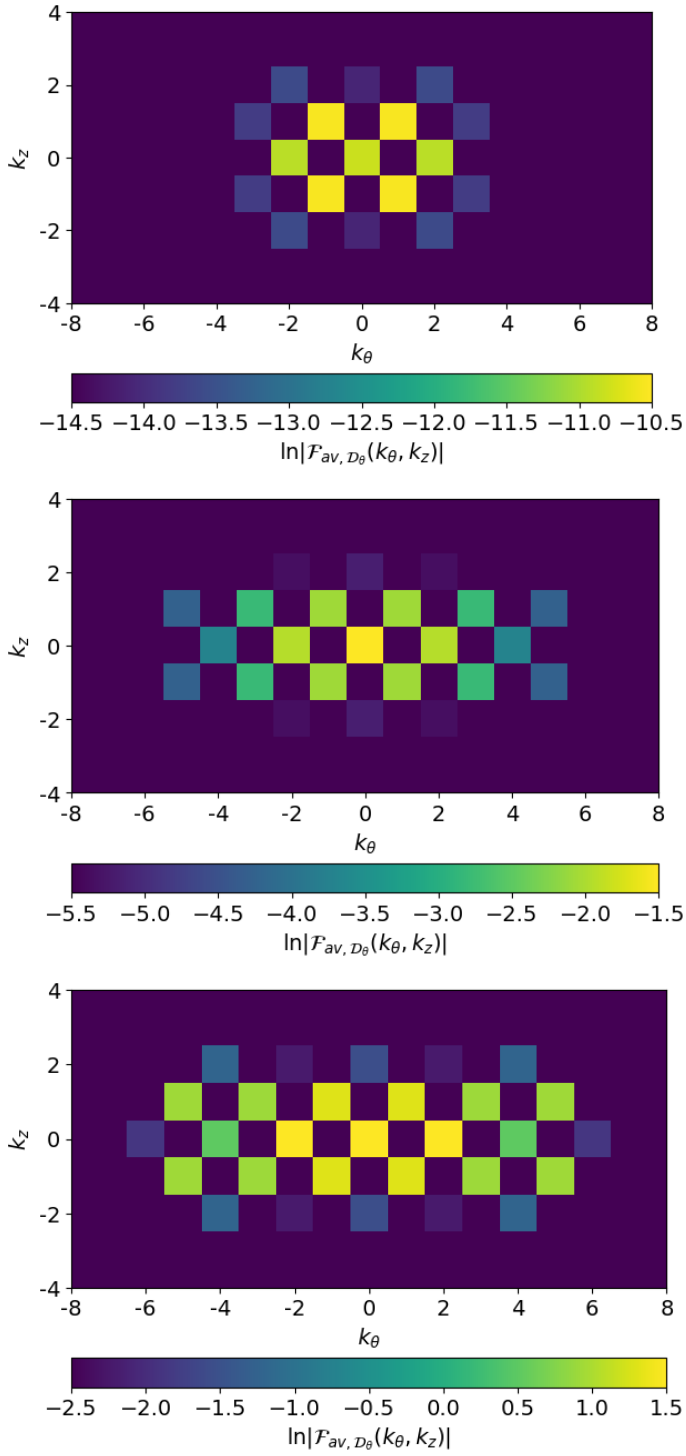

Fig. 5.5 Logarithmic plot of the 2D Fourier eigenmode amplitudes of the massive radiation Π_ϕ from a $\lambda = 1$ string at late time $t = 140.75$, measured on a cylinder at $R = 64$ and time averaged over approximate period $\Delta t = 33/4$. The horizontal axis is the angular eigenvalue m, while the vertical is the z-dependent wavenumber n. The top figure is for an initial amplitude $A_0 = 1$, the middle is for intermediate $A_0 = 4$ and the bottom is large $A_0 = 8$, showing an increasing trend of higher harmonics and a significant increase in amplitude, highlighted by the changing scales.

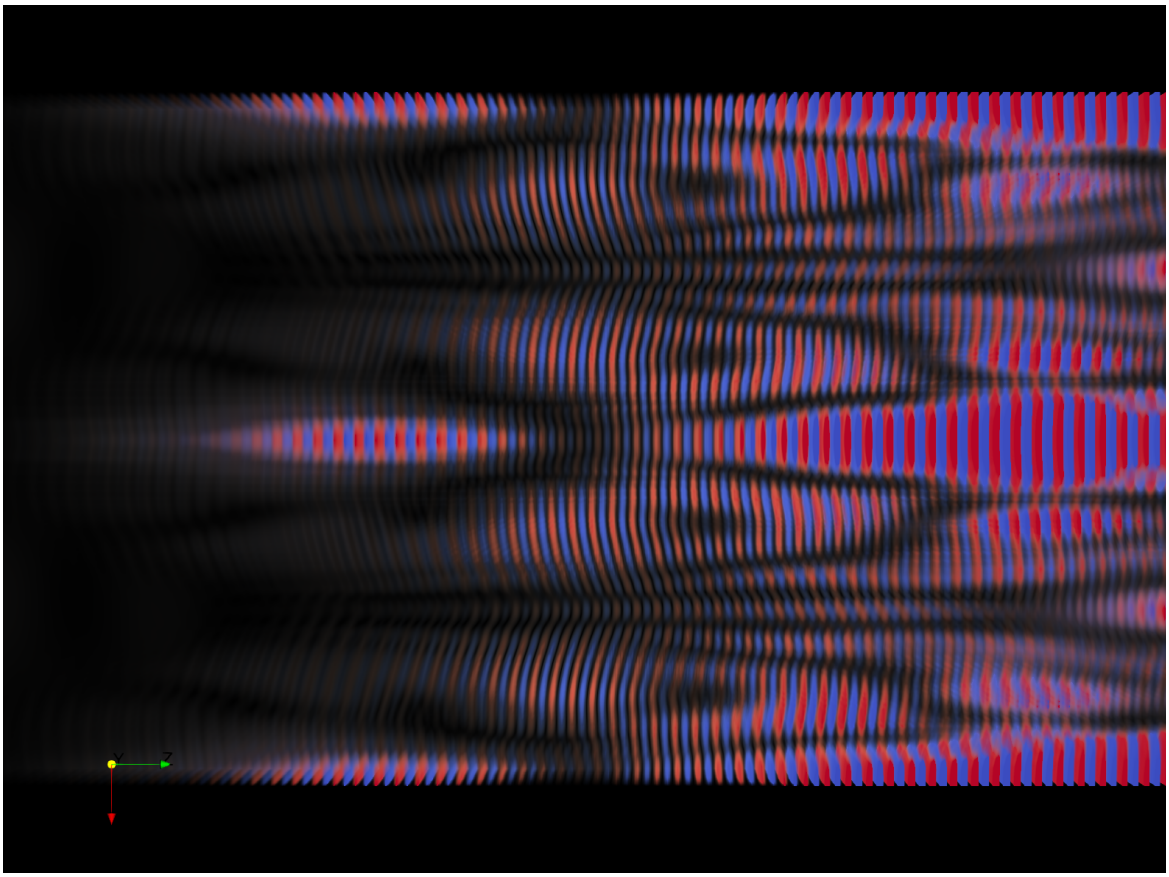

Fig. 5.6 Volume rendering in spacetime (t, θ, z) of the massive radiation Π_ϕ from a $\lambda = 10$ string with initial amplitude $A_0 = 1$ over time, measured on a cylinder at $R = 64$. The time axis runs left to right and azimuthal angle θ from bottom to top. Complex resonant patterns characterise the radiation.

(see equation (5.7)). At this low amplitude, it is difficult to characterise the radiation, as it becomes significantly more complex and more susceptible to numerical effects due to the high level of refinement required. The signal begins as an isolated dipole with a $\{1711\}$ mode contribution ($p_{\min} \approx 16.1$).[2] We later begin to observe resonant effects introducing higher angular harmonics including $m = 2, 3, 4$ which interchange amplitudes and generally increase during the simulation, with the quadrupole mode $\{1720\}$ becoming comparable in magnitude to the dipole. Due to the dependence on numerical resolution, this behaviour may not necessarily be robust to changes in the adaptive mesh, meaning that aspects of the spectrum may be unphysical. However, in this case we note that the massive amplitude is

[2] Again, the p harmonic is determined by considering the mode decomposition in a similar way to Figure 5.4.

$\sim 300\times$ smaller than the corresponding massless radiation signal, so has a negligible effect on string motion.

5.2.2 Relative Energy Loss to Massive and Massless Modes

To determine the energy loss via massive radiation in comparison to massless, it is necessary to calculate a quantitative estimate of the magnitude of the dominant modes. We have already observed from Figure 4.3 that for the simulations studied in Chapter 4, the massive radiation was so negligible as not to be noticeable as a contribution to the total energy loss. Figures 5.7 and 5.8 show the time-average for the six strongest modes for $\lambda = 1$ and $\lambda = 10$ strings for initial amplitudes $A_0 = 4$ and $A_0 = 8$ respectively, with the time-average calculated in the same way as in Chapter 4. The configuration with $A_0 = 1$ is omitted, as it is deemed to be too severely affected by numerical artefacts. We observe for both amplitudes that there is a difference in scale of $\sim 3000\times$ (noting the natural logarithmic scale) between the magnitude of the most dominant modes for $\lambda = 1$ and $\lambda = 10$, with the $\lambda = 10$ radiation heavily suppressed as predicted by the increase in mass threshold. Comparing to the massless radiation in Figure 4.11, we observe that the magnitude of the massless modes for $\lambda = 1$ and $A_0 = 4$ is also $\sim 3000\times$ larger than the massive modes, meaning that radiation via massive radiation can effectively be taken to be negligible. This ratio is even more extreme for $\lambda = 10$, where we observe a difference of $\sim 10^7\times$. The comparison with the massless modes in Figure 4.14 for $A_0 = 8$ is less extreme, where we have a factor of only $\sim 400\times$ between the massless and massive modes for $\lambda = 1$. This is due to the fact that the higher initial amplitude corresponds to more relativistic string oscillations and larger accelerations, allowing the massive modes to be activated more easily.

We have determined that the massive radiation is typically negligible as an energy loss mechanism for the configurations described above, particularly for high λ and low amplitude ε. However, it is possible for energy loss from massive modes to compete with massless modes for very relativistic configurations with curvature comparable to the string width, i.e. in the opposite limit with low λ and high ε. This makes it easier to activate massive modes, due to the lower mass threshold and more relativistic motion. Figure 5.9 shows the massive and massless components of the Poynting diagnostic (4.14), $\Pi_\phi \mathscr{D}\phi$ and $\Pi_\vartheta \mathscr{D}\vartheta$, integrated over the diagnostic cylinder for a highly relativistic $\lambda = 0.8$ string with $A_0 = 6$ and z-dimension $L = 16$. We observe that the energy emitted via massive radiation is of a comparable magnitude to the massless channel, until some boundary reflections and resonance effects begin to affect the spectrum at $t \approx 200$. This is likely to be relevant to fixed

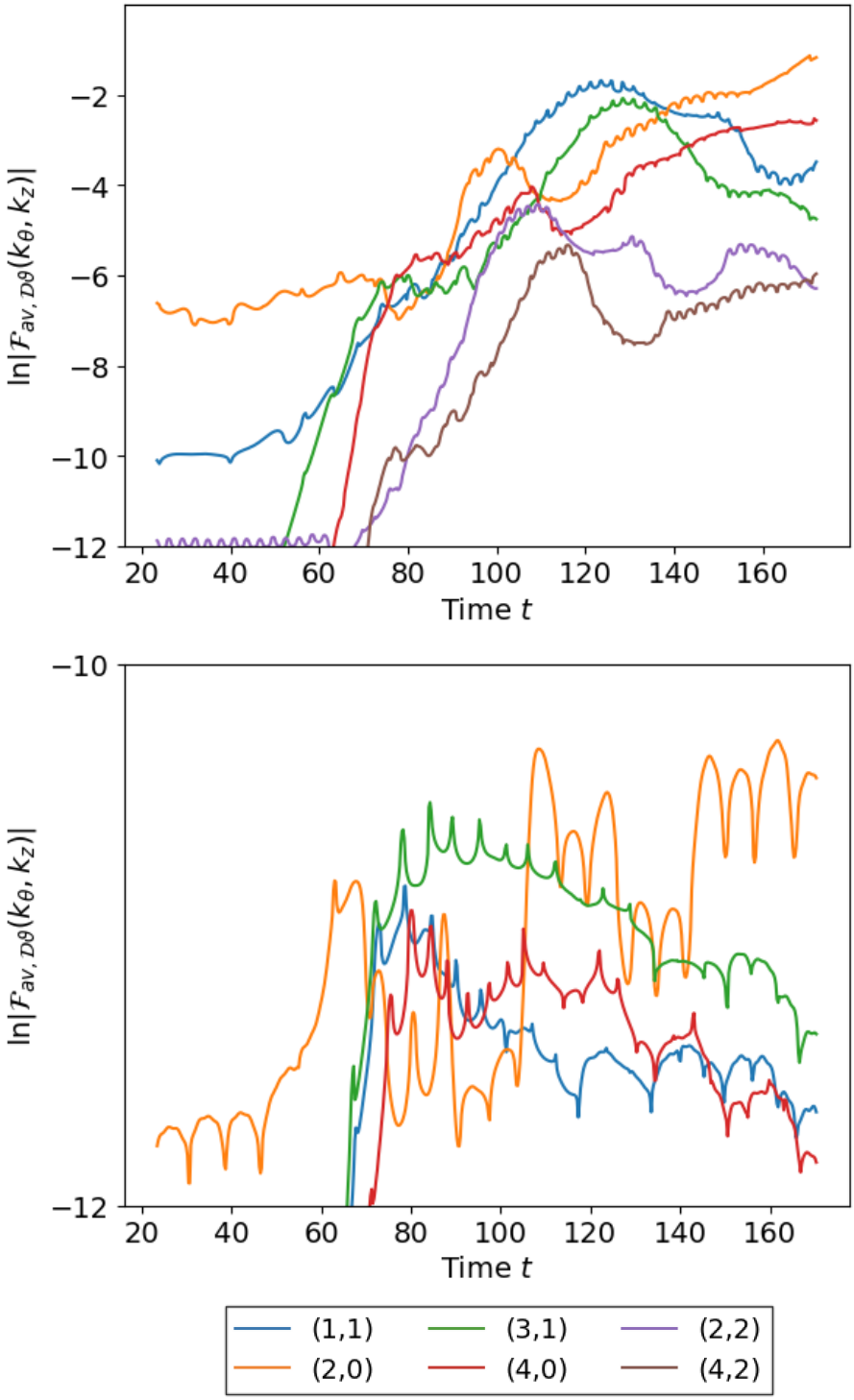

Fig. 5.7 Logarithmic plots of the dominant 2D Fourier modes of the massive radiation Π_ϕ from a $\lambda = 1$ (top) and $\lambda = 10$ (bottom) string with initial amplitude $A_0 = 4$, measured on a cylinder at $R = 64$ and time averaged over approximate period $\Delta t = 33/4$.

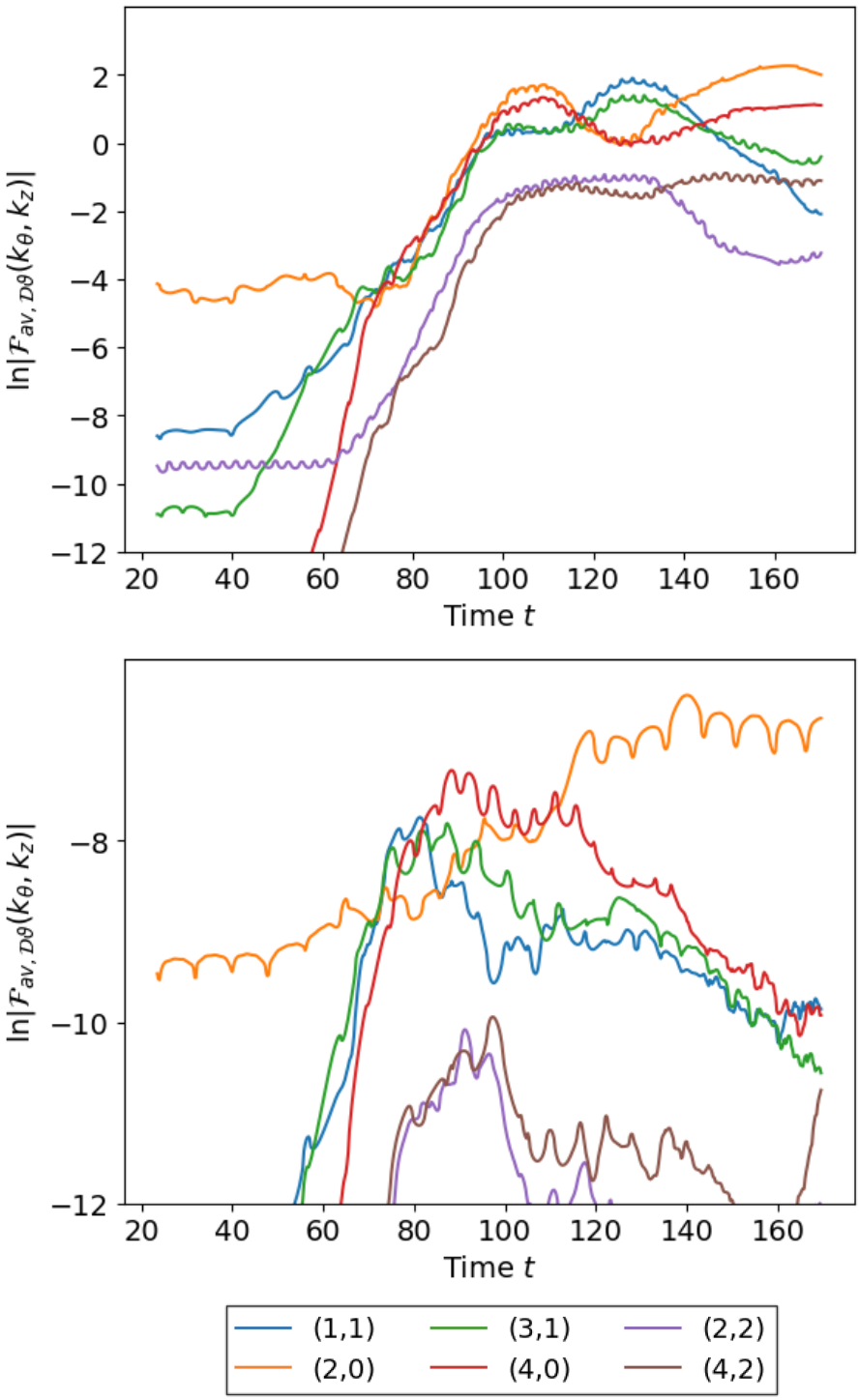

Fig. 5.8 Logarithmic plots of the dominant 2D Fourier modes of the massive radiation Π_ϕ from a $\lambda = 1$ (top) and $\lambda = 10$ (bottom) string with initial amplitude $A_0 = 8$, measured on a cylinder at $R = 64$ and time averaged over approximate period $\Delta t = 33/4$.

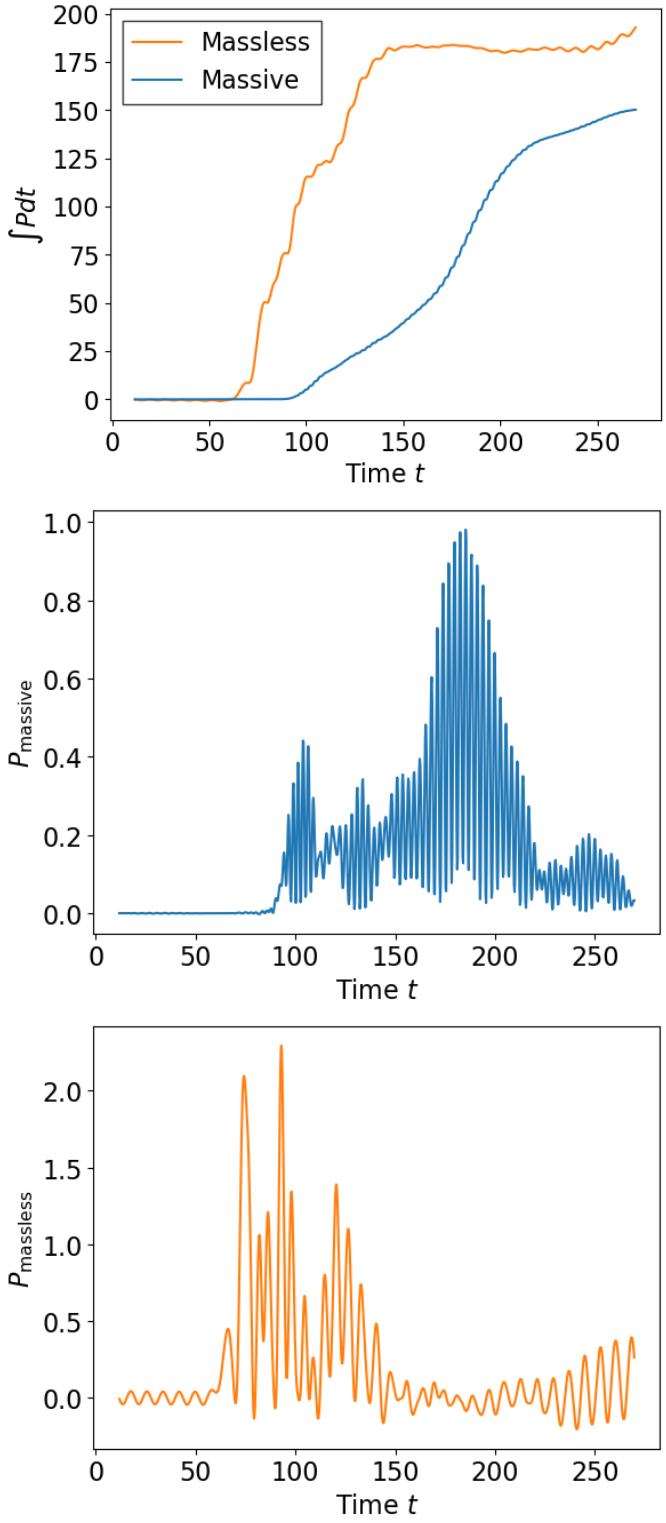

Fig. 5.9 Plots of the massive and massless radiation emitted from a $\lambda = 0.8$ string with amplitude $A_0 = 6$ and $L = 16$, effectively giving $\varepsilon > 1$, a highly relativistic configuration. The top graph shows the cumulative integrated massive and massless components of the Poynting vector, $\Pi_\phi \mathscr{D}\phi$ and $\Pi_\vartheta \mathscr{D}\vartheta$ (4.14), on the diagnostic cylinder at $R = 64$ over time. The middle and bottom graphs show the massive and massless components respectively integrated over the diagnostic cylinder and plotted over time.

comoving width simulations, which have a low effective λ. These implications are discussed in Chapter 7.

5.2.3 Radiation Harmonics and λ-Dependence

Having analysed massive radiation in depth for $\lambda = 1$ and 10, in this section we scan over a range of $0.3 \leq \lambda \leq 2.8$ to determine the more detailed λ-dependence of the massive spectrum. We concentrate primarily on two amplitudes $A_{\text{rel}} = 0.5$ ($A_0 = 4$ with $L = 32$) and $A_{\text{rel}} = 0.875$ ($A_0 = 3.5$ with $L = 16$).

Using the relationship derived in equation (5.8), we calculate the λ_{pn} threshold values at which the lowest p harmonic, p_{min}, that can be activated for a certain amplitude changes. These values are presented in Table 5.2a for $A_{\text{rel}} = 0.5$ and Table 5.2b for $A_{\text{rel}} = 0.875$. Both tables consider two models for the fractional increased path length α; the Nambu-Goto model α_{NG} calculated numerically using equation (5.17) and the sinusoidal model α_{sin} using equation (5.13). For each model, we obtain different λ_{pn} values for each p_{min} and for different values of n. Taking a $\lambda = 1.8$ string with $A_{\text{rel}} = 0.875$ as an example, from the Nambu-Goto model we obtain $\alpha_{\text{NG}} = 1.437$, which gives for the dipole $(n = 1)$ mode $p_{min} = 6$, but $p_{min} = 5$ for the quadrupole $(n = 0)$ mode. For the same configuration using the sinusoidal model, we obtain $\alpha_{\text{sin}} = 1.373$, which gives $p_{min} = 5$ for both the $n = 1$ and $n = 0$ modes. This means that in practice, there are a range of potential λ_{pn} for each p_{min} due both to the theoretical uncertainty about the appropriate α model and the range of available n modes.

An example of a change of the dominant radiative mode is presented in Figure 5.10, which shows the Fourier mode decomposition for $\lambda = 0.8$ and 2.0, again for $A_{\text{rel}} = 0.875$. We clearly observe that the Fourier decomposition of the radiation changes depending on λ; $\lambda = 0.8$ radiates primarily in the $\{1\,1\}$ dipole mode, but $\lambda = 2$ primarily in the $\{2\,0\}$ quadrupole mode. This corresponds with the thresholds in Table 5.2b; $\lambda = 0.8$ lies below the dipole threshold values for p_{min} for all models, whereas $\lambda = 2$ lies between the dipole and quadrupole thresholds for the sinusoidal model for $p_{min} = 5$. We also observe that the frequency of the modes increases and the magnitude of the radiation decreases as λ increases. We note that the use of the string wavelength $L = 16$ in Table 5.2b provides easier access to lower p_{min} compared with $L = 32$ in Table 5.2a, as well as a larger difference in λ_{pn} between the dipole and quadrupole thresholds.

Table 5.2 λ-dependence of p_{min} for the dipole ($n = 1$) and quadrupole ($n = 0$) Fourier modes for strings with initial amplitude $A_0 = 4$ and wavelength $L = 32$, characterised by $A_{\rm rel} = 0.5$, and initial amplitude $A_0 = 3.5$ and wavelength $L = 16$ with $A_{\rm rel} = 0.875$. Two models for α are considered, the Nambu-Goto model $\alpha_{\rm NG}$ calculated using equation (5.17) and the sinusoidal model $\alpha_{\rm sin}$ using equation (5.13). Strings radiate primarily into the Fourier mode p_{min} when $\lambda < \lambda_{pn}$, its corresponding threshold. As λ is increased, the value of p_{min} also increases, so lower frequency modes become unavailable.

p_{min}	λ_{pn}			
	$\alpha_{\rm NG} = 1.15$		$\alpha_{\rm sin} = 1.14$	
	$n = 1$	$n = 0$	$n = 1$	$n = 0$
3	0.224	0.262	0.228	0.267
4	0.428	0.466	0.436	0.475
5	0.690	0.729	0.703	0.742
6	1.011	1.049	1.029	1.068
7	1.390	1.428	1.415	1.454
8	1.827	1.866	1.860	1.899
9	2.323	2.361	2.364	2.403

(a) $A_{\rm rel} = 0.5$, $L = 32$

p_{min}	λ_{pn}			
	$\alpha_{\rm NG} = 1.437$		$\alpha_{\rm sin} = 1.373$	
	$n = 1$	$n = 0$	$n = 1$	$n = 0$
2	0.145	0.299	0.173	0.327
3	0.518	0.672	0.582	0.736
4	1.041	1.195	1.155	1.309
5	1.713	1.867	1.891	2.045
6	2.534	2.688	2.791	2.945
7	3.505	3.659	3.854	4.008

(b) $A_{\rm rel} = 0.875$, $L = 16$

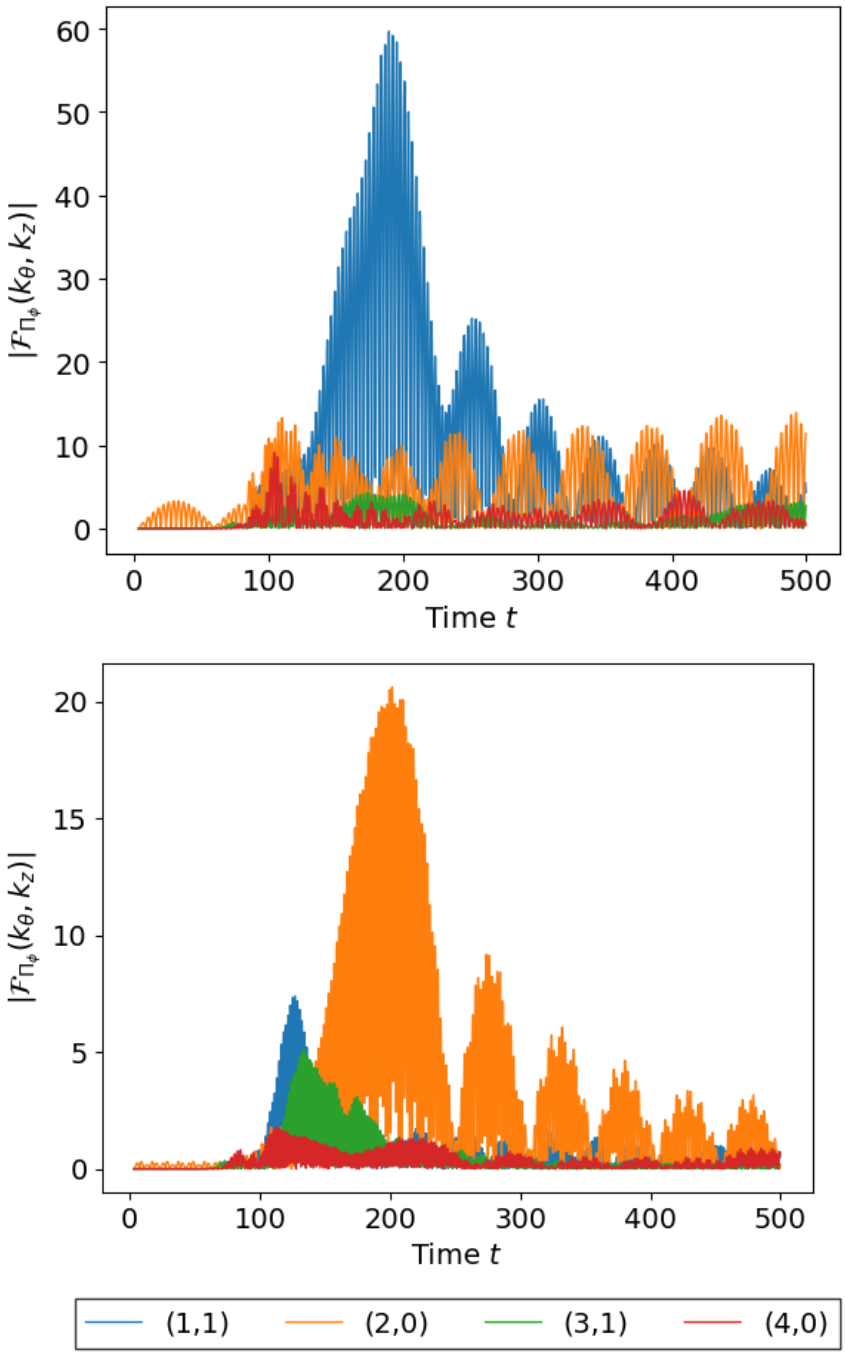

Fig. 5.10 Plot of the absolute value of the $\{mn\} = \{00\}, \{11\}, \{20\}, \{31\}$, and $\{40\}$ Fourier modes of the massive radiation Π_ϕ from strings with $A_{\text{rel}} = 0.875$, measured on a cylinder at $R = 64$ for $\lambda = 0.8$ (top) and $\lambda = 2$ (bottom). Although dipole radiation usually dominates, as in the $\lambda = 0.8$ case, the mass threshold λ_{p0} for quadrupole radiation for a given p is higher than for dipole modes (i.e. easier to satisfy $\lambda < \lambda_{pn}$), as shown in Table 5.2b. The quadrupole mode can therefore be dominant in some tuned cases, as shown for $\lambda = 2$.

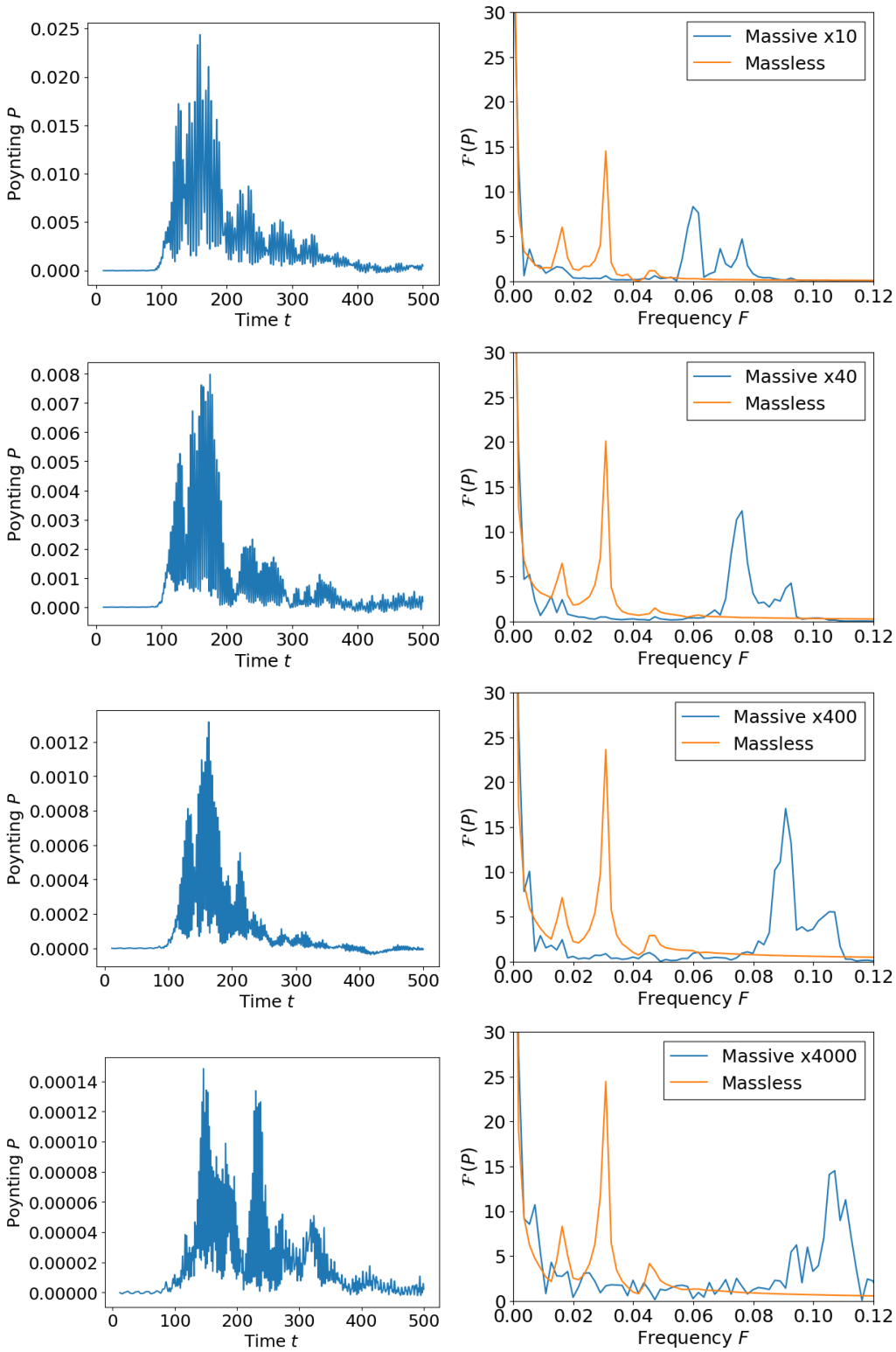

Fig. 5.11 Plots of the massive field $\Pi_\phi \mathscr{D}\phi$ integrated over a diagnostic extraction cylinder at $R = 64$ over time (left), with the corresponding Fourier mode decomposition for the massive and massless modes (right), for $A_{\text{rel}} = 0.5$. From top to bottom, we have $\lambda = 0.4$, $\lambda = 0.6$, $\lambda = 0.9$ and $\lambda = 1.2$. To obtain the Fourier decomposition graphs on the right, the signal on the left has been integrated from $t = 90$ to 228 to capture the initial burst of signal, whilst minimising effects of radiation reflected from the boundaries. We note the change in scale of the massive radiation for each λ by a ratio indicated in the legend.

In order to test the accuracy of the λ_{pn} threshold predictions, we qualitatively analyse the emitted massive spectra from the $A_{\text{rel}} = 0.5$ and $A_{\text{rel}} = 0.875$ configurations. Figure 5.11 shows results obtained for $A_{\text{rel}} = 0.5$, where the λ values plotted have been chosen to lie between the p_{min} threshold values λ_{pn} in Table 5.2a; $\lambda = 0.4, 0.6, 0.9$ and 1.2. The left column of Figure 5.11 shows the massive part of the Poynting diagnostic from equation (4.14), $\Pi_\phi \mathscr{D}\phi$, integrated over the diagnostic cylinder for the chosen λ values and plotted over time from $0 \leq t \leq 500$. We first observe that the frequency of the radiation increases as λ increases, although this is difficult to see directly from the data due to the high frequencies. We further note that the maximum magnitude of the radiation decreases as λ increases, as expected from the increasing mass threshold.

We can extract more detailed quantitative information about these general trends by performing Fourier transforms on the extracted signals. To the right of each of the time domain graphs in Figure 5.11 is the corresponding Fourier transform of the same massive diagnostic, as well as of the corresponding massless signal, $\Pi_\vartheta \mathscr{D}\vartheta$. These Fourier transforms are not taken of the entire plotted signal, due to the possibility of reflections from the simulation boundaries being erroneously included in the analysis. Instead, we choose an appropriate time interval over which to integrate. This is not a straightforward choice, as observing the massive diagnostic over time, we see that the length of the initial signal varies significantly and in some cases unpredictably between λ. We choose to integrate from $90 \leq t \leq 228$, judging by the extracted signals that this is sufficient to capture the initial burst without including artificial reflections from boundaries. We also note that this is equivalent to approximately eight periods of oscillation of the strings.

The Fourier transforms in Figure 5.11 provide a very clear picture of the mode decomposition of the massive signal for $A_{\text{rel}} = 0.5$ and $L = 32$. We first note that the massless signal in each case radiates primarily into the $p = 2$ harmonic, as determined from Fourier decomposition in Figure (4.11), along with a smaller $p = 1$ signal. This provides a very clear benchmark against which the massive signals can be compared. We clearly observe the increase in the massive p_{min} as λ increases, and can deduce the values by comparison with the massless peak. In order to be consistent with the model outlined in Section 5.1, we expect p_{min} to take integer values, increasing stepwise as the minimum radiative mode increases with λ. We observe $p_{min} = 4, 5, 6$ and 7 for $\lambda = 0.4, 0.6, 0.9$ and 1.2 respectively, agreeing with the predicted λ_{pn} presented in Table 5.2a. We further note that, as predicted, the massive peak is not a clean signal, often comprising of a double peak. This is consistent with the different λ_{pn} predicted for different n harmonics.

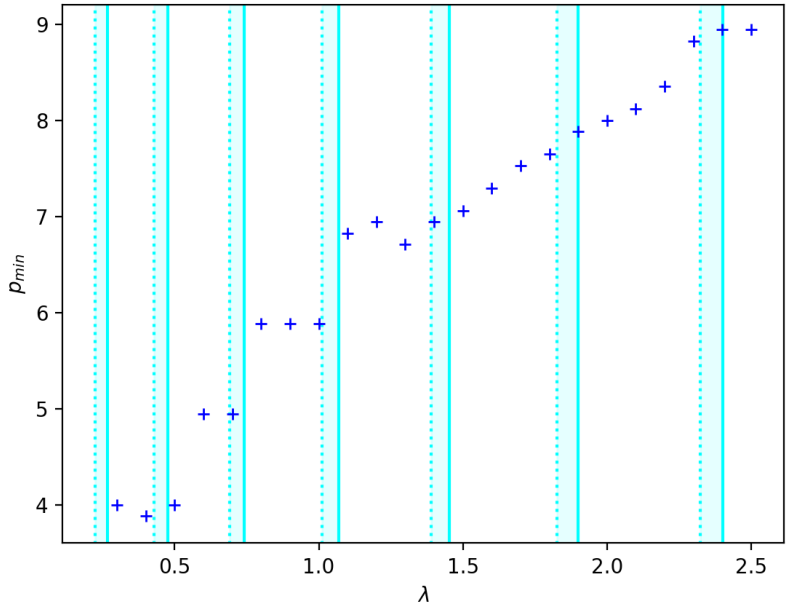

Fig. 5.12 Plots of the measured p_{min} against λ for massive radiation from string configurations with $A_{\text{rel}} = 0.5$. The graph summarises data from approximately twenty simulations. Shaded regions in cyan show the predicted thresholds λ_{pn} from Table 5.2a, where the shading encompasses the dependence on α and n; the solid cyan line represents the highest predicted λ_{pn}, coming from the α_{sin} model with $n = 0$ for each p and the dashed cyan line is the lowest reasonable λ_{pn}, coming from α_{NG} with $n = 1$. We observe four clear harmonic suppression thresholds before the radiation becomes so weak that it becomes dominated by numerical precision errors.

Figure 5.12 shows the ratio of the measured massive peak p_{min} normalised against the quadrupole $p = 2$ massless peak for $0.3 \leq \lambda \leq 2.8$ spaced by $\Delta\lambda \approx 0.1$, for $A_{\text{rel}} = 0.5$. Measured p_{min} values are obtained by numerically extracting the position of the peak of the Fourier transform of the massive signal from Figure 5.11. We indicate the predicted thresholds λ_{pn} from Table 5.2a using shaded regions to encompass the dependence on the α model and n harmonic. We observe the presence of distinct thresholds as predicted in Section 5.1 corresponding to the predicted integer values of p_{min} as expected until $\lambda \approx 1.5$, where the levels begin to become less distinct and merge together. This provides strong evidence for the underlying mechanism for radiation into massive modes being via higher harmonic excitations of the fundamental mode of string oscillation. We also note that the thresholds correspond more closely with the sinusoidal model of the path length than the Nambu-Goto model.

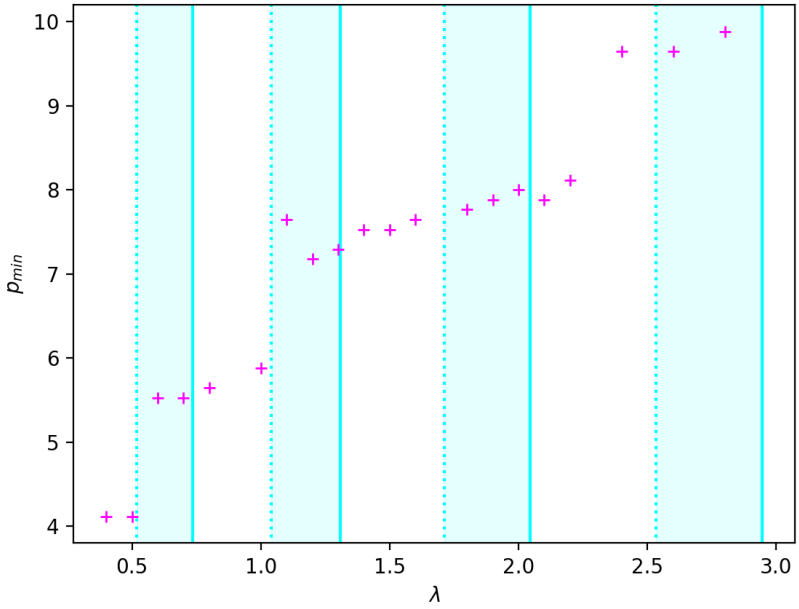

Fig. 5.13 Plots of the measured p_{min} against λ for massive radiation from string configurations with $A_{\text{rel}} = 0.875$. The graph summarises data from approximately twenty simulations. Shaded regions in cyan show the predicted thresholds λ_{pn} from Table 5.2b, where the shading encompasses the dependence on α and n; the solid cyan line represents the highest predicted λ_{pn}, coming from the α_{sin} model with $n = 0$ for each p and the dashed cyan line is the lowest reasonable λ_{pn}, coming from α_{NG} with $n = 1$. Here, we observe three clear harmonic radiation thresholds.

Figure 5.13 shows p_{min} plotted against λ, determined using the same method as above, for the highly non-linear regime with $A_{\text{rel}} = 0.875$. We observe qualitatively the same behaviour as for $A_{\text{rel}} = 0.5$, namely that distinct thresholds are present, in this case for the full range of λ values plotted. However, these thresholds do not correspond as well with integer values of p_{min} predicted in Table 5.2b, with the value of p_{min} consistently higher than predicted. This less good agreement is expected, as the λ_{pn} model is derived for low relative amplitude and is hence less accurate for $A_{\text{rel}} = 0.875$. The position of the thresholds does mostly correspond with the predicted thresholds λ_{pn}, where we note in this case that the Nambu-Goto model seems to be more accurate than the sinusoidal model, in contrast with $A_{\text{rel}} = 0.5$. This also agrees with our expectations, as string configurations diverge further from the sinsoidal approximation as ε increases. Further investigation is required to fully understand the discrepancies with the predicted p_{min}, although it is likely that finite width

or relativistic effects from the higher amplitude results in behaviour that deviates from the analytic model.

5.2.4 Exponential Dependence of Massive Radiation

The results from the previous subsection clearly indicate that the mechanisms generating massive radiation are perturbative. As expected, massive radiation is only emitted in harmonic frequencies ω_p of the oscillatory source ω_0 above the frequency given by the mass threshold $\omega_m = m_H$ (see (5.7)). For this reason, massive radiation in this perturbative model is strongly suppressed with increasing mass, as confirmed numerically. Like other massive phenomena, such as Yukawa couplings and inter-string forces, we typically expect this to be exponentially suppressed, with the radiated energy per unit length, behaving as

$$p_{\text{rad}} \propto \exp\left[-\beta \frac{m_H}{\omega_0}\right], \tag{5.22}$$

where $m_H = \sqrt{\lambda}\eta$ and β is a constant to be determined.

In order to develop this model further to describe our radiating string configurations, we need to more explicitly include the amplitude of oscillation which influences how relativistic the oscillations are. A simple phenomenological model has been proposed in [176] to describe radiation from Abelian-Higgs strings in terms of the local radius of curvature of the string R. The energy radiated per unit length is given by

$$p_{\text{rad}} \propto \exp\left[-\alpha R\right], \tag{5.23}$$

where α is a constant.[3] This model and the corresponding simulations consider a fixed amplitude $A = L/2$ for sinusoidal perturbations with varying z-periodicity L, as described by (5.10). Integrating over the length L and one time period yields the overall energy of the emitted radiation

$$E_{\text{rad}} \propto \sqrt{L}\exp\left[-\alpha \frac{L}{2\pi^2}\right]. \tag{5.24}$$

We can adapt this simple model by incorporating a variable amplitude using the relative amplitude $A_{\text{rel}} = 4A/L$ (i.e. $L \to L/A_{\text{rel}}$) and the mass dependence $\alpha \propto \beta m_H$ from (5.22) to

[3] We note that this α is not related to the increased path length parameter.

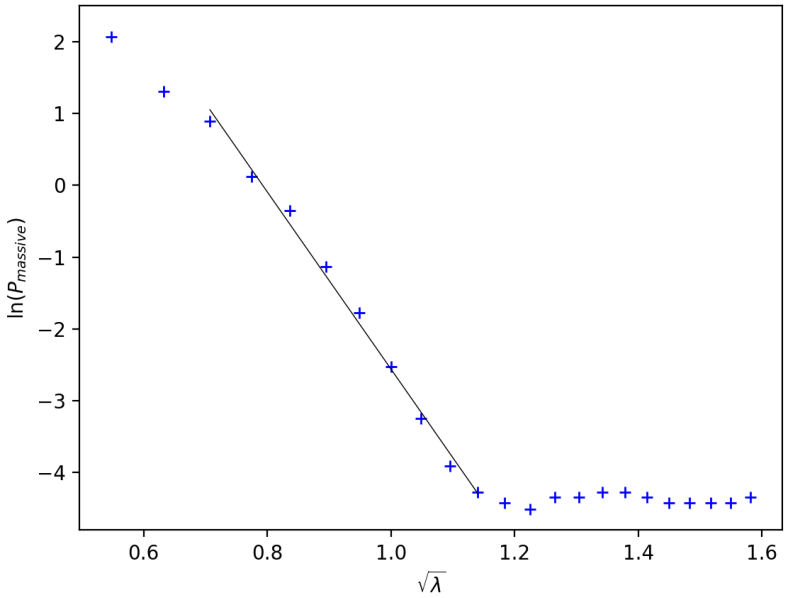

Fig. 5.14 Log-linear plot of the massive radiation diagnostic $\Pi_\phi \mathscr{D}\phi$ integrated over a diagnostic cylinder at $R = 64$ from $90 \leq t \leq 228$ (labelled P_{massive}) for $A_{\text{rel}} = 0.5$ and a range of $0.3 \leq \lambda \leq 2.5$. The black line indicates an exponential fit to the data for $0.5 \leq \lambda \leq 1.2$.

obtain the energy loss per period

$$E(L, A_{\text{rel}}, \lambda) = \sqrt{LA_{\text{rel}}} \exp\left[-\gamma\sqrt{\lambda}\frac{L}{A_{\text{rel}}}\right], \tag{5.25}$$

where γ is a constant to be determined. Other contrasting models [95] instead predict a power law decay via a primary radiation channel of massive particles.

In Figure 5.14, we plot the extracted massive signal $\Pi_\phi \mathscr{D}\phi$ integrated over time from $90 \leq t \leq 228$ for $A_{\text{rel}} = 0.5$ and $L = 32$ to obtain a quantitative estimate for the energy loss through the massive channel. Plotting the natural logarithm of the integrated signal against $\sqrt{\lambda}$, we observe a clear exponential decay from $0.7 \lesssim \sqrt{\lambda} \lesssim 1.1$ ($0.5 \lesssim \lambda \lesssim 1.2$), consistent with the prediction in (5.25). Comparing this to the power law dependence predicted by [95] using the log-log plot in Figure 5.15, we observe that the exponential model clearly provides a more accurate fit. (In any case, this would represent an extremely rapid power law fall-off.) We perform a least-squares regression, also plotted in Figure 5.14, to obtain γ from the gradient,

$$\gamma = 0.193\ (\pm\ 0.007) \tag{5.26}$$

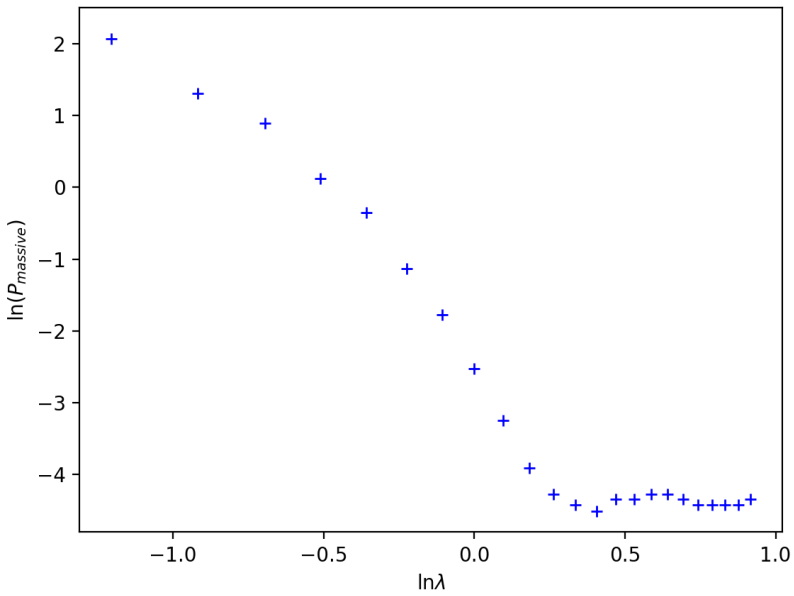

Fig. 5.15 Log-log plot of the massive radiation diagnostic $\Pi_\phi \mathscr{D}\phi$ integrated over a diagnostic cylinder at $R = 64$ from $90 \leq t \leq 228$ (labelled P_{massive}) for $A_{\text{rel}} = 0.5$ and a range of $0.3 \leq \lambda \leq 2.5$. No power law can be straightforwardly fit to the data.

and the intercept $\ln\sqrt{LA_{\text{rel}}} = 9.80\ (\pm\, 0.41)$. The root mean square error, quoted in brackets in both cases, is calculated from the accuracy of the fit and does not take into account the choice of points. We note that in this analysis, the first two points have been excluded due to finite width effects that cause slower decay, and that points with $\sqrt{\lambda} \gtrsim 1.1$ ($\lambda \gtrsim 1.3$) are also excluded because numerical resonance effects have become dominant, overtaking the physical energy loss. We further note that these numerical effects at higher λ are not significant when comparing to massless radiation as the magnitude is relatively small, and so should not have a significant effect on the simulation overall. By this stage, for $A_{\text{rel}} = 0.5$, the massive radiation is $\approx \mathscr{O}(1000)\times$ smaller than massless radiation.

Figure 5.16 shows the same extracted massive signal as above for the configuration $A_{\text{rel}} = 0.875$ and $L = 16$. We observe a far more complex λ-dependence of the decay in this highly non-linear regime, where sharp drops in the emitted energy loosely correspond with the regions encompassing the λ_{pn} thresholds. Excluding points $\lambda \leq 0.7$ due to finite width effects, we again calculate the gradient of the decay using a least-squares best fit to an exponential model, obtaining

$$\gamma = 0.229\ (\pm\, 0.026) \tag{5.27}$$

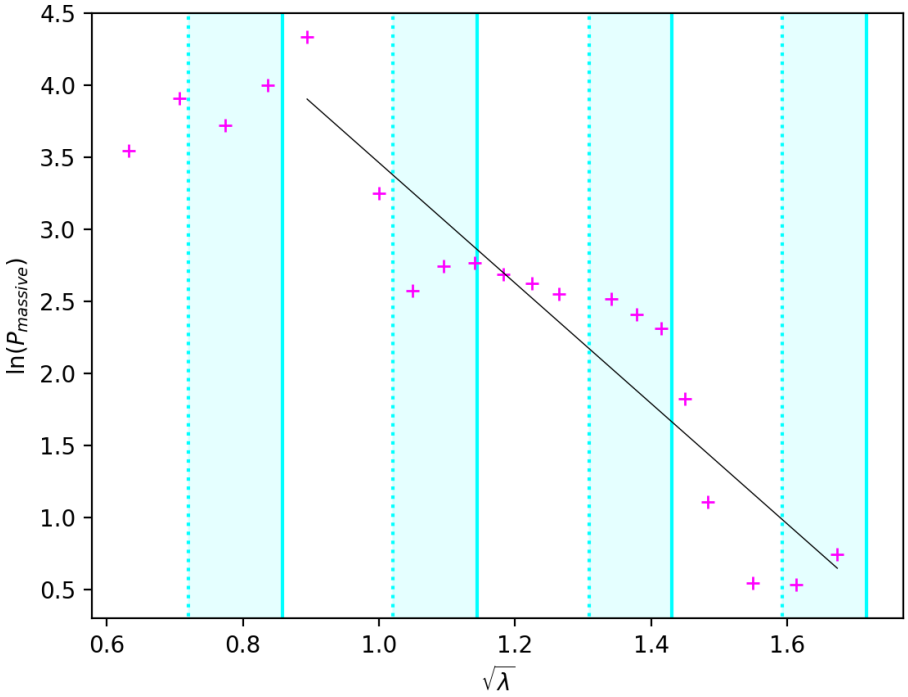

Fig. 5.16 Log-linear plot of the massive radiation diagnostic $\Pi_\phi \mathscr{D}\phi$ integrated over a diagnostic cylinder at $R = 64$ from $90 \leq t \leq 228$ (labelled $P_{massive}$) for $A_{\rm rel} = 0.875$ and a range of $0.4 \leq \lambda \leq 2.8$. The black line indicates an exponential fit to the data for $0.8 \leq \lambda \leq 2.8$. Shaded regions in cyan show the predicted thresholds λ_{pn} from Table 5.2b, where the shading encompasses the dependence on α and n; the solid cyan line represents the highest predicted λ_{pn}, coming from the $\alpha_{\rm sin}$ model with $n = 0$ for each p and the dashed cyan line is the lowest reasonable λ_{pn}, coming from $\alpha_{\rm NG}$ with $n = 1$.

and the intercept $\ln\sqrt{LA_{\rm rel}} = 7.64\ (\pm 0.62)$. The parameter γ is therefore consistent within two standard errors. Furthermore, we expect the ratio between the intercepts r to be given by $\ln(32 \times 0.5)/\ln(16 \times 0.875) \approx 1.1$. We obtain $r = 1.28 \pm 0.18$, which again agrees with the prediction.

To provide a contrasting model, fitting a power law to the same data for $A_{\rm rel} = 0.5$ plotted against $\ln(\sqrt{\lambda})$ yields the decay coefficient $\gamma_{\rm pow} \approx -13$, indicating a very large suppression. This does not fit well with claims made by the power law model that massive radiation is an important channel. Moreover, it is also inconsistent with the power law found for the $A_{\rm rel} = 0.875$ data, which gives $\gamma_{\rm pow} \approx -5$. We therefore conclude that, despite the increased complexity of the higher harmonic radiation, massive radiation is indeed exponentially suppressed even for highly non-linear configurations, in regimes where the numerics have

sufficient resolution to characterise it accurately. Further investigation is required to characterise the exponents and prefactors in (5.25) more precisely and to understand the nature of the decay for highly relativistic configurations with large amplitude $\varepsilon \approx \mathcal{O}(1)$.

Chapter 6

Towards Cusps and Networks

In this chapter, we outline work that is currently underway on relativistic string configurations, primarily global cosmic string cusps and string networks. Although the simulations presented in this chapter are in their preliminary stages, they form the basis of significant future projects to determine the gravitational wave signatures of cusps, as well as high resolution, large-scale simulations of global string networks which will yield a new accurate estimate for the dark matter axion mass. We hence present this work as an important intermediate step, as well as for physical interest in its own right.

The string network simulation in this chapter has been presented by me as part of several high profile outreach activities, including at international high performance computing conferences SC18 and SIGGRAPH 2019 to demonstrate the potential applications of exascale computing, ray-tracing and 'in-situ visualisation,' i.e. where the visualisation of data is performed as the simulation is running (discussed further in Section 6.2). The visualisation of this simulation was also presented by me in a documentary filmed by Discovery in the Department of Applied Mathematics and Theoretical Physics, University of Cambridge, which has been released online this year.[1] The visualisation was developed with Kacper Kornet and in collaboration with Jim Jeffers and Carson Brownlee of the Intel Advanced Rendering and Visualisation Team.

[1] https://www.discoveryplus.co.uk/show/universe-unravelled-with-the-stephen-hawking-centre

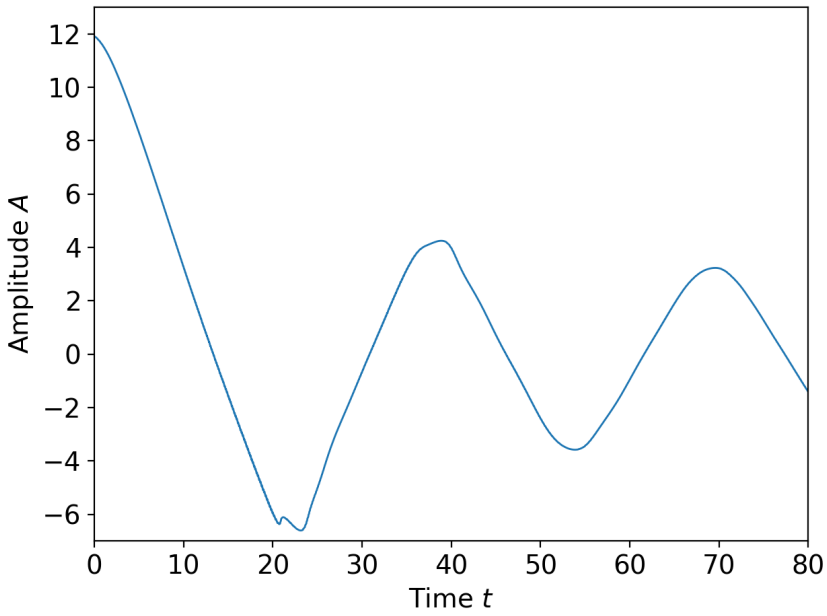

Fig. 6.1 Plot of string amplitude over time for a $\lambda = 1$ string with an initial amplitude $A_0 = 12$. At early times the string core reaches $\sim 0.99\times$ the speed of light, satisfying the condition for a cusp. The motion is subluminal on the second pass through the centre.

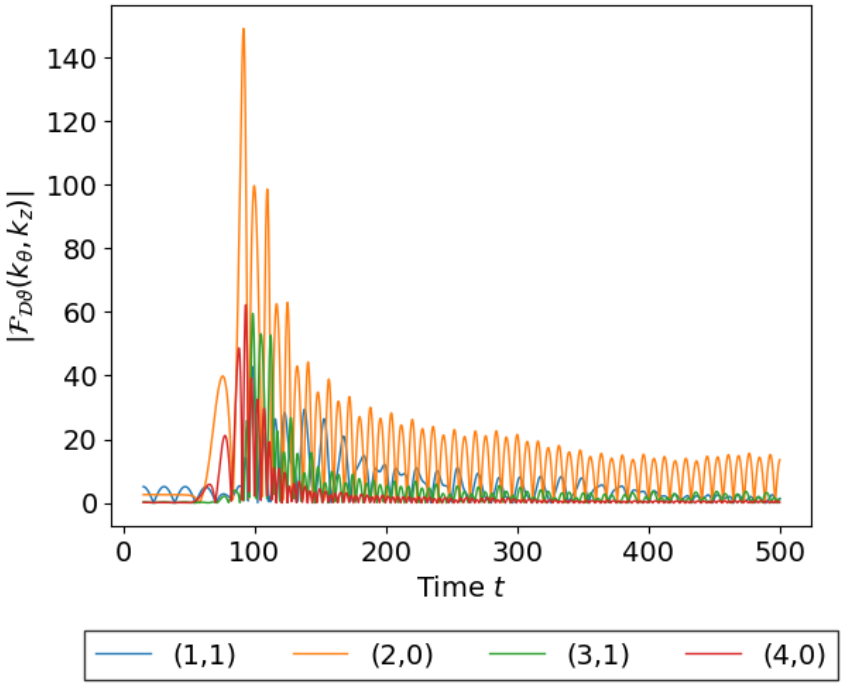

Fig. 6.2 Plot of the absolute value of the $\{mn\} = \{1\,1\}, \{2\,0\}, \{3\,1\}$, and $\{4\,0\}$ Fourier modes of the massless radiation $\mathscr{D}\vartheta \cdot \hat{\mathbf{r}}$ from a $\lambda = 1$ string with initial amplitude $A_0 = 12$, measured on a cylinder at $R = 64$.

6.1 Cusps

In this section, we present preliminary quantitative and qualitative results from simulations of global cosmic string cusps, where we define cusps to be string configurations which approach the speed of light. The simulations are carried out using `GRChombo`, with a coarse simulation box size of $256 \times 256 \times 32$, using periodic boundary conditions in the z-direction and Sommerfeld (outgoing radiation) boundary conditions in the x- and y- directions. Initial conditions are obtained using two different methods; dissipative evolution from an extreme amplitude to $A_0 = 12$ (where the string periodicity is $L \equiv N_3 = 32$), and travelling wave solutions as described in Section 3.3.2. We set $\lambda = 1$ and choose a regridding threshold $|\phi_{threshold}| = 0.25$, base grid resolution $\Delta x = 1$, base timestep $\Delta t = \Delta x/4$ and Kreiss-Oliger damping coefficient $\sigma = 1$. The simulations use a maximum of three levels of mesh refinement.

We first present results from a cusp set up using a similar method to the sinusoidal strings in Chapters 4 and 5. If the string is given a sufficient amplitude, it will approach the speed of light close to the centre of its oscillation and emit an initial burst of radiation. This is demonstrated in Figure 6.1 which plots the amplitude of a $\lambda = 1$ string with intial amplitude $A_0 = 12$ over time. The string reaches $\sim 0.99\times$ the speed of light in the early stages of the oscillation, until the position of the core reaches approximately zero. We further note that the position of the string core 'bounces' slightly at the first minimum, indicating internal core oscillations that may have become more pronounced at this high amplitude.

Figure 6.2 shows the massless signal $\mathscr{D}\vartheta \cdot \hat{\mathbf{r}}$ from which we observe, as expected, that the overall intensity of the radiation is higher than the equivalent cases with lower amplitude, for example in Figures 4.12 and 4.13. The pulse of radiation from the first oscillation has $\approx 2.5\times$ the energy of the second pulse. There is also a proportionally larger contribution from higher harmonics. However, we also note that bursts of radiation from cusps are highly directional or 'beamed.' This means that the angular Fourier decomposition naturally has higher proportions of higher angular harmonics, so it will be necessary to analyse the signal more carefully, notably the underlying frequency dependence, to determine the radiation spectrum.

Although this high initial amplitude configuration reaches approximately the speed of light and hence satisfies the condition for a cusp, as discussed in Section 3.3, these initial conditions may not produce a clean signal. For such an extreme configuration, there may not be sufficient time for the dissipative evolution to damp the internal massive oscillations to achieve an appropriate initial state, potentially resulting in an artificial initial burst of radiation that could

be difficult to separate from the true cusp signal. It is therefore of interest to explore other options for obtaining accurate cusp initial conditions. We present preliminary qualitative results obtained using the travelling wave initial conditions presented in Section 3.3.2, with two Gaussian wavepackets with amplitude $A = 4$ travelling towards each other along the string and colliding. A visualisation of these initial conditions is shown in Figure 6.3. This initial configuration is an exact solution of wave equations (2.10), therefore eliminating the uncertainty introduced with static initial conditions around the amount of dissipative evolution to apply. It also minimises any artificial radiation emitted at the start of the simulation, as the string does not need to settle to an initial configuration. Figure 6.4 shows the evolution of the position and velocity of a travelling wave configuration over time in the Nambu-Goto limit. We observe that the string instantaneously straightens out after the wavepackets collide, at which time two points on the string reach approximately the speed of light $v = 1$, as required for a cusp. These configurations become highly relativistic for any $A \geq \sqrt{e}\sigma_d$, where σ_d is the standard deviation, which is satisfied for our configuration $A = 4$ and $\sigma_d = 2$ (see Section 3.3.2).

Figure 6.5 shows an initial visualisation of the massless radiation from the collision of the Gaussian travelling waves. We observe a string self-field contribution that travels with the waves themselves, as well as a burst of radiation in the centre emitted from the collision. This qualitative result requires further analysis and investigation. These preliminary results show the ability of these AMR simulations to track the relativistic evolution of cusp-like string trajectories, as well as the efficacy of the diagnostic tools to analyse the radiation in both massive and massless channels.

6.2 Networks

In this section, we present qualitative observations from an adaptive mesh simulation of a global cosmic string network in a flat background. This has been performed as a first step towards network simulations in an expanding cosmological background. The simulation is carried out using `GRChombo` on a 128^3 grid, with periodic boundary conditions and initial conditions obtained as described in Section 3.3.3. We choose the string width $\lambda = 3$ as an appropriate intermediate between $\lambda = 1$, which has potentially large backreaction effects (as shown in previous chapters), and $\lambda \geq 10$, for which the high resolution required means that the simulation takes too long to run. We also choose a regridding threshold $|\phi_{threshold}| = 0.5$, base grid resolution $\Delta x = 1$, base timestep $\Delta t = \Delta x/100$ and Kreiss-Oliger

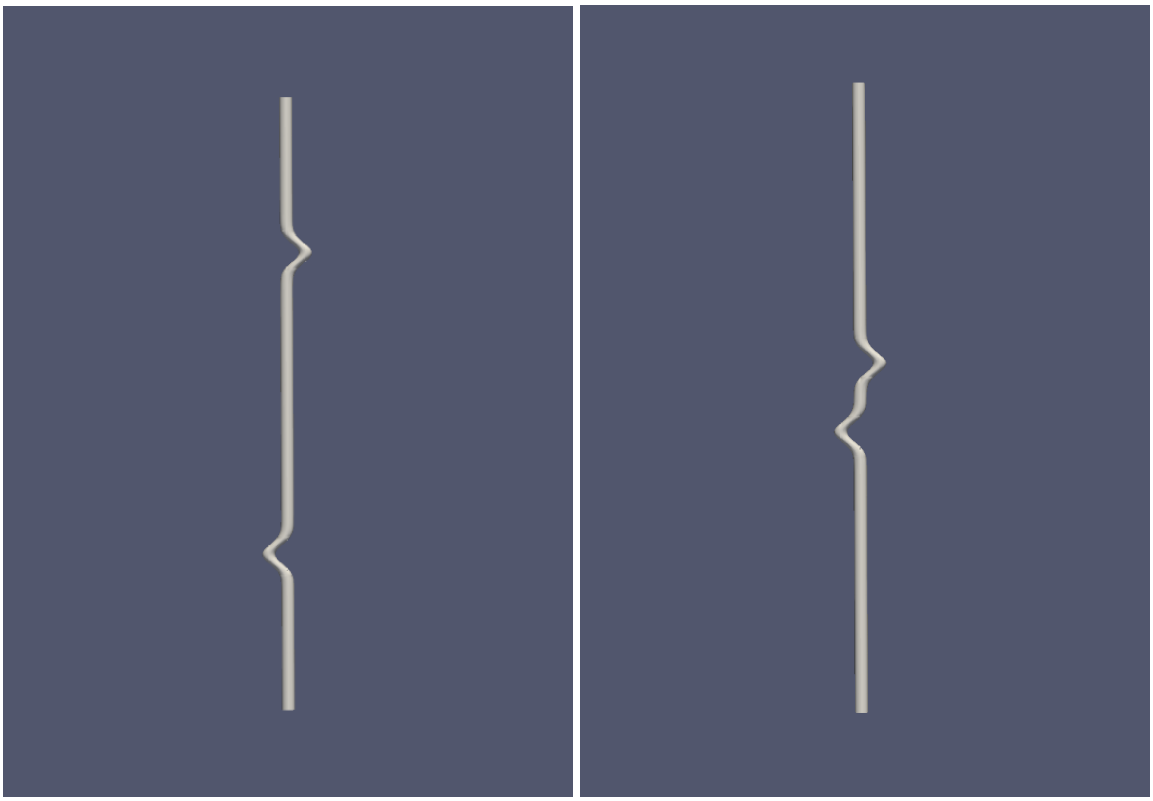

Fig. 6.3 Visualisation of initial conditions for a cosmic string cusp using two Gaussian travelling waves with $A = 4$ and standard deviation $\sigma_d = 2$ propagating along a straight $\lambda = 1$ string. The two Gaussian wavepackets start with an intial velocity towards each other and propagate along the string, where they eventually collide.

damping coefficient $\sigma = 0.3$. The simulation uses a maximum of four levels of mesh refinement. We also comment on the suitability of large string simulations for so-called 'in-situ visualisation.'

We first qualitatively outline our observations from three-dimensional visualisations of string network radiation. Figures 6.6-6.10 show volume renderings of the massive Π_ϕ and massless Π_ϑ radiation emitted from the network at different times throughout the simulation, revealing new qualitative phenomena. We note that although Π_ϑ is contaminated by the string self-field (see Section 4.1.2), it still provides a useful qualitative picture of the overall behaviour of the radiation. We observe in Figure 6.6 the network just after the start of the evolution, with a dense network of strings and string loops beginning to form. In Figure 6.7, we observe from the massive radiation that targeted bursts are beginning to be emitted from relativistic regions formed as a result of a string reconnection, which are close or equivalent to cusp configurations, as well as from collapsing loops. The massless radiation emitted is more

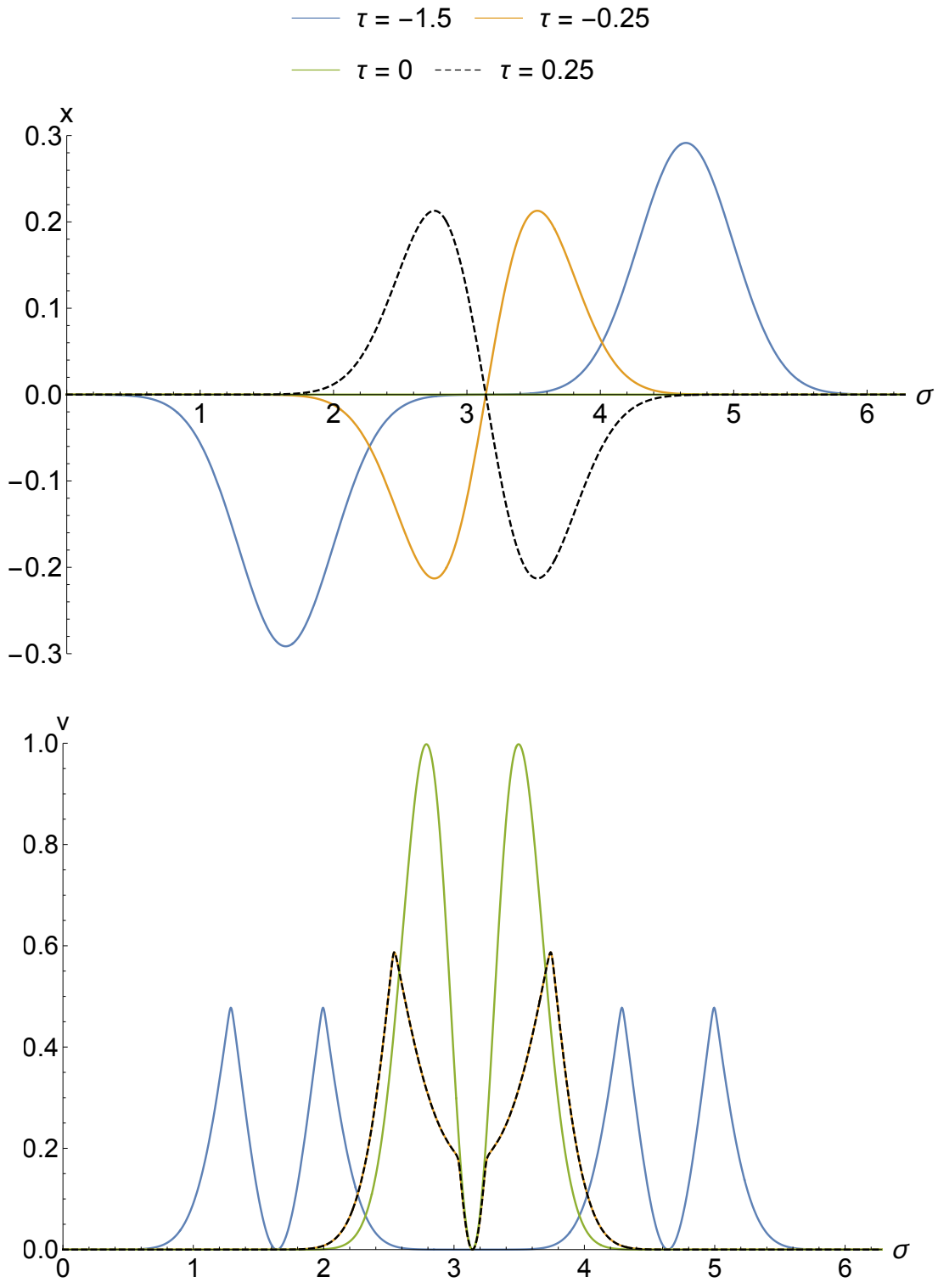

Fig. 6.4 Position x and velocity v for a travelling wave configuration with two Gaussian wavepackets with opposite sign. The configuration evolves with time τ and, as the string straightens at $\tau = 0$, two points reach approximately the speed of light $v = 1$, as required for a cusp. Here, $A = \sqrt{e}\sigma_d$, where σ_d is the standard deviation.

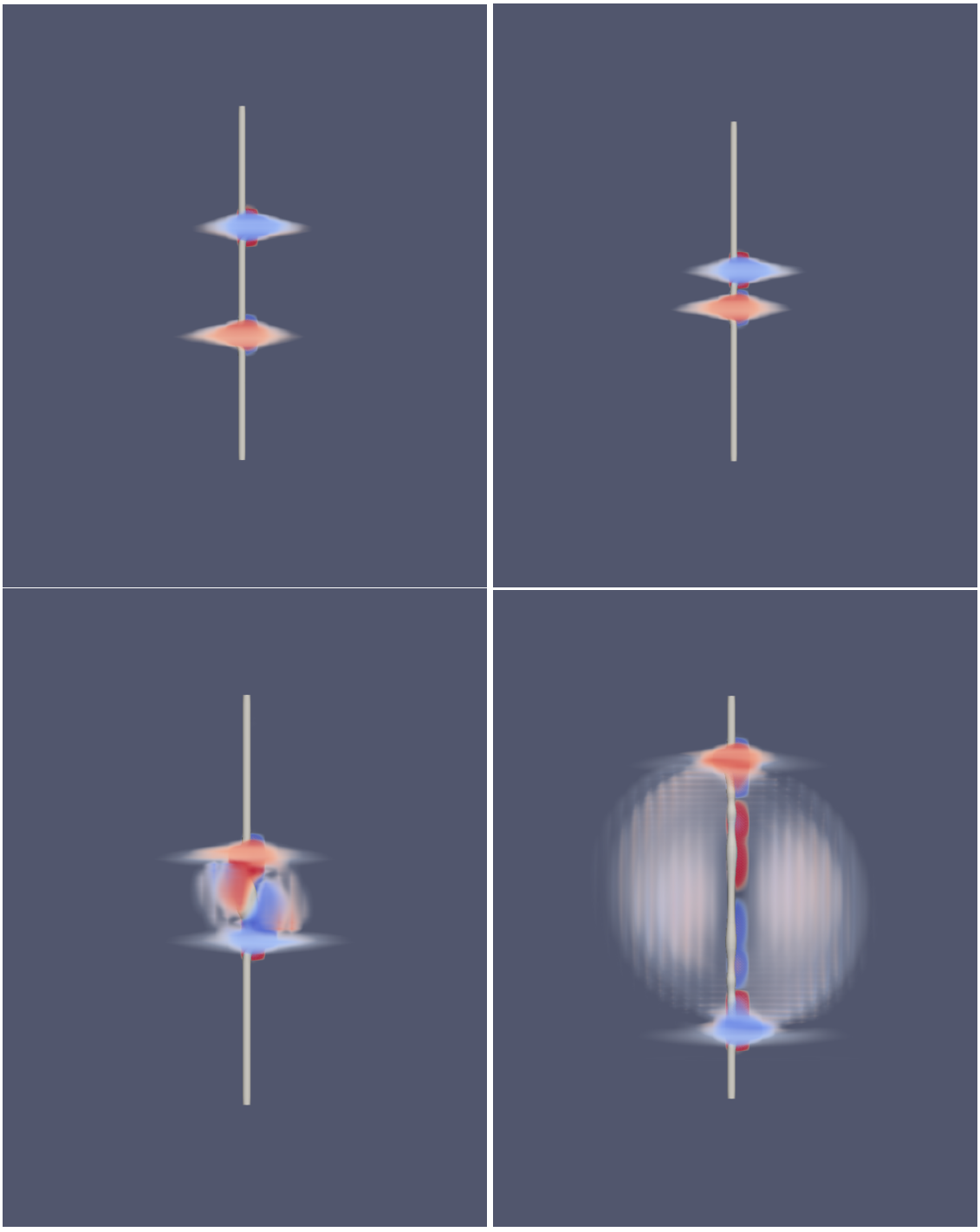

Fig. 6.5 Visualisation of the massless radiation diagnostic $\mathscr{D}\vartheta \cdot \hat{\mathbf{r}}$ from two colliding Gaussian wavepackets for a $\lambda = 1$ string over time from top to bottom, left to right.

diffuse, and is becoming increasingly significant. Figure 6.8 shows clear beamed massive signals from relativistic sections and approximately spherical signals from loop collapse. We also observe that the string network density is beginning to decrease as loops collapse and strings are annihilated. Both of these trends continue in Figure 6.9, and finally in Figure 6.10 we observe more diffuse massive and massless radiation distributed throughout the simulation box, again with a decreased density of strings. In general, we observe that massless radiation eminating from the strings is spread quite diffusely throughout the volume, whereas massive radiation is much more localised to the specific configurations described.

Several interesting qualitative conclusions can be drawn from the contrasting nature of the massive and massless radiation from a string network. Although the massive radiation signals are impressive, particularly the dramatic and explosive demise of small loops, we note that all of these massive signals are localised to regions of high curvature, on scales comparable to the string width. For regions where the string motion is coherent and the curvature is lower, massive radiation is almost entirely absent. In comparison, this is very different behaviour from the massless radiation, which is much more pervasive from all strings in the evolving networks. Whereas the simulation box is largely filled with massless radiation at the late stage in Figure 6.10, there are still many voids evident in the massive radiation due to its connection to rare non-linear string phenomena. This has important implications for the extrapolation to cosmological strings, where the existence of curved regions comparable to the string width occurs much less frequently. We can therefore expect massive radiation to be strongly suppressed and localised, especially relative to the global emission of massless modes. Using AMR network simulations, we aim to test this expectation quantitatively in the near future.

During the course of this work, we have collaborated with Intel in several areas to develop visualisation tools for large-scale HPC simulations. Work has been performed on Intel's ray-tracing visualisation package for many-core systems (OSPRay), using which the figures presented here have been created. Most significantly, AMR cosmic string network simulations provide an ideal example of a future application of in-situ visualisation and exascale computing (systems that can execute 10^{18} floating point operations per second (FLOPS)). As exascale computing develops, the visualisation of very large datasets by so-called 'post hoc' processing, i.e. loading saved data files from file systems into RAM for analysis, will become impractical, and in-situ visualisation of datasets as a simulation is running will become more important. This network simulation has been used by Intel as motivation for development

of their in-situ visualisation capabilities, demonstrated by me at the Intel CREATE event at SIGGRAPH 2019, Los Angeles, and at the Intel Booth at SC18.

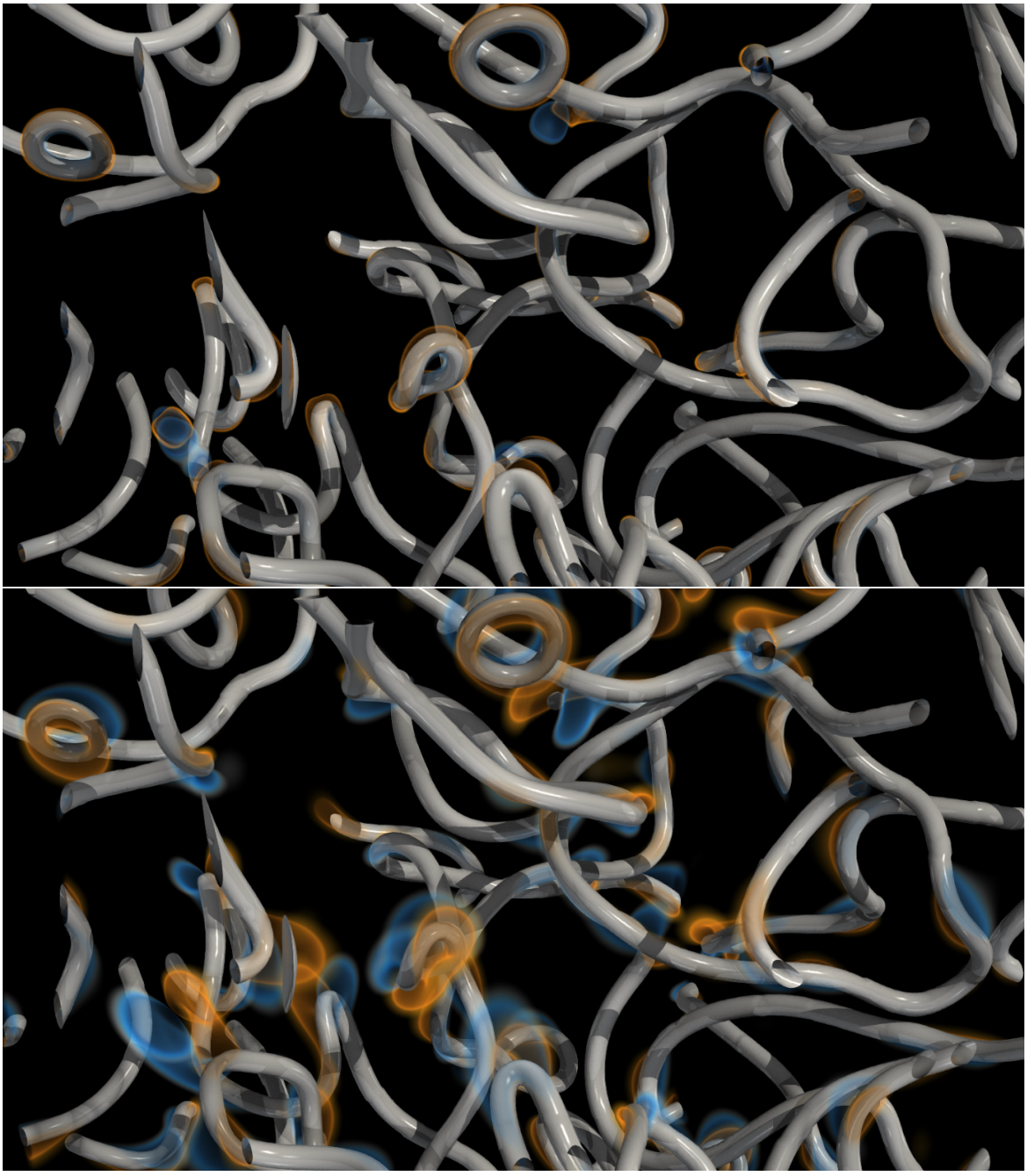

Fig. 6.6 Volume rendering in 3D space (x, y, z) of massive Π_ϕ (top) and massless Π_ϑ (bottom) radiation from a $\lambda = 3$ string network. Strings are indicated by grey contours around the cores, and both channels of radiation are indicated in blue and yellow (maxima and minima). This snapshot at $t \approx 0$ (a few timesteps after $t = 0$) essentially shows the random initial conditions for the string network. At this early stage, only high curvature regions have been accelerated, with massless radiation most evident [1/5].

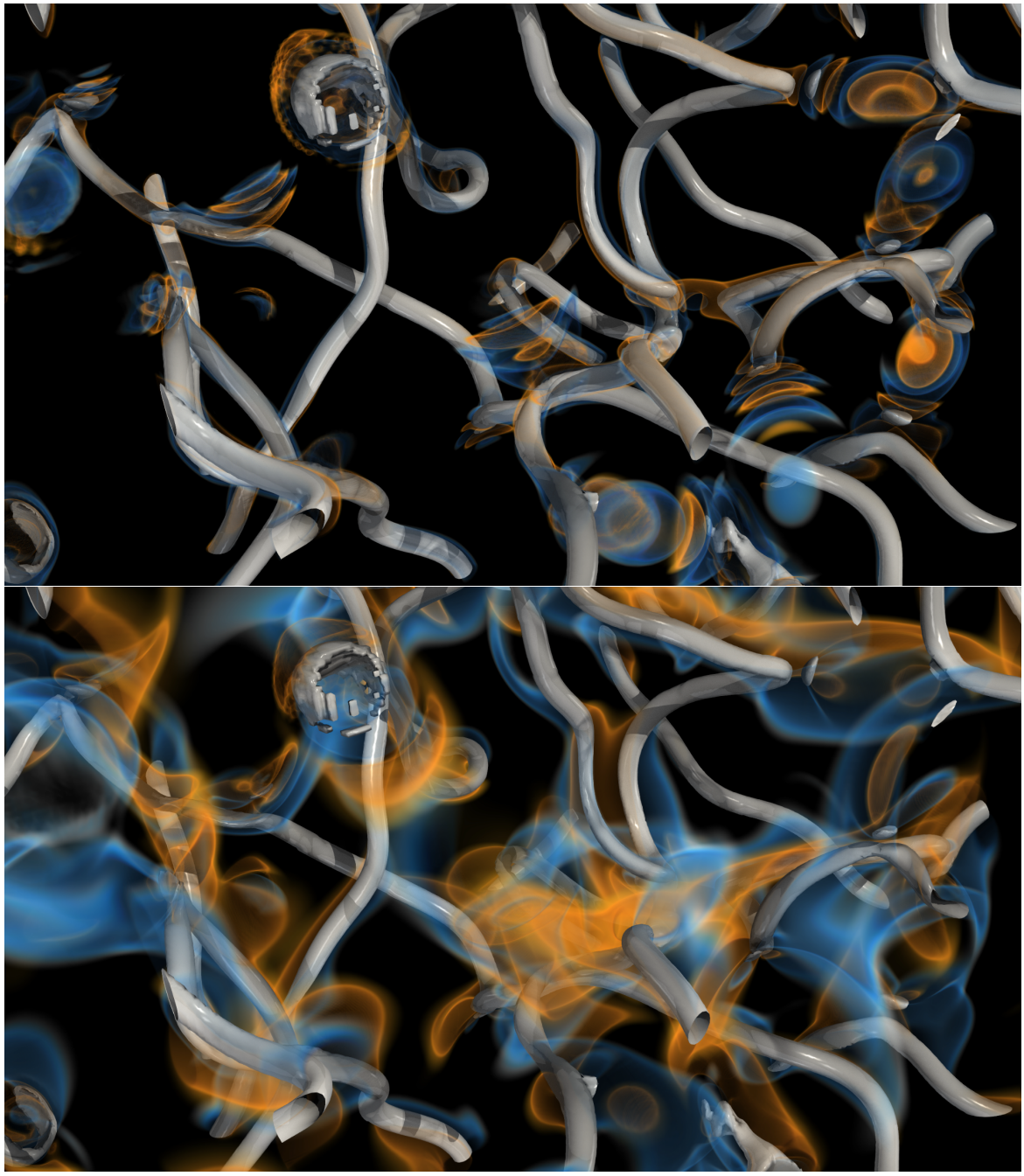

Fig. 6.7 Volume rendering in 3D space (x,y,z) of massive Π_ϕ (top) and massless Π_ϑ (bottom) radiation from a $\lambda = 3$ string network. Strings are indicated by grey contours around the cores, and both channels of radiation are indicated in blue and yellow (maxima and minima) at $t \approx 15$. Massless radiation emission is becoming generic for all moving strings, while highly non-linear regions show massive radiation in localised regions [2/5].

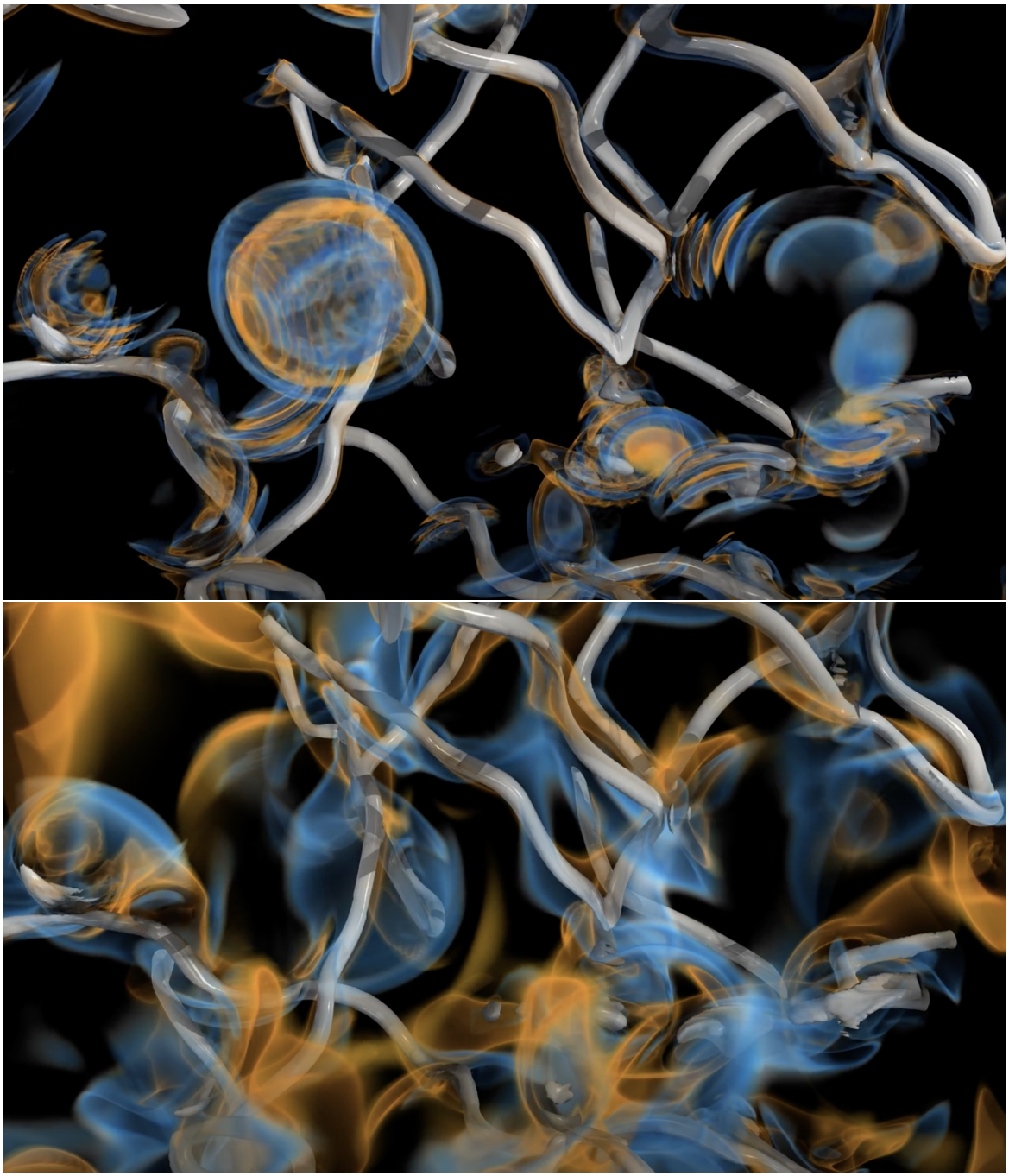

Fig. 6.8 Volume rendering in 3D space (x, y, z) of massive Π_ϕ (top) and massless Π_ϑ (bottom) radiation from a $\lambda = 3$ string network. Strings are indicated by grey contours around the cores, and both channels of radiation are indicated in blue and yellow (maxima and minima) at $t \approx 20$. Massless radiation is beginning to fill the space, with explosive shells of massive radiation resulting from the annihilation of small loops [3/5].

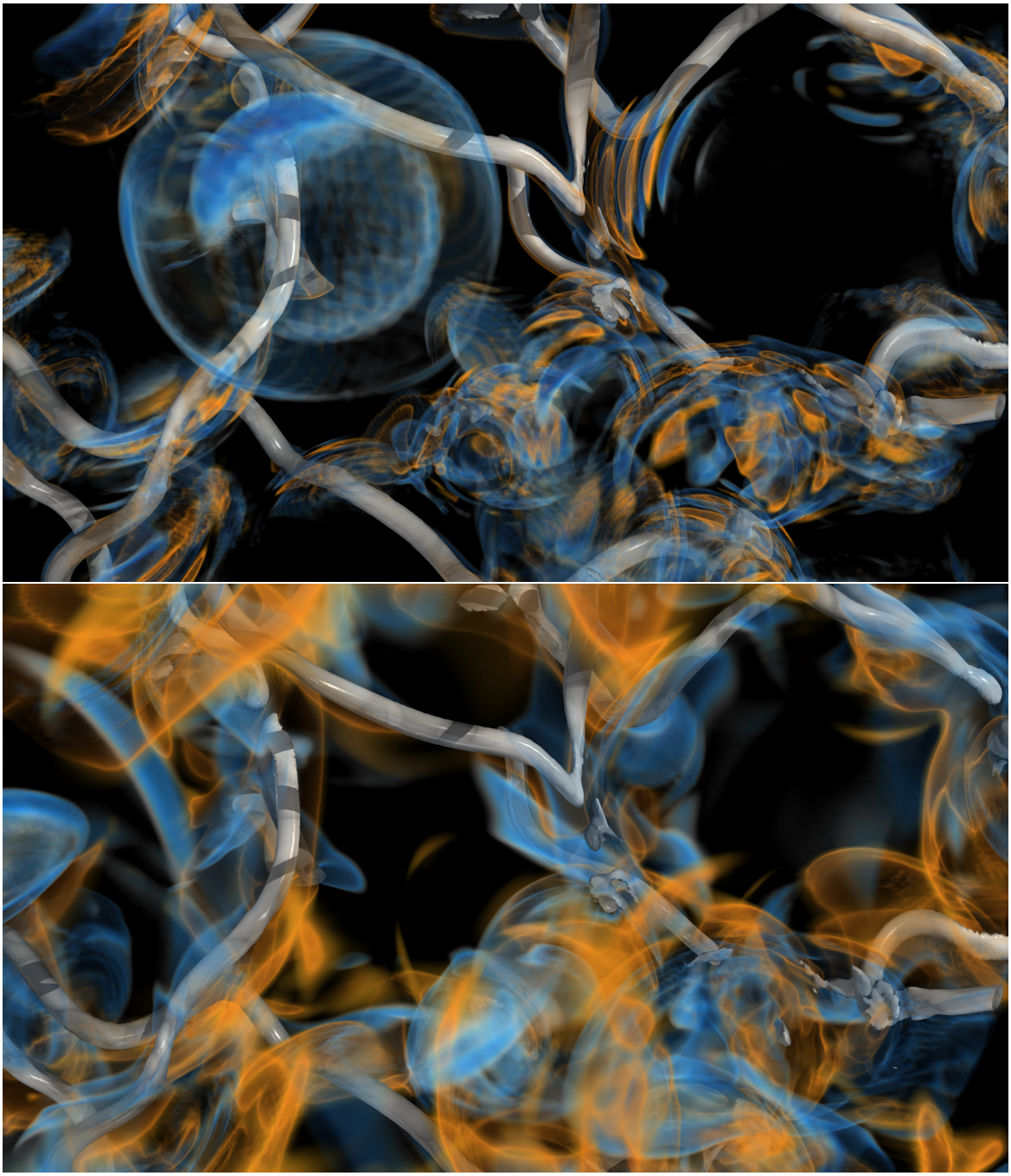

Fig. 6.9 Volume rendering in 3D space (x, y, z) of massive Π_ϕ (top) and massless Π_ϑ (bottom) radiation from a $\lambda = 3$ string network. Strings are indicated by grey contours around the cores, and both channels of radiation are indicated in blue and yellow (maxima and minima) at $t \approx 30$. Massless radiation continues to fill the space, and we observe clear indications of massive radiation from highly curved regions which are either cusp-like and highly relativistic or else aligning and self-annihilating [4/5].

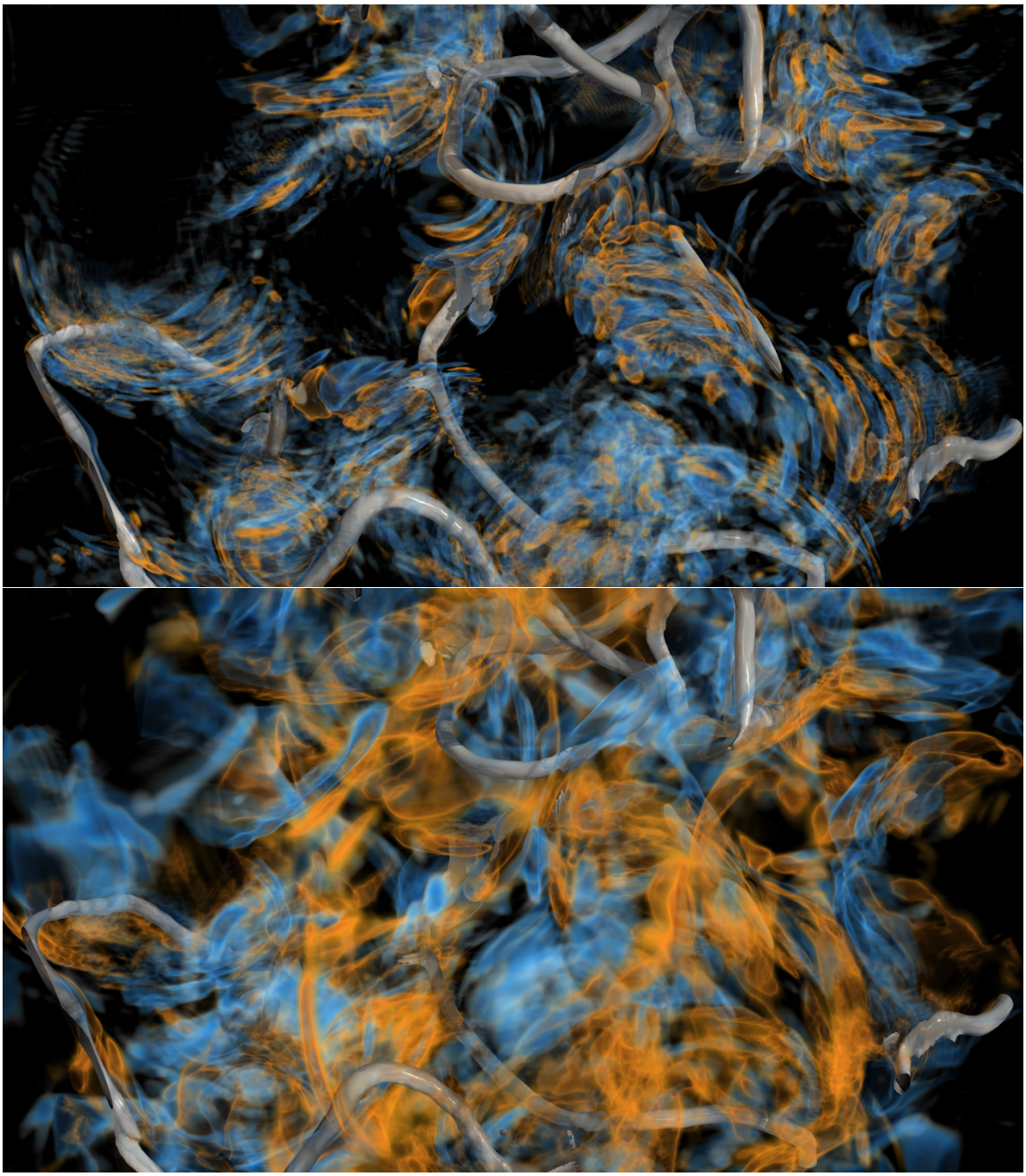

Fig. 6.10 Volume rendering in 3D space (x,y,z) of massive Π_ϕ (top) and massless Π_ϑ (bottom) radiation from a $\lambda = 3$ string network. Strings are indicated by grey contours around the cores, and both channels of radiation are indicated in blue and yellow (maxima and minima) at $t \approx 50$. Massive radiation is localised and comprised of remnants from annihilating loops and highly curved strings, unlike the generic space-filling massless radiation [5/5].

Chapter 7

Conclusion and Future Directions

In this thesis, we have presented results from the first fully adaptive mesh simulations of individual and networks of global cosmic strings, using the code `GRChombo`. We have derived quantitative diagnostics for both the massless (Goldstone boson) and massive (Higgs) radiation emitted, separating propagating modes from the string self-field. These have been used to determine the eigenmode decomposition of the radiation, along with three-dimensional visualisation to help with qualitative and quantitative interpretation of results.

We have performed a detailed analysis of the massless radiation from configurations of individual sinusoidally displaced strings, investigating a wide range of string widths defined by the parameter $1 \leq \lambda \leq 100$ and initial amplitudes $A_0 = 1, 3, 4$ and 8. We have determined that the primary radiation channel for massless radiation is the quadrupole eigenmode $\{220\}$, in agreement with analytic predictions, which dominates as the primary energy loss mechanism in comparison with higher harmonics. As the initial amplitude is increased towards the nonlinear regime with $\varepsilon \to 1$, the relative proportion of higher harmonics increases (as well as the overall magnitude of the radiation). However, there also appears to be more significant backreaction, leading to a more rapid radiation decay as the simulation progresses. The massless radiation rate at a given small amplitude is independent of λ to leading order for $L \gg \delta$, although finite size effects appear to cause some suppression around $\lambda \approx 1$.

We have also investigated in detail the effects of massless radiation backreaction, comparing oscillating string trajectories with an inverse square amplitude backreaction model [135] which uses the Nambu-Goto model and accounts for radiation energy loss. Mitigating against finite width effects, we have found excellent correspondence over the wide range $3 \lesssim \lambda \lesssim 100$

and, critically, have determined that the radiation damping rate depends inversely on the string tension $\mu = 2\pi \ln(R/\delta)$, where the string width $\delta \propto 1/\sqrt{\lambda}$. From this, we have concluded that global string evolution tends towards the behaviour predicted in the Nambu-Goto (thin-string) limit. This provides confidence that this is the appropriate large-scale (or cosmological) limit for global strings.

Furthermore, we have undertaken a detailed investigation of the massive radiation emitted from similar configurations of individual global strings. In this case, we have examined the range of widths $0.3 \leq \lambda \leq 10$ and amplitudes $A_0 = 1, 4$ and 8. We have shown that the massive radiation spectrum is significantly more complex than massless radiation, due to the mass threshold $m_H \approx \sqrt{\lambda}/\eta$ that must be overcome for modes to propagate. This leads to a complex radiation pattern with different phase and group velocities, which is highly sensitive to grid resolution. It also means that the massive channel is significantly suppressed relative to the massless channel as λ is increased. At the opposite extreme, we have also shown that relativistic configurations with low λ and high invariant amplitude ε can lead to massive radiation becoming competitive with massless channels, which is important when interpreting field theory simulations in the literature. Detailed Fourier analysis of the radiation for $0.3 \lesssim \lambda \lesssim 2.8$ has revealed distinct λ thresholds in the lowest p_{min} harmonic that is available to propagate that correspond with analytic predictions for intermediate amplitude $A_{\mathrm{rel}} = 0.5$ ($\varepsilon = 0.68$). This agreement deviates when the amplitude is increased to $A_{\mathrm{rel}} = 0.875$ ($\varepsilon = 0.96$), although radiation thresholds are still present. Finally, we have found that massive radiation is exponentially suppressed with the square root of the mass parameter λ, in agreement with an extended version of the model presented in [176], and that a power law decay model is disfavoured. This will be explored further in future work.

We have also presented quantitative and qualitative results from preliminary simulations of string cusps and networks, making particular use of three-dimensional visualisation to observe their evolution and radiation. The massless spectrum from cusps with initial conditions obtained using dissipative evolution was similar to high amplitude strings in previous chapters, as expected. However, from travelling wave initial conditions we observe a spherical 'burst' of massless radiation emitted as two Gaussian waves collide. From our simulation of a string network, we observe the emission of beamed massive signals from relativistic sections, as well as further massive bursts from the collapse of loops. Both sets of preliminary simulations will form the basis for significant future work.

Finally, we have presented contributions made towards the development and optimisation of the `GRChombo` code, including the implementation of diagnostic tools and profiling, as well as work done in collaboration with Intel on ray-tracing and in-situ visualisation.

The work presented in this thesis provides a significant step towards more accurate simulations of cosmic and axion string networks. This will enable current discrepancies in the literature of both fields to be addressed, allowing more accurate prediction of observables such as the axion mass and cosmic string gravitaional wave signatures. In the final two sections of this chapter, we outline the future directions this work will take, particularly in relation to axions and gravitational waves.

7.1 Dark Matter Axions

The present work has implications for the study of axion radiation from global axion strings in the early Universe, for scenarios in which the Peccei-Quinn $U(1)$ symmetry is broken after inflation and a network of axion strings forms. As discussed in the Introduction and Section 2.4, two approaches have been used to calculate the number and spectrum of axions radiated by such a network; first, analytic radiation modelling combined with the results of Nambu-Goto string simulations and, second, direct numerical simulations of the underlying string field theory in an expanding Universe. Our present work using field theory allows considerably higher numerical resolution than previous studies and offers some insight into the lack of agreement between these approaches. Given that most axion string network simulations to date use the comoving width (or 'fat string') algorithm, they have an effective $\lambda \lesssim 1$ when compared to the configurations investigated here. This is a regime where we are able to identify a breakdown in correspondence with predictions from the thin-string limit and is also where light massive radiation channels begin to become competitive with massless radiation for nonlinear amplitudes. Our next step forward involves high resolution simulations of global string networks in an expanding background which are currently underway. By exploring different string widths with a range of λ values and using our radiation diagnostics, we will endeavour to determine whether convergence towards the thin-string limit occurs and whether cosmological extrapolations are feasible numerically. These are important considerations which should reduce uncertainty in the present string predictions for the dark matter axion mass.

Since the network simulation presented in this thesis was run, significant optimisation work has been performed both to speed up the code itself and also to better understand choosing

appropriate regridding parameters, as discussed in Chapter 3.2. This is already a significant step towards enabling us to probe higher λ and larger grid sizes with future simulations. For the simulation presented here, the initial damping stage took of the order of weeks, which significantly limited the maximum tractable box size. From preliminary tests with the most recent code version, initial damping has been performed closer to the order of a few days for box sizes of 512^3 and 1024^3.

In future work, we will utilise AMR for axion string simulations to determine whether the assumption of Nambu-Goto behaviour on cosmological scales is accurate. Once axion string evolution has been implemented, convergence tests for AMR parameters will be carried out. This will include determination of the number of refinement levels required to accurately evolve an expanding Universe configuration whilst maximising dynamic range. Accurate diagnostics for the massless string radiation rate will be determined as for cosmic strings. Axion string network evolution will also be implemented using random global string network initial configurations and used to determine the scaling density of strings as a function of the string tension. Finally, an improved estimate of the axion mass will be obtained based on string network radiation rates, which are relevant for dark matter axion experimental searches.

7.2 Gravitational Wave Signatures

Gravitational wave signatures from astrophysical and cosmological sources have become an area of intense scientific interest since their first detection from a binary black hole merger in 2015 by LIGO. Research is currently underway into multiple other potential sources, including extreme mass ratio inspirals (EMRIs), massive black hole binaries (MBHBs), galactic binaries and stellar objects, as well as more exotic burst-type sources such as cosmic strings [54], which can also superpose to create a stochastic gravitational wave background. These have the potential to be detected not only by future generations of LIGO [94, 177–179] and Advanced LIGO [180], but by other gravitational wave experiments such as the Laser Interferometer Space Antenna (LISA) [181, 182], the Square Kilometre Array (SKA) [183], TianQin [184, 185], the Atomic Experiment for Dark Matter and Gravity Exploration (AEDGE) [186], the Atom Interferometer Observatory and Network (AION) [187] and the Einstein Telescope [188, 189]. More specifically, LISA is predicted to be able probe cosmic string tensions of $G\mu \gtrsim \mathcal{O}(10^{-17})$, improving on current constraints from pulsar timing experiments by six order of magnitude [37]. Further to this, although a stochastic

gravitational wave background has so far not been detected by LIGO [190], recent data from the NANOGrav pulsar timing experiment has shown strong evidence for such a background process [191–193], which could possibly be attributed to a cosmic string network.

One approach to determine accurate gravitational waveforms from cosmic string configurations using field theory (for example, see [194]) is to measure them directly using numerical relativity. The first such simulations of cosmic strings have been carried out by `GRChombo` collaborators to determine the gravitational wave signature from the collapse of a cosmic string loop [195]. We plan to implement cosmic string simulations in full general relativity in the near future, in particular to measure the gravitational waveform for cosmic string cusps, defined as points on a string that instantaneously reach the velocity of light [129]. These are of particular interest for local strings in cosmological scenarios, as they are predicted to arise generically on oscillating loops and at string reconnection sites, and emit a strongly beamed pulse of gravitational wave radiation [55]. This has meant that cusps have recently become an area of focus for LIGO [89] and future searches with LISA [196, 54].

Finally, despite being the most seemingly straightforward method of determining gravitational waveforms, numerical relativity involves many complexities, amongst them being choosing an appropriate gauge, damping of constraints and a large number of evolution variables which must be stored in memory. It is therefore of significant potential benefit to be able to perform simplified simulations. As outlined in Section 2.3.3, the gravitational power spectrum for local strings takes a very similar form to the massless radiation from global strings. We therefore plan to extend the work performed in Chapter 6 to calculate information about the gravitational wave spectrum of local string cusps by analysing the massless axion radiation from their global string counterparts.

References

[1] M. J. Bowick et al. The Cosmological Kibble Mechanism in the Laboratory: String Formation in Liquid Crystals. *Science*, 263(5149):943–945, 1994.

[2] T. H. R. Skyrme. Particle States of a Quantized Meson Field. *Proc. Roy. Soc.*, 262(1309):237–245, 1961.

[3] Y. Nambu. Quasi-Particles and Gauge Invariance in the Theory of Superconductivity. *Phys. Rev.*, 117(3):648–663, 1960.

[4] J. Goldstone. Field Theories with Superconductor Solutions. *Il Nuovo Cimento*, 19(1):154–164, 1961.

[5] Y. Nambu. Proceedings of Int. Conf. on *Elementary Particles*, Y. Tanikawa, ed., (Publications Office, Progress in Theoretical Physics, Kyoto). 1966.

[6] H. B. Nielsen and P. Olesen. Vortex-Line Models for Dual Strings. *Nucl. Phys. B*, 61:45–61, 1973.

[7] G. 't Hooft. Magnetic Monopoles in Unified Gauge Models. *Nucl. Phys. B*, 79(2):276–284, 1974.

[8] A. M. Polyakov. Particle Spectrum in Quantum Field Theory. *JETP Lett.*, 20(6):430–433, 1974.

[9] D. A. Kirzhnits. Weinberg Model and the 'Hot' Universe. *JETP Lett.*, 15(12):745–748, 1972.

[10] D. A. Kirzhnits and A. D. Linde. Macroscopic Consequences of the Weinberg Model. *Phys. Lett. B*, 42(4):471–474, 1972.

[11] T. W. B. Kibble. Topology of Cosmic Domains and Strings. *J. Phys. A: Math. Gen*, 9(8):1387–1398, 1976.

[12] T. Vachaspati and A. Vilenkin. Formation and Evolution of Cosmic Strings. *Phys. Rev. D*, 30(10):2036–2045, 1984.

[13] R. Jeannerot, J. Rocher, and M. Sakellariadou. How Generic is Cosmic String Formation in SUSY GUTs. *Phys. Rev. D*, 68(103514), 2003.

[14] S. Sarangi and S. H. H. Tye. Cosmic String Production Towards the End of Brane Inflation. *Phys. Lett. B*, 536(3-4):185–192, 2002.

[15] N. T. Jones, H. Stoica, and S. H. H. Tye. The Production, Spectrum and Evolution of Cosmic Strings in Brane Inflation. *Phys. Lett. B*, 563(1-2):6–14, 2003.

[16] E. J. Copeland, Myers R. C., and J. Polchinski. Cosmic F and D Strings. *JHEP*, 06(013), 2004.

[17] G. Dvali and A. Vilenkin. Formation and Evolution of Cosmic D Strings. *JCAP*, 03(010), 2004.

[18] R. D. Peccei and H. R. Quinn. CP Conservation in the Presence of Pseudoparticles. *Phys. Rev. Lett.*, 38(25):1440–1443, 1977.

[19] R. L. Davis. Cosmic Axions from Cosmic Strings. *Phys. Lett. B*, 180(3):225–230, 1986.

[20] A. Vilenkin. Cosmic Strings as Gravitational Lenses. *Astrophys. J.*, 282:L51–L53, 1984.

[21] B. Shlaer and M. Wyman. Cosmic Superstring Gravitational Lensing Phenomena: Predictions for Networks of (p,q) Strings. *Phys. Rev. D*, 72(123504), 2005.

[22] R. Brandenberger, H. Firouzjahi, and J. Karouby. Lensing and CMB Anisotropies by Cosmic Strings at a Junction. *Phys. Rev. D*, 77(083502), 2008.

[23] R. H. Brandenberger. On the Decay of Cosmic String Loops. *Nucl. Phys. B*, 293:812–828, 1987.

[24] M. Srednicki and S. Theisen. Nongravitational Decay of Cosmic Strings. *Phys. Lett. B*, 189(4):397–400, 1987.

[25] P. Bhattacharjee, C. T. Hill, and D. N. Schramm. Grand Unified Theories, Topological Defects, and Ultrahigh-Energy Cosmic Rays. *Phys. Rev. Lett.*, 69(4):567–570, 1992.

[26] T. Damour and A. Vilenkin. Cosmic Strings and the String Dilaton. *Phys. Rev. Lett.*, 78(12):2288–2291, 1997.

[27] U. F. Wichoski, J. H. MacGibbon, and R. H. Brandenberger. High Energy Neutrino, Photon, and Cosmic Ray Fluxes from VHS Cosmic Strings. *Phys. Rev. D*, 65(063005), 2002.

[28] M. Peloso and L. Sorbo. Moduli from Cosmic Strings. *Nucl. Phys. B*, 649(1-2):88–100, 2003.

[29] E. Sabancilar. Cosmological Constraints on Strongly Coupled Moduli from Cosmic Strings. *Phys. Rev. D*, 81(123502), 2010.

[30] T. Vachaspati. Cosmic Rays from Cosmic Strings with Condensates. *Phys. Rev. D*, 81(043531), 2010.

[31] A. J. Long, J. M. Hyde, and T. Vachaspati. Cosmic Strings in Hidden Sectors: 1. Radiation of Standard Model Particles. *JCAP*, 09(030), 2014.

[32] N. Kaiser and A. Stebbins. Microwave Anisotropy due to Cosmic Strings. *Nature*, 310:391–393, 1984.

[33] J. R. Gott III. Gravitational Lensing Effects of Vacuum Strings: Exact Solutions. *Astrophys. J.*, 288:422–427, 1985.

[34] A. Vilenkin. Gravitational Radiation from Cosmic Strings. *Phys. Lett. B*, 107(1-2):47–50, 1981.

[35] M. Sakellariadou. Gravitational Waves Emitted from Infinite Strings. *Phys. Rev. D*, 42(2):354–360, 1990. [Erratum: *Phys. Rev. D* 43(12):4150, 1991].

[36] Planck Collaboration. *Planck* 2013 Results. XXV. Searches for Cosmic Strings and Other Topological Defects. *Astronomy and Astrophysics*, 571(A25), 2014.

[37] P. Auclair et al. Probing the Gravitational Wave Background from Cosmic Strings with LISA. *JCAP*, 04(034), 2020.

[38] R. M. Shannon et al. Gravitational Waves from Binary Supermassive Black Holes Missing in Pulsar Observations. *Science*, 349(6255):1522–1525, 2015.

[39] P. D. Lasky et al. Gravitational-Wave Cosmology across 29 Decades in Frequency. *Phys. Rev. X*, 6(011035), 2016.

[40] J. J. Blanco-Pillado, K. D. Olum, and X. Siemens. New Limits on Cosmic Strings from Gravitational Wave Observation. *Phys. Lett. B*, 778:392–396, 2018.

[41] LIGO Scientific Collaboration and Virgo Collaboration. GW190814: Gravitational Waves from the Coalescence of a 23 Solar Mass Black Hole with a 2.6 Solar Mass Compact Object. *Astrophys. J. Lett.*, 896(2), 2020.

[42] LIGO Scientific Collaboration and Virgo Collaboration. GW190521: A Binary Black Hole Merger with a Total Mass of 150 $M_{\odot}$. *Phys. Rev. Lett.*, 125(101102), 2020.

[43] LIGO Scientific Collaboration and Virgo Collaboration. GW170104: Observation of a 50-Solar-Mass Binary Black Hole Coalescence at Redshift 0.2. *Phys. Rev. Lett.*, 118(221101), 2017. [Erratum: *Phys. Rev. Lett.* 121(129901), 2018].

[44] LIGO Scientific Collaboration and Virgo Collaboration. GW170814 : A Three-Detector Observation of Gravitational Waves from a Binary Black Hole Coalescence. *Phys. Rev. Lett.*, 119(141101), 2017.

[45] LIGO Scientific Collaboration and Virgo Collaboration. GW170608: Observation of a 19-Solar-Mass Binary Black Hole Coalescence. *Astrophys. J. Lett.*, 851(2), 2017.

[46] LIGO Scientific Collaboration and Virgo Collaboration. Observation of Gravitational Waves from a Binary Black Hole Merger. *Phys. Rev. Lett.*, 116(061102), 2016.

[47] LIGO Scientific Collaboration and Virgo Collaboration. GW151226: Observation of Gravitational Waves from a 22-Solar-Mass Binary Black Hole Coalescence. *Phys. Rev. Lett.*, 116(241103), 2016.

[48] LIGO Scientific Collaboration and Virgo Collaboration. GW170817: Observation of Gravitational Waves from a Binary Neutron Star Inspiral. *Phys. Rev. Lett.*, 119(161101), 2017.

[49] P. Amaro-Seoane et al. Laser Interferometer Space Antenna. *arXiv:1702.00786*, 2017.

[50] E. Barausse et al. Prospects for Fundamental Physics with LISA. *Gen. Rel. Grav.*, 52(81), 2020.

[51] C. Caprini et al. Science with the Space-Based Interferometer eLISA. II: Gravitational Waves from Cosmological Phase Transitions. *JCAP*, 04(001), 2016.

[52] C. Caprini and D. G. Figueroa. Cosmological Backgrounds of Gravitational Waves. *Class. Quant. Grav.*, 35(16), 2018.

[53] C. Caprini et al. Detecting Gravitational Waves from Cosmological Phase Transitions with LISA: an Update. *JCAP*, 03(024), 2020.

[54] LISA Waveform Working Group. LISA Waveform Modelling Whitepaper. *in prep.*, 2020.

[55] A. Vilenkin and E. P. S. Shellard. *Cosmic Strings and Other Topological Defects*. Cambridge University Press, 1994.

[56] T. Damour and A. Vilenkin. Gravitational Radiation from Cosmic (Super)strings: Bursts, Stochastic Background, and Observational Windows. *Phys. Rev. D*, 71(063510), 2005.

[57] T. Damour and A. Vilenkin. Gravitational Wave Bursts from Cusps and Kinks on Cosmic Strings. *Phys. Rev. D*, 64(064008), 2001.

[58] X. Siemens et al. Gravitational Wave Bursts from Cosmic (Super)strings: Quantitative Analysis and Constraints. *Phys. Rev. D*, 73(105001), 2006.

[59] S. A. Sanidas, R. A. Battye, and B. W. Stappers. Constraints on Cosmic String Tension Imposed by the Limit on the Stochastic Gravitational Wave Background from the European Pulsar Timing Array. *Phys. Rev. D*, 85(122003), 2012.

[60] P. Binétruy et al. Cosmological Backgrounds of Gravitational Waves and eLISA/NGO: Phase Transitions, Cosmic Strings and Other Sources. *JCAP*, 06(027), 2012.

[61] L. Sousa and P. P. Avelino. Probing Cosmic Superstrings with Gravitational Waves. *Phys. Rev. D*, 94(063529), 2016.

[62] S. Kuroyanagi et al. Forecast Constraints on Cosmic String Parameters from Gravitational Wave Direct Detection Experiments. *Phys. Rev. D*, 86(023503), 2012.

[63] J. J. Blanco-Pillado and K. D. Olum. Stochastic Gravitational Wave Background from Smoothed Cosmic String Loops. *Phys. Rev. D*, 96(104046), 2017.

[64] B. Allen and P. Casper. A Closed-Form Expression for the Gravitational Radiation Rate from Cosmic Strings. *Phys. Rev. D*, 50(4):2496–2518, 1994.

[65] B. Allen and R. R. Caldwell. Kinky Structure on Strings. *Phys. Rev. D*, 43(8):R2457–R2460, 1991.

[66] J. M. Wachter and K. D. Olum. Gravitational Backreaction on Piecewise Linear Cosmic String Loops. *Phys. Rev. D*, 95(023519), 2017.

[67] T. Vachaspati and A. Vilenkin. Gravitational Radiation from Cosmic Strings. *Phys. Rev. D*, 31(12):3052–3058, 1985.

[68] A. Albrecht and N. Turok. Evolution of Cosmic Strings. *Phys. Rev. Lett.*, 54(16):1868–1871, 1985.

[69] A. Albrecht and N. Turok. Evolution of Cosmic String Networks. *Phys. Rev. D*, 40(4):973–1001, 1989.

[70] D. P. Bennett and F. R. Bouchet. Cosmic String Evolution. *Phys. Rev. Lett.*, 63(26):2776–2779, 1989.

[71] B. Allen and E. P. S. Shellard. Cosmic-String Evolution: A Numerical Simulation. *Phys. Rev. Lett.*, 64(2):119–122, 1990.

[72] B. Allen and E. P. S. Shellard. Gravitational Radiation from Cosmic Strings. *Phys. Rev. D*, 45(6):1898–1912, 1992.

[73] V. Vanchurin, K. D. Olum, and A. Vilenkin. Scaling of Cosmic String Loops. *Phys. Rev. D*, 74(063527), 2006.

[74] K. D. Olum and V. Vanchurin. Cosmic String Loops in the Expanding Universe. *Phys. Rev. D*, 75(063521), 2007.

[75] J. J. Blanco-Pillado, K. D. Olum, and B. Shlaer. Large Parallel Cosmic String Simulations: New Results on Loop Production. *Phys. Rev. D*, 83:083514, 2011.

[76] J. J. Blanco-Pillado, K. D. Olum, and J. M. Wachter. Energy-Conservation Constraints on Cosmic String Loop Production and Distribution Functions. *Phys. Rev. D*, 100(123526), 2019.

[77] J. J. Blanco-Pillado and K. D. Olum. Direct Determination of Cosmic String Loop Density from Simulations. *Phys. Rev. D*, 101(103018), 2020.

[78] C. Ringeval and T. Suyama. Stochastic Gravitational Waves from Cosmic String Loops in Scaling. *JCAP*, 12(027), 2017.

[79] P. Auclair et al. Cosmic String Loop Production Functions. *JCAP*, 06(015), 2019.

[80] J. Lizarraga et al. New CMB Constraints for Abelian Higgs Cosmic Strings. *JCAP*, 10(042), 2016.

[81] S. Henrot-Versillé et al. Improved Constraint on the Primordial Gravitational-Wave Density using Recent Cosmological Data and its Impact on Cosmic String Models. *Class. Quant. Grav.*, 32(045003), 2015.

[82] A. Lazanu and E. P. S. Shellard. Constraints on the Nambu-Goto Cosmic String Contribution to the CMB Power Spectrum in Light of New Temperature and Polarisation Data. *JCAP*, 02(024), 2015.

[83] C. J. A. P. Martins and E. P. S. Shellard. Fractal Properties and Small-Scale Structure of Cosmic String Networks. *Phys. Rev. D*, 73(043515), 2006.

[84] C. J. A. P. Martins and E. P. S. Shellard. Scale-Invariant String Evolution with Friction. *Phys. Rev. D*, 53(2):R575–R579, 1996.

[85] C. J. A. P. Martins and E. P. S. Shellard. Quantitative String Evolution. *Phys. Rev. D*, 54(4):2535–2556, 1996.

[86] C. J. A. P. Martins and E. P. S. Shellard. Extending the Velocity-Dependent One-scale String Evolution Model. *Phys. Rev. D*, 65(043514), 2002.

[87] C. J. A. P Martins et al. Generalised Velocity-Dependent One-Scale Model for Current-Carrying Strings. *arXiv:2011.09700*, 2020.

[88] P. Auclair. Impact of the Small-Scale Structure on the Stochastic Background of Gravitational Waves from Cosmic Strings. *JCAP*, 11(050), 2020.

[89] LIGO Scientific Collaboration and Virgo Collaboration. Constraints on Cosmic Strings using Data from the First Advanced LIGO Observing Run. *Phys. Rev. D*, 97(102002), 2018.

[90] J. J. Blanco-Pillado, K. D. Olum, and B. Shlaer. The Number of Cosmic String Loops. *Phys. Rev. D*, 89(023512), 2014.

[91] L. Lorenz, C. Ringeval, and M. Sakellariadou. Cosmic String Loop Distribution on All Length Scales and at Any Redshift. *JCAP*, 10(003), 2010.

[92] C. Ringeval, M. Sakellariadou, and F. Bouchet. Cosmological Evolution of Cosmic String Loops. *JCAP*, 02(023), 2007.

[93] J. M. Wachter and K. D. Olum. Gravitational Smoothing of Kinks on Cosmic String Loops. *Phys. Rev. Lett.*, 118(051301), 2017. [Erratum: *Phys. Rev. Lett.* 121(149901), 2018].

[94] LIGO Scientific Collaboration and Virgo Collaboration. Search for the Isotropic Stochastic Background using Data from Advanced LIGO's Second Observing Run. *Phys. Rev. D*, 100(061101(R)), 2019.

[95] G. Vincent, N. D. Antunes, and M. Hindmarsh. Numerical Simulations of String Networks in the Abelian-Higgs Model. *Phys. Rev. Lett.*, 80(11):2277–2280, 1998.

[96] M. Hindmarsh, S. Stuckey, and N. Bevis. Abelian Higgs Cosmic Strings: Small-Scale Structure and Loops. *Phys. Rev. D*, 79(123504), 2009.

[97] M. Hindmarsh et al. Scaling from Gauge and Scalar Radiation in Abelian-Higgs String Networks. *Phys. Rev. D*, 96(023525), 2017.

[98] D. Harari and P. Sikivie. On the Evolution of Global Strings in the Early Universe. *Phys. Lett. B*, 195(3):361–365, 1987.

[99] R. L. Davis and E. P. S. Shellard. Do Axions Need Inflation? *Nucl. Phys. B*, 324(1):167–186, 1989.

[100] R. A. Battye and E. P. S. Shellard. Axion String Constraints. *Phys. Rev. Lett.*, 73(22):2954–2957, 1994. [Erratum: *Phys. Rev. Lett.* 76(12):2203-2204, 1996].

[101] M. Yamaguchi, M. Kawasaki, and J. Yokoyama. Evolution of Axionic Strings and Spectrum of Axions Radiated from Them. *Phys. Rev. Lett.*, 82(23):4578–4581, 1999.

[102] J. N. Moore, E. P. S. Shellard, and C. J. A. P. Martins. Evolution of Abelian-Higgs String Networks. *Phys. Rev. D*, 65(023503), 2001.

[103] T. Hiramatsu et al. Production of Dark Matter Axions from Collapse of String-Wall Systems. *Phys. Rev. D*, 85(105020), 2012. [Erratum: *Phys. Rev. D* 86(089902), 2012].

[104] G. D. Moore. Axion Dark Matter and the Lattice. *EPJ Web Conf., 35th International Symposium on Lattice Field Theory (Lattice 2017)*, 175(01009), 2018.

[105] M. Gorghetto, E. Hardy, and G. Villadoro. Axions from Strings: the Attractive Solution. *JHEP*, 07(151), 2018.

[106] M. Kawasaki et al. Long-Term Dynamics of Cosmological Axion Strings. *PTEP*, 2018(9):091E01, 2018.

[107] M. Hindmarsh et al. Scaling Density of Axion Strings. *Phys. Rev. Lett.*, 124(021301), 2020.

[108] R. Battye and A. Moss. Updated Constraints on the Cosmic String Tension. *Phys. Rev. D*, 82(023521), 2010.

[109] D. Matsunami et al. Decay of Cosmic String Loops due to Particle Radiation. *Phys. Rev. Lett.*, 122(201301), 2019.

[110] P. Auclair, D. A. Steer, and T. Vachaspati. Particle Emission and Gravitational Radiation from Cosmic Strings: Observational Constraints. *Phys. Rev. D*, 101(083511), 2020.

[111] J. Preskill, M. B. Wise, and F. Wilczek. Cosmology of the Invisible Axion. *Phys. Lett. B*, 120(1-3):127–132, 1983.

[112] A. Ringwald and K. Saikawa. Axion Dark Matter in the Post-Inflationary Peccei-Quinn Symmetry Breaking Scenario. *Phys. Rev. D*, 93(085031), 2016. [Erratum: *Phys. Rev. D* 94(049908), 2016].

[113] M. Kawasaki, K. Saikawa, and T. Sekiguchi. Axion Dark Matter from Topological Defects. *Phys. Rev. D*, 91(065014), 2015.

[114] L. Fleury and G. D. Moore. Axion Dark Matter: Strings and their Cores. *JCAP*, 01(004), 2016.

[115] L. M. Fleury and G. D. Moore. Axion String Dynamics I: 2+1D. *JCAP*, 05(005), 2016.

[116] G. D. Moore. Intercommutation of U(1) Global Cosmic Strings. *arXiv:1604.02356*, 2016.

[117] V. B. Klaer and G. D. Moore. The Dark-Matter Axion Mass. *JCAP*, 11(049), 2017.

[118] S. Beurthey et al. MADMAX Status Report. *arXiv:2003.10894*, 2020.

[119] J. Redondo. *Dark Matter through the Looking Glass: the MADMAX Experiment*. HEP/GR Colloquium delivered 13/05/2020 at the Department of Applied Mathematics and Theoretical Physics, University of Cambridge.

[120] D. J. E. Marsh. Axion Cosmology. *Phys. Rept.*, 643:1–79, 2016.

[121] K. Clough et al. `GRChombo`: Numerical Relativity with Adaptive Mesh Refinement. *Class. Quant. Grav.*, 32(245011), 2016.

[122] M. Adams et al. Chombo Software Package for AMR Applications - Design Document. *Lawrence Berkeley National Laboratory Technical Report LBNL-6616E*, 2015.

[123] P. W. Higgs. Broken Symmetries, Massless Particles and Gauge Fields. *Phys. Lett.*, 12(2):132–133, 1964.

[124] H. B. Nielsen and P. Olesen. On the Magnetic Properties of Superconductors of the Second Group. *Sov. Phys. JETP*, 5(6):1174–1182, 1957.

[125] Y. Nambu. Proceedings of Int. Conf. on *Symmetries & Quark Models* (Wayne State University), Lectures at the Copenhagen Summer Symposium. 1970.

[126] T. Gotō. Relativistic Quantum Mechanics of a One-Dimensional Mechanical Continuum and Subsidiary Condition of Dual Resonance Model. *Prog. Theor. Phys.*, 46(5):1560–1569, 1971.

[127] M. Kalb and P. Ramond. Classical Direct Interstring Action. *Phys. Rev. D*, 9(8):2273–2284, 1974.

[128] T. W. B. Kibble and N. G. Turok. Self-Intersection of Cosmic Strings. *Phys. Lett. B*, 116(2-3):141–143, 1982.

[129] N. Turok. Grand Unified Strings and Galaxy Formation. *Nucl. Phys. B*, 242(2):520–541, 1984.

[130] N. Turok and P. Bhattacharjee. Stretching Cosmic Strings. *Phys. Rev. D*, 29(8):1557–1562, 1984.

[131] E. Witten. Cosmic Superstrings. *Phys. Lett. B*, 153(4-5):243–246, 1985.

[132] A. Vilenkin and T. Vachaspati. Radiation of Goldstone Bosons from Cosmic Strings. *Phys. Rev. D*, 35(4):1138–1140, 1987.

[133] R. L. Davis and E. P. S. Shellard. Antisymmetric Tensors and Spontaneous Symmetry Breaking. *Phys. Lett. B*, 214(2):219–222, 1988.

[134] D. Garfinkle and T. Vachaspati. Radiation from Kinky, Cuspless Cosmic Loops. *Phys. Rev. D*, 36(8):2229–2241, 1987.

[135] R. A. Battye and E. P. S. Shellard. Global String Radiation. *Nucl. Phys. B*, 423(1):260–304, 1994.

[136] M. Sakellariadou. Radiation of Nambu-Goldstone Bosons from Infinitely Long Cosmic Strings. *Phys. Rev. D*, 44(12):3767–3773, 1991.

[137] C. J. Burden. Gravitational Radiation from a Particular Class of Cosmic Strings. *Phys. Lett. B*, 164(4-6):277–281, 1985.

[138] G. Ballesteros et al. Standard Model-Axion-Seesaw-Higgs Portal Inflation. Five Problems of Particle Physics and Cosmology Solved in One Stroke. *JCAP*, 08(001), 2017.

[139] O. Wantz and E. P. S. Shellard. Axion Cosmology Revisited. *Phys. Rev. D*, 82(123508), 2010.

[140] R. A. Battye and E. P. S. Shellard. Radiative Backreaction on Global Strings. *Phys. Rev. D*, 53(4):1811–1826, 1996.

[141] W. H. Press, B. S. Ryden, and D. N. Spergel. Dynamical Evolution of Domain Walls in an Expanding Universe. *Astrophys. J.*, 347:590–604, 1989.

[142] V. B. Klaer and G. D. Moore. How to Simulate Global Cosmic Strings with Large String Tension. *JCAP*, 10(043), 2017.

[143] G. J. Verbiest and A. Achúcarro. High Speed Collision and Reconnection of Abelian Higgs Strings in the Deep Type-II Regime. *Phys. Rev. D*, 84(105036), 2011.

[144] T. Goodale et al. The Cactus Framework and Toolkit: Design and Applications. *Vector and Parallel Processing – VECPAR 2002, 5th International Conference, Lecture Notes in Computer Science*, Springer, 2003.

[145] F. Loffler et al. The Einstein Toolkit: A Community Computational Infrastructure for Relativistic Astrophysics. *Class. Quant. Grav.*, 29(115001), 2012.

[146] J. D. Brown et al. Turduckening Black Holes: an Analytical and Computational Study. *Phys. Rev. D*, 79(044023), 2009.

[147] Kranc: Kranc Assembles Numerical Code. *http://kranccode.org/*.

[148] T. W. Baumgarte and S. L. Shapiro. On the Numerical Integration of Einstein's Field Equations. *Phys. Rev. D*, 59(024007), 1999.

[149] M. Shibata and T. Nakamura. Evolution of Three-Dimensional Gravitational Waves: Harmonic Slicing Case. *Phys. Rev. D*, 52(10):5428–5444, 1995.

[150] U. Sperhake. Binary Black-Hole Evolutions of Excision and Puncture Data. *Phys. Rev. D*, 76(104015), 2007.

[151] M. Zilhao et al. Numerical Relativity for D Dimensional Axially Symmetric Space-Times: Formalism and Code Tests. *Phys. Rev. D*, 81(084052), 2010.

[152] P. Marronetti et al. Binary Black Holes on a Budget: Simulations using Workstations. *Class. Quant. Grav.*, 24(12):S43–S58, 2007.

[153] P. Galaviz, B. Brügmann, and Z. Cao. Numerical Evolution of Multiple Black Holes with Accurate Initial Data. *Phys. Rev. D*, 82(024005), 2010.

[154] M. Kunesch. Numerical Simulations of Instabilities in General Relativity. *Doctoral Thesis*, 2018.

[155] K. Clough, T. Dietrich, and J. C. Niemeyer. Axion Star Collisions with Black Holes and Neutron Stars in Full 3D Numerical Relativity. *Phys. Rev. D*, 98(083020), 2018.

[156] T. Helfer, J. C. Aurrekoetxea, and E. A. Lim. Cosmic String Loop Collapse in Full General Relativity. *Phys. Rev. D*, 99(104028), 2019.

[157] K. Clough et al. Robustness of Inflation to Inhomogeneous Initial Conditions. *JCAP*, 09(025), 2017.

[158] K. Clough, R. Flauger, and E. A. Lim. Robustness of Inflation to Large Tensor Perturbations. *JCAP*, 05(065), 2018.

[159] T. Helfer et al. Black Hole Formation from Axion Stars. *JCAP*, 03(055), 2017.

[160] P. Figueras, M. Kunesch, and S. Tunyasuvunakool. End Point of Black Ring Instabilities and the Weak Cosmic Censorship Conjecture. *Phys. Rev. Lett.*, 116(071102), 2016.

[161] J. Y. Widdicombe et al. Formation of Relativistic Axion Stars. *JCAP*, 10(005), 2018.

[162] P. Figueras et al. End Point of the Ultraspinning Instability and Violation of Cosmic Censorship. *Phys. Rev. Lett.*, 118(151103), 2017.

[163] T. Helfer et al. Gravitational Wave Emission from Collisions of Compact Scalar Solitons. *Phys. Rev. D*, 99(044046), 2019.

[164] K. Clough and E. A. Lim. Critical Phenomena in Non-spherically Symmetric Scalar Bubble Collapse. *arXiv:1602.02568*, 2016.

[165] J. Alexandre and K. Clough. Black Hole Interference Patterns in Flavour Oscillations. *Phys. Rev. D*, 98(043004), 2018.

[166] C. Joana and J. Clesse. Inhomogeneous Initial Conditions for Inflation: A Wibbly-Wobbly Timey-Wimey Path to Salvation. *arXiv:2011.12190*, 2020.

[167] J. Bamber et al. Growth of Accretion Driven Scalar Hair around Kerr Black Holes. *arXiv:2011.07870*, 2020.

[168] M. Berger and I. Rigoutsos. An Algorithm for Point Clustering and Grid Generation. *IEEE Transactions on Systems, Man and Cybernetics*, 21(5):1278–1286, 1991.

[169] M. J. Berger and P. Colella. Local Adaptive Mesh Refinement for Shock Hydrodynamics. *J. Comp. Phys.*, 82(1):64–84, 1989.

[170] M. J. Berger and J. Oliger. Adaptive Mesh Refinement for Hyperbolic Partial Differential Equations. *J. Comp. Phys.*, 53(3):484–512, 1984.

[171] M. Alcubierre. *Introduction to 3+1 Numerical Relativity*. Oxford Science Publications, 2008.

[172] H.-O. Kreiss and J. Oliger. Comparison of Accurate Methods for the Integration of Hyperbolic Equations. *Tellus*, 24(3):199–215, 1972.

[173] Vachaspati and T. Vachaspati. Travelling Waves on Domain Walls and Cosmic Strings. *Phys. Lett. B*, 238(1):41–44, 1990.

[174] A. Drew and E. P. S. Shellard. Radiation from Global Topological Strings using Adaptive Mesh Refinement: Methodology and Massless Modes. *arXiv:1910.01718*, 2019.

[175] A. Drew and E. P. S. Shellard. Radiation from Global Topological Strings using Adaptive Mesh Refinement: Massive Modes. *in prep.*, 2020.

[176] K. D. Olum and J. J. Blanco-Pillado. Radiation from Cosmic String Standing Waves. *Phys. Rev. Lett.*, 84(19):4288–4291, 2000.

[177] LIGO Scientific Collaboration. Exploring the Sensitivity of Next Generation Gravitational Wave Detectors. *Class. Quant. Grav.*, 34(044001), 2017.

[178] E. Thrane and J. D. Romano. Sensitivity Curves for Searches for Gravitational-Wave Backgrounds. *Phys. Rev. D*, 88(124032), 2013.

[179] LIGO Scientific Collaboration and Virgo Collaboration. GW150914: Implications for the Stochastic Gravitational Wave Background from Binary Black Holes. *Phys. Rev. Lett.*, 116(131102), 2016.

[180] The LIGO Scientific Collaboration. Advanced LIGO. *Class. Quant. Grav.*, 32(074001), 2015.

[181] N. Bartolo et al. Science with the Space-Based Interferometer LISA. IV: Probing Inflation with Gravitational Waves. *JCAP*, 12(026), 2016.

[182] C. Caprini et al. Reconstructing the Spectral Shape of a Stochastic Gravitational Wave Background with LISA. *JCAP*, 11(017), 2019.

[183] G.H. Janssen et al. Gravitational Wave Astronomy with the SKA. *Proc. of Science*, AASKA14(037), 2014.

[184] J. Luo et al. TianQin: a Space-Borne Gravitational Wave Detector. *Class. Quant. Grav.*, 33(035010), 2016.

[185] J. Mei et al. The TianQin Project: Current Progress on Science and Technology. *PTEP*, 2020(0000), 2020.

[186] Y. A. El-Neaj et al. AEDGE: Atomic Experiment for Dark Matter and Gravity Exploration in Space. *EPJ Quant. Technol.*, 7(6), 2020.

[187] L. Badurina et al. AION: An Atom Interferometer Observatory and Network. *JCAP*, 05(011), 2020.

[188] M. Punturo et al. The Einstein Telescope: A Third-Generation Gravitational Wave Observatory. *Class. Quant. Grav.*, 27(194002), 2010.

[189] S. Hild et al. Sensitivity Studies for Third-Generation Gravitational Wave Observatories. *Class. Quant. Grav.*, 28(094013), 2011.

[190] LIGO Scientific Collaboration and Virgo Collaboration. Upper Limits on the Stochastic Gravitational-Wave Background from Advanced LIGO's First Observing Run. *Phys. Rev. Lett.*, 118(121101), 2017. [Erratum: *Phys. Rev. Lett.* 119(029901), 2017].

[191] J. Ellis and M. Lewicki. Cosmic String Interpretation of NANOGrav Pulsar Timing Data. *arXiv:2009.06555*, 2020.

[192] S. Blasi, V. Brdar, and K. Schmitz. Has NANOGrav found First Evidence for Cosmic Strings? *arXiv:2009.06607*, 2020.

[193] Z. Arzoumanian et al. The NANOGrav 12.5-Year Data Set: Search for an Isotropic Stochastic Gravitational-Wave Background. *arXiv:2009.04496*, 2020.

[194] K. D. Olum and J. J. Blanco-Pillado. Field Theory Simulation of Abelian-Higgs Cosmic String Cusps. *Phys. Rev. D*, 60(023503), 1999.

[195] J. C. Aurrekoetxea, T. Helfer, and E. A. Lim. Coherent Gravitational Waveforms and Memory from Cosmic String Loops. *Class. Quant. Grav.*, 37(204001), 2020.

[196] S. Babak et al. Fundamental Physics and Cosmology with LISA. *Class. Quant. Grav.*, 28(114001), 2011.